The Astrophysics of Relativistic Radio Transients

Lauren E. Rhodes
St Catherine's College
University of Oxford

A thesis submitted for the degree of
Doctor of Philosophy

Trinity 2022

Statement of Originality

This work presented in this thesis is all original research completed by myself. Any methodology or results used to compliment my work is properly cited. At the beginning of each chapter, any work that is in preparation or accepted for publication in a peer-reviewed academic journal is stated as such. The work presented in this thesis has not been submitted as part of any other degree at the University of Oxford or any other university.

For Mum and Dad

Acknowledgements

Firstly, I would like to thank my supervisor Rob Fender for his support and inspiration over my DPhil. I look forward to working with him for the next three years during my post-doctoral research associate position at Oxford Astrophysics. I am incredibly grateful to my parents for their endless support throughout my education. Without them, I would not be where I am today. Many thanks go to Sara Motta, Dave Williams and Joe Bright. Over the past three years, they have been not only excellent colleagues but have become close friends. They have taught me so much, made me a better researcher, and fuelled my caffeine addiction. I appreciate the time he has spent listening to my practice talks and enthusiastic ramblings about my research. I wish to thank the friends I have made at Oxford Astrophysics and the Max Planck Institute für Radioastronomie: Alex, Jakob, Andy, Ed, Sean, Jamie, Jonah, Charlie and Geetam. Also, thank you to my housemates (both past and present)/friends: Kate, Dan, Rich, Leda, Zoe, Jen, Rosie, Clemmie and Rachael. Finally, my appreciation goes to my physics teachers Adrian Baker and Despina Savva for their enthusiasm and encouragement to study astrophysics.

Abstract

Astrophysical jets are ubiquitously associated with the most energetic phenomema in the Universe. In this thesis, I will present and discuss radio observations of two types of transient systems: neutron star X-ray binaries and gamma-ray bursts (GRBs).

In Chapter 2, I present the basics of radio interferometry: the method by which I collect data for this thesis. This is explained using a two-dish interferometry. I then go on to explain the data reduction process whereby voltages from individual antennas can form an image of the sky. Finally, the observing facilities I have used for the work in this thesis are presented.

In the Chapter 3, I present the last three years of GRB follow-up observations with the AMI-LA telescope. Several radio sources coincident with GRBs were detected with the AMI-LA telescope. I discuss two cases where a variable, radio-bright host galaxy was brightest than any afterglow emission preventing such a detection. I also discuss a single long GRB afterglow detection which I interpret as forward shock emission from a jet in an homogeneous environment. Finally, I discuss the results of the most up-to-date and complete radio monitoring campaigns of short GRBs that I have performed over the last three years. I have observed all short GRBs over the last three years on timescales of days with *e*-MERLIN in the north, and MeerKAT in the south. Of these triggers, two radio counterparts have been detected. The first was associated with short duration GRB 200826A (Rhodes et al., 2021a). Detections of a varying radio counterpart with *e*-MERLIN confirmed that this source was the afterglow. I combined the 5 GHz *e*-MERLIN light curve with data from *Swift*-XRT and interpreted it in two separate scenarios. The first scenario used to describe the afterglow uses a transition from an optically thick to thin regime. The second scenario requires the presence of a jet break. I rule out the second scenario on the lack of a jet break in the X-ray data. Both the radio and X-ray data are consistent with a stellar wind environment and therefore inconsistent with a binary neutron star progenitor. The second counterpart was associated with short-duration GRB 210726A. The light curves show a sharp delayed rise, it is the longest detected cosmological short GRB to date, followed by an achromatic break. The broadband radio spectra show that the low-frequency emission

is synchrotron self-absorbed. GRB 210726A so far appears to be a cosmological analogue of gravitational wave event GW 170817.

In Chapter 4, I discuss a newly discovered sub-group of long-duration GRBs that have very high energy (VHE) counterparts. I have collected multi-band data on three of the five VHE GRBs and present the interpretations here (Rhodes et al., 2020; Rhodes et al., 2022a). All three events show strong evidence of a forward shock component. Additionally, in the radio afterglow light curves of GRB 190829A I demonstrate the possible presence of a second shock: a reverse shock. Furthermore, the 15.5 GHz radio light curve from GRB 190829A is one of the best, highest cadence radio light curves of any GRB afterglow. The data set for GRB 201216C had sparse coverage, and as a result, I was able to demonstrate how flexible afterglow models are. I show that at 10s of days after the burst the jet launched gives way to a much wider, less energetic cocoon which is predicted in simulations. Finally, I present the beginning of a study into understanding whether the VHE GRBs are a separate population of GRBs or do all GRBs produce such high-energy photons. This is done by studying the luminosity functions of the VHE GRB population and comparing them to a flux limit sample as well as examining the variations in afterglow properties across the group.

In Chapter 5, I present the results of a long term radio and X-ray monitoring campaign of a newly discovered neutron star X-ray binary *Swift* J1858.6-0814 (hereafter, J1858, Rhodes et al., 2022b). J1858 went into outburst in late 2018, it remained radio-bright (i.e. in the hard state) for 18 months before undergoing a rapid transition to the soft state. I tracked the outburst of J1858 with radio interferometers AMI-LA and MeerKAT throughout the outburst. The radio emission was consistent with a compact, self-absorbed jet. When the X-ray and radio emission from J1858 is compared to other X-ray binaries, it is one of the most radio-luminous neutron star X-ray binaries.

The research presented in this thesis has demonstrated the broad range of astrophysical knowledge of both jets, their environments and stellar evolution, that can be extracted from radio transients both within the Milky Way and at extra-galactic distances. I will use this understanding to explore links between X-ray binary and gamma-ray burst jets in the future along with applying blast wave models to transient radio emission from tidal disruption events.

Contents

List of Figures

List of Tables

Chapter 1

Introduction

1.1 The transient and variable radio sky

The radio sky is not static, wide-field, long-term radio surveys have repeatedly shown that about 5% of point-like sources are variable (e.g. Mooley et al., 2016; Sarbadhicary et al., 2021; Driessen et al., 2022). Much of the observed variability is a result of (1) active galactic nuclei (AGN) which can vary on timescales of days to decades (Valtaoja et al., 1992; Hovatta et al., 2008; Mooley et al., 2013) and (2) scintillation, which induces more rapid variability on timescales of minutes to days (e.g. Lovell et al., 2008). AGN are the product of accretion of matter onto a supermassive black hole (SMBH) at the centre of its host galaxy. The accretion of material leads to the production of jets: collimated outflows of plasma which emit at radio frequencies. The variability is thought to be a result of changes in the accretion rate / flow propagating through into the jet (Blandford et al., 2019). Scintillation is an extrinsic cause of variability in which electrons in the interstellar medium of the Milky Way scatter incoming radio waves into / out of the observer's line of sight (Rickett, 1977).

The behaviour described above dominates the variability parameter space. A small fraction of non-static sources are visible for a short period of time and then are never observed again, these are transients. Broadly speaking transients can be split into two categories: *coherent* and *incoherent* emission. The division is made based on the emitting source having a brightness temperature of greater than (coherent) or less than (incoherent) 10^{12} K. Brightness temperature is the temperature of a source under the assumption that is a blackbody, it is defined as

$$T_B = \frac{S_\nu c^2}{2k_B\Omega\nu^2} = \frac{S_\nu c^2 D^2}{2\pi k_B \nu^2 R^2}$$

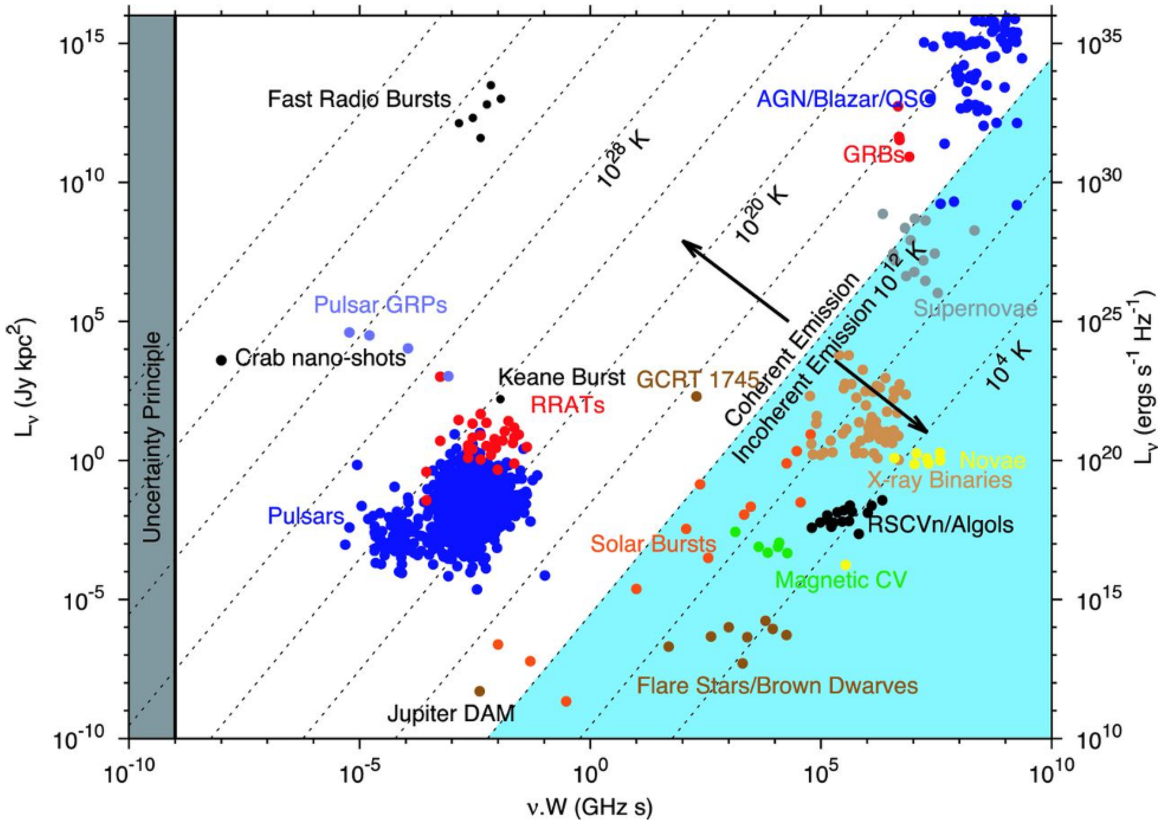

Figure 1.1: A plot of radio luminosity (y-axis) against characteristic variability timescale (x-axis) for a radio transients/ variables from Pietka et al. (2014). The diagonal dashed lines denote lines of constant brightness temperature under the assumption that the source has a size $c\delta t$ where δt is the variability timescale. Above 10^{12} K the emission is considered to be coherent (see Section 1.1.1) and below the emission is incoherent (Section 1.1.2). Each population of variables/transients is labelled.

where S_ν is the flux density of the source ($S = \int I_\nu \mathrm{d}\Omega \approx I_\nu \Omega$, I_ν is the specific intensity and Ω is the solid angle), k_B is the Boltzmann constant, c is the speed of light, R is the radius of the distance, D is distance, and ν is the observing frequency. The size of the source is inferred from the measured size on the sky or from the variability timescale (Δt) where the size R = cΔt. Synchrotron sources with brightness temperatures above 10^{12} K undergo rapid inverse Compton scattering allowing the electrons to cool and reduce the temperature to 10^{12} K again (Kellermann & Pauliny-Toth, 1969).

1.1.1 Coherent transients

Many of the sources of coherent emission are also known as *fast transients*. These are sources whose emission is seen to vary on timescales of a second or less. As a result, fast transients are not usually studied in the image plane. Instead, high time resolution data streams are collected to examine how the transients evolve on timescales as small as microseconds or even nanoseconds.

Possibly, the best example of a fast transients are pulsars (the blue circles in Figure 1.1, Hewish et al., 1968). Pulsars are rapidly rotating neutron stars with strong magnetic fields whose magnetic and rotation axes are misaligned (Gold, 1968). Luminous radio emission is produced along the field lines at the poles. The emission is beamed such that is acts as an astrophysical light house; emission is only observed when the beam is pointing at Earth. The emission appears as a series of regular pulses observed when the cone of radiation sweeps over the Earth. The pulsar emission mechanism is still unknown but the most likely origin is most probably a result of the strong magnetic field of the neutron star combined with the high rotation velocity resulting in a coherent emission mechanism (Lorimer & Kramer, 2005).

There are a subgroup of pulsars which have spin periods on the order of milli-seconds and are in binary systems. Such pulsars are called milli-second pulsars (MSPs, Backer et al., 1982). Their short rotation periods are thought to be a result of being *spun up* via the accretion of material from the stellar companion onto the pulsar (Alpar et al., 1982). Such a scenario makes neutron star X-ray binary systems excellent MSP progenitors (Chapter 5). FIRST J102347.67+003841.2 was the first source identified as having both MSP and accretion phases, as such it was denoted as a transitional MSP - one with has switched from being an X-ray binary to an MSP (Archibald et al., 2009).

Coherent emission is also detected at extra-galactic distances: fast radio bursts (FRBs - black data points in the upper left hand corner in Figure 1.1) are high luminosity bursts (Lorimer et al., 2007). It was initially thought to be the result of some cataclysmic event but the subsequent discovery of repeating FRB systems (Scholz et al., 2016) has required further theories (see Platts et al., 2019, for a review). Experiments such as CHIME (CHIME/FRB Collaboration et al., 2021) have demonstrated that FRBs are relatively common phenomena, detected out to high redshifts (Macquart et al., 2020), thus allowing FRBs to be used to study cosmology.

In some cases, synchrotron transients may appear to have a brightness temperature above 10^{12} K (e.g. AGN and gamma-ray bursts), where the high brightness temperatures are inferred from rapid variability. It is a result of the synchrotron radiation being beamed towards Earth. As such, the observed flux density ($S_{\nu,\,\mathrm{obs}}$) is significantly higher what would be observed if the source was not propagating at relativistic velocities ($S_{\nu,\,\mathrm{int}}$):

$$S_{\nu,\mathrm{obs}} = S_{\nu,\mathrm{int}}\delta^{\omega}$$

ω depends on the nature of the outflow and ranges between $3 - \alpha > \omega > 2 - \alpha$ where α is the spectral index of the source and $\delta = 1/(\Gamma(1 - \beta \cos\theta))$ where Γ is the bulk Lorentz factor of the source, β is the velocity of the source in units of c and $\cos\theta$ is the angle to the line of sight.

1.1.2 Incoherent transients

The collection of transients with brightness temperatures below 10^{12} K (in the cyan region of Figure 1.1) are known as incoherent or *slow transients*. They vary on a timescale greater than seconds and so are typically studied in the image plane.

Within the Milky Way, the radio transient parameter space is dominated by stellar flares (Güdel, 2002; Osten, 2008) and accreting binary systems containing both a star and a white dwarf, neutron star or black hole (Fender & Gallo, 2014; Coppejans & Knigge, 2020; van den Eijnden et al., 2021). Accreting neutron stars and black holes are called X-ray binaries (the brown circles in Figure 1.1). The radio emission from X-ray binaries, which varies on timescales of days to weeks (Pietka et al., 2017), is thought to be connected to the accretion process in which material travels towards the compact object via an accretion disc (see McClintock & Remillard, 2006, for a review). X-ray binaries are discussed further in Chapter 5.

Similarly to coherent transients, synchrotron radio emission is also seen at extra-galactic distances. These transients are orders of magnitude more energetic than those observed within the Milky Way. Figure 1.2 shows the radio luminosity for a range of extra-galactic radio transients as a function of time (Ho et al., 2020). The most luminous transients ($>10^{\sim 39}$ erg/s) in Figure 1.2 are a result of highly relativistic outflows ($\Gamma\beta >$ one in Figure 1.3 Coppejans et al., 2020). The two most well-studied classes of extra-galactic radio transients are supernovae and gamma-ray bursts (GRBs, the grey circles and blue squares in Figure 1.3, respectively).

GRBs are the signposts of cataclysmic events in which a massive, rapidly rotating star reaches the end of its life, or two neutron stars spiral inwards and merge to form a massive neutron star or black hole (Galama et al., 1998; Abbott et al., 2017a). The radio emission from GRBs is produced when a collimated, relativistic outflow collides with the circumburst burst environment, shocks it and emits synchrotron radiation. The study of radio emission from gamma-ray bursts forms the bulk of this thesis (Chapters 3 and 4).

All the transients mentioned so far originate from stellar mass systems, be it galactic or extra-galactic. This is because these systems evolve on human-observable timescales. There is short timescale variability observed from AGN jets but observing the AGN switching off or on typically occurs too slowly to be observed in a single lifetime (see Marscher et al.,

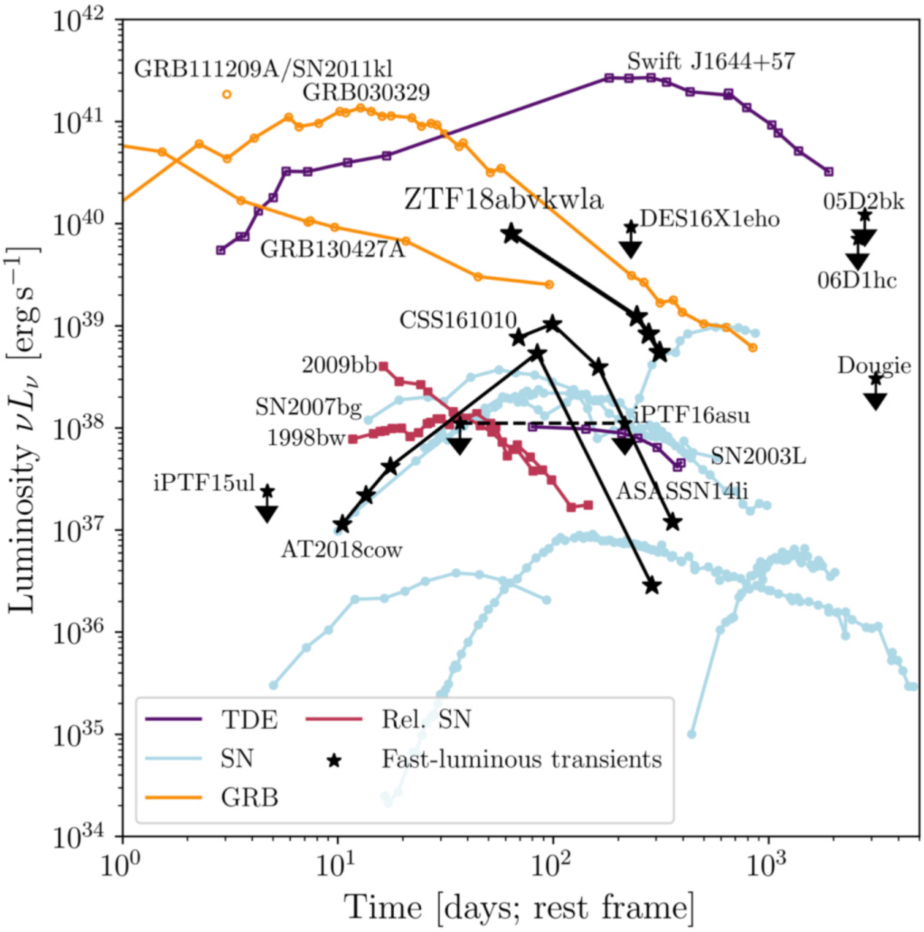

Figure 1.2: From Ho et al. (2020): radio luminosity light curves from a range of extragalactic transients. The least radio-luminous events originate from sub-relativistic events, e.g. supernovae where as the most luminous light curves correspond to highly relativistic transients such as gamma-ray bursts. For comparison, the radio luminosities of black hole X-ray binaries tend to be around 10^{30} erg/s (e.g. Bahramian et al., 2018).

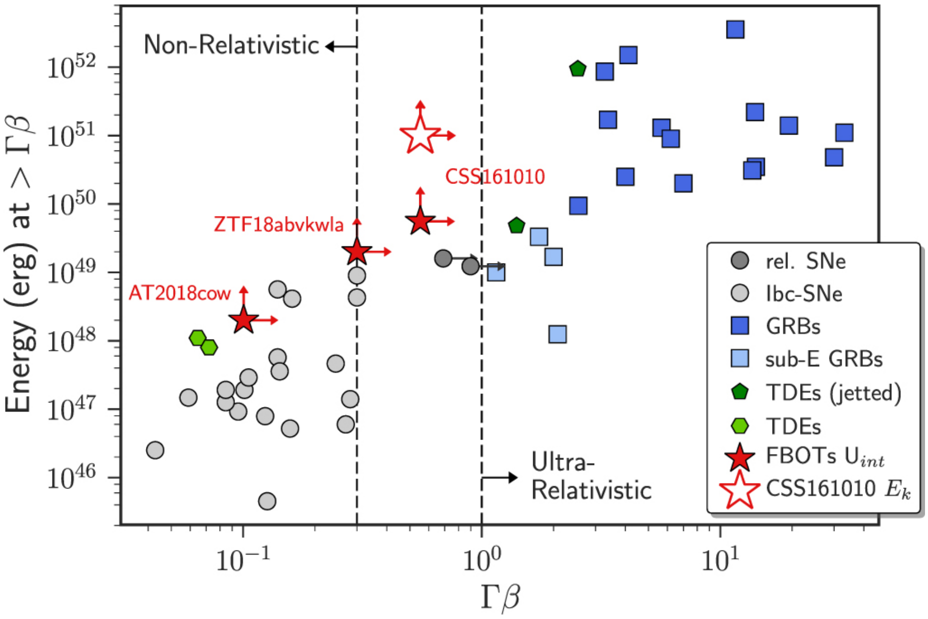

Figure 1.3: A summary of the kinetic energy against outflow velocity for a range of extragalactic transients (Coppejans et al., 2020). Non-relativistic transients include supernovae, and some TDEs and fast blue optical transients (FBOTs). The ultra-relativistic region of the figure is dominated by GRBs.

2002, for an exception). A tidal disruption event (TDE) is one of the best case for observing transient radio emission a SMBH (Alexander et al., 2020a).

TDEs occur when a star gets too close to a SMBH and the tidal forces of the black hole overcome the binding energy of the star such that is ripped apart. Half of the stellar material ia lost and the other half forms an accretion disc and accretes onto the SMBH (Rees, 1988). More and more TDEs are now being discovered to have radio emission on a range of timescales and luminosities (see the purple data points in Figure 1.2). With a larger sample size, it appears that there are two classes of TDEs. The first are *jetted* TDEs: whose radio emission is most consistent with a highly relativistic collimated outflow (see Section 6). The most well studied example is *Swift* 1644+57, whose luminous radio emission, interpreted as a jet, has been detected for nearly a decade after the initial discovery (Mimica et al., 2015). The second are thermal TDEs, whose radio emission is less luminous but shows a range of detection timescales (e.g. Bright et al., 2018a; Horesh et al., 2021).

1.2 Radiation processes

1.2.1 Synchrotron radiation

A population of electrons accelerated by magnetic fields will emit synchrotron radiation, in doing so they lose energy ('cool'). The spectral energy distribution of the emission has a characteristic shape which I define here.

Optically thin synchrotron emission from a population of electrons

A single, relativistic electron gyrating in a magnetic field will emit radiation at frequency $\nu \approx \gamma_e^2 \nu_g \sin\theta$ where γ_e is the electron Lorentz factor, ν_g is the gyro-frequency and $\sin\theta$ is the pitch angle between the electron's path and the magnetic field. Because the electron is relativistic, its emission will be heavily beamed such that radiation is only visible when the electron is moving towards the observer resulting in pulsed emission. The frequency of the radiation will be heavily affects by even the smallest changes in the electron energy, magnetic field or pitch angle so the radiation frequency will not be a delta function. The spectrum of the radiation observed is a Fourier transform of the electron's radiation:

$$P(\nu) = \frac{\sqrt{3}e^3 B \sin\theta}{m_e c^2} \frac{\nu}{\nu_c} \int_{\frac{\nu}{\nu_c}}^{\infty} K_{5/3}(\eta) \mathrm{d}\eta$$

where $K_{5/3}(\eta)$ is a modified Bessel function and the critical frequency $\nu_c = \frac{3}{2}\gamma_e^2 \nu_g \sin\theta$. In the low frequency regime ($\nu \ll \nu_c$) $P(\nu) \propto \nu^{1/3}$ and in the high frequency regime ($\nu \gg \nu_c$) $P(\nu) \propto e^{\nu/\nu_c}$. The spectrum peaks at $\sim 0.29\nu_c$.

In reality, when observing a synchrotron-emitting source, there is not a single electron but a whole population. Often in astrophysics, electrons are accelerated to relativistic velocities via Fermi acceleration (Fermi, 1949; Bell, 1978), the populations of electrons are accelerated into a power law distribution

$$N(E)\, \mathrm{d}E = N_0 E^{-p}\, \mathrm{d}E$$

The intensity of the emission is the product of the the emissivity (J(ν/ν_c, p)) and the source function (S$_\nu$, note that this is a different S$_\nu$ to flux density): I$_\nu$ = S$_\nu$(1-$e^{-\tau}$), where the optical depth, $\tau = \kappa_\nu s$, is the absorption coefficient multiplied by the depth of the emitting region. The source function is given by the ratio of the absorption to emission coefficients.

In the optically thin regime, $\tau << 1$, so via Taylor expansion, I$_\nu$ = $\epsilon_\nu s \propto \nu^{\frac{1-p}{2}}$. Therefore, in the spectral index for optically thin synchrotron radiation is $\frac{1-p}{2}$ (Pacholczyk, 1970).

Synchrotron Self-absorption

At low frequencies, synchrotron emission becomes optically thick: $\tau >> 1$ (Chevalier, 1998). Therefore, the $1 - e^{-\tau} \approx 1$ and the specific intensity is dictated by the source function.

$$I_\nu = S(\nu_1) = \frac{c_5}{c_6} B^{-\frac{1}{2}} \left(\frac{\nu}{\nu_1}\right)^{\frac{5}{2}}$$

where ν_1 is the frequency at which the optical depth of the emitting region is one: $\nu_1 = 2c_1(sc_6)^{\frac{2}{p+4}} N_0^{\frac{2}{p+4}} (B \sin\theta)^{\frac{p+2}{p+4}}$, $c_1 = \frac{3e}{4\pi m^3 c^5} = 6.27 \times 10^{18}$; c_5 and c_6 are dependent on p, for p = 2 they are 1.37×10^{-23} and 8.61×10^{-41}, respectively (Pacholczyk, 1970). The spectral index of the radiation in the optically thick regime is $\frac{5}{2}$.

In the case where the observing frequency falls below both the self-absorption frequency and the peak of the spectrum for the the lowest energy electrons, the spectral index follows ν^2. This is because the observed electron population has a single temperature and so has the same spectral evolution as an optically thick thermal spectrum.

Synchrotron cooling

Electrons with Lorentz factors above some value (γ_c) will cool rapidly, on a timescale shorter than the characteristic timescale of the jet. They emit most of their energy at $\gamma_e m_e c^2$ where $\gamma_e > \gamma_c$. The number of electrons with $\gamma_e > \gamma_c$ is proportional to $\gamma^{\text{1-p}}$. As a population they have a total energy proportional to $\gamma^{\text{2-p}}$. They deposit most of their energy in the range γ_c which means:

$$I_\nu \propto \gamma^{-p} = \nu^{-\frac{p}{2}}$$

1.2.2 Inverse Compton Radiation

Inverse Compton scattering occurs in which an electron scatters a photon up to higher energies. For a population of relativistic electrons, the frequency of the photons are upscattered by a factor of γ_e^2 (Rybicki & Lightman, 1986). The inverse Compton spectrum is a superposition of the energy of distribution of the electron population and the photon spectrum.

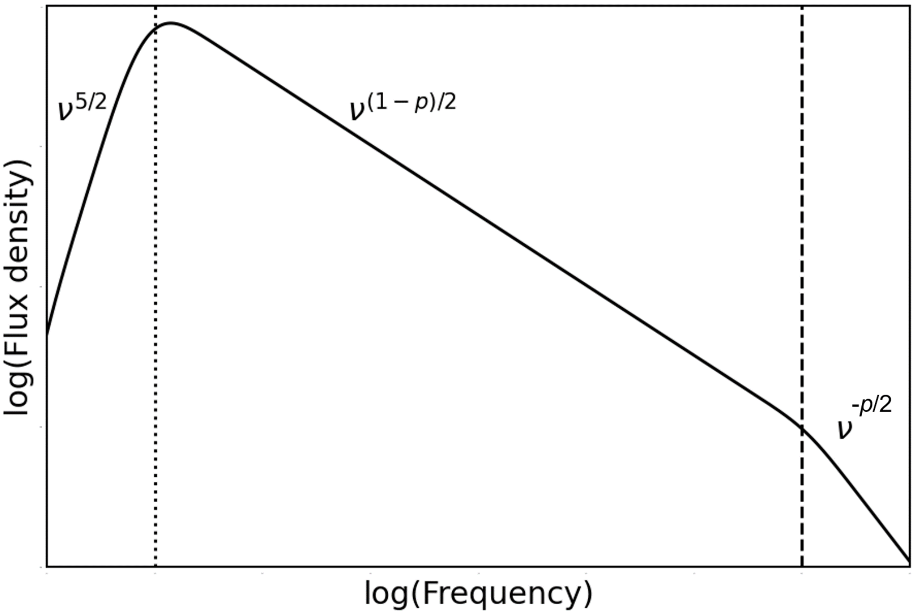

Figure 1.4: An example synchrotron spectrum as described in Section 1.2.1. At low frequencies the synchrotron emitting source is optically thick and has a $\nu^{5/2}$ spectral frequencies. Above some critical frequency, the source is optically thin and follows $\nu^{(1-p)/2}$. At high frequencies, electrons are radiating away a significant fraction of their energy and so are cooling rapidly. This branch of the synchrotron spectrum follows $\nu^{-p/2}$.

1.2.3 Thermal Emission

A population of particles that have a Maxwellian distribution of energies is a thermal population. The radiation they emit has a frequency distribution that can be described as a black body when in the optically thick regime and bremsstrahlung in the optically thin regime, which can be used to extract the temperature of the distribution. Supernovae and kilonovae, stellar explosions and binary neutron star mergers, are both astrophysical phenomena whose spectra are best described as a black body and are therefore thermal systems.

1.3 Jets

The production of jets and outflows is ubiquitous in astrophysics. They are observed on all scales and ejected from objects across orders of magnitude in mass range (e.g. Lightfoot & Glencross, 1986; Janssen et al., 2021). Furthermore, they are associated with some of the more energetic phenomena including many transient systems. Jets are highly collimated outflows, those of interest in this thesis emit synchrotron radiation (Section 1.2.1).

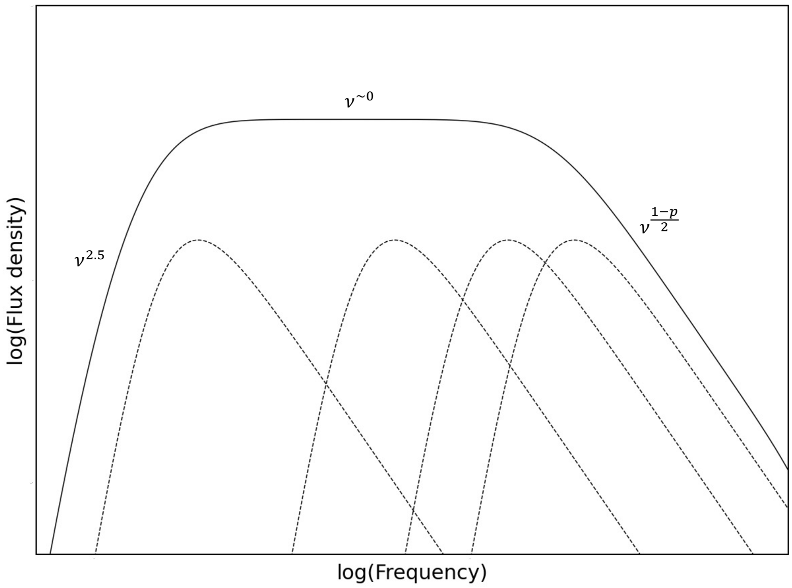

Figure 1.5: An example spectrum thought to be produced by a compact jet when the XRB is in the hard state. The superposition of multiple synchrotron-emitting regions results in a flat spectrum over many orders of magnitude. At low frequencies, the emission is self-absorbed ($\nu^{2.5}$). There is also a turn over at high frequencies above which the jet is optically thin ($\nu^{\frac{1-p}{2}}$ where $2 < p < 3$).

Within the Milky Way, X-ray binaries produce varying types of jets. In some accretion states, the radio emission is self-absorbed or flat (flux density $\propto \nu^{\gtrsim 0}$). This emission is most consistent with a canonical jet (Figure 1.5), where the flat spectrum arises from a superposition of many optically thick spectral components from different emission regions which peak at different frequencies (Blandford & Königl, 1979).

X-ray binaries can also produce discrete ejecta, in which blobs of plasma are ejected at speeds close to the speed of light. Observations of such ejecta have been made for multiple systems over the past decades (e.g. Mirabel & Rodríguez, 1994; Janssen et al., 2021). These ejecta are often described in terms of the van der Laan model.

1.3.1 The van der Laan Model

Many jet ejection models are based on a model by van der Laan (1966), in which a synchrotron emitting blob of material expands at a given rate. By considering a set expansion rate, and a number density and magnetic field that varies as the radius expands, the flux density which depends on the size of the source and the magnetic field will also evolve with time. If radius, magnetic field and number density evolve as

$$R(t) \propto t^a$$

$$B(t) \propto R(t)^b \propto t^{ab}$$

$$N_0(t) \propto R(t)^c \propto t^{ac}$$

where the default van der Laan (1966) assumptions are that a = 1 (i.e. that the expansion of the source is linear), b = -2 and c = -(2+p). Then

$$F_{thick} \propto t^u \text{ where } u = a\left(2 - \frac{b}{2}\right)$$

and

$$F_{thin} \propto t^w \text{ so that } w = a\left(3 + c + b\frac{(p+1)}{2}\right)$$

Again for the default van der Laan assumptions the rise follows t^1, and the decay follows t^{-2p}. The peak of the light curve is caused by the blob transitioning from optically thick to optically thin. Currently (van der Laan, 1966) is mainly used to describe X-ray binary jets (e.g. Fender & Pooley, 2000; Tetarenko et al., 2017). This model can also be adjusted to consider varying expansion speeds and can be adjusted for motion with some bulk Lorentz factor (Fender et al., 1999a).

Most areas of transient astrophysics use relativistic blast wave models instead of the van der Laan-type models.

1.3.2 Blast wave Models

For a shell of plasma travelling at highly relativistic velocities, a strong shock front is produced, often called a *blast wave*. The magnetisation of the plasma accelerates particles ahead of the shock front via Fermi acceleration which then cool emitting synchrotron radiation. Such scenarios occur in gamma-ray bursts where the observed radio emission originates from such a relativistic blast wave scenario ($\Gamma_0 > 100$). The blast wave moves freely, picking up material ahead of the shock. Once the collected mass is equal to the initial mass of the blast wave, the blast wave begins to decelerate. From the deceleration radius, the shock front follows a power law deceleration depending on the environment it is propagating through. At this point, such systems are observed to be indistinguishable from spherical expanding material (Blandford & McKee, 1976).

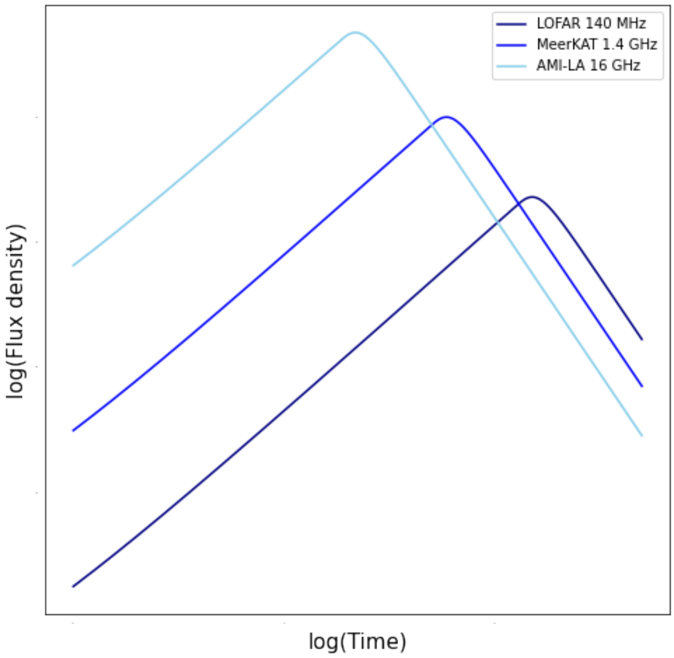

Figure 1.6: Example light curves at 16, 1.4 and 0.14 GHz produced by the model presented in van der Laan (1966). In this example, expansion is linear, the magnetic field and number density vary as R^{-2} and $R^{-(2+p)}$, respectively.

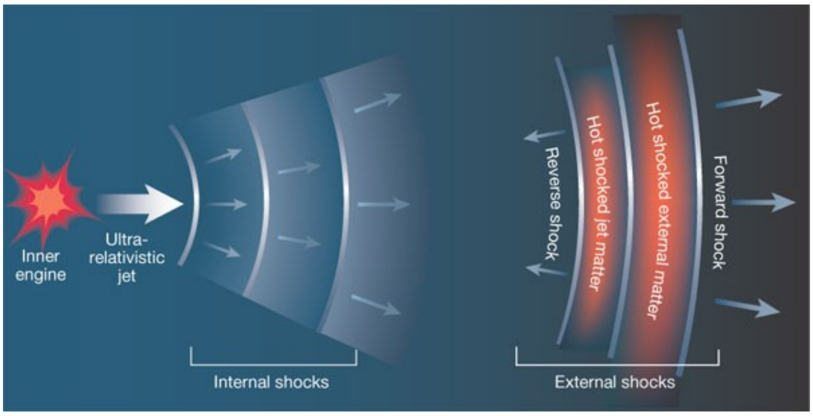

Figure 1.7: A schematic shows the production of synchrotron radiation as a result of external shocks when a jet is launched at relativistic velocities (Piran, 2003).

As deceleration continues, it reaches a point at which the spherical expansion approximation is no longer appropriate: the expansion becomes dominated by lateral spreading rather than radial motion. Around the same time, the deceleration is such that the observer can detect emission from the whole shock front, not just a fraction as a result of beaming. This occurs when $\theta_{\mathrm{j}} \sim 1/\Gamma$ where θ_{j} is the opening angle of the jet (Sari et al., 1999a). Deceleration continues until the blast wave can no longer be described as relativistic (i.e. $\Gamma < 2$ Taylor, 1950).

The work in this thesis considers highly relativistic blast wave-like ejecta (Chapters 3 and 4; compact, persistent jets and van der Laan like sources (the latter two in Chapter 5).

1.4 Multi-wavelength and multi-messenger counterparts

The radio transients presented in this thesis were all first discovered at other bands: X-ray binaries were first found by X-ray telescopes (Giacconi et al., 1964), gamma-ray bursts by gamma-ray facilities (Klebesadel et al., 1973a), even tidal disruption events are found by optical and X-ray telescopes (Gezari et al., 2003; Halpern et al., 2004). These radio transients are far from narrow band events, they are panchromatic: studying the events in different wave bands provide different clues as to the physics of the system in question. In some cases, transients are not just multi-wavelength but multi-messenger: supernovae and short gamma-ray bursts have associated neutrino and gravitational wave counterparts, respectively (Hirata et al., 1987; Abbott et al., 2017b). The benefit of studying these transients at radio frequencies is (1) that radio facilities provide high angular resolution which is used to locating / tracking the motion of a radio source with high precision; and (2) the radio emission is the main tracer of any kinetic feedback from the source, without observations in the radio band we would not be able to understand the kinetic energy of the system nor how it interacts with its surrounding environment.

Despite what I have written above, we are now entering the era of discovering transients at radio frequencies before any other band (e.g. Driessen et al., 2020; Andersson et al., 2022). This is thanks to the combination of wide-field radio observations and commensal search pipelines (Swinbank et al., 2015).

1.5 Thesis structure

The layout of this thesis is as follows: in Chapter 2, I present the methods by which radio interferometers are used to image transient systems and the facilities I have used during my DPhil. The science chapters: Chapters 3, 4 and 5 study transient radio emission from both galactic and X-ray galactic relativistic systems. Chapters 3 and 4 present and discuss the afterglow emission of a large sample of GRBs. Chapter 3 considers the observations of both short and long GRBs predominately at radio frequencies with data collected using the MeerKAT, *e*-MERLIN and AMI-LA telescopes. Chapter 4 focuses on a sub-sample of long GRBs detected at very high energies. Chapter 5 presents the work on a galactic radio transient: neutron star X-ray binary *Swift* J1858.6-0814. Finally, in Chapter 6, I will present my conclusions and discuss where the work presented in this thesis will lead. Throughout this thesis, standard ΛCDM cosmology is used: $\Omega_M = 0.3$, $H_0 = 70\mathrm{kms^{-1}Mpc^{-1}}$ and $\Omega_\Lambda = 0.7$.

Chapter 2

Radio observing techniques

This chapter describes the methods and observing facilities used during my DPhil. I have used a interferometric telescopes observing at radio frequencies, complimented withoptical and X-ray facilities. The methodology underpinning radio astronomy is vast and detailed. Here, I provide an overview at a level appropriate to understand the research I performed for my thesis. For more in depth reading I recommend Taylor et al. (1999); Thompson et al. (2017).

2.1 Interferometry fundamentals

Radio interferometry enables one to combine the electromagnetic radiation detected by individual dishes in such a way so that the array of radio antennas acts as a single, more sensitive, parabolic dish. The size of the individual dishes and layout of the antennas within the array dictates the angular resolution and largest angular scales that can be observed. The smallest angular resolution is given by ~longest baseline/λ and the largest angular scale is given by ~shortest baseline/λ (where λ is the observing wavelength). For example, the MeerKAT radio telescope, a Square Kilometre Array precursor, consists of 64 dishes across a range of baselines spanning 20 m to 8 km. A cluster of dishes at the centre of the array make it sensitive to diffuse emission. These are complimented by dishes at longer baselines which enables ~7" angular resolution (Mauch et al., 2020). Figure 2.1 shows the antenna distribution of the MeerKAT telescope.

A simple, two dish interferometer, as shown in Figure 2.2, best demonstrates how interferometry works: how one goes from a voltage detected by antenna to an image of the sky.

Interferometry relies on knowing the location of each antenna, to a high degree of accuracy, with respect to the others: the *baseline* between the two antennas ($\vec{b}$); and assuming that the radio waves from the observed source, in a direction $\vec{S}$, arrive in phase.

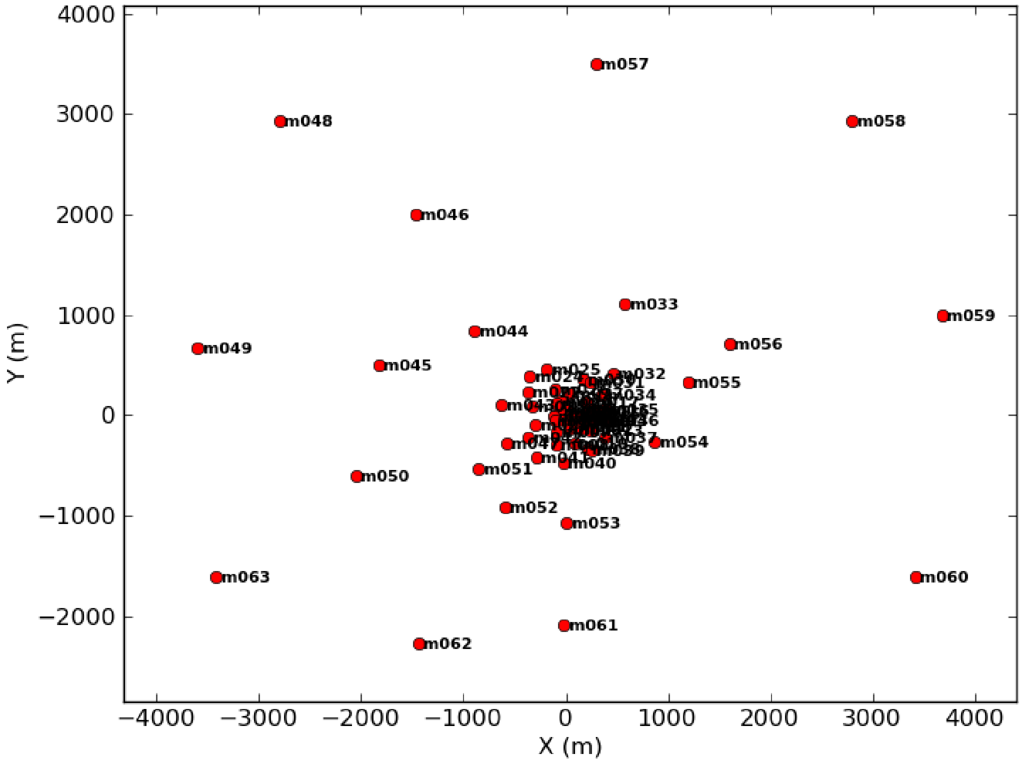

Figure 2.1: The distribution of antennas for the MeerKAT radio telescope. There is a central cluster of dishes complimented by longer baselines. This combination enables the array to have high angular resolution and be sensitive to diffuse emission.

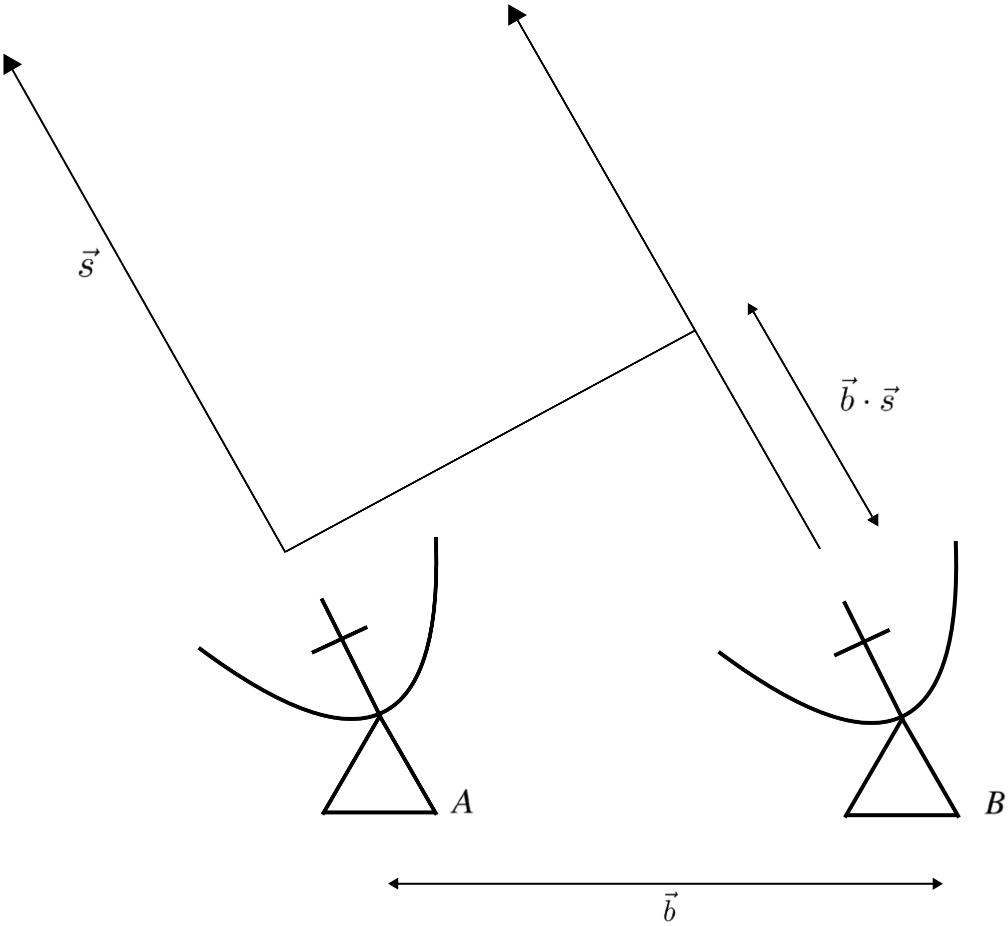

Figure 2.2: An example two element interferometer, where antenna A is the reference antenna. The two dishes are separated by the baseline $\vec{b}$ and pointing at a source in the direction $\vec{s}$.

Whilst pointed at an astronomical source, each antenna measures a voltage as a result of the antenna detecting electromagnetic radiation which creates an oscillating dipole. Assuming that the radio waves reach the Earth in phase, for a given wave front, there is a time delay between the wave front reaching antenna A and antenna B which can be calculated. This is called the geometric delay:

$$\tau_g = \frac{\vec{b} \cdot \vec{s}}{c} = \frac{b \cos\theta}{c}$$

Therefore, the voltage outputs of the two antennas in our array are given by:

$$V_A = E \cos(2\pi\nu t)$$

$$V_B = E \cos(2\pi\nu(t - \tau_g))$$

The voltage detected by antenna B has some offset with respect to antenna A. To consider the baseline, not the individual dishes, the antenna-measured voltages are multiplied (correlated) and averaged to produce two components varying on different timescales.

$$\langle V_{A,B} \rangle = \frac{P}{2}[\cos(4\pi\nu t) + \cos(2\pi\nu\tau_g)]$$

The first term varies rapidly with time and due to the infinite integration time (Δt_{int}) of the telescope, it averages to zero (the green solid line in Figure 2.3). The second term varies with τ_g: $R_C = \frac{P}{2}\cos(2\pi\nu\tau_g) = \frac{P}{2}\cos(\frac{2\pi b\cos\theta}{\lambda})$, it relates to the *fringe function* across the sky (the blue dashed line in Figure 2.3). The amplitude measured by the array varies across the sky.

So far, my model interferometer has been monochromatic, when in reality observations are made at some central frequency ν_0 with a bandwidth $\Delta\nu$. The finite bandwidth means that the correlator produces a series of R_C functions with different periods as a result of the different observing wavelengths. Summing over the whole bandwidth creates regions of both constructive (at the pointing centre) and destructive interference. Away from the pointing centre (phase centre), the superposition of cos waves creates destructive interference as shown in Figure 2.4. The finite bandwidth affects the shape of the *synthesised beam*.

The voltage outputs are also calculated in terms of sine terms (i.e there is also a sine correlator, R_S), with a 90° offset. Combining R_S and R_C terms produces a *complex visibility* with amplitude and phase terms:

$$V = R_C - iR_S = Ae^{i\phi} \tag{2.1}$$

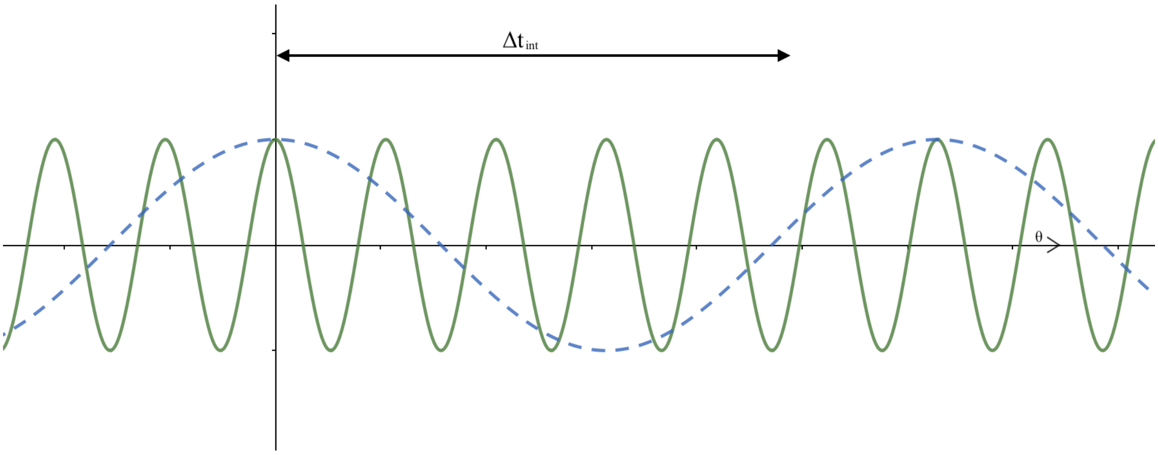

Figure 2.3: An example of the result of correlating the cosine components from Antennas A and B in Figure 2.2. The correlation results in two components, a rapidly varying element which averages to zero over the period of an integration (the green solid line), and a second slower varying term which varies with τ_g (the blue dashed line). The period Δt_{int} denotes the duration of a single integration, during which time the green solid line varies rapidly. Summing over Δt_{int} results in the green line going to zero.

$$A = \sqrt{R_C^2 + R_S^2}, \phi = \arctan\left(\frac{R_S}{R_C}\right) \tag{2.2}$$

where A and ϕ are the amplitude and phase terms, respectively. The dependence of V on A and ϕ mean that V is the same form as the sky brightness distribution. The sky brightness distribution and the complex visibilities (i.e. the quantity measured by the array) are related via a Fourier transform:

$$V = Ae^{i\phi} = \iint Ie^{\frac{-2\pi i\vec{b}\cdot\vec{S}}{\lambda}}\, d\Omega = \iint Ie^{\frac{-2\pi i b\cos(\theta)}{\lambda}}\, d\Omega \tag{2.3}$$

Therefore, a Fourier transform of the voltage response will give us the sky brightness distribution as sampled by the telescope. The amplitude of the complex visibility is linearly related to source flux density, independent of source location. The amplitude relates to the flux density of the source and the phase relates to its position (projected along the axis of the baseline).

Adding more dishes to the interferometer, will produce many more fringe patterns. How each set of fringes adds up in and out of phase when summing over all the fringe patterns will dictate the final image. As with two antennas, the precise location of each antenna with respect to some reference point is required, its location is given in terms of a coordinate system: (x, y, z). An analogous coordinate system on the sky (u, v, w) is used (it is often

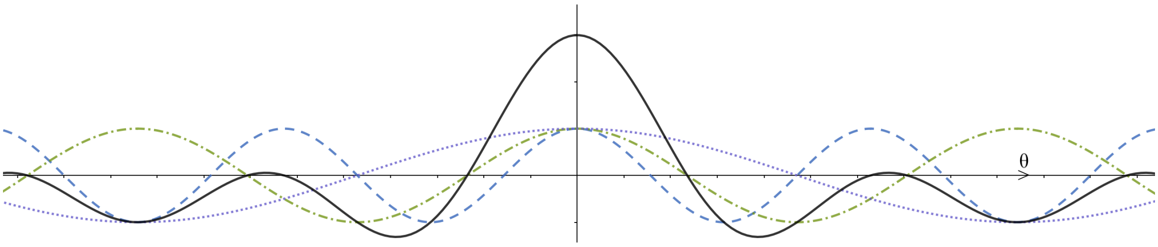

Figure 2.4: The effects of a finite observing bandwidth on the antenna sensitivity as a function of θ which is linearly dependent on τ_g. The dashed, dot-dashed and dotted lines represent three different slowly varying correlated cosine functions as a result of three different observing frequencies. The superposition of the three lines gives the black solid line. The superposition of cosine functions produces the synthesised beam.

assumed that w = 0 i.e. the sky is a co-planar). The components of $\vec{S}$ in our 'sky' coordinate system are: (l, m, n). Figure 2.5 demonstrates both of these coordinate systems.

Equation 2.3 can be written in terms of these coordinate systems:

$$\frac{\vec{b} \cdot \vec{s}}{\lambda} = ul + vm + wn = ul + vm$$

the w term is ignored here as it is assumed that the sky is two dimensional, which gives:

$$V(u, v) = \iint I(l, m) e^{-2\pi i(ul+vm)}\, dl dm \tag{2.4}$$

with a 2D Fourier transform between the sky brightness (*I(l,m)*) and the complex visibilities (*V(u,v)*), it is clear that in order to sample the sky brightness in the most complete way, we require good sampling of the (u,v) plane. For each baseline, an infinitely short integration (Δt_{int}) at a single frequency channel creates one point on the (u,v) plane spread out in the radial direction. A wider bandwidth with more spectral channels would also create more points on the plane. As the observation progresses, the rotation of the Earth fills out the (u,v) plane. Figure 2.6 shows an example of the (u,v) coverage for two observations with different interferometers. Better (u,v) coverage results in a more realistic representation of the sky brightness distribution.

2.2 Data reduction

2.2.1 Data editing

With the development of larger inteferometers has come wider observing bands. Frequently observing bandwidths span more than a giga-hertz (GHz). Such bandwidths are much larger than the allocated radio astronomy observing bands in which other services cannot transmit.

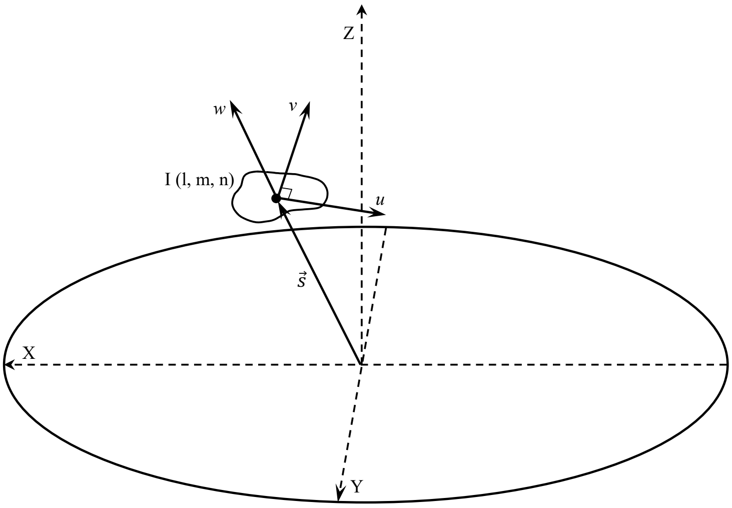

Figure 2.5: A schematic of the (*u, v, w*) coordinate system considering a source at $\vec{s}$ with a brightness distribution of I(l, m, n).

However, there is often spillover into the allocated channels where satellite downlinks or radio transmitters go outside of their allocated range. In addition, there is sometimes local interference such as electric fences which are not expected to emit in the radio astronomy bands but can suddenly appear.

The method by which the radio frequency interference (RFI) is accounted for is called *flagging*: where the data points affected by RFI are ignored by the software during the calibration and imaging stages. Flags are assigned to the individual data points which are affected by RFI. Some flags are known a priori, i.e. they are persistent at a particular time, frequency or affect a known baseline or antenna for that array, and can be automatically added. This also includes excising data due to antenna shadowing and at the edges of observing bands where the receivers are less sensitive.

For RFI that is not predictable, it is possible to excise RFI without losing too much astronomical data by splitting our observing data into narrow-band frequency channels and short ($\lesssim$10 second) integrations. Identifying non-predictable RFI is often relatively easy as it appears as bright spikes in amplitude vs frequency or time plots (see Figure 2.9). Once the flagging has been performed the raw data can be calibrated.

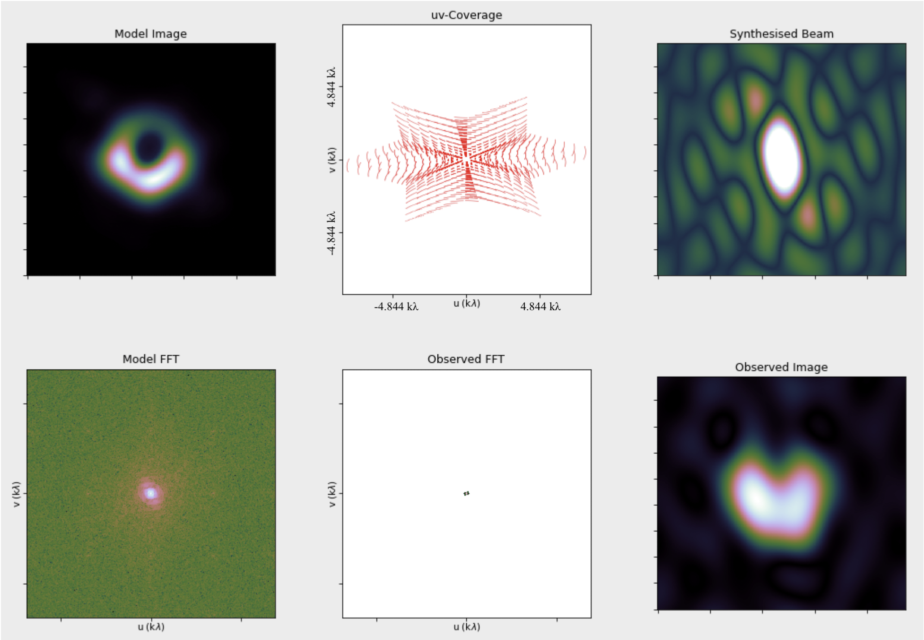

Figure 2.6: From Friendly Virtual Radio Inteferometer[a]. An example of how different interferometers and uv coverage can affect the final image. The top panel is a simulated one hour observation from the Karl G. Jansky Very Large Array (VLA) in D configuration. The top left panel shows an example of a model sky brightness distribution, here the event horizon telescope image of a black hole is used. The bottom left panel shows a fast Fourier transform of the model image. The top central panel shows the uv coverage of the simulated observation. The top right hand panel shows the synthesised beam. The bottom central plot shows the fast Fourier transform of the model image for the given uv coverage. The bottom right hand panel shows the observed image of the model according to the shape of the array and the duration of the observation. With a short observation and poor angular resolution, the beam shape is poor and the black hole image is not resolved.

---

[a] https://crpurcell.github.io/friendlyVRI/

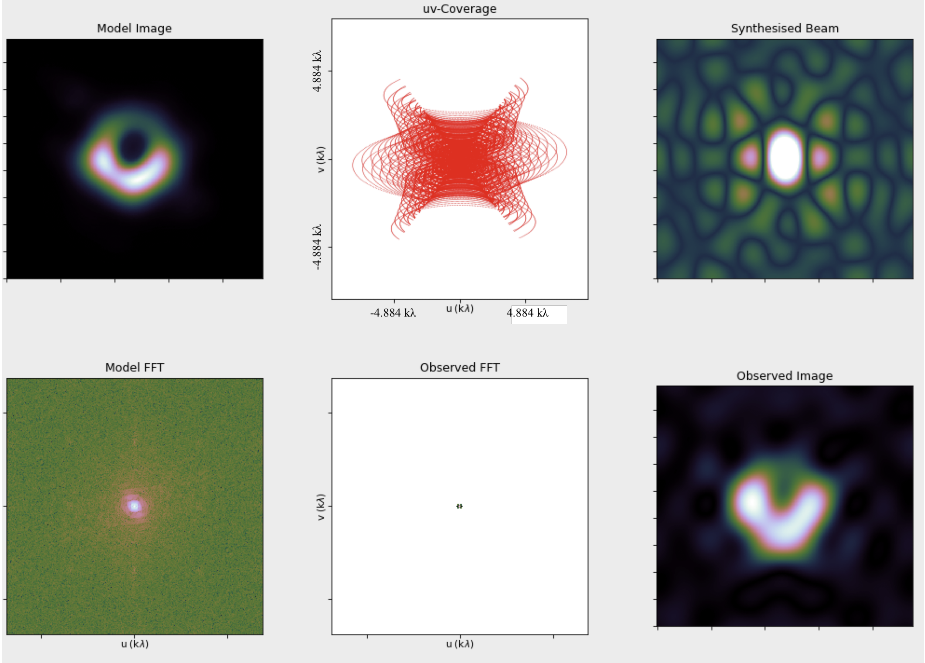

Figure 2.7: This simulation is six hours, much longer than in Figure 2.6 and as a result has a much better uv coverage meaning a better synthesised beam shape. However, the larger synthesised beam means that the black hole shadow cannot be fulled resolved. As a result, the black hole shadow to be fully resolved.

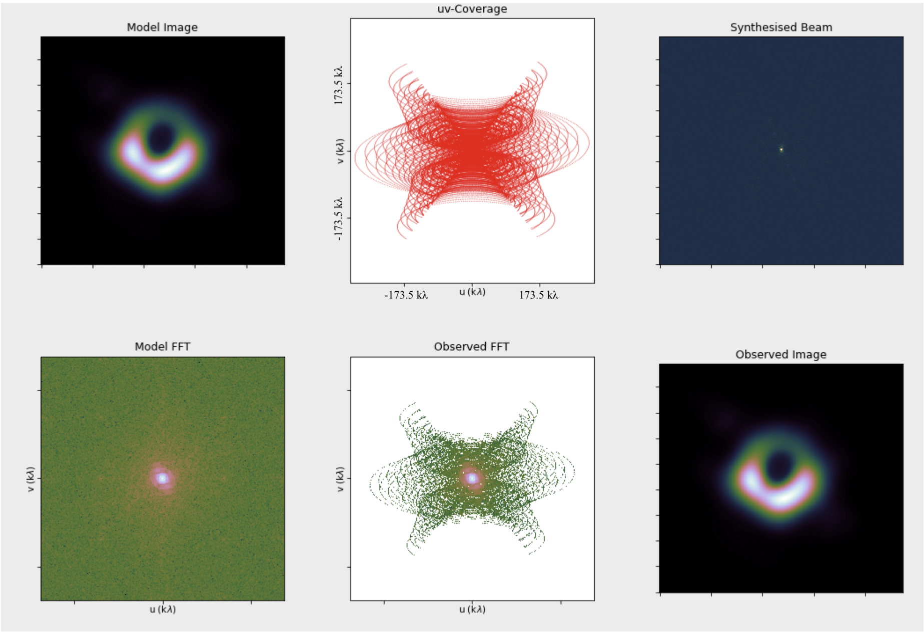

Figure 2.8: This figure simulates a six hour observation with the VLA in A configuration. The lay out if the same as Figures 2.6 and 2.7. With a much more extended configuration, and longer observation, the resulting observation has much better uv coverage and a smaller synthesised beam. As a result, the black hole shadow to be fully resolved.

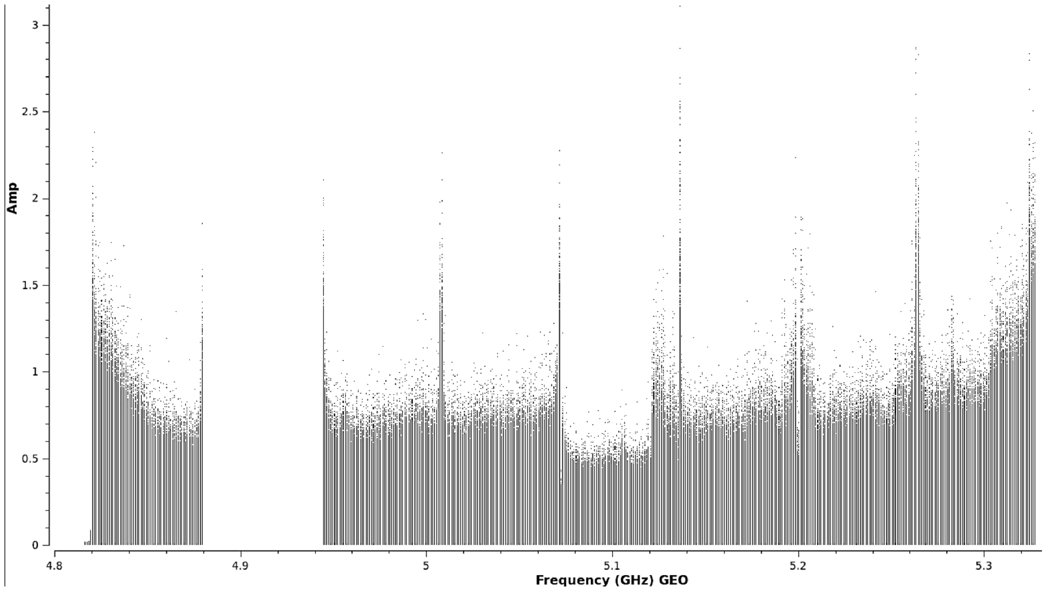

Figure 2.9: A plot of amplitude vs frequency for a 5 GHz observation. The bandwidth of the receiver is 0.5 GHz. The spikes with high amplitudes (above about 1) are examples of RFI and need to be flagged.

2.2.2 Calibration

In order to perform science on interferometric observations, the data needs to be *calibrated* to stabilise the amplitude and correct the phases (e.g. for a source at the phase centre, the phases are gathered from from between +180° and −180° to around 0°). This is done by calculating the corrections that need to be applied to the uncalibrated data set. The corrections made during the calibration form two main groups: instrumental factors and atmospheric factors. Instrumental factors consider effects on a range of timescales from correcting the slight changes in the antenna positions and baselines measurements to instrumental delays in the electronics as well as deformation of the dishes as function of parallactic angle due to gravity. The receiver's bandpass response also needs to be considered. Atmospheric factors include atmospheric attenuation as a function of zenith angle on top of short timescale variability due to tropospheric and ionospheric effects.

Calibration is performed using a method called *cross calibration* which relies on observing a series of well studied point sources. By knowing how the telescope responses to observing these sources, the correction terms can be calculated and applied to the target. The exact observing frequency will vary the calibration process requiring additional steps or calibrator sources. For the work in this thesis, the cross calibration performed is antenna-based calibration. This is the most efficient method as it requires fewer corrections (N_{ant} corrections) than baseline-based calibration ($\frac{1}{2}N_{ant}(N_{ant}$-1) corrections). Each antenna will have different amplitude and phase corrections relative to some reference antenna. Correcting these differences is called *gain calibration*.

A good gain calibrator needs to be very bright, resulting in high signal to noise, unresolved, and near the target on the sky. Relative variation in the atmosphere will be greater for sources further apart on the sky, therefore calibrators closer to the target will allow for a more accurate correction. The gain calibrator needs to be observed at regular intervals (more than once per hour, depending on the observing frequency) in order to track atmospheric movement which requires switching between observing the target and gain calibrator. Regular calibrator observations means that the gain corrections will be antenna based and time dependent.

In addition to a gain calibrator, a flux calibrator (often called a bandpass calibrator) is also required so that the data can be scaled to the correct flux density. Flux density scaling is performed by comparing the mean amplitude of the flux calibrator and the science target. Flux calibrators are tracked by observatories so any variations in flux density are well constrained. The basic calibration formula is:

$$V_{ij}^{\mathrm{obs}} = G_{ij} V_{ij}^{\mathrm{cal}} + \epsilon_{ij}(t) + \eta_{ij}(t) \tag{2.5}$$

where G_{ij} is the baseline complex gain, $\epsilon_{ij}(t)$ is the baseline complex offset and $\eta_{ij}(t)$ is the stochastic complex noise. $V_{i,j}^{\mathrm{obs}}$ is the observed complex visibilities of the calibrator. $V_{i,j}^{\mathrm{cal}}$ is the known complex visibility of the calibrator (which, as already mention, has a well constrained model), it is equal to one for the gain calibrator and the flux density for the flux calibrator. G_{ij} can be written as antenna based terms because most of the corruption occurs before correlation

$$V_{i,j}^{\mathrm{obs}} = G_i G_j^* V_{i,j}^{\mathrm{cal}} = a_i(t) a_j(t) e^{i(\phi_i(t) - \phi_j(t))} V_{i,j}^{\mathrm{cal}} \tag{2.6}$$

So for a single baseline, there is a gain correction for each antenna containing an amplitude and gain term. In order to calculate $G_i G_j^*$, χ^2 minimisation is performed. The resulting the corrections are then applied to the target.

In some cases, where the target source is detected at a high signal-to-noise level, self calibration can be performed. The aim of self-calibration is further improve the signal to noise, thus improving the dynamic range of the image. In some cases it can drop by nearly an order of magnitude, resulting in the detection of fainter sources. The process is iterative: an initial image is made from which a model is obtained, the model is then compared to the original data where complex gains are calculated and applied. A new image is made from corrected data set. The work in this thesis uses phase-only self-calibration.

2.2.3 Imaging

Imaging of the calibrated data set is done by performing a Fourier transform of the calibrated complex visibilities, producing a distorted version of the sky brightness distribution. Fourier transforms are very computationally expensive, so by regridding the irregular u,v sampling onto a regular grid allows for a fast Fourier transform (FFT) to be performed. The FFT of the regridded data produces a *dirty image*. During the FFT process, data on different baselines can be reweighted or tapered to improve or change the angular resolution and noise in the final image.

At this point, the u,v plane is still unevenly sampled, despite regridding. By performing an iterative deconvolution process, *cleaning*, extrapolation and interpolation of the regridded data fills in the u,v plane. Cleaning also removes artefacts in the image i.e. it creates an image closer to the true sky brightness distribution. The processes goes as follows:

1. An initial dirty image is made (e.g. the top panel of Figure 2.10).
2. The location and value of the brightness point in the dirty image is found and its position added to a clean component list. The peak, multiplied by a loop gain factor, is subtracted from the dirty image. The loop gain factor is a number between 0 and 1 which is a fraction of the peak value. The exact value chosen should be dependent on the image - too large a value can result in fewer point sources in the final image.
3. The peak is added to the sky model.
4. Check if the residuals of the dirty image is less or more than a given stopping criterion. If the residuals are greater than the stopping criterion then the above process is repeated.
5. If the residuals are less than the stopping criterion then a *clean image* can be made (the bottom panel of Figure 2.10.

The sky model is then convolved with the clean beam (an elliptical Gaussian fit to the main lobe of the dirty beam i.e. the point spread function of the dirty image) and added back onto the residuals from the dirty image to create the clean image

The minimum flux density detectable by the array ($\mathrm{S_{min}}$) is dictated by the noise in the final image. This is a function of many parameters: firstly, it cannot assume that a single dish's collecting area is 100 per cent efficient, instead it has some efficiency η which reduces the total collecting area to be the effective collecting area of the dish is $\mathrm{A_{eff}} = \eta\pi(D/2)^2$. When considering a whole array, the value of η is reduced further to consider

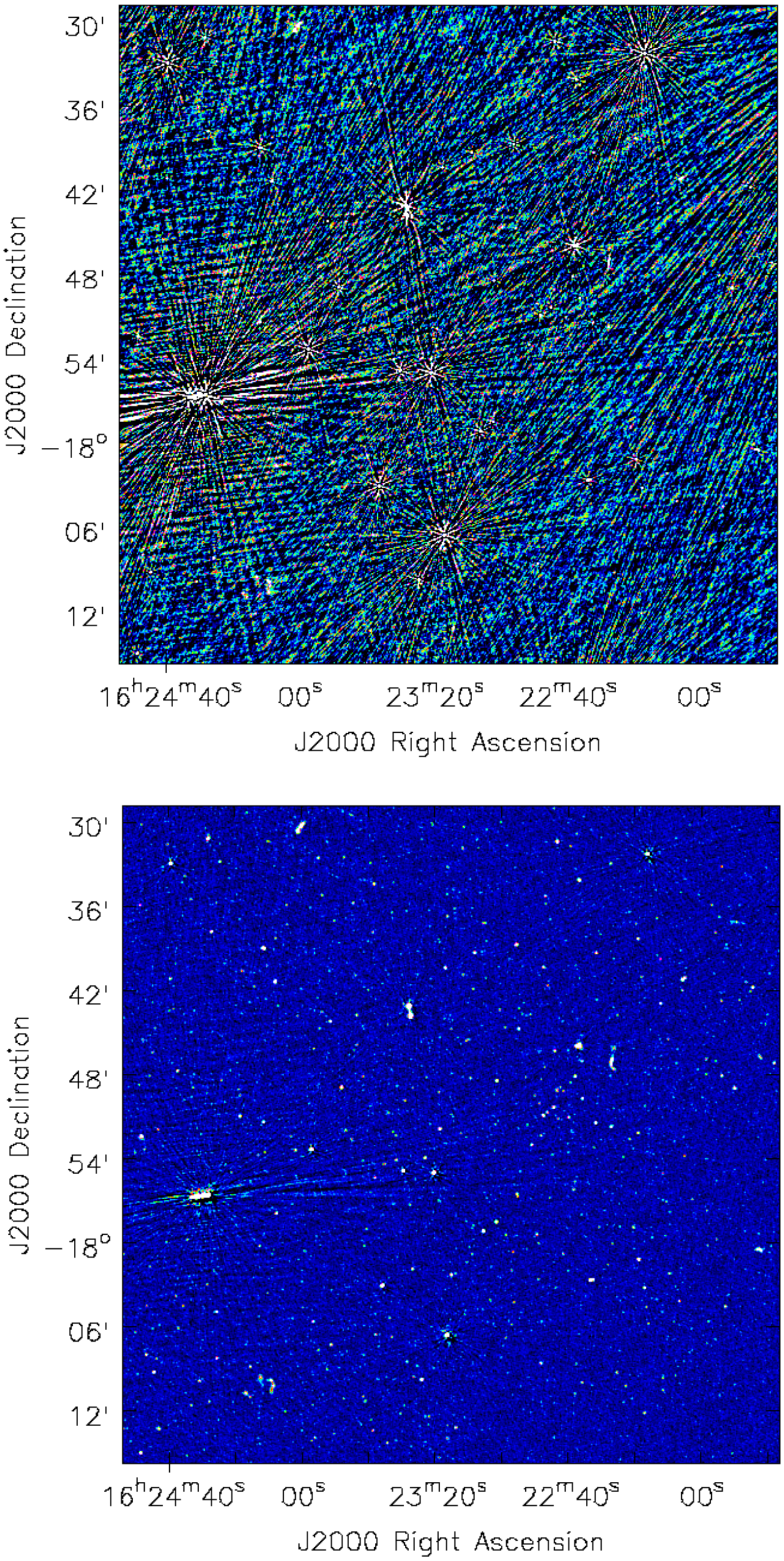

Figure 2.10: An example of a dirty and clean image from the MeerKAT radio telescope. The clean image has fewer artefacts and a lower residuals than the dirty image.

the gaps between the dishes. The effective area is now: $A_{\rm eff} = \eta\pi(D/2)^2\sqrt{N_{\rm ant}(N_{\rm ant}-1)}$. Secondly, the noise introduced by the telescope itself is considered (characterised by a *system temperature* ($T_{\rm sys}$)) as well as the observation length (Δt) and frequency bandwidth ($\Delta\nu$). Combined, the minimum flux density is given by:

$$S_{min} \approx \frac{2k_B T_{sys}}{\eta\pi(D/2)^2\sqrt{N_{\rm ant}(N_{\rm ant}-1)\Delta\nu\Delta t}} \tag{2.7}$$

Therefore, a longer observation, a wider bandwidth or more dishes in the array will enable the detection of fainter astronomical sources.

2.3 Facilities used

2.3.1 Arcminute Microkelvin Imager

The Arcminute Microkevlin Imager - Large Array (AMI-LA) is an eight dish interferometer based in Cambridge, United Kingdom (Zwart et al., 2008). Each antenna is 12.8 meters in diameter, which combined with a maximum baselines of 110 meters gives a synthesised beam size of ~30 arcseconds. A lower observing limit of -5 degrees is enforced, and equatorial sources often have a larger, more elongated beam (this is a common problem for east-west arrays). The array observes between 13.1 and 17.9 GHz (Hickish et al., 2018). AMI-LA is an excellent instrument for transient astrophysics due to automated response to Swift GRB detections and high cadence light curves (see Staley et al., 2013; Rhodes et al., 2020, respectively for examples).

The data reduction for AMI-LA uses a custom pipeline REDUCE_DC (Perrott et al., 2013). The data are flagged for RFI and calibrated using 3C286 as a bandpass and flux calibrator alongside a phase calibrator near the target. Imaging and deconvolution uses the task *clean* interactively within CASA (McMullin et al., 2007a). The uncertainties on the measured flux density combine a statistical and a 5 % calibration error in quadrature.

2.3.2 The *enhanced* Multi-Element Radio Linked Interferometer Network

The *enhanced* Multi-Element Radio Linked Interferometer Network (*e*-MERLIN) consists of seven dishes, spanning from 25 to 76 meters in diameter, located around the United Kingdom. The work in this thesis used *e*-MERLIN to observe at L and C band: 1.25-1.75 GHz and 4.3-7.5 GHz respectively. Such wide bandwidths enable 10s μJy noise to be reached with 6 hours on source. With a maximum baseline of 217 km, one can obtain 150 and 40 milli-arcsecond resolution, at L and C band, respectively (Garrington & Beswick, 2016).

e-MERLIN data are reduced using a custom pipeline[1] using CASA (McMullin et al., 2007a). The pipeline flags the data for RFI, the edges of each spectral channels and adds observatory flags. It averages down the data into fewer frequency channels to reduce data volume. Bandpass and gain calibration is performed and applied to the target followed by flux scaling. Finally, images of the target field are made.

The details of the observing campaigns are given in the appropriate chapters.

2.3.3 The Karl G. Jansky Very Large Array

The Karl G. Jansky Very Large Array (VLA) is an array of 27 dishes in New Mexico, United States of America (Thompson et al., 1980; Perley et al., 2009a). The dishes are laid out in a y-shape on tracks enabling four different configurations. The most compact configuration (D) has baselines between 0.035 and 1.03km. The most extended configuration (A) has baselines between 0.068 and 36.4 km. The VLA is able to observe between 74 MHz and 45 GHz resulting in a synthesized beam ranging between 0.043 and 850 arcseconds in diameter.

The details of the observing campaign in which the VLA was used is described in Chapter 4. The data is reduced using the VLA pipeline in CASA (Version 5.3.0, Kent et al., 2018). The pipeline performs flagging, creates a model of the flux calibration, and performs initial calibration including antenna position corrections. Delay, bandpass and gain corrections are derived and applied to the data after which further flagging is performed. Imaging was also performed in CASA using the task *tclean*. The uncertainties on the flux densities were calculated by combining the statistical error and 5% calibration uncertainty added in quadrature.

2.3.4 MeerKAT

The MeerKAT radio telescope in the Karoo Desert, South Africa consists of 64 13.5 metre dishes (Jonas & MeerKAT Team, 2016). The majority of the dishes are concentrated in the central cluster enabling sensitivity to diffuse structures, complimented by longer baselines extending out to 7.7 km (see Figure 2.1). Observations at made between 0.9 and 1.7 GHz resulting in a synthesised beam size of ~7 arcseconds (Mauch et al., 2020).

The MeerKAT data presented in this thesis was collected both as part of the ThunderKAT (The HUNt for Dynamic and Explosive Radio transients with meerKAT) large survey

---

[1] https://github.com/e-merlin/eMERLIN_CASA_pipeline

project (Fender et al., 2016) and through a series of successful Director's discretionary time proposals. In both cases, the data were reduced using OXKAT[2] a set of python scripts used for semi-automatic processing (Heywood, 2020). Firstly, the calibrator fields are flagged for RFI as well as the first and last 100 spectral channels. A spectral model from the primary calibrator is applied to the secondary. Delay, bandpass and complex gain calibration was performed on the primary and secondary calibrators and applied to the target field. Finally the target field is flagged using TRICOLOUR[3]. The data are imaged with WSCLEAN using a Briggs weighting with robust parameter of -0.7 (Offringa et al., 2014). A model is then derived from the image and used it to reimage after a round of phase-only self calibration. The uncertainties on the measured flux density include statistical uncertainties and a 10 % calibration error.

2.3.5 The Neil Gehrels *Swift* Observatory

The Neil Gehrels *Swift* Observatory (*Swift*) comprises of three separate instruments: the burst alert telescope (BAT), the X-ray telescope (XRT) and the ultra-violet optical telescope (UVOT, Burrows et al., 2005; Barthelmy et al., 2005; Roming et al., 2005). BAT has two main purposes: (1) to detect and localise GRBs with an uncertainty of a few arcminutes; (2) to perform an all sky monitoring program of hard X-ray emitting sources (Krimm et al., 2013). BAT detects emission between 15 and 150 keV. XRT observes at softer energies between 0.3-10 keV following up on GRB detections made by BAT in order to track the onset of the GRB afterglow. Target of Opportunity proposals can also be made to XRT to observe new transients such as X-ray Binaries. The image plane transient work in this thesis uses both BAT and XRT. Science-ready products are produced automatically and made public of both instruments (Evans et al., 2007, 2009).

2.3.6 The Monitor of All-sky X-ray Image

The Monitor of All-sky X-ray Image (MAXI) is a instrument installed onto the International Space Station (ISS) with the aim to perform an all sky survey between 2 and 20 keV, scanning the sky once per ISS orbit (Matsuoka et al., 2009). Such regular observing allows for excellent monitoring of transient sources such as X-ray binaries. The 4-10 keV count rate from MAXI was used in Chapter 5 to monitor the soft X-rays from *Swift* J1858.6-0814 throughout its 18 month outburst.

---

[2] https://github.com/IanHeywood/oxkat

[3] https://github.com/ska-sa/tricolour

Chapter 3

Gamma-ray burst follow up with MeerKAT, *e*-MERLIN and AMI-LA

This chapter presents the detection and analysis of both long and short gamma-ray bursts. It is based on the paper *An early peak in the radio light curve of short-duration Gamma-Ray Burst 200826A* (Rhodes et al., 2021a). It also contains work from Schroeder & Rhodes et al, *in prep*, and Laskar & Rhodes et al, *in prep*. All the additional data is provided in Appendix A.

3.1 Introduction

Gamma-ray bursts (GRBs) are the most powerful explosions known. They are most likely caused by the launch of relativistic jets in cataclysmic events. GRBs were first detected by the Vela satellites; crafts carrying X-ray and gamma-ray detectors to monitor the Earth's surface for evidence of nuclear bomb testing. Later Vela satellites had improved timing accuracy, which enabled Klebesadel et al. (1973b) to prove that 16 detections did not originate from either the Sun or Earth, that they must be cosmic in origin.

3.1.1 Prompt Emission

The initial flash of gamma-rays is called the prompt emission. These flashes last from tens of milli-seconds to thousands of seconds (Ajello et al., 2019). The prompt GRB emission varies rapidly, indicative of a very small emitting region. The leading interpretation is that the emission is produced in internal jet processes combined with strong beaming (see Van Paradijs et al., 2000, for a review). Large numbers of prompt emission light curves show that the prompt emission phase can be divided into two sub-groups (Kouveliotou et al., 1993): short GRBs, which have a duration less than 2 seconds; and long GRBs, that last longer than 2 seconds.

Long GRBs are thought to be produced during the core collapse of a sub-population of fast rotating massive stars (Woosley, 1993; Levan et al., 2016, for a recent review). Evidence for this connection has come from the presence of Type Ib/c broadline supernovae signatures in the optical afterglow spectra of long GRBs (e.g. Hjorth et al., 2003; Cano et al., 2014). Long GRBs span orders of magnitude in luminosity space spanning upwards from $L_{\gamma,\,\mathrm{ISO}} \sim 10^{51}$erg/s ($L_{\gamma,\,\mathrm{ISO}}$ is the isotropic equivalent luminosity of the prompt emission). As a result long GRBs have been detected out to redshifts of $z > 9$ (Amati et al., 2002; Ghirlanda et al., 2005; Gehrels et al., 2009; Ajello et al., 2019). The spectra of the prompt emission from long GRBs are very soft (Shahmoradi & Nemiroff, 2015).

Short GRBs were first hypothesised to originate from neutron star mergers in the 1980s (Eichler et al., 1989). However, it was not until 2017 that such a connection was proven. GW170817 was the first binary neutron star merger to be detected by LIGO (Laser Interferometer Gravitational-Wave Observatory)/Virgo, followed by a short GRB detected by Fermi GBM (Abbott et al., 2017a). The localisation of the two events were consistent, thus confirming the origin of short GRBs.

Compared to long GRBs, short GRBs have lower rates, have harder spectra (Shahmoradi & Nemiroff, 2015) and tend to have lower luminosities ($L_{\gamma,\,\mathrm{ISO}} \leq 10^{52}$erg/s, although there is still some over lap with the long GRB population Amati et al., 2002).

The prompt duration and spectra are used in conjunction with each other to classify the type of GRB being observed. However, in the same manner to the overlap between the luminosity distributions, there are cases where collapsing massive stars appear to produce short GRBs (as shown in Section 3.3.1) and binary neutron star mergers can produce long GRBs (GRB 211211A Rastinejad et al., 2022).

3.1.2 The Afterglow

The prompt emission is followed by a broadband afterglow, usually detected between X-ray and radio frequencies, which, in some cases, is visible for years (e.g. Frail et al. 2000b; Van der Horst et al. 2008). The afterglow is interpreted in the context of the *fireball model*: a spherical sector of a spherically symmetric, relativistic blast wave made of a shell of ejecta of some finite width, that propagates outwards into the surrounding interstellar medium (ISM) and produces shocks (Rees & Meszaros, 1992). Initially, the blast wave is highly relativistic ($\Gamma_0 > 100$) as ISM material is swept up, the blast wave begins to decelerate. As explained in Section 1.3.2, late time observations have required evidence that the blast wave is in fact a jet. The bulk Lorentz factor and radius of the jet (distance from the launch point) follow scaling laws dependent on the circumburst environment (for adiabatic expansion Blandford & McKee, 1976; Sari, 1997; Granot & Sari, 2002):

$$R \propto t^{\frac{1}{4-k}} \tag{3.1}$$

$$\Gamma \propto t^{-\frac{3}{2(4-k)}} \tag{3.2}$$

(where k parameterises the ISM density profile: $\rho \propto r^{-k}$, k = 0 or 2 for a homogeneous or stellar wind environment (Chevalier & Li, 1999)).

Interaction between the ISM and jet causes ambient ISM electrons to be accelerated by magnetic fields across the shock front into a power law distribution: $N(E)dE \propto E^{-p}dE$, where p is typically between 2 and 3. The electrons subsequently cool and emit synchrotron radiation. This emission produced from the jet propagating forwards is associated with the *forward shock* (FS). The FS can be visible for months or even years after the burst.

The rapid deceleration of the jet results in a second shock component: the *reverse shock* (RS). As the jet decelerates, material behind the shock from catches up and increases the pressure at the front of the ejected shell of material. The difference in pressure and density across the shell causes a rarefaction wave to form. The rarefaction wave turns into a compression wave that move backwards through the shell. Due to the low sound speed, the wave quickly accelerates and becomes a shock. The reverse shock then propagates back towards the newly formed compact object through the ejected material (Sari et al., 1999a). Kinetic energy in the expanding shell accelerates electrons in the reverse shock resulting in a deceleration in the bulk Lorentz factor of the shell (Blandford & McKee, 1976; Sari, 1997). The synchrotron emission from the reverse shock generally appears as a decaying component which dominates at early times, but usually fades on the timescale of days as the FS becomes dominant (e.g. Laskar et al., 2013; Van der Horst et al., 2014; Bright et al., 2019).

Observations of some GRB afterglows have shown evidence of a second forward shock component originating from a wider outflow (Resmi et al., 2005; Starling et al., 2005; Racusin et al., 2008; Kamble et al., 2009; Filgas et al., 2011; Van der Horst et al., 2014; Lan et al., 2018; Chen et al., 2020; Rhodes et al., 2022a). This second component is sometimes interpreted as a cocoon (e.g. Chen et al., 2020). Cocoons are often invoked to explain why GRB jets are so highly collimated. Magnetohydrodynamical numerical simulations show that as the relativistic jet propagates through the collapsing star, it deposits a large amount of energy into the surrounding material forming a cocoon. Whilst propagating through the collapsing star, the surrounding material that will form the cocoon reduces the lateral expansion of jet, resulting in a high degree of collimation when the jet breaks free (Ramirez-Ruiz et al., 2002; Zhang et al., 2004; De Colle et al., 2018). The kinetic energy of the cocoon is expected to be several orders of magnitude less than the jet ($\sim 10^{49}$ erg), more similar to (relativistic) supernovae, with a bulk Lorentz factor lower than the core of the jet (De Colle et al., 2018). The signature of the cocoon can appear similar to that of the jet due to the cocoon's interaction with the circumburst medium producing synchrotron emission (Nakar & Piran, 2017). However, the cocoon emission is unlikely to be observed unless the jet is viewed off-axis, or the system has a favourable combination of energetics and geometry, when the core jet cannot dominate the observed emission at all times.

Each shock component produces its own synchrotron signature. Synchrotron radiation is a broadband process, its spectrum is characterised by three frequencies: the self-absorption frequency (ν_{SA}); the minimum electron frequency (ν_M), and the cooling frequency (ν_C), and normalised to a peak flux density ($\mathrm{F}_{\nu,\,\mathrm{max}}$). The frequency breaks and $\mathrm{F}_{\nu,\,\mathrm{max}}$ evolve with time. The evolution of each shock is dependent on the density and profile of the ISM (parameterised by n or $\mathrm{A}_\star$, depending on the presence of a homogeneous or stellar wind environment), kinetic energy in the jet ($\mathrm{E}_{\mathrm{K,\,ISO}}$) and the microphysical parameters: the fraction of kinetic energy given to the electrons and magnetic fields (ϵ_e and ϵ_B, respectively).

The evolution of the spectrum can fall into one of two categories: fast cooling and slow cooling. Fast cooling occurs when $\nu_M > \nu_C$, the majority of the electrons are emitting at frequencies above the cooling break and so on average each electron is losing most of its energy in the system to radiation. As a result, the cooling timescale is shorter than the characteristic jet timescale (the timescale over which an observer tracks the afterglow). The upper panel of Figure 3.1 shows an example of a fast cooling spectrum. Fast cooling is only likely to occur at very early times. The break ν_M evolves faster than ν_C and so when $\nu_C = \nu_M$ the source transitions to slow cooling. In the slow cooling phase, ν_M is below ν_C and expansion is adiabatic, most of the electrons cool on a timescale slower than the jet characteristic timescale. An example of a slow cooling spectrum is shown in the lower panel of Figure 3.1.

As well as showing examples of instantaneous spectra in the fast and slow cooling regimes, both panels of Figure 3.1 demonstrate how the spectral breaks and $\mathrm{F}_{\nu,\,\mathrm{max}}$ evolve. Each break and $\mathrm{F}_{\nu,\,\mathrm{max}}$ has two power law indices indicating its evolution in a homogeneous (top) and stellar wind environment (bottom).

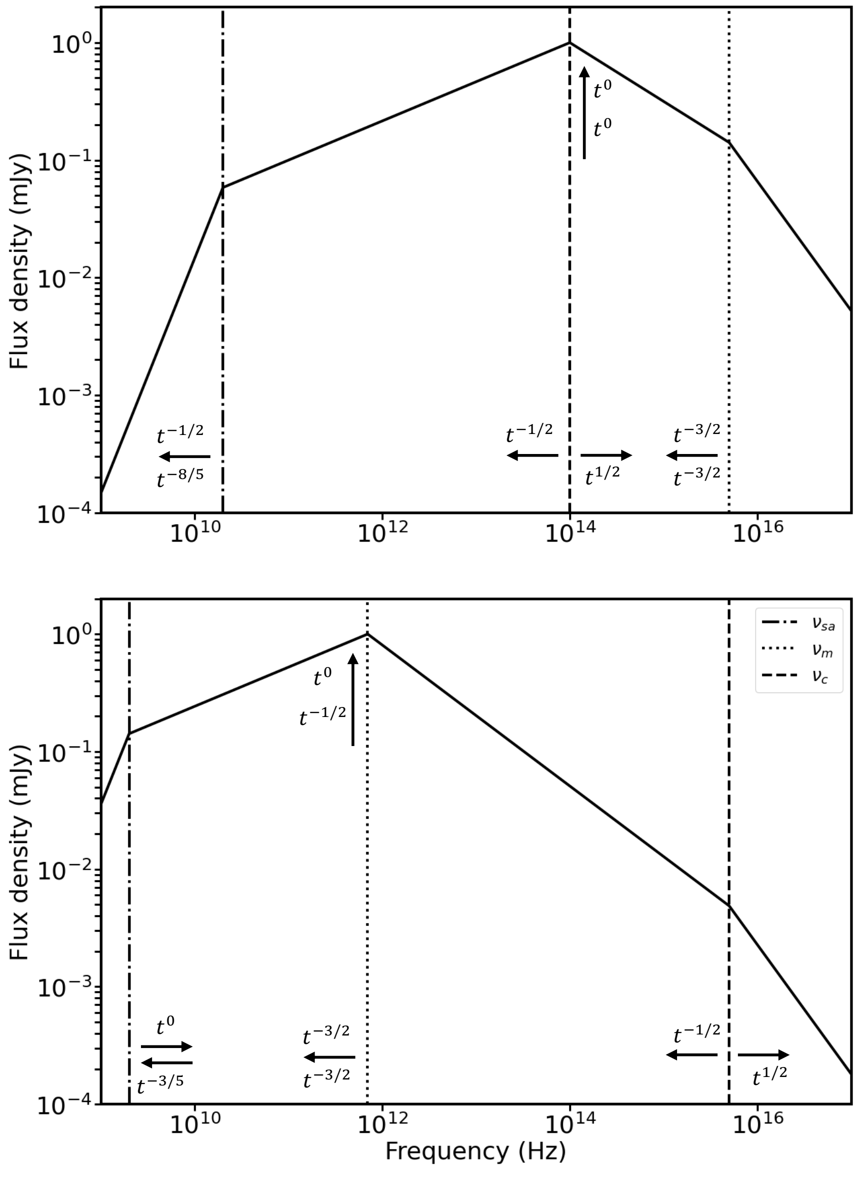

Figure 3.1: Examples of fast (upper panel) and slow (lower panel) cooling synchrotron afterglow spectra. In the upper panel that $\nu_C > \nu_m$ implying that the afterglow is in the fast cooling, i.e. radiative cooling cooling regime. In the lower panel, the afterglow is slow cool, it is cooling adiabatically. The time-dependence labels on each spectrum demonstrate how $F_{\nu,\,\max}$ and the break frequencies evolve with time. For each spectral component there are two scenarios, the upper number is for a homogeneous environment and the lower number is for a stellar wind environment.

The evolution of the synchrotron spectrum results in very different light curves in different wave bands. The optical light curve often shows a combination of RS and FS components. The RS can dominate from seconds post burst. It is further complicated as the thermal counterpart (e.g. the supernova) can dominated on a timescales of days. Figure 3.2(a) shows the optical light curve of GRB 130702A showed the afterglow, a supernova and the host galaxy (Mazzali et al., 2021).

The synchrotron spectrum is most apparent in the radio band and so is the most appropriate for studying the long term evolution of the FS. For some low redshift, high luminosity bursts, emission can be detected for over a year. It is possible to observe both ν_{SA} and ν_m pass through the band. At early times, a few days post burst, the RS can also be observed. Figure 3.2(b) is an example of a possible radio light curve which contains contributions from both a FS and RS component for the afterglow of GRB 130427A (Anderson et al., 2014).

In the X-ray band, the light curve often contains the decay of the prompt emission as well as flaring from later accretion episodes before the afterglow dominates from a few hours post-burst (see Figure 3.2(c)). The forward shock light curve decays as a power law, sometimes containing a break as a result of ν_C passing through the band. Such a break is accompanied with a change in the spectral index.

Both the optical and radio radiation can be affected by material along the line of sight to the burst. As a result the observed radio and optical emission can be significantly different from the true afterglow evolution. This is expanded on in Section 4.1.2.

Geometric Effects

Most of the observed breaks in afterglow light curves are a result of spectral evolution. Some light curves also show achromatic breaks where the light curve changes in all bands simultaneously. These breaks are caused by changes as a result of the jet's geometry. The most commonly observed signature is called a jet break and occurs in the transition from

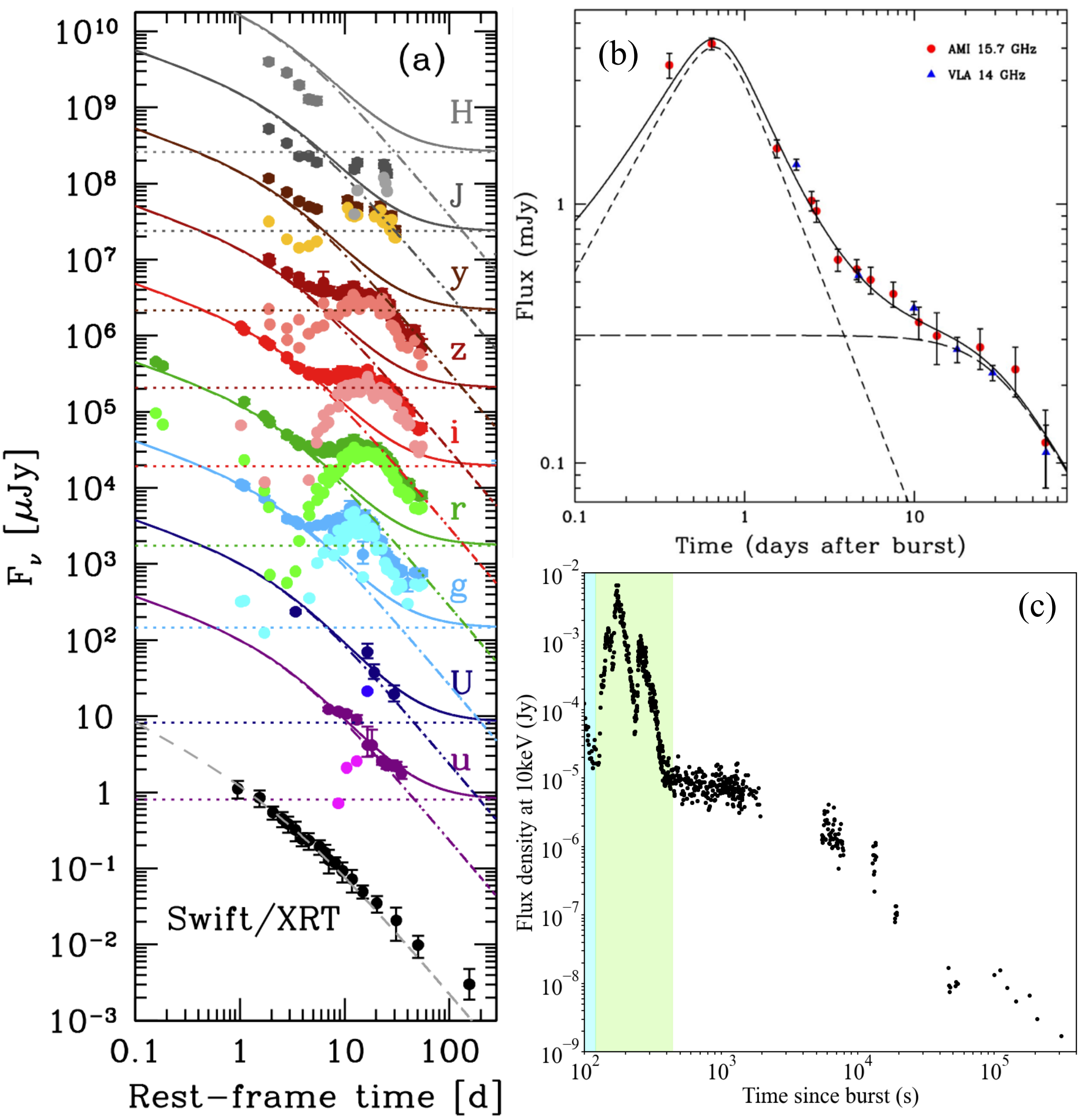

Figure 3.2: (a) An example of the optical light curve associated with GRB 130702A. The dotted-dashed lines show the modelling of the afterglow in each band, the solid lines are the afterglow and galaxy. Any excess emission is attributed to the supernova. (b) The 15.5 GHz radio light curve from Anderson et al. (2014) of GRB 130427A. This is an example of two separate shocks: a reverse and forward shock, contributing to the radio light curve. (c) The X-ray counterpart to long GRB 130609B as detected by *Swift*-XRT (Evans et al., 2010). The afterglow is not the only source of X-ray photons: the decay of the prompt emission is highlighted in blue and flaring activity is highlight in green. Only after the additional processes have faded can the synchrotron afterglow be detected.

$\Gamma > 1/\theta_j$ to $\Gamma < 1/\theta_j$, where Γ is bulk Lorentz factor of the of the forward shock and θ_j is the opening angle of the jet. Figure 3.3 shows a schematic of how the deceleration of the jet results in the jet break. The break occurs when the deceleration of the jet is such that the beaming cone widens allowing the observer to see the edges of the jet (see Figure 3.3). Before the jet break, the apparent flux density evolution has been slowed by the combination of seeing a growing emitting region size and a decrease in emission from the shock front. Once the whole of the jet is viewable, only the reduction in emission from the shock front is visible resulting in a sudden break and more rapid light curve decay. Large sample studies of long GRB jet opening angles show jets to be highly collimated with $\theta_j = 7^{+11}_{-4}\,^{\circ}$ on average (Laskar et al., 2014). Short GRBs have a similar opening angle range of $\sim 6^{\circ}$ but there are far fewer events from which to draw conclusions (Jin et al., 2018).

Conversely, very sharp light curve rises ($F \propto t^{\gtrsim 3}$) can be interpreted as a jet which is initially beamed out of the observer's line of sight and decelerates thus becoming visible (Granot et al., 2002; Peng et al., 2005). All sky surveys such as the VLA Sky Survey (VLASS, Myers et al., 2014) are excellent targets to search for off-axis emission. Mooley et al. (2022) found a FIRST J141918.9+394036, a potential off-axis afterglow corresponding to a GRB that would have been detected in the early 1990's if it were on-axis.

3.1.3 Radio afterglow properties of short gamma-ray bursts

At radio frequencies, detections of short GRBs are extremely rare, with only nine published detections to date (including GW 170817 Berger et al., 2005; Soderberg et al., 2006; Fong et al., 2014; Lamb et al., 2019; Fong et al., 2021; Hajela et al., 2021). Eight of the nine published radio detections are shown in Figure 3.4. All of the bursts in Figure 3.4, with the exception of GRB 210726A (which is discussed in Section 3.4.1), have only been obtained before ten days post-burst, they are seen to quickly fade below detection limits resulting in one or two detections per event. The low afterglow luminosities mean that so far, the community has only been able to detect radio emission from short GRBs below redshift

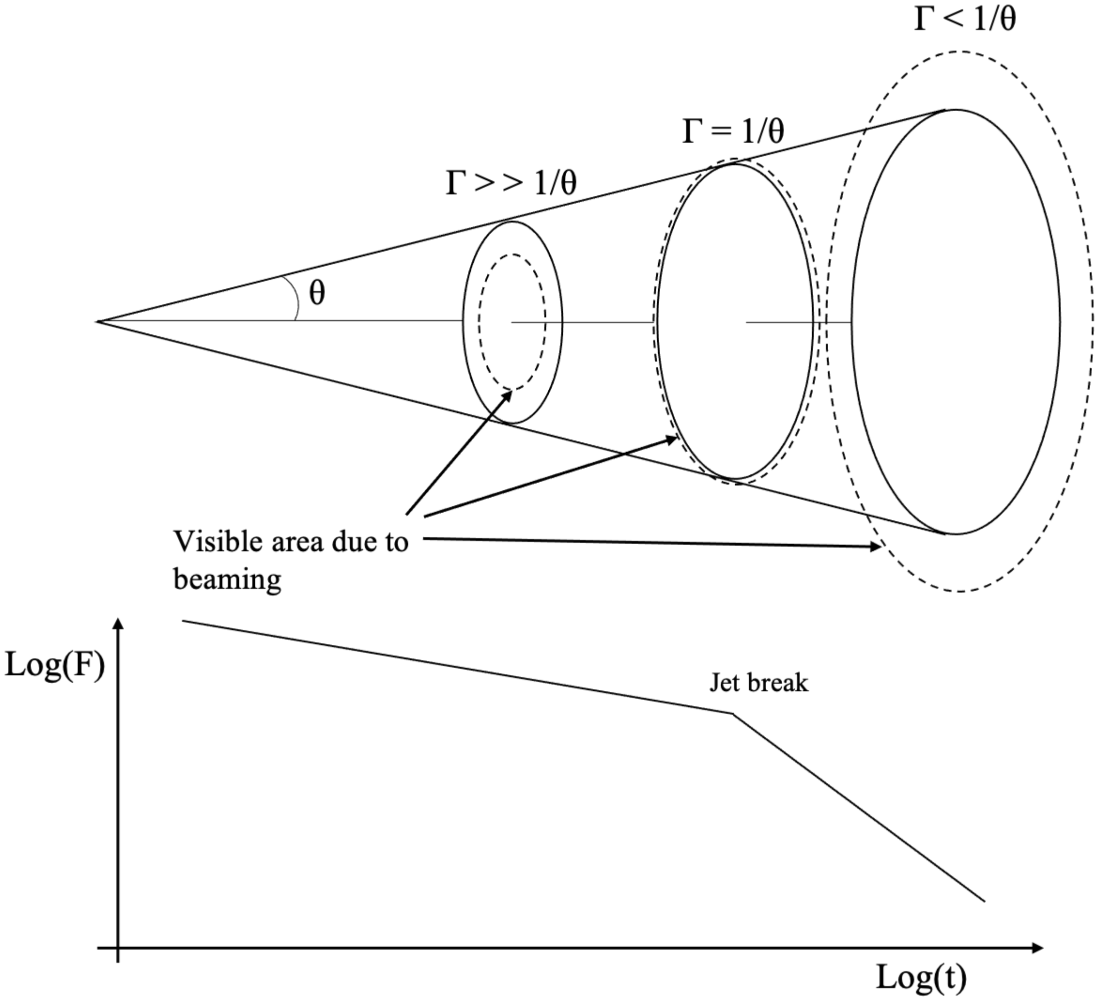

Figure 3.3: A schematic of how the jet deceleration creates achromatic breaks in afterglow light curves. At all times the luminosity of the jet is decreasing with time. At earlier times, Γ is higher and so the portion of the jet visible to the observer (denoted by the dashed oval) is smaller than the actual jet area: some of the emission is beamed out of the observer's line of sight. As the jet decelerates, the entire jet becomes visible to the observer. The increase in observable emission region size combined with the decrease in jet luminosity results in a slow light curve decay. The point at which $\Gamma = 1/\theta$ is the point at which the an achromatic break in the light curve occurs after which the flux observed decays much faster. At this point only the intrinsic flux decay of the shock front is observed.

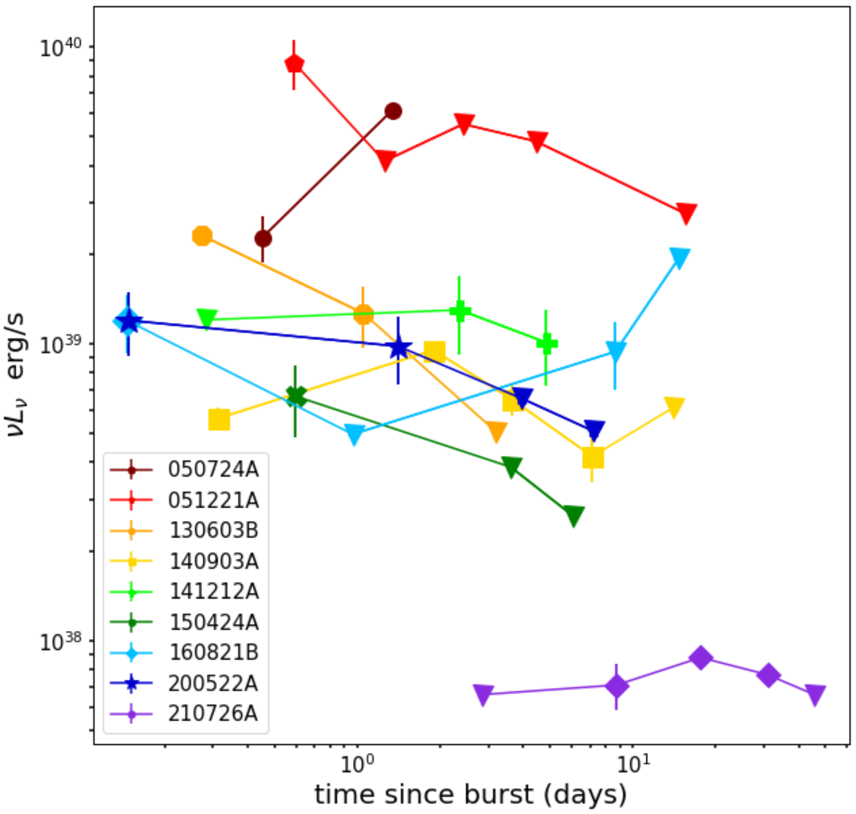

Figure 3.4: The radio afterglows for all short gamma-ray bursts to date except for the afterglow associated with GW 170817. The y-axis shows the radio luminosity of the afterglow as a function of rest frame time. This plot is an adapted of figure 1 in Fong et al. (2021) with the addition of MeerKAT detections of GRB 210726A that I obtained.

0.6.

For each of the events in Figure 3.4, the emission is interpreted as originating from a forward shock that is viewed on axis, with the exception of GRB 051221A and GRB 160821B (Soderberg et al., 2006; Lamb et al., 2019) which show evidence of a reverse shock component and GRB 210726A in which the interpretation is ongoing (Schroeder, Rhodes et al *in prep*). With so few data points and events, inferring more complex interpretations with multiple shock components as well as robust afterglow modelling is increasingly difficult and prevents afterglow models from being tested strongly. With more sensitive observing facilities coming online, more afterglow counterparts can be detected allowing for better understanding of short GRB jets. For example, there is only a single event with data ascertaining to the lateral structure of the jet: GW 170817 is the only doff-axis binary neutron star merger to be detected to date. In Section 3.4.1, I will present preliminary results of an ongoing project where I show the results of the first off-axis short GRB at cosmological distances. These detections are possible because facilities like the VLA and MeerKAT which can reach μJy noise levels.

3.1.4 Radio afterglow properties of long gamma-ray bursts

Long GRBs are more common and tend to be more luminous than their short duration counterparts and so the community's understanding of the radio properties of long GRB afterglows is much more comprehensive. The first radio detection of a long GRB afterglow was in 1997 from GRB 970508 (Frail et al., 1997). Since then regular detections of afterglows have been obtained from hours to years post-burst (e.g. Anderson et al., 2014; Leung et al., 2021). Large observing campaigns to search for radio counterpart have found that between 15 and 30% of long GRBs have detectable counterparts with an average flux density of 290±30 μJy (Chandra & Frail, 2012; Gusinskaia et al., 2017).

The evolution of the afterglow is much slower at radio frequencies compared to shorter wavelengths, with light curves peaking on average between 3 and 6 days (Chandra & Frail, 2012). When considering the long timescales over which the radio counterpart can be observed for, both ν_{SA} and ν_m can be observed to pass through the band. Therefore, observations of long GRBs in the radio band are more sensitive to the circumburst environment as well as the kinetic energy in the jet and its geometry.

Long GRB radio studies are also benefited by negative k-correction which enables afterglow detections out to high redshifts. The current most distant radio-detected GRB is GRB 090429B at z = 9.4, (Cucchiara et al., 2011), where the average redshift is 2.0 (Chandra & Frail, 2012). The GRB results presented in this thesis have host galaxies inferred to be at redshift 1.5 and below.

Radio detections across a broad redshift range mean that searching for trends in the properties of a whole population without considering the implications of long term galactic evolution is unlikely to produce many significant results. Furthermore, with so many detections, the inferred parameters are very broad. Aksulu et al. (2022) performed uniform modelling of a group of 26 long GRBs and determined that there was equal preference to homogeneous and stellar-wind environments amongst the long GRBs such a result is not uncommon: many afterglow light curves can be described by both stellar-wind-like and homogeneous environments (Starling et al., 2008; Schulze et al., 2011). Starling et al. (2008) also showed that probes of the blastwave physics from the power law index of the energy distribution of electrons (p) was uniformly distributed between two and three. The kinetic energies inferred for long GRBs span six orders of magnitude from 10^{50} to 10^{56} erg Aksulu et al. (2022).

Low redshift, high radio luminosity long GRBs ($>10^{31}$ erg s^{-1} Hz^{-1}) are excellent targets for Very Long Baseline Interferometry (VLBI). VLBI observations have provided direct evidence for the relativistic motion of GRB jets via the detection of superluminal expansion/motion (Taylor et al., 2004; Mooley et al., 2018a). Superluminal expansion/motion is an observational effect in which the expansion/proper motion speed of a source is measured to be greater than the speed of light. For such an effect to occur the source itself must be moving relativistically.

At the other extreme, because the afterglow is brighter in the radio band its deceleration can be tracked until it becomes sub-relativistic. In the sub-relativistic regime, calorimetric calculations can be performed and extract accurate kinetic energy calculations (Frail et al., 2005; Van der Horst et al., 2008; Berger et al., 2004).

Finally, multiple long GRBs have strong evidence of reverse shock emission, often revealed as an early time radio flare. The importance of synchrotron self absorption at low frequencies means that it is possible to disentangle shock components in both time and frequency space. The reverse shock evolution is dependent the depth of the shell: a thicker shell will give the reverse shock to accelerate more until it becomes relativistic whereas

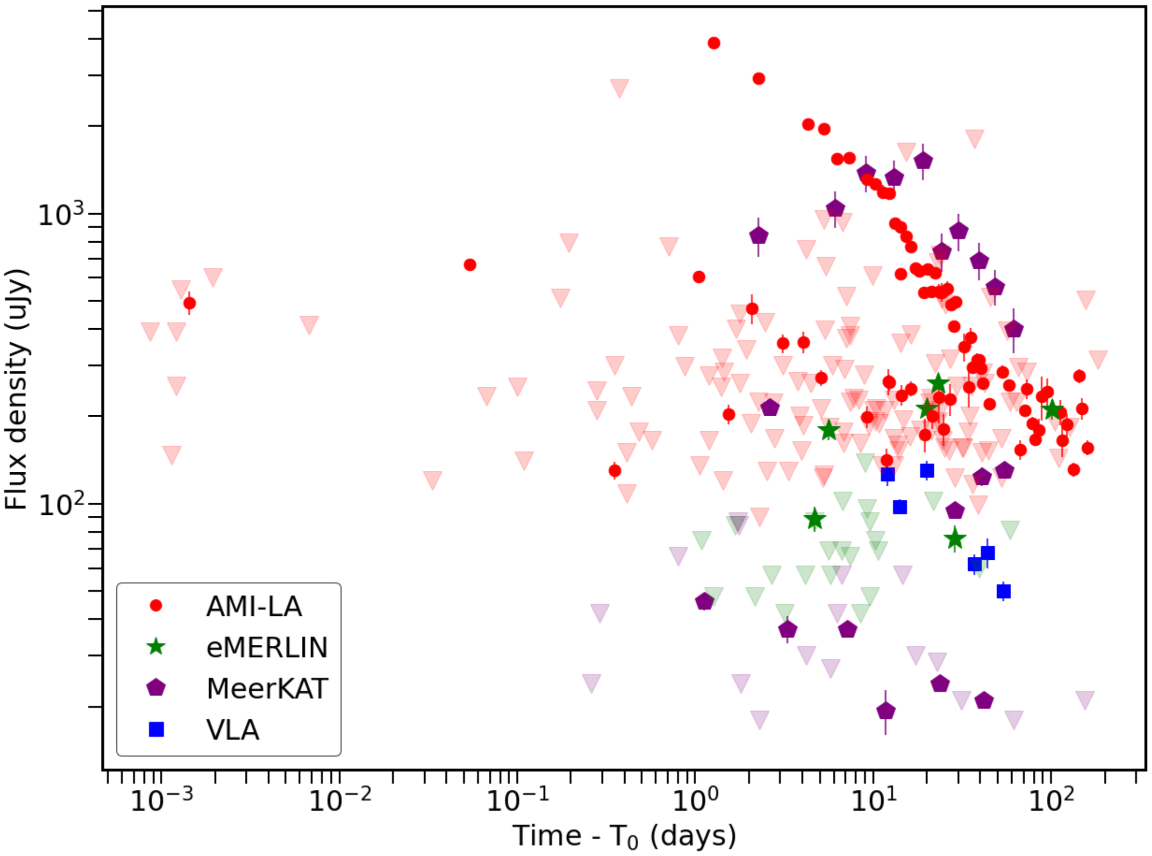

Figure 3.5: A summary of all the *Swift*-triggered GRB afterglow observations made with AMI-LA, *e*-MERLIN, MeerKAT and the VLA that I have worked on during my DPhil. The circles, stars, squares and pentagons represent detections and the faint downwards facing triangles are 3σ upper limits.

a thin shell will only produce a Newtonian shock. The evolution is also dependent on its environment: low density environments are particularly sensitive to strong reverse shock emission (Resmi & Zhang, 2016). Tracking the reverse shock is important in order to understand the nature of the outflowing material itself. Polarisation detections can be used to place constraints on the magnetisation of the jet, which is important for understanding the microphysical parameters (Laskar et al., 2019).

Despite the wealth of information that can be obtained from radio observations of long GRBs, comprehensive follow up consisting house of observing time is required to obtain this information. As a result, there are very few unbiased radio follow up programs for long GRBs because detailed observing campaigns for a single event are often preferred over less

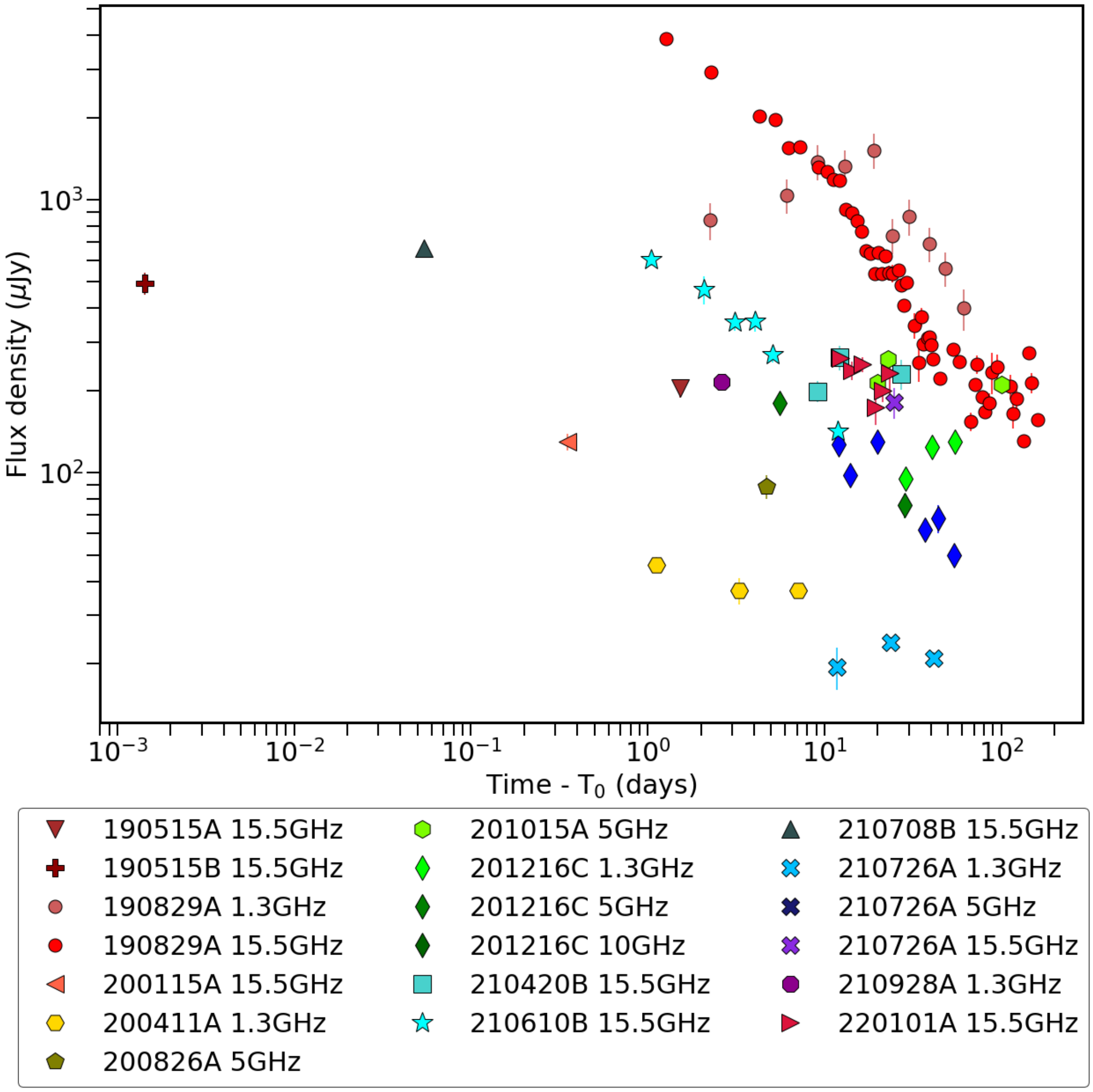

Figure 3.6: A summary of all the afterglow detections obtained with AMI-LA, *e*-MERLIN, MeerKAT and the VLA for GRBs I have observed during my DPhil. The frequency of the detection for each light curve is shown in the legend. The detections of GRBs 190819A, 201015A and 201216C are discussed in more detail in Chapter 4.

comprehensive studies of a larger sample. Often radio follow up is decided based on the optical properties of the afterglow: e.g. is there a bright optical counterpart or is the host galaxy at a particularly high or low redshift. As a result, there is a large range in the quality of radio coverage for long GRBs. In Section 3.2, I described the radio follow up performed using the AMI-LA interferometer which triggers on visible *Swift* GRBs independent of whether they are considered interesting or special.

3.2 Follow up with AMI-LA

GRB follow up with AMI-LA is performed by the ALARRM system (Staley et al., 2013). Upon the detection of a GRB by *Swift*-BAT, a notification is sent out via a VOEvent[1] which AMI-LA receives (Staley & Fender, 2016). Before March 2020, such a notification would trigger a fully automated observation in which the position of the GRB would be observed as soon as possible, i.e. when it reached at least 15° above the horizon.During the COVID-19 pandemic, the AMI-LA radio telescope was not used. After March 2022, the scheduler is notified of the trigger and adds the new GRB to the schedule. In both cases, the initial observation would last two hours.

Swift detects over 100 GRBs every year, of which approximately half are visible by AMI. Since January 2019, I have observed 57 GRB triggers with AMI-LA. All the detections and 3σ upper limits from AMI-LA are plotted in red in Figure 3.5. Of the 57 GRBs observed, nine data sets showed radio sources with coordinates consistent with those from *Swift*-BAT/XRT or an optical facility. The detections are summarised in Figure 3.6. The observations of GRB 210610B are presented in Section 3.2.2 and the multi-telescope observing campaign of GRB 210726A is summarised in Section 3.4.1. GRB 190829A is discussed further in Chapter 4.

Figure 3.7 shows the radio light curves for all GRBs observed with AMI where a radio

---

[1] https://wiki.ivoa.net/bin/view/IVOA/IvoaVOEvent

source was detected but was not the GRB afterglow: GRBs 190326A, 190515A, 190515B, 200115A, 210420B, 210704A, 210708B and 220101A. The top panel of Figure 3.7 shows the four triggers where only a single observation was made and a radio source was detected. GRB 190515A was a short GRB detected by Fermi. Fermi detections have large uncertainty regions and so whilst a radio source was detected within the localisation area, the high radio flux density but no optical or *Swift* detection means that the radio source is unlikely to be associated with the GRB trigger. GRB 190515B was triggered by *Swift*-BAT but a lack of optical counterpart did not motivate further observations. *Swift*-XRT was unable to slew to the position of GRB 200115A and GRB 210708B and as a result the uncertainty on the localisation of the event was 3 arcminutes. With such a large localisation region, again no optical follow up is performed. The initial BAT trigger meant that in both cases a single AMI-LA observation was made but the lack of multi-wavelength counterparts stopped subsequent epochs.

The second panel of Figure 3.7 shows the radio light curve of a source detected at the coordinates of GRB 210420B, interspersed with 3σ upper limits deeper than the detections. Variability on timescales of days is not expected from GRB afterglows. Such variability could be a result of scintillation but is unlikely at 15 GHz (see table 1 of Granot & Van der Horst, 2014). Instead the radio emission is attributed to the host galaxy which contains an AGN.

The middle panel of Figure 3.7 shows the radio light curve of a source associated with GRB 220101A. The light curve is flat across 20 days, uncharacteristic of an afterglow. The lack of variability in the radio emission means that it is most likely from star formation in the host galaxy. AMI-LA's 30 arcsecond beam diameter, means that regularly any host galaxy radio emission is blended with any afterglow emission.

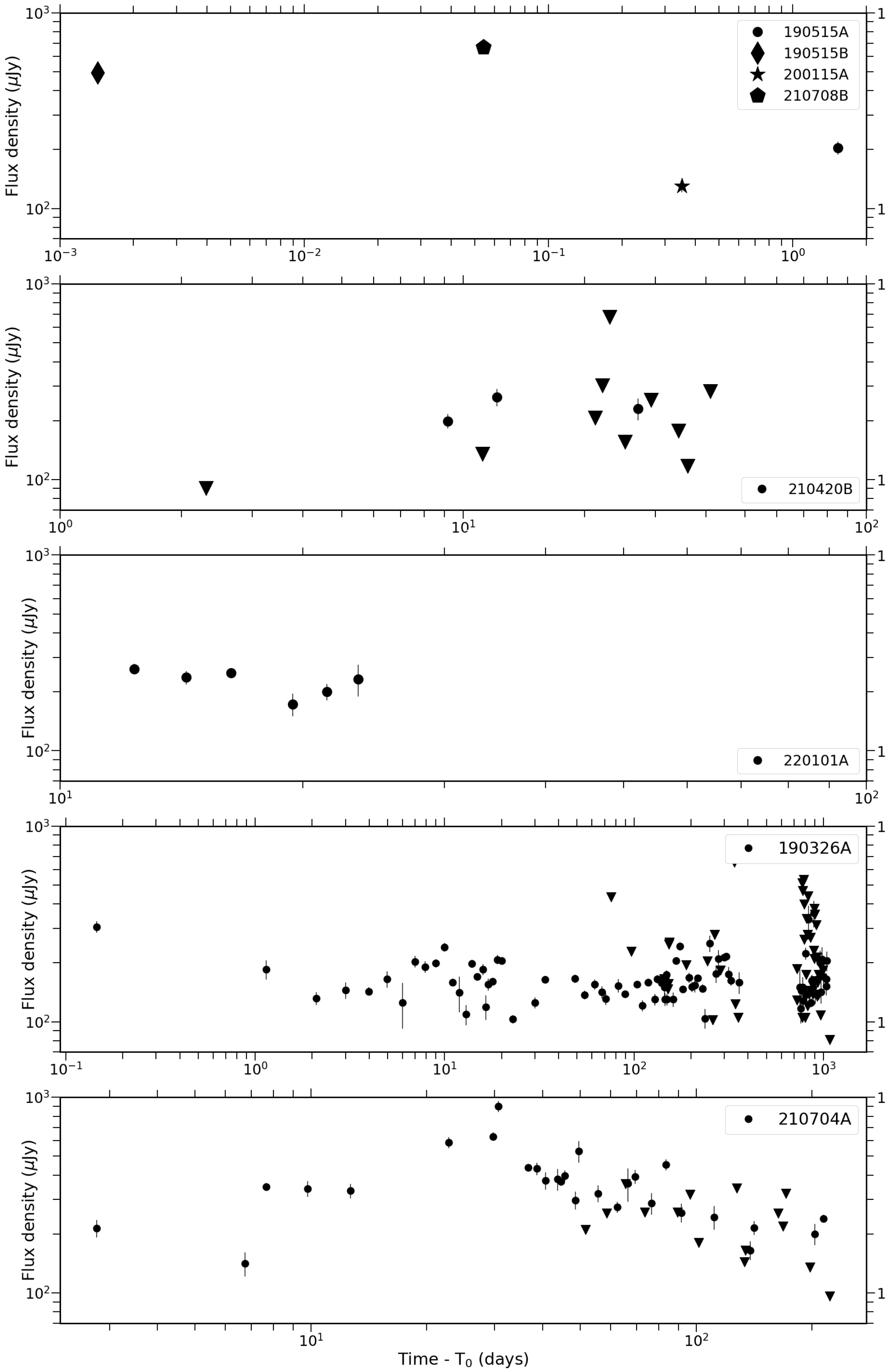

Figure 3.7: Caption on the following page

Figure 3.7: Radio detections obtained with AMI-LA which are not discussed elsewhere in this thesis. The top panel shows single detections of four separate long GRBs. The second panel shows a series of detections and non-detections of a radio source associated with GRB 210420B. The deep upper limits with respect to the detections show that the radio source is variable on day-time scales indicating that is not likely to be the GRB afterglow. GRB 220101A was observed for 6 epochs between 10 and 30 days post-burst. The VLA detected a counterpart at ~200 μJy at 6 GHz about 4 days post burst (Laskar, 2022). The bottom two panels show radio light curves of the host galaxies of two short GRBs.

3.2.1 Interesting sources

The bottom two panels of Figure 3.7 show long term light curves with clear non-GRB like trends. Early time observations of short GRBs 190326A and 210704A showed power law rise/decay behaviour i.e. what is expected from a GRB afterglow (see before day 10 and ~30 in the second to bottom and bottom panels of Figure 3.7, respectively).

GRB 190326A

The first observation of GRB 190326A was performed ~2 hours post burst. The detection of a source at 300 μJy prompted daily observations as well as Directors discretionary time (DDT) observations at 5 GHz with *e*-MERLIN. The early light curve could be interpreted as a GRB afterglow with its power law evolution. However, a flat spectral index was between 5 and 15.5 GHz at multiple epochs which is inconsistent with the expected afterglow evolution. Subsequent radio monitoring of the source showed day-to-day variability that deviates from the power law-like afterglow evolution.

A photometric redshift from the Gran Telescopio Canarias places the source at redshift $\gtrsim 2$. At z = 2, the radio luminosity would be over an order of magnitude higher than any previous short GRB afterglow. Figure 3.8 shows that the ratio of the optical and radio flux density is consistent with a GRB, but also with quasars. Extrapolation of the quasar sample (blue circles in Figure 3.8) to lower flux densities would overlap with the position of GRB 190326A. The multi-epoch flat radio spectral index is also more consistent with a quasar scenario than that of a GRB. The high radio luminosity, the optical-radio flux ratio and the flat spectral index indicates that the radio source was more likely a quasar. Therefore, it is possible that the binary neutron star merger occurred in a galaxy hosting a quasar resulting in a coincidental event.

It is also possible that the GRB prompt emission did not originate from a binary neutron star merger. Analysis of the *Swift*-BAT prompt emission spectra showed an unusually soft spectra for a short GRB. At z = 2, GRB 190326A would be the most high-redshift short GRB to date (Berger, 2007). Instead, I propose that GRB 190326A was instead a X-ray/gamma-ray flare from a quasar which mimicked a short duration GRB (Dermer & Giebels, 2016). It would be hard to rectify the long inspiral time with the high red-shift host galaxy. Could it be that a gamma-ray flare was only luminous enough to be detected by BAT for less than a second? As a result it would not have been possible to detect any radio afterglow, only the quasar.

GRB 210704A

The bottom panel of Figure 3.7 shows the 15.5 GHz light curve of GRB 210704A. The event was a short GRB detected by the AGILE Mini Calorimeter (Ursi et al., 2021). Two potential host galaxies at z=0.203 and z=0.0817 (the GRB was in a region of high galactic number density) as well as an afterglow counterpart were identified by rapid optical follow up (Levan et al., 2021; Kim et al., 2021; Kann et al., 2021). At optical wavelengths, the localisation of GRB 210704A is precise enough such it can be separated from the nuclear region of either potential host galaxy, but with with AMI-LA the large beam size encompasses many of the galaxies in the vicinity of the GRB on the sky. It is possible that one of these galaxies contained an AGN.

The radio light curve for GRB 210704A follows a similar pattern to that of GRB 190326A: a power law-like rise and decay combined with inter-epoch variability. The optical-radio flux density ratio is similar to that of GRB 190326A. The lower redshift of GRB 210704A makes the radio luminosity more in agreement with other short GRBs

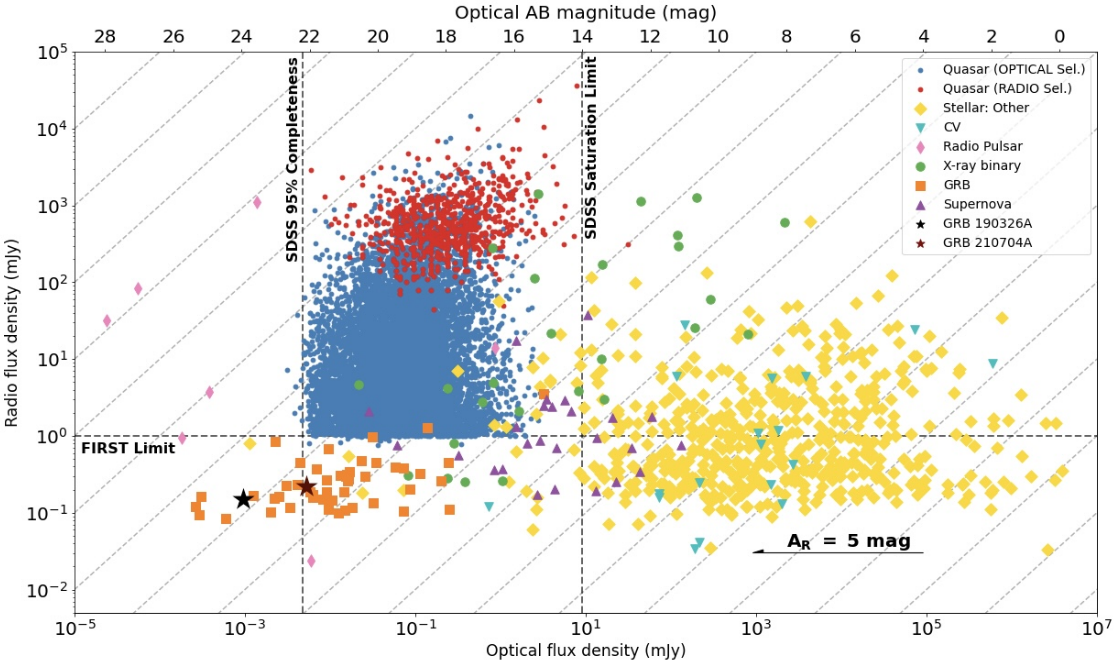

Figure 3.8: From Stewart et al. (2018) with a data points from GRB 190326A and GRB 210704A. The data for GRB 190326A is from AMI-LA and GTC and for GRB 210704A, I use data from AMI-LA and a detection of an optical counterpart from de Ugarte Postigo et al. (2021). Both GRBs are consistent with a GRB afterglow but it is also possibly consistent with a quasar.

(Figure 3.4). The peak flux density corresponds to a luminosity around 10^{40} erg/s. With the current data set, it is not possible to confidently identify the origin of the radio emission. Given the short timescale variability in the radio light curve, the AGN origin is favoured over an afterglow.

3.2.2 GRB 210610B: an early jet break and possible reverse shock

GRB 210610B was first detected by *Swift*-BAT on on 10th June 2021 at 19:51:27 UT along with a bright optical afterglow (Page et al., 2021). Optical spectroscopy placed the host galaxy of the GRB at z = 1.13 (Fynbo et al., 2021; De Ugarte Postigo et al., 2021).

AMI-LA observations were triggered and the first epoch started ~seven hours post-burst. No radio emission was detected in the preliminary observation. Nine hours post-burst, the

VLA detected an afterglow counterpart at approximately same flux density as the AMI-LA upper limit (Alexander et al., 2021). The position of GRB 210610B was observed eight more times with AMI-LA. This analysis is contributing to a paper Laskar, Rhodes et al (*in prep*).

Results and Interpretation

Figure 3.9 shows the 15.5 GHz, optical and 10 keV light curves for GRB 210610B. Observations with *Swift*-XRT lasted between 0.05 and 4.8 days post burst. The XRT light curve scaled to 10 keV follows a broken power law with a break at 0.7±0.4 days. The power law exponents are -0.6±0.2 and -2.2±0.5, i.e. the flux is always decreasing with time.

The radio light curve at around 15 GHz combines data from both the VLA and AMI-LA. Observations started at 0.3 days post-burst and lasted 20 days. The light curve follows a broken power law peaking at 0.9±0.3 days. The pre- and post-break light curve exponents are -0.2±0.2 and -1.1±0.2, respectively.

The optical light curve is more complex compared to the radio or X-ray ones: there is a power law decay which breaks around 0.05 days and rebrightens before decaying again after 0.5 days. A phenomenological fit to the optical light curve is made using three power law components. Until 0.05 days post burst, the light curve can be described with single power law decay: $t^{-0.8\pm0.1}$. The second component follows a broken power law with a turnover (0.9±0.3 days) around the same time as the break in the X-ray light curve: $t^{-0.2\pm0.2}$ and the decay follows $t^{-2\pm2}$. The large uncertainties on the decay rate of the second component are due to the low number of data points.

There are similar break times in the optical, radio and X-ray light curves implying that the break is not spectral but more likely is a jet break. A joint fit to the optical, X-ray and radio light curves gives a break time of 0.5±0.1 days. When fit together, the forward shock optical and X-ray light curves evolve as $t^{-0.1\pm0.2}$ and $t^{-2.1\pm0.2}$ pre and post-break, respectively. The post-break decay exponent is consistent with a jet break decay following t^{-p}, where p

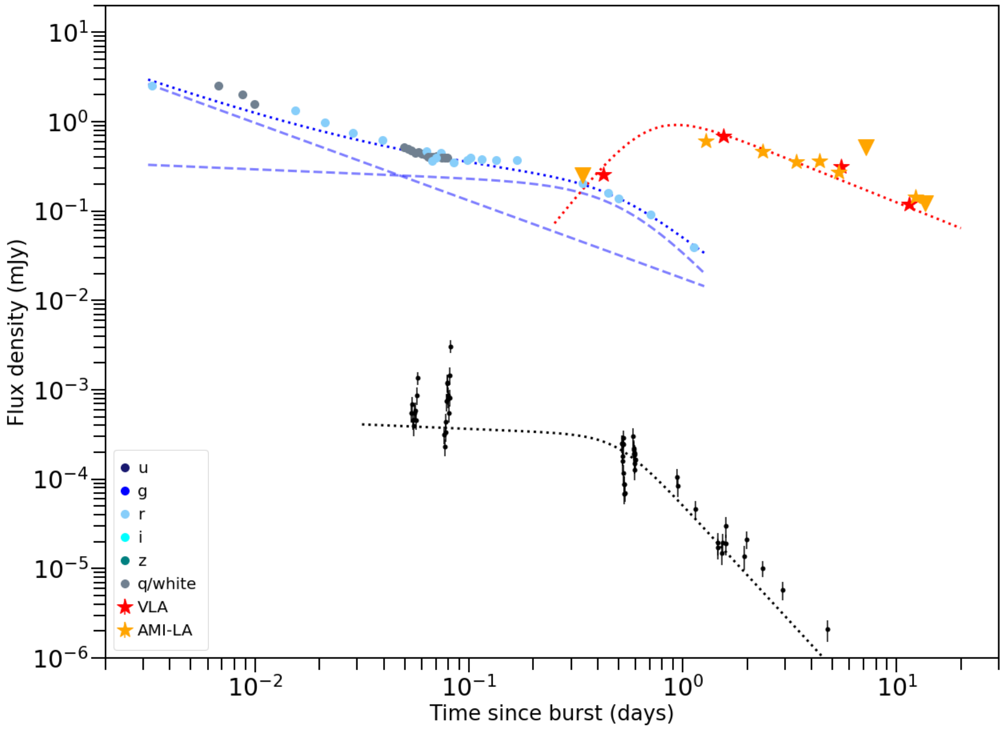

Figure 3.9: The 15 GHz, optical and X-ray light curves for GRB 210610B. The radio and X-ray light curves are both dominated by forward shock emission. The forward shock models fit to the radio and X-ray data are denoted by the red and black dotted lines, respectively. The optical light curve shows but the total fit to the data as well as the contribution from the forward shock, calculated from the X-ray and radio data. The excess emission is from a reverse shock. The models of the two separate emission regions are given in blue dashed lines and the total optical model is denoted by the blue dotted line.

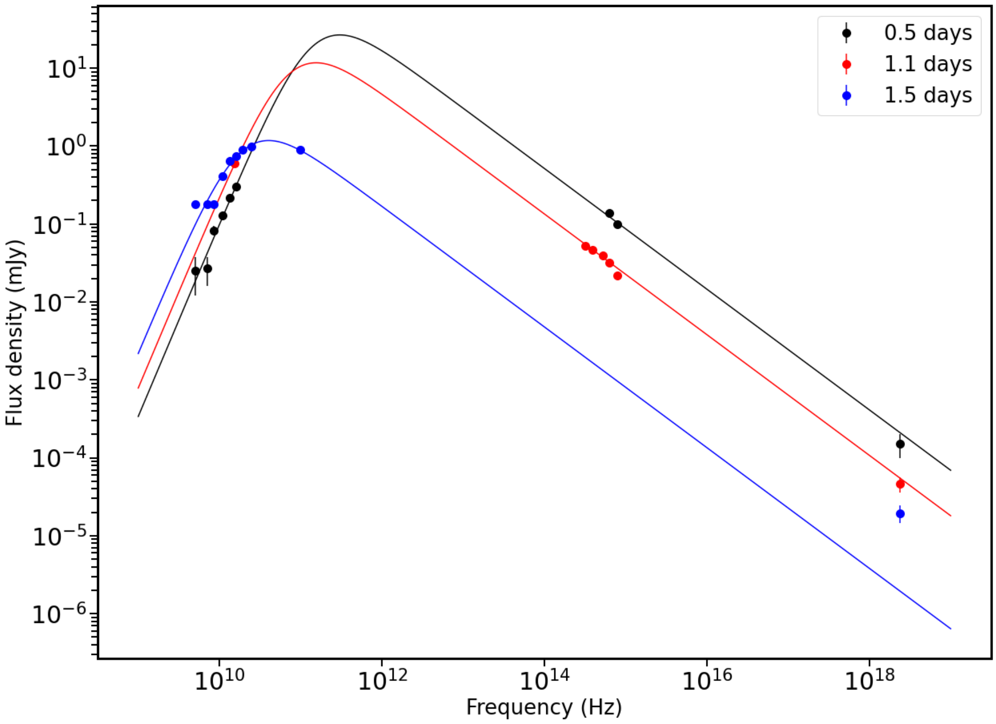

Figure 3.10: Broadband spectra from GRB 210610B at three epochs: 0.5, 1.1 and 1.5 days post burst.

T-T$_0$ (days)	F$_{\nu,\,\mathrm{max}}$ (mJy)	ν_{peak} (Hz)
0.5	21±9	(1.5±0.5)×10^{11}
1.1	9±9	(8±2)×10^{10}
1.5	0.89±0.07	(2.0±0.2)×10^{10}

Table 3.1: The flux density and frequency location of the peak of the spectrum in each epochs where there is at least radio and optical data. A joint fit has been made to all three data sets allowing only the peak flux density and corresponding frequency to move.

= 2.1±0.2. The light curve-derived value of p is consistent with that obtained from the broadband spectral fits at a 2σ level (Figure 3.10, p = 2.5±0.1). The pre-break decay is very flat for optically thin synchrotron however the complicated optical light curve prevents a better constraint on the early optical forward shock emission. The early optical light curve is complicated by the likely presence of a reverse shock component. Such a component, combined with the rising forward shock is producing a flatter light curve and therefore affects the fitting of the light curve.

Figure 3.10 shows broadband spectra spanning from radio to X-rays at 0.5, 1.1 and 1.5 days post burst. The spectra at all three epochs are consistent with coming from a single shock component. All three epochs are from the period where the second optical component i.e. the forward shock is dominating. A joint fit to all three epochs, allowing F$_{\nu,\,\mathrm{max}}$ and ν_{peak} to vary from epoch to epoch, and assuming the spectral indices were constant. Table 3.1 summarises the values of F$_{\nu,\,\mathrm{max}}$ and ν_{peak} for each epoch. The measured spectral indices are +2.5±0.2 and -0.78±0.07. The steep positive spectral index is most consistent with the radio band falling above ν_m and below ν_{SA} so that ν_{SA} causes the peak of the spectrum. The negative spectral index is consistent with the 0.3-10 keV in-band index ($\beta_X = -0.9 \pm 0.1$), implying that the optical and X-ray emission are from the same branch of the synchrotron spectrum and that there is no spectral break between the optical and X-ray bands after 0.1 days. If ν_C fell between the optical and X-ray bands, one would expect $\beta_X = \beta_{opt} - 0.5$ which is not observed. The full spectrum follows: $\nu_m < radio < \nu_{SA} < \nu_{opt} < \nu_X < \nu_C$. From the broadband spectrum, p = 2.5±0.1. Therefore, the radio, X-ray and optical emission (from 0.5 days onwards) is all from a forward shock and all three light curves show a break just before/around one day post-burst.

Despite the excellent spectral coverage, there is no evidence of ν_m and ν_C, ν_m must be above 5 GHz and ν_C must be above 10 keV. Using the values of ν_{SA} and $F_{\nu,\,\mathrm{max}}$ it is possible to calculate the density and kinetic energy in the jet by assuming values of ϵ_e and ϵ_B (0.1 and 0.01, respectively). The radio spectra at 0.5 days can be recreated if the kinetic energy is $\sim 1.6\times10^{52}$ erg and the ISM density is 1.8 cm^{-3} (Granot & Sari, 2002). With these values, a jet break at 0.5 days corresponds to an opening angle of about 3° which is similar to other measured long GRB opening angles (Frail et al., 2001).

The interpretation above only considers the forward shock component which dominates the optical light curve before ~0.05 days. More work is required to understand this part of the data considering that the exact decay rate of reverse shock component heavily affects the optical/x-ray joint fit.

3.3 Follow up with *e*-MERLIN

The observing campaign with AMI-LA is most sensitive to radio detections of long GRBs. In an effort to expand the population size of radio-detected short GRBs and to obtain an unambiguous reverse shock detection I have obtained observing time through open time calls to search for radio afterglow emission from short GRBs across five observing terms (as well as DDTs to observe two long GRBs: GRB 201015A and 201216C - these are discussed in Chapter 4) with *e*-MERLIN. The observations are summarised in Figure 3.5 as green stars and downwards facing triangles.

There are two short GRBs with radio detections that infer the presence of a reverse shock components, (Soderberg et al., 2006; Lamb et al., 2019), however in order to come to said conclusion multi-wavelength data is required. Early time observations are important in order to catch the reverse shock before it decays and the forward shock begins to dominate. Predictions of reverse shock emission from events where forward shocks have been observed show that the reverse shock counterpart should be detectable (Lloyd-Ronning, 2018). Multi-frequency, higher cadence observations are required to more confidently detect reverse shock emission.

Each trigger of my *e*-MERLIN short GRB observing campaign consisted of four observations in the first four days post-burst, followed by a further three observations made every other day. Each observation consisted of eight hours on source in order to reach 20 μJy rms noise. Such high cadence observations were justified given that previous short GRB afterglow detections were all made before 10 days post-burst.

The low radio luminosities of short GRB afterglows makes detecting counterparts very difficult: GRB 200826A was the only short-duration GRB detected with *e*-MERLIN over the past three years, which is discussed in Section 3.3.1. With *e*-MERLIN, I have obtained unamibiguous detections of a single short duration GRB and published the results in Rhodes et al. (2021a).

3.3.1 The afterglow of GRB 200628A, a collapsar masquerading as a binary neutron star merger

GRB 200826A was first detected by the Fermi Gamma-ray Burst Monitor at 04:29:52 UT on 2020 August 26 (T_0) (Fermi GBM Team, 2020). With a T_{90}=1.1±0.1s between 50-300 keV, it was classified as a short GRB. The *Swift* X-Ray Telescope (XRT) reported seven uncatalogued sources within the Fermi error region (Evans et al., 2010). A potential afterglow candidate, ZTF20abwysqy, was identified at redshift 0.714±0.137 by the Zwicky Transient Facility (ZTF, Ahumada et al., 2020a) with coordinates consistent with source three from *Swift*-XRT. Alexander et al. (2020b) reported the first radio detection of this source at 2.28 days post burst with a flux density of ~40 μJy at 6 GHz. Since the initial detection, further spectral analysis by Svinkin et al. (2020) showed that GRB 200826A may have been a long GRB at the short end of the T_{90} distribution. Optical observations using the Gemini North telescope have detected emission bright enough to originate from a supernova as opposed to a kilonova, the thermal counterpart associated with short GRBs, providing further evidence that this may be a long GRB (Ahumada et al., 2020b).

Observations

Observations of GRB 200826A with the *enhanced Multi Element Remotely Linked Interferometer Network* (*e*-MERLIN) were obtained through proposal CY10002 (PI: Rhodes). The field of GRB 200826A was observed for six separate epochs between four and eleven days post-burst at 5 GHz, with a bandwidth of 512 MHz. All dishes except for the Lovell were used. Each measurement set was averaged down to 4 second integrations and 512 channels. A priori flags were applied due to RFI followed up with additional flagging to improve the quality of datasets. Calibration was performed using the *e*-MERLIN pipeline[2]. Initial bandpass calibration was performed using J1407+2827, before calculating complex gains using J0012+3353. Absolute flux scaling was applied from 3C 286. Calibration tables were then applied to the target field. The calibrated measurement set was imaged using *tclean* in CASA (McMullin et al., 2007a).

Results

Here, the results of the previously described *e*-MERLIN radio observations, along side publicly available data from the VLA (Alexander et al., 2020b), the upgraded Giant Meterwave Radio Telescope (uGMRT), (Chandra et al., 2020) and XRT are presented. The data are interpreted in the context of the fireball model by fitting phenomenological models to the data. All results are presented following the convention $F_\nu \propto t^\alpha \nu^\beta$, t is the time since burst, ν is the central frequency or energy of the observing band, and α and β are the power law indices.

---

[2] https://github.com/e-merlin/eMERLIN_CASA_pipeline

T-T$_0$(days)	ΔT (days)	Flux Density (μJy)	Photon Index
0.70	0.01	0.4± 0.1	1.2±0.4
0.75	0.01	0.035± 0.009	1.2 ±0.3
0.8	0.1	0.028±0.007	1.3± 0.3
1.8	0.3	0.005± 0.001	1.6± 0.3
2.6	0.3	0.0035± 0.0008	1.8± 0.4
6.4	2.2	0.0027± 0.0006	1.7± 0.4

Table 3.2: *Swift*-XRT flux densities at 10 keV and photon indices between 0.3-10 keV. 'T' is the time in the middle of each observation and 'T$_0$' is 04:29:52 UT on 2020 August 26 (Fermi GBM Team, 2020). ΔT (days) reflects the duration of each observation (Evans et al., 2007).

Results: X-ray

The afterglow candidate of GRB 200826A was observed by *Swift*-XRT from ~0.7 to 8 days post burst (D'Ai et al., 2020) in the 0.3-10 keV band. The XRT data points are shown as black filled circles in the upper panel of Figure 3.11. All data points have been corrected for absorption. The light curve is fit with a single power law decay. The decay follows F$\propto t^{-1.8\pm0.4}$ and is shown in Figure 3.11 as the green dot-dashed line. The fit has a reduced χ-squared of 3.5. The last data point shows an excess flux with respect to the given model. This lends itself to the possibility that the light curve could also be fit with a broken power law, however an f-test performed on the data set allow a broken power law to be rejected in favour of a single power law fit (Evans et al., 2009).

The *Swift* burst analyser fit an absorbed power law spectrum to each GRB 200826A epoch (Evans et al., 2010). The lower panel of Figure 3.11 shows the photon index evolution, i.e. the power law fit to each spectrum. There appears to be no significant evolution of photon index over the period where GRB 200826A is detected. The average photon index is 1.5 ± 0.2, corresponding a spectral index of $\beta = -0.5 \pm 0.2$ (green horizontal dot-dashed line in the lower panel of Figure 3.11).

All flux and photon index results are given in Table 3.2.

T-T$_0$(days)	Flux Density (μJy)	T$_c$-T$_0$(days)	Flux Density (μJy)
4.92±0.5	93 ± 16	-	-
5.91±0.46	< 57	6.4 ± 0.9^a	68 ± 8
6.90±0.42	< 102		
7.65±0.83	< 66	8.7 ± 1.9^b	< 34
8.92±0.79	< 42		
9.96±0.67	< 48		

Table 3.3: Table of 5 GHz observations from *e*-MERLIN. 'T' is the time in the middle of each observation and 'T$_0$' is 04:29:52 UT on 2020 August 26 (Fermi GBM Team, 2020). In order to reach lower noise levels, I concatenated some of data sets. The central time of each concatenated dataset is shown in the column labelled T$_c$. ^{a}: a concatenation of epochs two and three starting at 5.91 and 6.90 days post burst. ^{b}: epochs four, five and six combined. The errorbars quoted with the observation times reflect the duration of each observation. Any flux density value prefixed by '<' is a 3σ upper limit.

Results: Radio

The first *e*-MERLIN observation of the GRB 200826A field, starting 4.67 days post burst, showed a point source with coordinates: (J2000) R.A. $00^h27^m08.54^s$ and Dec +34°01'38.34". The positional uncertainty is ±0.01". The location of the VLA source reported by Alexander et al. (2020b) is consistent with our more precisely measured position. The remaining five epochs were non-detections, when examined individually. To increase the possibility of detecting the afterglow, epochs two and three were combined into a single longer observation to reduce the rms noise in the field resulting in a 4σ detection. The two initial observations had rms noise levels of 19 and 34 μJy/beam, respectively. Epochs four, five and six, which had rms levels of 22, 14 and 16 μJy/beam, were also combined but still showed no detection. The flux densities and non-detections are shown in Table 3.3.

The radio light curve in upper panel of Figure 3.11, shows the *e*-MERLIN data combined with that from the VLA, and the uGMRT. The *e*-MERLIN data points are blue squares and the downward facing triangle, Alexander et al. (2020b)'s VLA detection is shown as the light purple star and the uGMRT upper limit is given as a dark purple downwards-facing

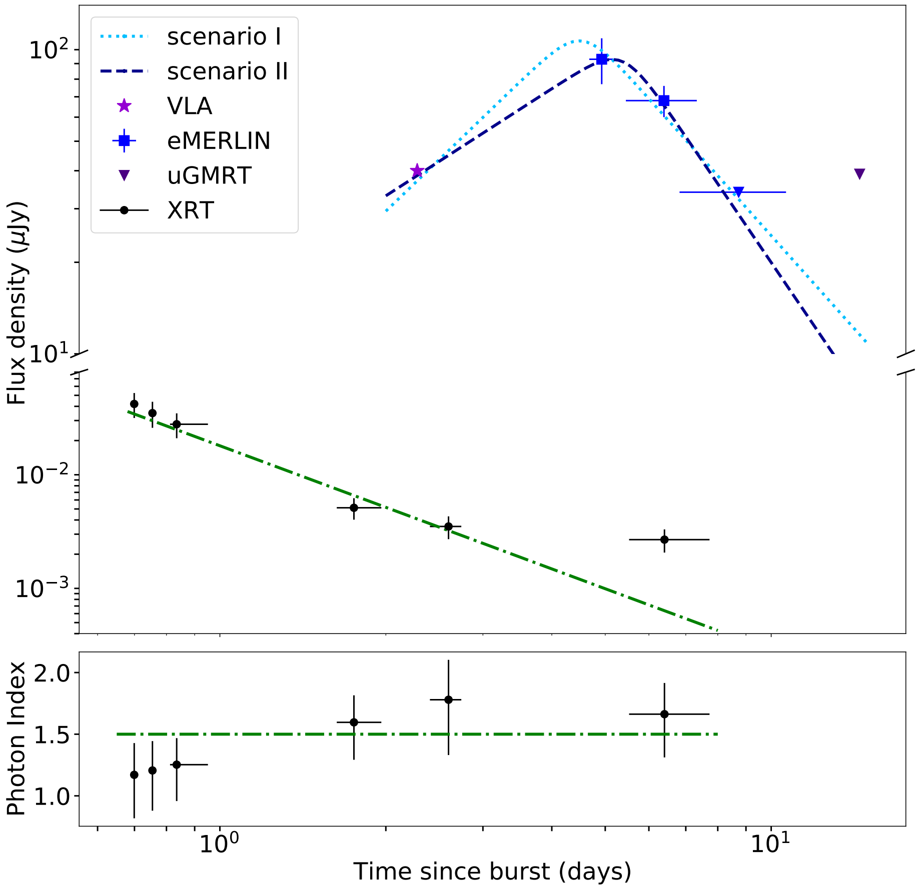

Figure 3.11: *Upper panel*: Radio light curve of GRB 200829A combining *e*-MERLIN 5GHz data with Alexander et al. (2020b)'s VLA reported flux and Chandra et al. (2020)'s uGMRT upper limit as shown in blue squares and upside down triangle, the light purple star, and dark purple upside down triangle, respectively. The horizontal error bars on the *e*-MERLIN data points show the duration of the observations required to make the respective detections or non-detections. The uGMRT data point is scaled from 1.25 GHz to 5 GHz using a spectrum that transitions from optically thick to thin. The light blue dotted and dark blue dashed lines correspond to the models presented in sections 3.3.1 and 3.3.1, respectively. The black circles are from *Swift*-XRT showing a power law decay - the green dot-dashed line. *Lower panel*: The spectrum was analysed for each epoch and fit using an absorbed power law with an average photon index: 1.5 ± 0.2, denoted by a green dot-dashed line.

triangle (Chandra et al., 2020). The VLA observation was made at a central frequency of 6 GHz but with a wide bandwidth of 4 GHz, there is comfortably enough overlap between the VLA and *e*-MERLIN observing frequencies. The uGMRT observation was made at 1.25 GHz and so this was scaled to an upper limit of 48.6 μJy to 39 μJy at 5 GHz. In scaling the upper limit, the location of synchrotron self-absorption frequency is considered, and discussed in section 3.3.1, at 2.1 GHz at the time of the observation and corrected the flux density accordingly. For the analysis of this data set, given the low flux level of the source, a 15% error on the VLA point is assumed.

Discussion

The XRT light curve, the upper panel of Figure 3.11, may be from synchrotron emission from a FS either above or below the cooling break. The expected temporal exponent for emission from above the cooling break, where synchrotron losses are significant, is $\alpha = \frac{2-3p}{4}$, independent of circum-burst environment, which for a measured $\alpha_{10\,\mathrm{keV}} = -1.8 \pm 0.4$ gives $p = 3.1 \pm 0.7$. The temporal exponent for emission below the cooling break is $\alpha = \frac{3(1-p)}{4}$ and $\frac{1-3p}{4}$ for an ISM and wind environment, respectively (Granot & Sari, 2002). Comparing these exponents to that measured would give $p = 3.4 \pm 0.8$ and $p = 2.7 \pm 0.6$. Within uncertainties, all the above values of p fall within the expected range (Troja et al., 2019).

To determine which branch of the synchrotron SED the emission detected by XRT originates from, the X-ray spectrum is required. An average photon index of 1.5 ± 0.2, gives $\beta = -0.5 \pm 0.2$, which is too shallow to originate from above the cooling break. Below the cooling break, this value of β gives $p = 2.0 \pm 0.8$, which is more in agreement with the stellar-wind scenario than the ISM case from the X-ray light curve. A shallow spectrum is expected from optically thin synchrotron emission, suggesting that the 0.3-10 keV emission likely originates from below the cooling break. Combining this information with that from the light curve, these data show us that the FS is moving through a medium with a wind-like density profile.

The radio light curve is more complex to interpret. Firstly, I use the radio luminosity to help determine whether GRB 200826A is a short or long GRB. The luminosity of the first *e*-MERLIN data point is $1.6^{+0.4}_{-0.6} \times 10^{30}$ erg s^{-1}Hz^{-1}. Long GRBs of such low luminosity have been detected previously, (Chandra & Frail, 2012; Anderson et al., 2018; Rhodes et al., 2020), but at higher frequencies and only at very low redshift <0.1, far lower than the redshift of GRB 200826A. On the other hand, comparison to the radio luminosities in figure 13 of Fong et al. (2021) shows no significant differences between the luminosity of GRB 200826A and the rest of the radio-detected short GRB population. I acknowledge that the radio-detected short GRB population is very small compared to the corresponding long GRB population.

There is a span of a few days between the VLA reported detection and the first *e*-MERLIN detection, where there is no radio data, and so the location of the radio light curve peak is not well constrained. Therefore, I consider two separate scenarios to interpret these radio data based on the time of the light curve peak. In the first scenario, the peak of the light curve is assumed to precede the first *e*-MERLIN observation but after the VLA epoch. In the second scenario, the first *e*-MERLIN data point is assumed to be the light curve peak.

Scenario I: Radio peak comes from ν_{SA} moving through the radio band

To determine the earliest possible peak of the radio light curve, the rise from the VLA point needs to be as steep as possible without being unphysical. The steepest rise, which would produce the earliest light curve break would occur if the FS shock is optically thick. In a wind-like environment the flux evolves quickly as $F \propto t^{1.75}$ (Granot & Sari, 2002). The break following the rise would be due to ν_{SA} passing through the band. In an ISM environment, i.e. one with a constant electron number density, the rise would follow $F \propto t^{1.25}$. This shallower rise would cause the break to occur during our first observation. Additionally, the XRT light curves favour a wind environment, which further disfavours this scenario. If the break was due to ν_M, the rise would be far shallower than for an optically thick FS: $F \propto t^{1/2}$ or t^0 for an ISM or wind density profile, respectively. Either case is too shallow to be consistent with the radio light curve.

Therefore, a broken power law, with the rise fixed as $t^{1.75}$, is fit to the data using the Monte Carlo Markov Chain (MCMC) sampler EMCEE (Foreman-Mackey et al., 2013). The optimum fit was found using maximum likelihood analysis with flat priors on all variables. The analysis uses 700 independent walkers, each taking 10000 steps, the first 6000 of which were burnt. The mean, lower and upper uncertainties quoted from the analysis are the 50th, 16th and 84th percentiles of the samples in the marginalised distributions, respectively. The results from fitting a broken power law to the data this way are consistent with those if a single power law is fit to only the *e*-MERLIN data.

The resulting fit is shown as the light blue dotted line in Figure 3.11 (the corner plot of the fit is shown in the Appendix, Figure B). The decay seen in the *e*-MERLIN data can be described using a power law decay of $F \propto t^{-2.0^{+0.6}_{-0.8}}$, denoted by the light blue dotted power law in the upper part of Figure 3.11. Comparison with theoretical light curves from Granot & Sari (2002), shows that the *e*-MERLIN data are also in agreement with emission from the optically thin branch of the synchrotron spectrum i.e. on the same branch as the XRT light curve. Equating $\alpha_{5\,\mathrm{GHz}}$ with the exponents for an ISM and wind environment, gives $p = 3.7 \pm 1$ and $p = 3.0^{+0.9}_{-1.2}$, respectively. Only the value of p for a stellar wind environment ($p = 3.0$) is in agreement with the results from our XRT data. Both the X-ray and *e*-MERLIN light curves may have been produced by an optically thin FS propagating through a wind-like density profile circum-burst medium.

From the light curves, it is possible to conclude that the *e*-MERLIN and XRT data sets both are produced by optically thin synchrotron emission. This is confirmed by measuring a radio-X-ray spectral index. The radio-X-ray spectral index of $\beta_{5\mathrm{GHz}-10\mathrm{keV}} = -0.52 \pm 0.01$ is obtained at around six days post-burst. It is consistent with optically thin synchrotron, confirming that both the 5 GHz and 10 keV data points originate from the same branch of the synchrotron SED. The value for $\beta_{5\mathrm{GHz}-10\mathrm{keV}}$ converts to $p = 2.04 \pm 0.04$, which is shallower than the result from radio-derived values but is in agreement from that calculated from the XRT photon indices.

Therefore, for the peak in the light curve to occur before the first data point, an optically thick rise through a wind-like environment is required. The *e*-MERLIN data are in the regime such that $\nu_M < \nu_{SA} < 5\,\mathrm{GHz} < \nu_C$.

From inferring that the peak in the light curve is due to the transition from optically thick to optically thin, it is possible to place constraints on the emitting region size and the minimum energy present in the jet as the time of the light curve peak. In addition, by assuming a jet geometry I am able to estimate the bulk Lorentz factor of the jet. Using Barniol Duran et al. (2013), equipartition theory is applied, extended for synchrotron sources with a bulk relativistic velocity, to the radio light curve assuming that the peak of the light curve is not observed but instead it occurred about 4.5 days post-burst, where the light curve reached a peak flux of about $110\,\mu$Jy. The jet geometry assumed is $\Gamma = 1/\theta_j$ because I have no prior knowledge of the jet geometry. At 4.5 days, the size of the emitting region is 2×10^{17} cm, with a minimum energy of 3×10^{47} erg, it should be noted that these values and all those in the following analysis have large uncertainties and are not quantified due to the number of additional assumptions in the underlying model. I estimate Γ to be ~5 at the peak of the light curve, i.e the jet is mildly relativistic at the peak of the light curve. The assumption of $\Gamma \sim 1/\theta_j$ means that the previous statement can be used to predict an opening angle of $\sim 11^\circ$. From the requirement of a $\mathrm{t}^{1.75}$ light curve, the jet must be propagating through a wind environment, which is parameterised by $A_\star$, which related to the constant, A, from the assumed density profile $\rho = Ar^{-2}$. A value of $A_\star = 0.4$ is measured making $A = 2 \times 10^{11}\mathrm{g\,cm^{-1}}$, where $A = \dot{M}/4\pi V_W = 5 \times 10^{11} A_\star \mathrm{g\ cm^{-1}}$; $\dot{M}$ and V_W are the mass loss rate and wind velocity of the progenitor star, respectively, (Chevalier & Li, 2000).

The presence of a wind-like circumburst environment, despite the low afterglow luminosity, lends this event to appear more similar to the afterglows of long GRBs where the jet is propagating through the material blown off the star in the late stages of its lifetime

(Chevalier & Li, 2000). This is in contention with the duration of the prompt emission leading to the initial interpretation of GRB 200826A as a short GRB, however, as mentioned in the introduction, analysis of the prompt emission has led to the suggestion that this event is a long GRB at the short end of the prompt emission duration distribution (Svinkin et al., 2020).

Scenario II: Jet break occurs around the time of the radio light curve peak

In the second scenario, it is assumed that the peak of the light curve in the radio light curve is observed, and that the break occurred as late as possible, at the time of the first *e*-MERLIN data point. All of the the radio data is fit with a broken power law in one instance using EMCEE (Foreman-Mackey et al., 2013).

The results of the MCMC fitting show that the rise of the light curve follows $F \propto t^{1.2\pm0.3}$ to a peak of $90 \pm 10\,\mu$Jy at $5.4^{+0.5}_{-0.6}$ days followed by a decay following $F \propto t^{-2.7\pm0.9}$. The results are shown as the dark blue dashed line in Figure 3.11 and the corresponding corner plot is Figure B.2.

The rise of the radio light curve, $F \propto t^{1.2\pm0.3}$, is shallower than for Scenario I and more consistent with optically thick FS emission propagating into an ISM environment. In this second scenario, the decay is steeper compared to the first: $F \propto t^{-2.7\pm0.9}$. The uncertainties here are large due to the close proximity in time between the two *e*-MERLIN detections and the break followed by an upper limit. The decay is consistent with the XRT light curve at a 68% confidence level ($\alpha_{10\mathrm{keV}} = -1.8 \pm 0.4$). When considered without the XRT result, the steeper *e*-MERLIN decay is not compatible with an optically thin decay. Instead, I suggest a different interpretation, one which is not caused by a SSA turnover but by a jet break. The decay following the break is steep enough to be due to a jet break, where the jet begins to spread laterally causing the flux to decay as $F \propto t^{-p}$ (Sari et al., 1999a). However, when combined with the optically thick rise, the post-break decay should plateau for an optically thick jet or follow a shallow decay of $F \propto t^{-1/3}$ when $\nu_{SA} < \nu < \nu_M$, and no decay as steeply as observed (Sari et al., 1999a). The observed break may only be possible if the jet becomes optically thin during the peak, as shown in our first interpretation, when ν_{SA} passes through the band during the break time.

This scenario is further complicated by the fact that jet breaks are achromatic and there is no evidence of a break in the X-ray light curve. The final XRT observation starts before the break in the radio light curve and shows an excess in flux with respect to the single power law decay. If such an excess, if real, it could originate from long lived central engine activity and therefore could hide a jet break (Metzger & Piro, 2014; Fong et al., 2014).

The break in the radio light curve can be used to calculate the opening angle of the jet (Sari et al., 1999a; Frail et al., 2001) with the equation:

$$\theta_j = 9.51 t_{\mathrm{j,d}}^{3/8} (1+z)^{-3/8} E_{\mathrm{K,\,ISO,52}}^{-1/8} n_0^{1/8} \mathrm{deg}$$

The isotropic equivalent energy of this event $\mathrm{E_{K,\,ISO}} = 4.7 \times 10^{51}$erg, where the source is at a redshift of 0.714±0.137 (Svinkin et al., 2020; Ahumada et al., 2020a). The luminosity of this GRB is consistent with that of a short GRB, however, given the evidence that this may be a long GRB, a range of circumburst density values (n_0) is used to calculate the jet opening angles (Ahumada et al., 2020b; Svinkin et al., 2020). For short GRBs, I assume $\sim$ 0.01cm^{-3} and for long GRBs, a higher density environment of $n_0 \sim$ 1cm^{-3} (Chandra & Frail, 2012; Fong et al., 2015). From these values, $\theta_j = \sim 9^\circ$ and $\sim 16^\circ$ for a short and long GRB, respectively. No uncertainty for each θ_j measurement is given because of the large assumptions made in addition to the numerical uncertainties on each input value.

Jet break detections from previous short GRB systems, gives $\theta_j = 3 - 8^\circ$, this range increases to larger opening angles once lower limits are considered, (Fong et al., 2015). Long GRBs θ_j measurements have a larger range at $7.4^{+11}_{-6.6}{}^\circ$ (Laskar et al., 2014; Goldstein et al., 2016). The calculations of θ_j for long and short GRBs are in agreement with results for both of their respective populations.

Comparing the two interpretations I have presented the second scenario is far more complex than that described in scenario I. Furthermore, the conclusions reached in scenario I are more consistent with other multi-wavelength observations of this source and the optically thick to thin scenario is favoured.

3.4 Follow up with MeerKAT

With *e*-MERLIN, I have been able to observe all northern hemisphere short GRBs as well as those above -30° for the past two and a half years. As part of the ThunderKAT collaboration, I have been observing the positions of the southern hemisphere short GRBs. Of the seven short GRBs observed, I have detected radio counterparts to short GRBs: GRB 200411A and 210726A. A radio source associated with GRB 200411A was detected over three epochs (the yellow points in Figure 3.12). The lack in change of flux density over ten days means that the detected emission is mostly likely from from the GRB's host galaxy rather than the afterglow. The radio counterpart to GRB 210726A is discussed in Section 3.4.1.

I have also used MeerKAT to observe three long GRBs: GRB 190829A, 201216C and 210928A. The detections are summarised in Figure 3.12. GRB 190829A and 201216C are discussed further in Chapter 4. GRB 210928A was a Fermi Gamma-ray burst monitor (GBM) detected event (Fletcher & Meegan, 2021). Simultaneously, the Fermi Large Area Telescope (LAT) detected a new transient: Fermi J1623-1752 identified as a possible counterpart to recurrent nova U Scorpii (Rani et al., 2021). Axelsson et al. (2021) showed that the two sources were coincident, that this event was a GRB. Within the ThunderKAT X-ray binary monitoring program, GRB 210928A was observed for 15 minutes. The source was detected 215±6 μJy, the purple data point in Figure 3.12 (Rhodes et al., 2021b).

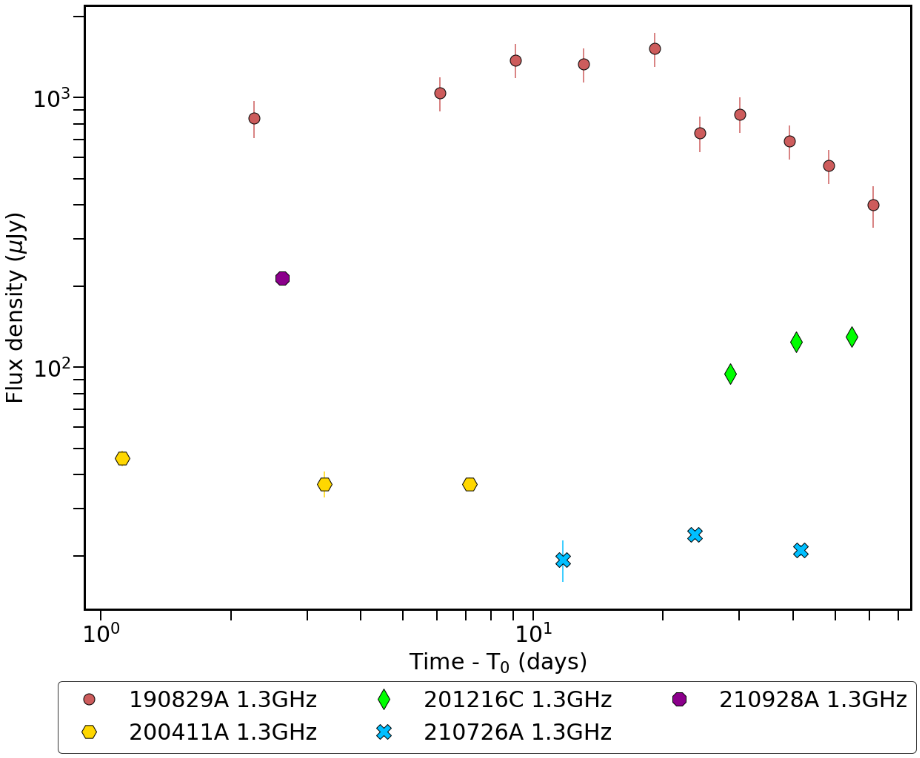

Figure 3.12: All the GRB detections obtained with MeerKAT during my DPhil.

3.4.1 GRB 210726A

Short GRB 210726A was detected by *Swift*-BAT and placed at z = 0.35±0.15 (Bernardini et al., 2021; Watson et al., 2021). It was the first short GRB afterglow to be detected as part of the ThunderKAT follow up program. A radio counterpart was detected with MeerKAT in three of the seven observations made. The MeerKAT campaign was complimented by *e*-MERLIN at 5 GHz and AMI-LA at 15.5 GHz. GRB 210726A was also the first short GRB to be detected with AMI-LA. The first detection was made 10 days post-burst (blue data points in Figure 3.12) later than any previous short GRB radio detection. Schroeder et al. (2021) also detected the afterglow with the VLA. The final detection was at 61 days at 6 GHz. Figure 3.13 and 3.14 shows the radio light curves and spectral energy distributions for GRB 210726A, respectively. This work will go into a paper jointly led between Genevieve Schroeder at Northwestern University and myself.

Results and Interpretation

Figure 3.13 shows the light curves for GRB 210726A at 1.3, 3, 6, 10 and 15.5 GHz, as well as the non-detections at 5 GHz. The most detections were obtained at 1.3 and 6 GHz. A joint fit to the light curves at these two frequencies was performed to determine is the afterglow evolution was achromatic (the red amd cyan lines in Figure 3.13). The two light curves peak at the same time with a peak at 17±1 days. The decay is steeper at 6 and 10 GHz than at 1.3 GHz. The rise in the 6 GHz light curve follows $t^{\gtrsim 3}$ and a decay of $\mathrm{t}^{-2.5\pm0.3}$. The 1.3 GHz rise and decay follow $\mathrm{t}^{1.1\pm0.4}$ and $\mathrm{t}^{-0.6\pm0.1}$, respectively. The steep rise observed in the 6 GHz light curve is indicative of an off axis rise - such an rise is too steep to sit with an on-axis afterglow scenario (Granot & Sari, 2002). Until 160 days post-merger, the light curve for GW 170817 increased as $\mathrm{t}^{0.7}$, (Margutti et al., 2018), far shallower than the 6 GHz rise observed in GRB 210726A. The rise at 1.3 GHz follows $\mathrm{t}^{1.1\pm0.5}$, much shallower than the 6 GHz rise. Such a difference in the slope of the rise components of each event could imply a different lateral jet structure. Sharper rises are associated with top hat jets (Granot et al., 2002). The steep decay is consistent with a jet break, a similar decay was observed in GW 170817 (Mooley et al., 2018b).

The spectral evolution for this afterglow is shown in Figure 3.14. The observations between days 23 and 29 (the middle panel in the right hand column of Figure 3.14) and 39 and 41 days (lower left panel) have in the best spectral coverage. They show a smooth turn over revealing the peak of the synchrotron spectrum at 7±3 GHz. Comparison of these two epochs shows and the epochs at 19 and ~60 days (the middle left and bottom right panels of Figure 3.14) show that the location of the peak frequency is unchanging over 40 days. Such behaviour is not replicated in GRB afterglow models.

$\mathrm{F}_{\nu,\mathrm{max}}$ is brightest at day 19, with a value of 100 μJy. The subsequent decay follows $\mathrm{F}_{\nu,\mathrm{max}} \propto\sim t^{-1.6}$. This decay is steeper than expected for post jet break decays (Sari et al., 1999a). Furthermore, the spectral indices above the turnover are much steeper than normally measured for optically thin synchrotron below the cooling break ($-0.5 - -1$). A high frequency spectral index of -3.5±1.9 measured is within 1σ of the expected value range.

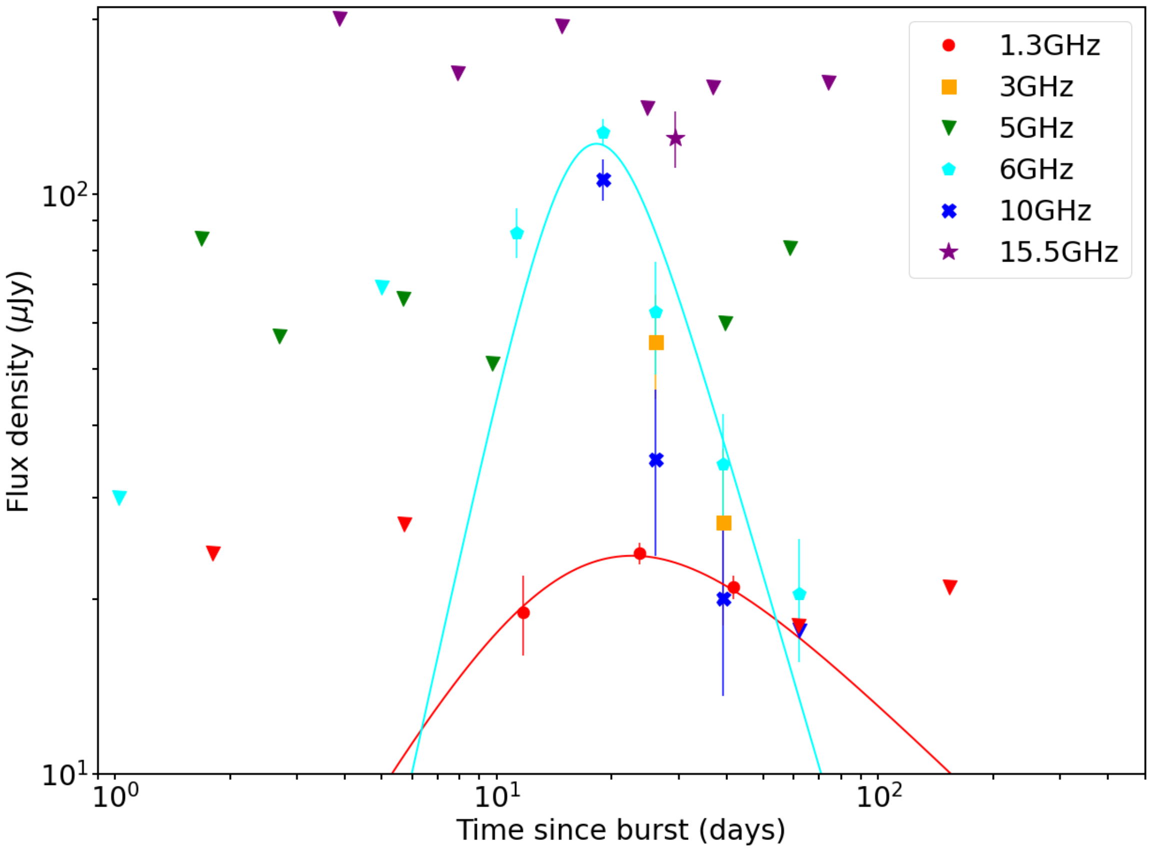

Figure 3.13: Multi-frequency light curves for short GRB 210726A. The 3σ upper limits as shown as downward facing triangles. The solid red and cyan lines are phenomenological fits to the 1.3 and 6 GHz light curves, respectively. These fits are used to determine if the peak times at 1.3 and 6 GHz are the same which would imply a jet break. Both the rise and decay exponents from the fit provide information of which branches of the synchrotron spectrum the 1.3 and 6 GHz bands lie on. From Schroeder, Rhodes et al (*in prep*).

X-ray data from XRT and Chandra will be used to better constrain this branch of the spectrum.

GRB 210627A has the most comprehensive set of radio detections of any short GRB to date, both in frequency space and time. Preliminary interpretation is hinting at the possibility of a mildly off-axis event, similar to GW 170817 but at cosmological distances. More observations of similar events in the future are required to better understand the lateral structure of short GRB jets.

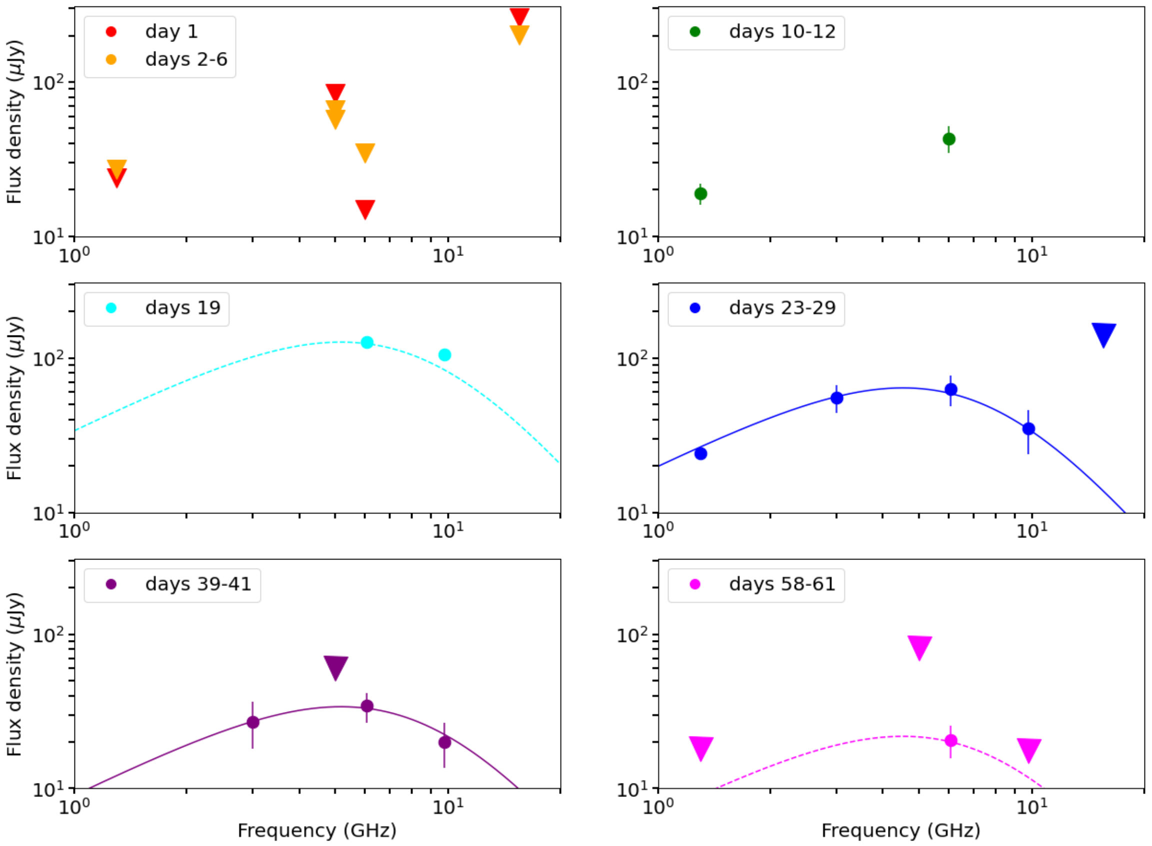

Figure 3.14: Radio spectral energy distributions for short GRB 210726A. The 3σ upper limits as shown as downward facing triangles. The solid lines in the 23-29 and 39-41 day epochs are smoothly broken power law curves fit to the radio data. The dashed lines are approximate fits to the data using the same spectral indices and break locations as derived from broken power law fits. From Schroeder, Rhodes et al (*in prep*).

3.5 Follow up with the Karl G. Jansky Very Large Array

I observed long GRB 201216C with the VLA at 10 GHz over six epochs between December 2020 and January 2021. This event is discussed further in Chapter 4.

3.6 Summary

Over the course my DPhil, I have performed follow up of over 60 GRBs, 15 of which have result in detections of a radio source: 13 from long GRB triggers and 2 from short GRBs.

With AMI-LA, I have performed radio follow up of as many northern hemisphere GRBs detected by *Swift*-BAT as possible. This followup was conducted independently of the properties of the GRB: whether it was long or short; whether it had an optical counterpart; or whether it had an identified host galaxy and therefore a redshift. The initial observations were performed over a range of timescales from minutes post-burst. However, if there is no evidence of multi-wavelength follow up and no radio detection, no subsequent radio observation are made which prevents any later time detections if the afterglow is heavily self-absorbed. Through the AMI-LA follow up campaign, a number of potential host galaxies / contaminating sources have been identified due to the large beam size (30 arcminutes across). This has resulted in two mis-identified afterglows for GRBs 190326A and 210704A. The large number of triggers made as also allowed for three new radio afterglows to be detected: GRB 190829A (see Chapter 4), GRB 210610B (Section 3.2.2) and GRB 210726A (Section 3.4.1). I have briefly discussed the multi-wavelength detections of GRB 210610B, which has demonstrated the AMI-LA's observational capabilities particularly regarding obtaining high cadence light curves. Combining optical, X-ray and radio data, the afterglow of this event is most consistent with a forward + reverse shock scenario where the forward shock undergoes a jet break before one day post-burst. The work on GRB 210610B will go into a paper: Laskar, Rhodes et al (*in prep*).

With *e*-MERLIN, I performed observations at 5 GHz of GRB 200826A from four to eleven days after the burst. Initially classed as a short GRB, Ahumada et al. (2020a)'s redshift measurement for GRB 200826A's potential host galaxy would make this event the most distant radio-detected short GRB to date. Further analysis into the prompt emission hinted that this maybe a long GRB the short end of the T_{90} distribution (Svinkin et al., 2020). Two possible interpretations are considered for the *e*-MERLIN detections, used together with a single detection reported from the VLA, (Alexander et al., 2020b) as a result of differing peak ties. Both include an optically thick rise from a jet propagating through different density profiles. Breaks occurring at different times have different underlying causes: a break before the first observation may be due to synchrotron self-absorption break passing through the band. If the peak of the light curve occurred during the first *e*-MERLIN epoch, the resulting break may be caused by a jet break combined with a transition from an optically thick to optically thin regime around the same time. Jet opening angle values are calculated for both long and short GRB environments deriving 16° and 9°, respectively. The jet break scenario is not supported by the X-ray light curve, instead the data are consistent with optically thin synchrotron emission lasting for the first ~6 days. Given the relative complexity of the jet break second scenario with respect to the first, the first interpretation is favoured: the break in the radio light curve originates from the synchrotron self-absorption frequency. The presence of a stellar wind-like environment supports the idea that GRB 200628A is a long GRB with prompt emission lasting less than 2 seconds. To date, the duration of the prompt emission has been the default classification scheme for long vs short GRBs. This work has shown that the afterglow can be a strong indicator of whether a GRB originates from the collapsar or a binary neutron star merger and that the current classification method requires is not accurate enough to be blindly followed.

Finally, I have presented multi-frequency radio observations of short GRB 210726A. With the exception of GW 170817, GRB 210726A has the highest number of radio detections of any short GRB to date. It has also been detected later than any other on-axis short GRB. As a result, I interpret this event as top-hat jet that is initially view off-axis. Around 20 days post-burst the jet comes into the observer's line of sight. This work will contribute to a paper in the next six months (Schroeder, Rhodes et al *in prep*) and demonstrates the power or newer more sensitive radio telescopes. The new generation of interferometers are allowing for fainter and later-time detections of short GRBs, a sample so small that any additional detection adds significantly to the community understanding of these rare events.

Chapter 4

Long gamma-ray bursts detected at Very High Energies

4.1 Introduction

As discussed in Chapter 3, a long gamma-ray burst (GRB) is most likely produced when a jet is launched during the collapse of a massive star at the end of its lives. The jet emits synchrotron radiation as a result of shocks interacting with the circumburst environment. Some afterglow datasets deviate from the simple fireball model presented in Chapter 3 in two ways.

For about two decades, it has been suggested that an additional high energy spectral component may exist as a result of inverse Compton up-scattering (Sari & Esin, 2001; Fan et al., 2008). There are cases where the presence of inverse Compton emission has been inferred from the synchrotron afterglow (e.g. Harrison et al., 2001). GRB 130427A was so luminous that it was detected above 30 GeV (Ajello et al., 2019). The spectrum showed an upturn at 10 GeV, evidence of an additional, high energy spectral component, which was interpreted as originating from synchrotron self-Compton emission (Ackermann et al., 2014). GRB 180720B was the first long GRB to be detected above 100 GeV providing conclusive evidence of an additional high energy component (Abdalla et al., 2019).

An afterglow can appear to deviate from the fireball model as a result of material along the line of sight can cause the attenuation of incoming photons. Dust and plasma along the line of sight can significantly affect the observed optical and radio emission, respectively.

The work presented in this chapter is published in Rhodes et al. (2020) and Rhodes et al. (2022a).

4.1.1 Very high energy detections

The typical GRB afterglow is usually visible between the radio and X-ray wavebands. For the most luminous events, detections at GeV energies can occur (Ackermann et al., 2013). The Fermi Large Area Telescope (LAT) has previously detected photons to energies greater than 30 GeV from GRBs such as GRB 130427A (Ajello et al., 2019). Despite intensive follow up campaigns, no VHE (Very High Energy, E > 100 GeV) emission has been detected from any GRB by any ground based Atmospheric Cherenkov Telescopes until mid-2018 (e.g. H. E. S. S. Collaboration et al., 2014). However in the past four years, VHE detections of GRB afterglow have finally been made (MAGIC Collaboration et al., 2019a; H. E. S. S. Collaboration et al., 2021). There are currently five VHE GRBs. For each event, the VHE detections were obtained seconds to hours after the long GRB prompt emission. Their light curves are very similar to those observed in the X-ray band, implying a connection to the afterglow rather than the prompt emission (Blanch et al., 2020a; De Naurois & H. E. S. S. Collaboration, 2019).

Given that *Swift* identifies at least 100 long GRBs each year and so five VHE detections over four years is a very low detection rate. VHE detections associated with long GRBs are limited in redshift range due to pair production between the VHE photons and the extra-galactic background light: optical and infrared photons produced by star formation processes. As a result, VHE photons from sources above redshift 1.5 are highly attenuated, and are not expected to be detectable. This is supported by the VHE GRBs detected thus far: all at redshifts of about 1.5 or below (Vreeswijk et al., 2018; Castro-Tirado et al., 2019; Valeev et al., 2019; Izzo et al., 2020a; Vielfaure et al., 2020).

In order to detect VHE emission, the Imaging Atmospheric Cherenkov Telescopes (IACTs) need to be on source as soon as possible after the burst, ideally within minutes to hours. Both the Major Atmospheric Gamma Imaging Cherenkov (MAGIC) and High Energy Stereoscopic System (H.E.S.S.) telescopes have transient follow up programs in place where one of the main focuses is GRB follow up (Berti et al., 2019; Hoischen et al., 2022). Both facilities are limited in the number of observing hours in a given day due to sunlight and high moonlight levels. Therefore, some GRBs may be observable immediately after they are detected by *Swift* and some events may only be observable hours or days later by which time any detectable emission may have faded.

For the VHE GRBs detected to date, three different production mechanisms have been invoked to explain the VHE emission: synchrotron, synchrotron self-Compton component (SSC), or external inverse Compton (EIC). Synchrotron emission is only possible if no upper limit is placed on the maximum electron energy allowing the synchrotron spectrum to continue to TeV energies. Such a scenario requires either: the forward shock to have a very high ($\sim$100) bulk Lorentz factor hours after the burst (H. E. S. S. Collaboration et al., 2021) which is in disagreement with the fireball model; or a non-power law distribution of accelerated electrons. Synchrotron emission has been postulated as the origin of the VHE emission in GRB 190829A (H. E. S. S. Collaboration et al., 2021), however they acknowledge that the whilst a synchrotron origin is the best fit to the data such a scenario requires an unphysical set up.

SSC is the most commonly invoked origin of the VHE emission. In SSC, synchrotron photons are up-scattered by electrons in the shock front resulting in an additional high energy bump in the spectral energy distribution. They are upscattered by the same electrons that produced them, hence 'self-Compton'. The SSC spectrum will look very similar to the synchrotron spectrum just at higher energies. The synchrotron photons are up-scattered by a factor γ_e^2 where γ_e is the Lorentz factor of the scattering electrons. SSC emission is expected to dominate at early times when the afterglow is in a fast cooling regime ($\nu_C < \nu_m$) and the jet has a low level of magnetisation. Both MAGIC GRB 190720B and 190114C have invoked SSC as the origin of the VHE photons (Abdalla et al., 2019; MAGIC Collaboration et al., 2019b). They rule out synchrotron emission on the grounds that the jet cannot have a bulk Lorentz factor of at least 10 several hours after the burst. This scenario is still not perfect because $\gamma_e \approx 2 \times 10^3$ which is very low given the location of the synchrotron spectral peak at the time of the VHE detections. It is rectified by assuming that the system is in the Klein-Nishina scattering regime (Nakar et al., 2009).

EIC is the final possibility for the origin of the VHE counterpart. Here, the seed photons originate from somewhere separate to the jet e.g. X-ray flaring from late time accretion events (Wang & Mészáros, 2006) or from a cocoon (Toma et al., 2009). It may even be possible to up-scatter reprocessed infrared radiation from a dusty environment in the vicinity of the GRB. This scenario would require $\gamma_e \approx 1 \times 10^6$. Such high values of γ_e have been inferred from the jets of black hole X-ray binary systems (e.g. Corbel et al., 2002; Espinasse et al., 2020). The seed photons interact with the jet front and are up-scattered to TeV energies. Zhang et al. (2021) suggested that the flare observed in the *Swift* XRT light curve could be a contributing seed photon field to the VHE detections associated with GRB 190829A. Instead of single emission mechanism, they invoked a combination of SSC and EIC to model the multi-wavelength light curves and H.E.S.S. spectrum.

With such a small population of events, there is no clear singular explanation for the origin of the VHE photons. I have been studying the synchrotron afterglows of the VHE GRBs with with the aim of understanding their properties as well as searching for any differences between the VHE and ‘regular’ GRB populations.

4.1.2 Propagation effects

Once the photons have left the GRB jet, they propagate through the inter-stellar medium (ISM) of the host galaxy, the inter-galactic medium and the ISM of the Milky Way. These media along the line of sight can dramatically affect the observed afterglow emission.

Some long GRBs have appeared to be optically faint, so called *dark GRBs*. Chandra & Frail (2012) showed that about 25% of Swift GRBs do not have detected optical counterparts. There are three possible explanations for dark GRBs (Jakobsson et al., 2004; Resmi et al., 2005): (1) they occur at high redshift resulting in the Lyman break falling in the optical band, (2) dust along the line of sight absorbs the optical photons, and (3) additional emission components at X-ray energies, increasing the X-ray flux with respect to the optical emission.

For many dark GRBs, it is dust along the line of sight that causes the optical darkness. Significant amounts of dust is expected in the regions of long GRBs as they occur in areas of high star formation, near to the birth-sites of their progenitor, since their lifetime is short. In some cases the V-band extinction is greater than 10 magnitudes (Zauderer et al., 2013). When compared to the measured neutral hydrogen column densities inferred from the X-ray spectra, such high optical extinction deviates strongly from the linear A_V-N_H relationship measured within the Milky Way $N_H \approx 2\times10^{21} A_V$ (Predehl & Schmitt, 1995; Güver & Özel, 2009). It is likely that this is a result of a combination of the A_V-N_H relation varying from galaxy to galaxy, and a non-uniform distribution of gas within each galaxy. This is supported by observations of dark GRBs' host galaxies which appear to have 'normal' colours, implying a lack of increased dust across the galaxy as a whole but instead the dust is localised to regions of increased star formation (Perley et al., 2009b).

Material along the line of sight can also affect radio emission in the form of interstellar scintillation (ISS; Walker, 1998; Goodman, 1997). Turbulence in the Milky Way's ISM causes flux density fluctuations up to order unity. The strength of the observed ISS is dependent on the projected size of the background source on the sky and the observing frequency. ISS can be divided into weak and strong scintillation. Weak scintillation occurs above some characteristic transition frequency. Strong scintillation occurs at frequencies below the transition frequency and can be further divided into diffractive (DISS) and refractive ISS (RISS). DISS is a narrow-band effect resulting from multi-path propagation whereas RISS, a broadband effect, occurs due to the focusing and defocusing of rays as they propagate through the ISM. If observed, DISS will dominate at early times when the GRB jet is more compact, but as the size of the jet on the sky grows, the effects of DISS fade away leaving RISS (Frail et al., 1997). The effects of RISS will also quench at some time when the jet has expanded beyond a certain angular size on the sky. The angular size dependence of DISS and RISS can be used to place on constraints on the size of the jet at different epochs (Frail et al., 1997, 2000a; Chandra et al., 2008; Alexander et al., 2019). The effects of scintillation on afterglow observations are discussed further in Section 4.4.3.

4.2 H.E.S.S. GRB 190829A

GRB 190829A was first reported by the Fermi Gamma-ray Burst Monitor (GBM) at 19:55:53 UT (T_0, Fermi GBM Team 2019) and shortly thereafter by the *Swift* Burst Alert Telescope (BAT) on 29th August 2019 (Dichiara et al., 2019) and followed by XRT. Four hours post-burst, the High Energy Stereoscopic System (H.E.S.S.) started observing the position of the GRB. VHE emission was detected at around 20σ significance between 0.18 and 3.3 TeV (H. E. S. S. Collaboration et al., 2021). Spectroscopic measurements with the Gran Telescopio Canarias showed the host galaxy to be 10" from the GRB's XRT localised position and placed the host at $z = 0.079 \pm 0.005$, making it one of the closest GRBs detected so far (Valeev et al., 2019).

4.2.1 Observations

Arcminute Microkelvin Imager - Large Array

The *Swift*-BAT detection of GRB 190829A triggered observations with the Arcminute Microkelvin Imager - Large Array (AMI-LA) as part of a GRB follow up program: ALARRM (AMI-LA Rapid Response Mode, Staley et al., 2013; Anderson et al., 2018).

Observations with AMI-LA commenced 1.33 days post-burst. The observation lasted three hours, using seven out of eight antennas. The data were reduced using a custom pipeline REDUCE_DC (Perrott et al., 2013). The data were flagged for RFI and calibrated using 3C286 and J0301+0118 as the bandpass and phase calibrators, respectively. Imaging and deconvolution was performed interactively in CASA using the task CLEAN.

The first observation showed a 4 mJy point source, its coordinates consistent with those from XRT. The initial detection triggered a long term monitoring campaign, with daily observations until 41 days post-burst before moving to bi-weekly observations. Observations ceased 143 days post-burst. A full list of the observations is given in Table C.1. The flux uncertainties include statistical and a 5 % calibration error. The background colour map in Figure 4.1 shows a concatenation of 5 AMI-LA data sets. The AMI-LA beam was 95" by 26", the elongation is due to the low declination of the source with respect AMI-LA's observing range.

MeerKAT

GRB 190829A was observed with MeerKAT for ten epochs, the first starting 2.38 days post-burst, and varying between 30 and 90 minutes in duration. The observations were carried out at a central frequency of 1.28 GHz and bandwidth of 856 MHz split into 4096 channels. The primary calibrator used was J0408-6565, which was observed at the start of each observation for 5 minutes. Target scans lasted between 10 and 20 minutes. The secondary calibrator used in each of the observations was J0240-2309, which was observed

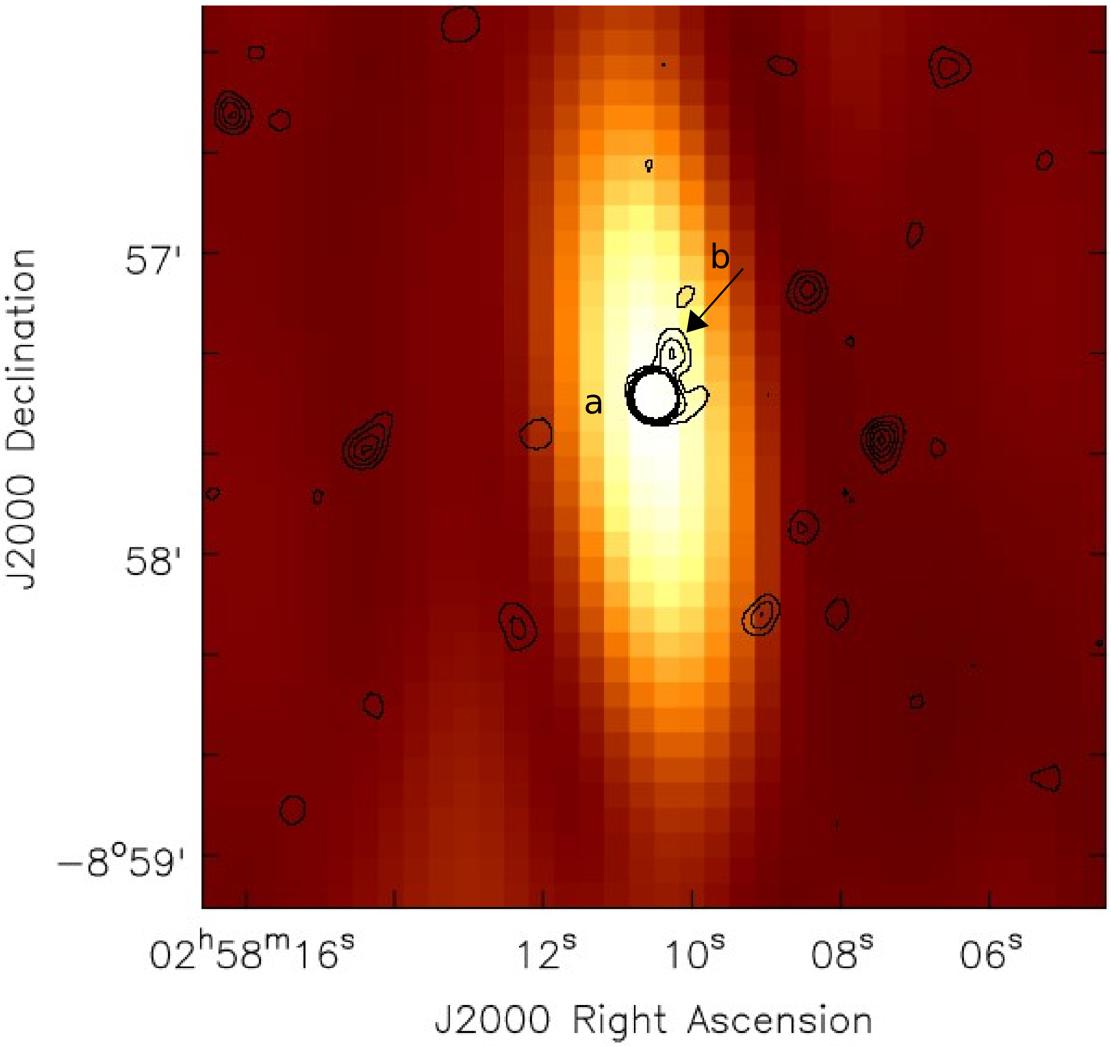

Figure 4.1: Comparison between MeerKAT (1.3 GHz) and AMI-LA (15.5 GHz) images of the field of GRB 190829A. The MeerKAT image (contours) is from a concatenated measurement set of all 10 observations. The contours are at 3, 6, 9, 12, and 15σ, with an image rms noise of 8μJy/beam. The bright object at the centre of the image, labelled 'a' is the GRB and the second source seen to the north-west labelled 'b' is the host galaxy. The AMI-LA (pixel) map is made from a concatenation of 5 separate observations and has a rms noise of ~50μJy/beam. In the AMI-LA observations, GRB is not resolved from the host galaxy (due to much shorter baselines, despite the higher frequency). This is an important factor to consider when examining the AMI-LA light curve which shows a late time plateau component that most likely originates from the host galaxy.

for 2 minutes per cycle. The data reduction was performed using CASA (McMullin et al., 2007a) where the data were flagged for radio frequency interference (RFI) and the first and last 150 channels (out of 4096 channels) of the band were removed. Further flagging was performed using the auto-flagging algorithms RFLAG and TFCROP. The calibration was performed, using the flux density of the primary calibrator. We then solved for the phase-only and antenna-based delay corrections on the primary calibrator. The bandpass corrections for the primary were then applied. Solutions for the complex gains on the primary and secondary were made, and proceeded to scale the gain corrections from the primary to the secondary and target source. Finally, images were made using WSCLEAN (Offringa et al., 2014). A full list of observations and results are given in Table C.2. The flux uncertainties include statistical uncertainties and a 10 % calibration error.

The contours in Figure 4.1 shows a point source from the MeerKAT image with coordinates consistent with the GRB (‘a’) as reported by XRT. A second source was found 10" away (‘b’) was identified as the host galaxy reported in Heintz et al. (2019), a 2MASS source: SDSS J025810.28-085719.2. No counterpart is found in the NRAO VLA Sky Survey (NVSS) catalogue. NVSS has a flux limit of 1 mJy at 1.3 GHz, a factor of four brighter than the second source detected in the MeerKAT observation.

Swift-XRT

Swift-XRT started observing the field of GRB 190829A 110s after the initial trigger (Gehrels et al. 2004; Evans et al. 2019). XRT observed in the band 0.3-10 keV, until 115 days after the burst. The data used in this work were collected in photon counting mode after 4000s and extracted using the *Swift* Burst Analyser (Evans et al. 2009, 2010).

4.2.2 Results

The results of the observations described above are given in tables C.2 and C.1, and shown in Figures 4.2 and 4.3 with the fluxes reported in Tables C.2 and C.1. The analysis is performed using a phenomenological model of power laws of the form $F_\nu \propto t^\alpha \nu^\beta$, where t is the time elapsed since the burst, ν refers to the central frequency of the observing band and α and β are the power law indices. Subscripts refer to the frequency or energy band.

All fits to the data were performed using EMCEE (Foreman-Mackey et al., 2013), a MCMC (Monte Carlo Markov Chain) sampler. 700 independent walkers were used and the first 5000 of 10000 steps were burnt, which resulted in a total of 3,500,000 samples. Non-informative priors were used for all parameters. Maximum likelihood analysis was used to find the minimum chi-squared corresponding to the best fit. The 50th percentile of the samples in the marginalised distributions is quoted as the best fit with the 16th and 84th percentiles quoted as the lower and upper uncertainties, respectively.

Radio

The radio data were fit using a smoothly broken power law equation:

$$F_\nu(t) = A\left[\frac{1}{2}\left(\frac{t}{t_b}\right)^{-5\alpha_1} + \frac{1}{2}\left(\frac{t}{t_b}\right)^{-5\alpha_2}\right]^{-\frac{1}{5}} + B \tag{4.1}$$

The free parameters in the fit were A, t_b, α_1, α_2 and B; where A is the amplitude, t_b is the break time, α_1 and α_2 are the exponents of the two power laws, and B is a constant offset. The factor of 5 is a fixed smoothness parameter.

The 1.3 GHz MeerKAT data (the blue squares in Figure 4.2) show a rise until a maximum at 14±2 days when the light curve turns over into a decay that continues for the rest of the observation. For the MeerKAT data set, B was set to zero. Flat priors were used: $500 <$ A (μJy/beam) < 3500, $0 < \alpha_1 < 3$, $-3 < \alpha_2 < 0$, and $10 <$ t_b (days) < 30. The results for the 1.3 GHz fit are shown in Table 4.1 with the corner plot given in Appendix C.1.

The AMI-LA data (grey circles in Figure 4.2) are best described by two decaying power laws with a break at 12.6±0.9 days followed by a plateau component after 70 days. The AMI-LA light curve shows day-to-day variability which increases in amplitude in

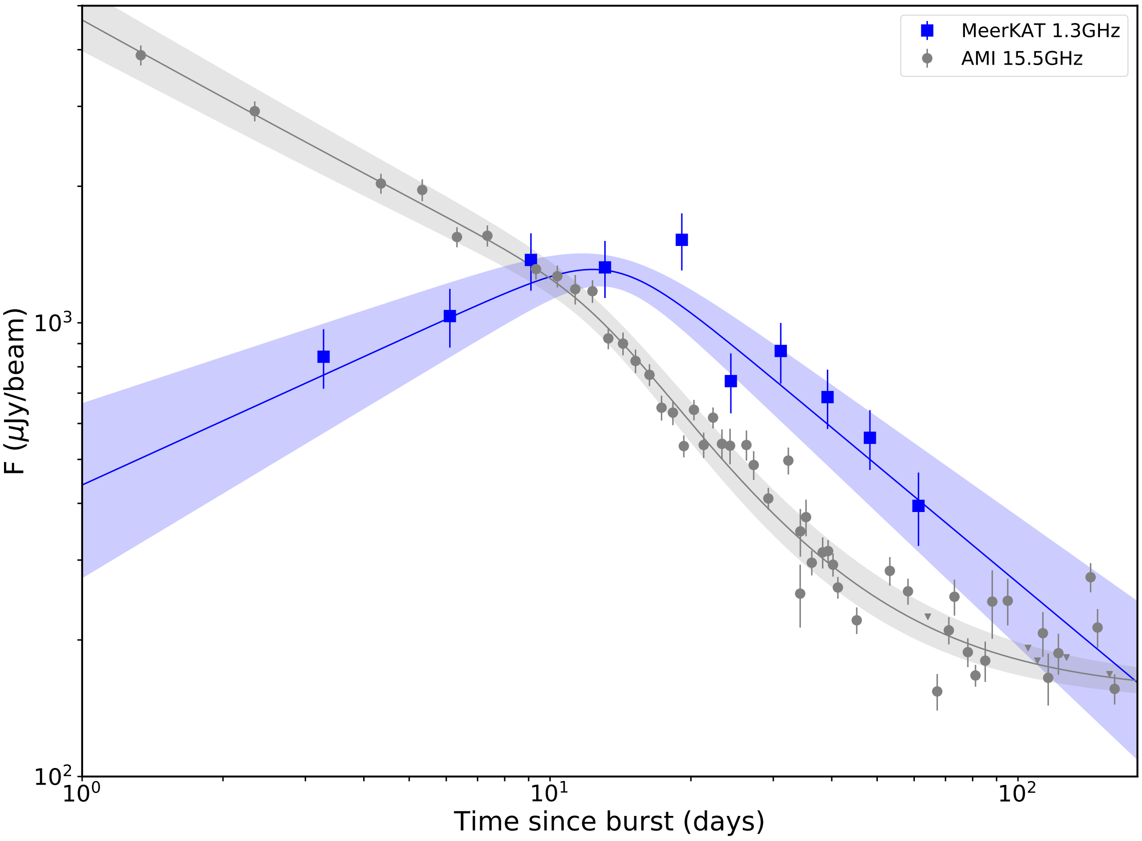

Figure 4.2: Light curves of the AMI-LA and MeerKAT data of GRB 190829A at 1.3 GHz and 15.5 GHz up to day 180, respectively, with equation 4.1 fit to each data set. The error bars on the data points include the statistical 1σ uncertainty and a calibration error (5 % for AMI-LA and 10 % for MeerKAT) added in quadrature. The shaded regions represent the 16th and 84th percentiles from their respective fits.

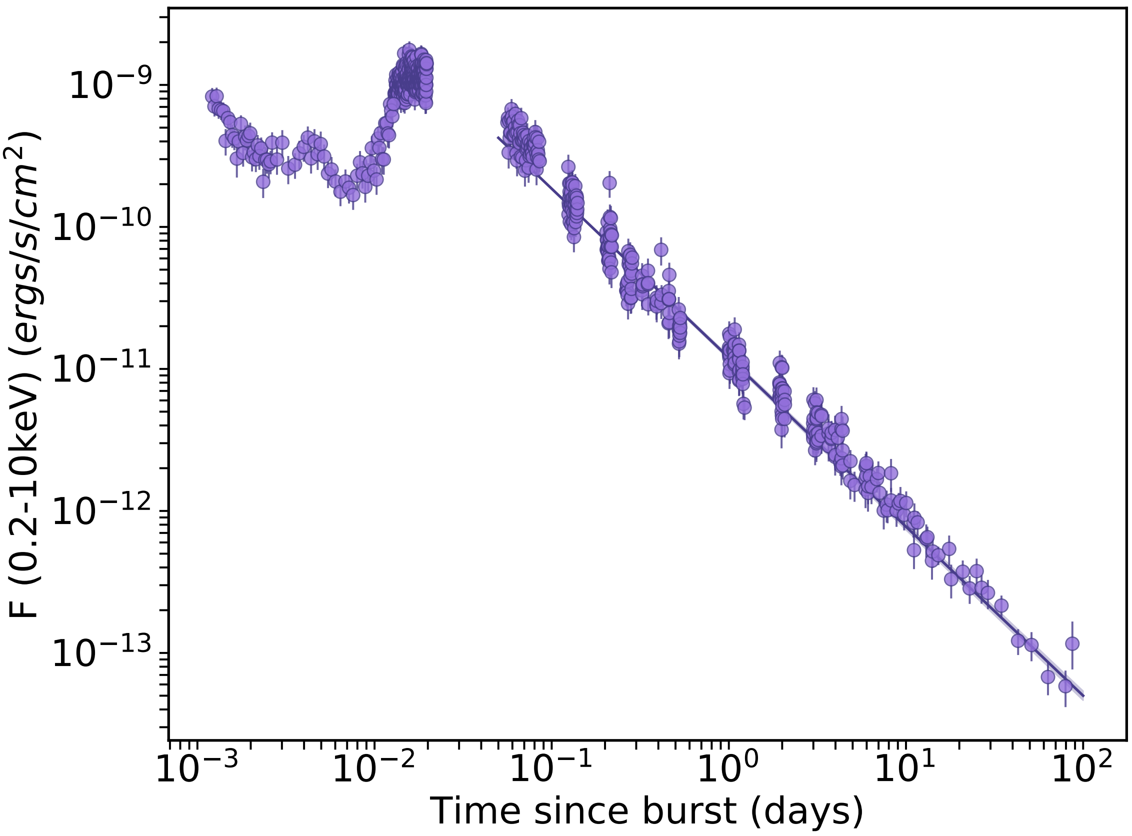

Figure 4.3: *Swift*-XRT light curve for GRB 190829A with data points from both photon counting and window timing modes, with uncertainties quoted to 1σ. Fitted to the data, from 0.1 days, is a power law where $F \propto t^{\alpha_X}$ and $\alpha_X = -1.19 \pm 0.01$.

Observing range	A (μJy)	α_1	α_2	t_b (days)	B (μJy)
1.3 GHz	1400 ± 100	0.5 ± 0.1	−0.9 ± 0.1	14 ± 2	–
15.5 GHz	880^{+80}_{-70}	−0.59 ± 0.03	$-1.71^{+0.08}_{-0.09}$	12.6 ± 0.9	152^{+7}_{-8}
0.3-10keV	0.50 ± 0.01	−1.19 ± 0.01	–	–	–

Table 4.1: The results of the MCMC fitting code parameters which describes the MeerKAT 1.3 GHz and AMI-LA 15.5 GHz light curves as given by equation 4.1 and the X-ray light curve by a single power law function. The values quoted are the mean with uncertainties at the 16th and 84th percentile.

the plateau section of the light curve with fractional variability $\sim$ 15%. The variability cannot be attributed to scintillation because it is not seen in the earliest epochs. If due to scintillation, significant flux variation would be observed at the earliest times when the jet is most compact. The variability could be due to a combination of telescope pointing error, intrinsic variability and seeing, it is mostly likely not intrinsic to the source. Equation 4.1 was fit to the 15.5 GHz data, with flat priors of: $0 < \mathrm{A}\,(\mu\mathrm{Jy/beam}) < 5000$, $-1 < \alpha_1 < 0$, $-3 < \alpha_2 < -1$, $5 < \mathrm{t_b}\,(\mathrm{days}) < 20$ and $0 < \mathrm{B}\,(\mu\mathrm{Jy/beam}) < 500$. A list of fluxes are given in Table C.1 and the results of the fits are given in Table 4.1 with the associated corner plot given in Appendix C.

The plateau component, most likely, can be attributed to the host galaxy because of the second component seen in the MeerKAT field within the AMI-LA beam in Figure 4.1. The galaxy component has an 1.0-1.5 GHz in-band spectral index of $\beta_{1.0-1.5} = 0.5 \pm 0.7$. Extrapolating to 15.5 GHz, the flux density of the source would be $10^{-(3.6\pm1.6)}$ Jy/beam. The flattening of the light curve seen from around day 70 has a flux level within the uncertainties of the predicted host galaxy flux at 15.5 GHz.

X-Rays

The full XRT light curve is given in Figure 4.3. The early time *Swift*-XRT data are highly variable most likely due to the decay of the prompt emission and possible flaring/accretion episodes. The light curve shows a steady decay of $\alpha_X = -1.19 \pm 0.01$ from 0.1 days post burst.

The spectral properties of the XRT data are also used to contextualise the X-ray emission. The late time-averaged spectrum (after 4400s), from the *Swift* Burst Analyser (Evans et al., 2010)[1] is characterised by a photon index of $\Gamma = 2.10 \pm 0.09$, corresponding to a spectral index of $\beta_{0.2-10\text{keV}} = -1.01 \pm 0.09$.

4.2.3 Interpretation

Here, the results of the observations are interpreted in the context of the fireball model in which a forward shock (FS) propagating forward into the surrounding medium accelerates electrons producing a time-evolving synchrotron spectrum.

X-Rays: Forward Shock

The late-time *Swift*-XRT light curve shows a single power law decline with no breaks, indicating that no break frequency passes through the observing band. The data can be described by a power law in the form of $F \propto t^{-1.19\pm0.01}$, and is steep enough in time to be above the cooling break of a FS component giving $p = 2.25 \pm 0.02$ (where p is the power law exponent from the electron energy distribution), independent of the GRB's surrounding density profile (Granot & Sari, 2002). The late-time-averaged spectrum also shows that the observed emission originates above the cooling break, the spectral index of $\alpha = -1.10 \pm 0.09$ gives p = 2.2 ± 0.2. The values of p from the light curve and time averaged spectrum are in good agreement with each other.

Radio: Forward Shock

The 1.3 GHz MeerKAT observations also fit with the FS model. The rise in flux ($t^{0.5\pm0.1}$) up to day 14±0.2 is consistent, within errors, with emission above ν_{SA} and below ν_M as the FS propagates through a homogeneous environment. The turnover at 14 days corresponds to the peak frequency (ν_M) passing through the observing band. The decay component

---

[1] https://www.swift.ac.uk/xrt_spectra/00922968/

follows $F \propto t^{-0.71^{+0.08}_{-0.09}}$. Using the scaling for a homogeneous medium, where the exponent is equal to $\frac{3(1-p)}{4}$, results in $p = 2.1 \pm 0.3$, a result consistent with that from the XRT light curve and time averaged spectrum.

There is a difference of 0.3 ± 0.1 between the exponents of the XRT and post-break MeerKAT light curves, with the MeerKAT one being the shallower of the two. Such a difference indicates that ν_C is between the two observing bands (the theoretical difference is $\Delta\alpha = 0.25$). This result implies that $1.3\,\mathrm{GHz} \leq \nu_C \leq 0.3\,\mathrm{keV}$.

The AMI-LA data set is inconsistent with the FS model. On top of the host galaxy emission, the early decay follows $F \propto t^{-0.59\pm0.03}$. If the emission originated from the optically thin branch (i.e. above ν_M) of the FS synchrotron spectrum, the light curve would give $p = 1.80 \pm 0.09$ which is far shallower than obtained with MeerKAT and XRT. The early 15.5 GHz decay is shallower than the MeerKAT decay. Furthermore, if the MeerKAT and AMI-LA light curves are both from the FS, we would expect to see a break in the AMI-LA data at an earlier time as a result of ν_M passing through the band.The frequency break ν_M evolves as $t^{-\frac{3}{2}}$ independent of the structure of the surrounding environment; working backwards one expects to see a break at about 2.7±0.4 days in the AMI-LA light curve given the MeerKAT break time. No such break is observed and the observed flux levels are too high to be consistent with the FS seen in the MeerKAT data.

The AMI post-break decay is steeper than both the MeerKAT and XRT light curves. Therefore, the emission observed at 15.5 GHz cannot originate from a FS component. The possibility of a jet break can also be ruled out. A jet break would result in a simultaneous steepening of both the radio and X-ray light curves so that they follow $F \propto t^{-p}$. While breaks in the AMI and MeerKAT light curves occur at the same time, the post break decays both too shallow to be from a jet break and are at different rates. Furthermore, there is no evidence of a break in the XRT light curve. The MeerKAT and XRT slopes are too shallow to originate from a jet break in the FS.

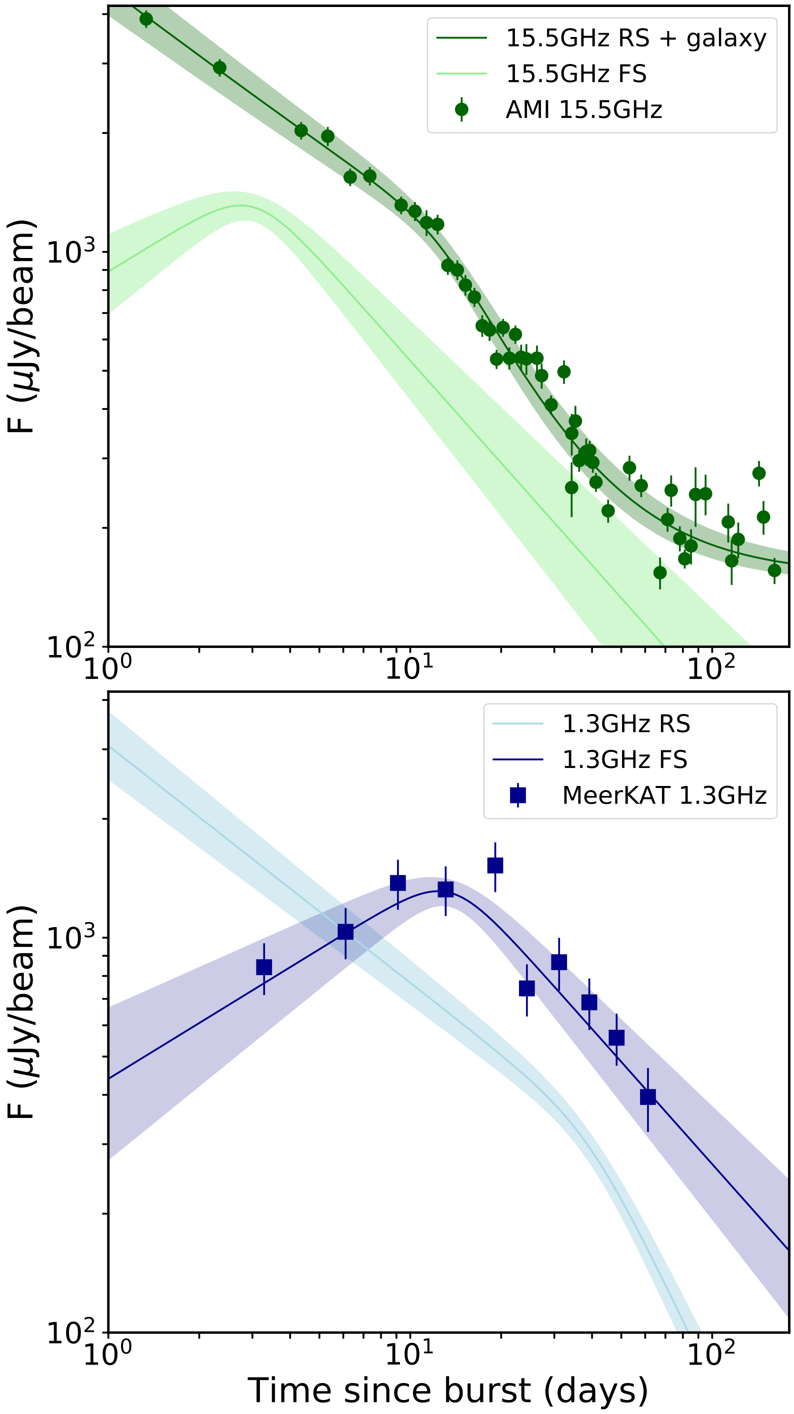

Figure 4.4: *Upper panel:* The AMI-LA light curve, in dark green, shows the RS and underlying galaxy component. The light green broken power law shows how the FS would evolve in a homogeneous environment at 15.5 GHz. *Lower panel:* The FS-dominated MeerKAT light curve with the theorised RS component as seen at 1.3 GHz, derived from the 15.5 GHz light curve.

Radio: Forward and Reverse Shock

The AMI light curve can be explained with an additional component a reverse shock (RS). Considering both the thick and thin shell regimes; the pre-break emission in the AMI light curve is the most similar to the RS where $\nu_{SA} \leq 15.5\,\mathrm{GHz} \leq \nu_M,\nu_C$. In the thick shell regime, for $k = 0$ the power law exponent of the slope would be -0.47 and for $k = 2$, it would be -0.5. In the thin shell regime, the expected slope is around -0.46 (Van der Horst et al., 2014). All three of these values are close to the fitted result of 0.59 ± 0.03. The difference between the theoretical and observed result may be from time varying microphysics, or a steeper density profile.

Post-break, the slope falls at a rate consistent with optically thin synchrotron ($\nu_{SA} \leq \nu_M \leq 15.5\,\mathrm{GHz} \leq \nu_C$) from the RS, for a homogeneous environment and $p = 2.5 \pm 0.1$ in a thick shell regime. The decay is too steep to be physically representative in the thin shell regime. Both the forward and reverse shocks show evidence of a homogeneous environment.

It is possible to check if the FS contributes significantly to the AMI-LA light curve. Using a spectral index of -0.75 ± 0.03, derived from the MeerKAT optically thin data, the 1.3 GHz light curve is extrapolated to 15.5 GHz. Using the 1.3 GHz data points and table 1 from Van der Horst et al. (2014), I produced a theoretical FS light curve at 15.5 GHz. The simulated light curve is shown in the upper panel of Figure 4.4 along side the original AMI data set with their respective fits and shaded 68% confidence level uncertainty regions. At all times the FS shock emission at 15.5 GHz is fainter than the measured flux density values. Past 30 days, the simulated FS component becomes comparable to the AMI light curve but this is also where emission from the host galaxy begins to dominate.

Similarly, it is possible to check if the RS component detected at 15.5 GHz contributes significantly to the 1.3 GHz MeerKAT light curve. The AMI light curve is extrapolated to 1.3 GHz. The predicted RS light curve at 1.3 GHz is shown in the lower panel of Figure 4.4. Except for the first data point, where the theoretical 1.3 GHz RS dominates over the FS, it is clear that the FS is the main emission component in the MeerKAT data set. This early emission at 1.3 GHz could be suppressed by synchrotron self-absorption of the RS emission.

In knowing that the reverse shock does not produce a significant contribution to the MeerKAT light curve, it is possible to extract some physical parameters from the forward shock. The peak of the MeerKAT light curve provides the peak flux density $F_{\nu,max}$ and the time at which ν_m passes through the 1.3 GHz observing band. Combined with the average XRT flux density at the time ν_m = 1.3 GHz and time-averaged spectrum, it is possible to constrain the location of ν_c to between 0.04-0.3 keV. By assuming fiducial values for the fraction of kinetic energy within the jet given the electrons (0.1), the circumburst density, jet kinetic energy and fraction of energy given to the magnetic fields can be calculated. The radio light curves are consistent with a jet propagating through a homogeneous environment, they can be reproduced with a very low density environment of (1-3)×10^{-5} cm^{-2} is derived. Such low densities have been reported before (Perley et al., 2014) but it still considered significantly lower than the average ISM density (1cm^{-2}). Such a low density could be a result of the GRB's location within its host galaxy: from the MeerKAT observations (Figure 4.1) it can be inferred that the GRB site is on the outskirts of the host galaxy. The same calculations also result in a very low kinetic energy $E_{\rm K,\,ISO}$ = (5-8)×10^{50} erg and value of ϵ_B = (5-9)×10^{-4}.

The MeerKAT and *Swift*-XRT light curves show no evidence of any achromatic behaviour that would suggest the presence of a jet break, allowing limits to be places on the opening angle of the jet. For the derived kinetic energy and density values, the minimum opening angle of the jet is 8°. Such a value is completely consistent with the opening angles of other long GRB jets (Laskar et al., 2014).

In summary, the radio and X-ray observations of GRB 190829A is best described using a combination of two shocks: MeerKAT and XRT light curves show forward shock emission and the AMI-LA light curve shows a reverse shock component fading until around 70 days post burst where emission from the host galaxy dominates.

Table 4.2: Peak flux densities and 3σ upper limits of 15.5 GHz observations for GRB 180720B. Observations were made with AMI-LA as part of the ALARRM (Staley et al., 2013; Anderson et al., 2018).The table shows the time since burst (T_0), the peak flux for each epoch with a detection along with uncertainties (including statistical and 5% calibration error) and duration. On occasions where the source was not detected, a 3σ upper limit is denoted with the prefix ' <'.

T-T_0(days)	Flux (μJy/beam)	Duration (hrs)
1.69	1100±60	4
3.66	580±50	2
5.65	340±40	4
6.66	<220	4.5
25.59	<190	3

4.3 H.E.S.S. GRB 180720B

GRB 180720B was detected by *Swift*-BAT on 2018 July 20 14:21:44 UT, (Siegel et al., 2018). Observations with the X-shooter spectrograph on the Very Large Telescope (VLT) placed the GRB at a redshift of 0.654 (Vreeswijk et al., 2018). H.E.S.S identified a 5σ source consistent with the GRB's position 10 hours after the initial detection but did not report the detection until 2019 (Abdalla et al., 2019).

4.3.1 Observations: AMI-LA

The *Swift*-BAT detection of GRB 180720B triggered observations with AMI-LA (Staley et al., 2013; Anderson et al., 2018). In total, 5 logarithmically spaced observations were made. The observations were reduced using the same method described for GRB 190829A. A list of fluxes and upper limits measured are listed in Table 4.2. The radio light curve is shown in Figure 4.5.

4.3.2 Results and Interpretation

The radio light curve is best characterised by a power law decay following $F \propto t^{-1.0\pm0.1}$, until 6 days post-burst, after which only upper limits around 200 μJy were obtained. The decay

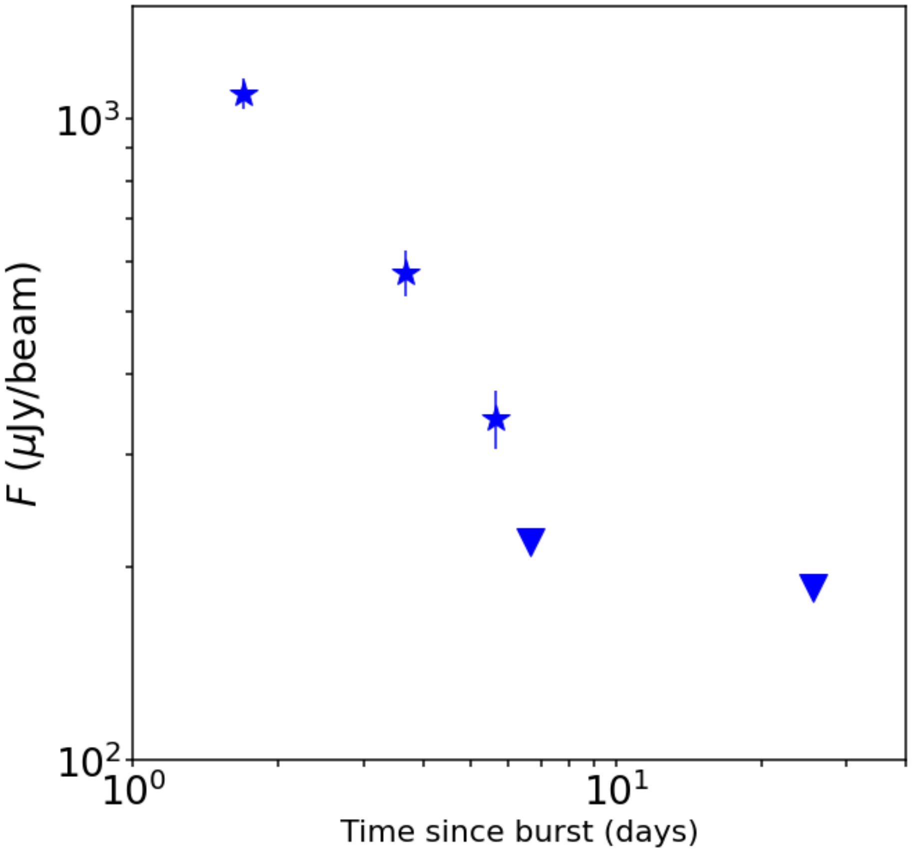

Figure 4.5: The 15.5 GHz radio light curve for the first VHE GRB: GRB 180720B. The light curve follows a power law decay of $t^{-1.0\pm0.1}$. The afterglow is no longer detected after six days post-burst.

is consistent with optically thin emission ($\nu_M \leq 15.5\,\mathrm{GHz} \leq \nu_C$) produced by a forward shock propagating into a homogeneous environment. The optical light curve (Fraija et al., 2019) also shows a power law decay of $F \propto t^{-1.0\pm0.1}$ indicating that both the optical and radio observing bands are on the same branch of the synchrotron spectrum. The *Swift* XRT light curve shows a slightly steeper decay around $F \propto t^{-1.38\pm0.01}$. The difference between the X-ray and optical/radio decay rates is (0.4±0.1) large enough to be a result of ν_C falling below the XRT band. However the X-ray and optical spectral indices are both around -0.8, implying that both bands lie on the optically thin ($< \nu_C$) branch of the spectral, for p ≈ 2.6. This interpretation means that the optically thin branch spans from below 15.5 GHz to above 10 keV. Comparison of the optical, radio and X-ray data at one, three and five days post-burst show that the optical data points are too bright compared to the radio and X-ray such that they all originate from the same branch of the synchrotron spectrum where there is a single power law spectrum from 15.5 GHz to 10 keV.

This interpretation is not a perfect fit to the data. It is possible that other emission components are contaminating the data such that a forward shock-only model is not accurate. However with so few data points, it is difficult to quantify the contribution of additional shock components to the light curves. Reverse shock emission often dominates in the optical and radio bands in the first days after the burst. Therefore, a significant reverse shock component could result in an overall reduction in the light curve decay observed at radio and optical compared to that with XRT. The X-ray light curve, p = 3.0±0.1, which is much steeper than the optical and radio decays result of p = 2.3±0.1. When fitting broad band spectral models to the afterglow data, the model favours a steeper p value around 3, reinforcing the idea that some additional emission component is contributing to the optical and radio emission.

4.4 MAGIC GRB 201216C

The prompt emission from GRB 201216C was detected on 2020 December 16 at 23:07:31 UT by the Neil Gehrels *Swift* Observatory (here after *Swift*) Burst Alert Telescope (BAT, Beardmore et al., 2020). Three optical observatories also reported detections of a counterpart from early-time observations. A team searching for the afterglow with the Very Large Telescope (VLT) detected a source within the BAT error region at 21.81±0.05 magnitudes (r'-band) 2.19 hours after the burst (Izzo et al., 2020b). The VLT also measured a very steep optical spectral index ($\nu^{-4.1\pm0.2}$) and placed GRB 201216C at redshift z = 1.1 (Vielfaure et al., 2020). Jelinek et al. (2020) and Shrestha et al. (2020) confirmed the optical source as the the afterglow. A number of other observatories reported deep upper limits (Oates et al., 2020; Belkin et al., 2020; Gokuldass et al., 2021). There was no report of a detection of a supernova component. The reported optical detections and upper limits are shown in Figure 4.6 as the squares and downwards facing grey triangles, respectively.

The *Swift*-X-ray Telescope (XRT) started observing ~50 minutes post burst. The XRT unabsorbed fluxes were very high with respect to the optical counterpart. When combined with the steep optical spectral index, GRB 201216C was classified as a dark GRB (Vielfaure et al., 2020). It is unlikely that such a steep optical spectral index is a result of galactic extinction as the reddening in the direction of the burst is E(B-V) = 0.05 (Oates et al., 2020). This is discussed further in Section 4.4.4.

MAGIC reported the detection of a significant VHE counterpart less than a minute after the initial burst detection (Blanch et al., 2020b), making GRB 201216C is the highest redshift VHE GRB to date. Upon the notification of a VHE detection from the MAGIC Collaboration, I commenced a multi-frequency radio campaign with a series of successful Director's discretionary time observations (DDTs) with *e*-MERLIN, the Karl G. Jansky Very Large Array (VLA) and MeerKAT as well as late-time Target of Opportunity (ToO) observations with *Swift*-XRT.

4.4.1 Observations

A list of observing dates, peak flux density measurements and uncertainties are given in Table 4.3. Spectral indices are calculated in epochs with high enough signal to noise ratios.

***e*-MERLIN**

GRB 201216C was observed by *e*-MERLIN three times through successful DDT proposals at 5, 12 and 29 days post burst (PI: Rhodes, project codes: DD10010 and DD11001). Observations were made at 5 GHz with a bandwidth of 512 MHz. Each epoch consisted of 60 minutes on the flux calibrator (3C286) and 90 minutes on the bandpass calibrator (OQ208) followed by eight hours of interleaved target and phase calibrators cycles: six minutes on the target and two minutes on the phase calibrator (J0056+1625).

The *e*-MERLIN pipeline was used to reduce the observations[2](Moldon, 2021). The pipeline performs flagging, delay and bandpass calibration, and calculates phase and frequency dependent amplitude gain corrections which are all applied to the target field, along with flux density scaling from the flux calibrator. The calibrated measurement set was imaged in CASA (Version 5.3.0) using the *tclean* task (McMullin et al., 2007b). The uncertainties associated with the flux density measurements combine the statistical uncertainty and a 5% calibration error.

Karl G. Jansky Very Large Array

Six VLA observations were obtained through a DDT proposal (PI: Rhodes, project ID: 20B-456), spread out between 12 and 53 days post burst. The observations were made at 10 GHz with a bandwidth of 4 GHz. For each epoch, the target field was observed for ten minutes, book-ended with the phase calibrator (J0121+1149) and the primary calibrator (3C147). The observations were reduced using the VLA pipeline in CASA (Version 5.3.0, Kent et al., 2018). The pipeline performs flagging, creates a model of the flux calibration,

---

[2] `https://github.com/e-merlin/e-MERLIN_CASA_pipeline`

and performs initial calibration including antenna position corrections. Delay, bandpass and gain corrections are derived and applied to the data after which further flagging is performed. Imaging was also performed in CASA. The uncertainties on the flux densities were calculated by combining the statistical error and 5% calibration uncertainty added in quadrature.

MeerKAT

I obtained four DDT observations with MeerKAT (PI: Rhodes, DDT-20210107-LR-01) at 22, 29, 40 and 54 days post burst. Each observation lasted 140 minutes, made up of a five minute scan of a primary calibrator (J0408−6545) preceded by a series of 20 minute scans of the target interleaved with two minute scans of the secondary calibrator (J1808+0134). The observations were made at a central frequency of 1.28 GHz with a bandwidth of 856 MHz, split into 4096 channels.

The MeerKAT data were reduced using `OxKAT`, a set of python scripts used for semi-automatic processing (Heywood, 2020). Firstly, the calibrator fields were flagged for RFI as well as the first and last 100 spectral channels. A spectral model from the primary calibrator was applied to the secondary. Delay, bandpass and complex gain calibration was performed on the primary and secondary calibrators and applied to the target field. Finally the target field was flagged using TRICOLOUR[3]. The data were imaged with WSCLEAN using a Briggs weighting with robust parameter of -0.7 (Offringa et al., 2014). The image was derived to create a model to use in a round of phase-only self-calibration after which the field was reimaged. The flux uncertainties include statistical uncertainties and a 10 % calibration error.

---

[3] https://github.com/ska-sa/tricolour

T-T$_0$ (days)	ΔT (hours)	$\Delta\nu$ (GHz)	S$_\nu$ (μJy)	β
		e-MERLIN		
5.6	8	4.8−5.2	180±23	7±4
21.9	6	4.8−5.2	<102	-
28.7	6	4.8−5.2	66±10	-
		VLA		
12.1	0.2	8−12	127±12	1.8±0.8
14.0	0.2	8−12	98±6	1.5±0.8
20.0	0.2	8−12	124±13	0.4±0.6
36.0	0.2	8−12	62±6	-
44.0	0.2	8−12	68±9	-
53.0	0.2	8−12	50±5	-
		MeerKAT		
22.8	2	0.9−1.7	<29	-
28.7	2	0.9−1.7	95±11	> −0.3
40.6	2	0.9−1.7	124±15	−1.1±0.6
54.5	2	0.9−1.7	130±14	−0.7±0.5

Table 4.3: A table of the radio observations made of GRB 201216C with *e*-MERLIN, the VLA and MeerKAT. The columns are the following: T-T$_0$, the time between the burst detection and the centre of the observation, in days; ΔT, the duration of the observation, in hours; $\Delta\nu$, the observing frequency range; S$_\nu$, the peak flux density (or 3σ upper limit); β, the in-band spectral index. The uncertainties on each flux density measurement are a combination of the fitting error and a calibration error (5% for *e*-MERLIN and VLA, 10% for MeerKAT) added in quadrature. Values for β are given for epochs when the source is bright enough to be detected in at least one half of the band.

Neil Gehrels Swift Observatory - X-ray Telescope

The *Swift* X-ray Telescope (XRT) observed the field of GRB 201216C from 3000 s until 22 days after the initial burst (Evans & Swift-XRT Team, 2021). This included two ToO observations obtained between days 20 and 27 post burst. Each epoch was automatically fitted with a power-law spectrum. The light curve and spectra are made public on the *Swift* Burst Analyser (Evans et al., 2007, 2009, 2010). The X-ray flux densities used in the analysis are calculated at 5 keV to avoid systematic under or over estimations in calculating the flux density at the edge of the observing band (i.e. at 0.3 or 10 keV).

4.4.2 Results

In the following sections, the convention $F_\nu \propto t^\alpha \nu^\beta$ is used where t is the time post burst, ν is the observing frequency, and α and β are the exponents. Any subscripts are used to indicate the relevant part of the spectrum or frequency band.

Light curves

Light curves: Radio

Figure 4.6 shows the radio light curves from the observing campaign. The flux densities and upper limits are given in Table 4.3. Radio emission at 5 GHz was detected in two of the three observations with *e*-MERLIN, during epoch one and three (the green crosses in Figure 4.6).

The 10 GHz light curve (blue stars in Figure 4.6) from the VLA covers the largest time range, from 12 to 54 days post burst. The 10 GHz behaviour is best described as a shallow power-law decay ($\alpha_{10\,\mathrm{GHz}} = -0.5 \pm 0.1$) from $\sim 120\mu$Jy at 12 days to $\sim 50\mu$Jy at 54 days. On top of the decaying flux, there is inter-observation variability, which is possibly due to ISS (see Section 4.4.3). The epoch-to-epoch variability could cause the observed decay rate to deviate significantly from the intrinsic evolution.

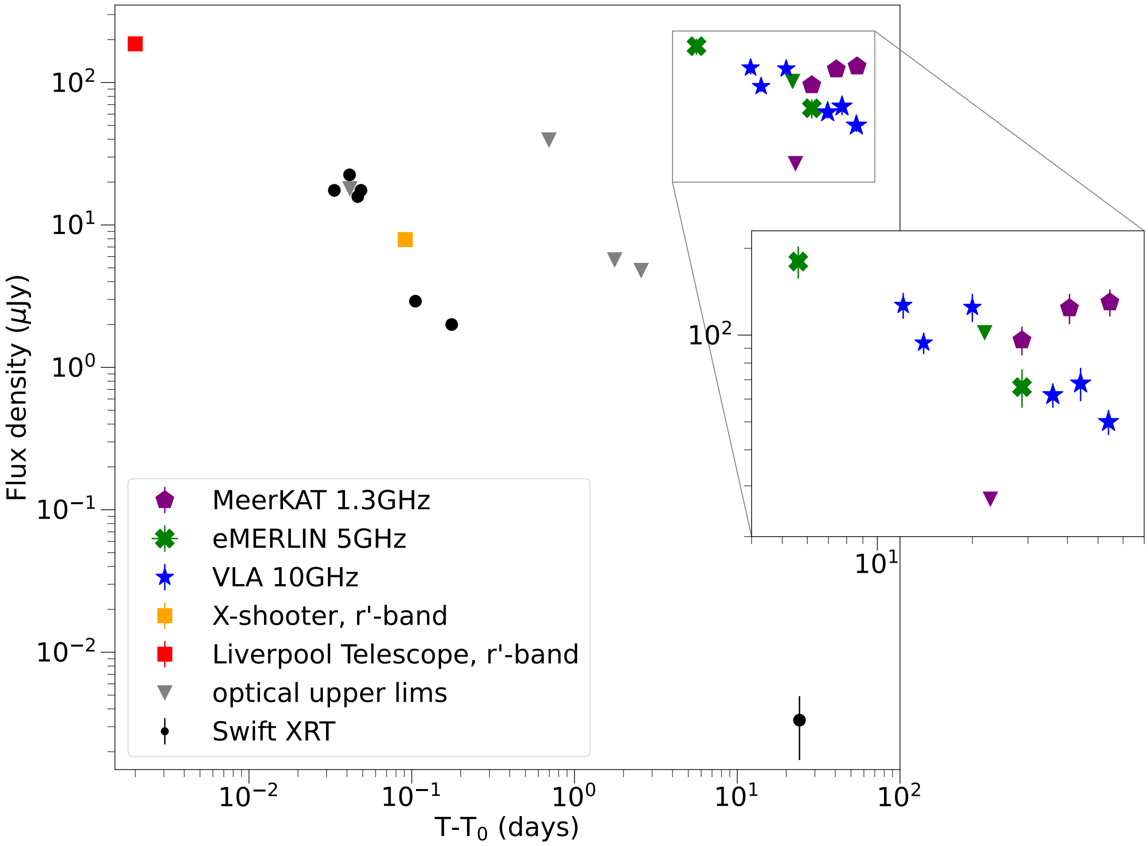

Figure 4.6: X-ray, optical and radio observations from GRB 201216C. The flux densities for the radio data points are given in Table 4.3. The optical flux densities and upper limits are from the Gamma-ray burst Coordinates Network Circulars (Shrestha et al., 2020; Izzo et al., 2020b; Belkin et al., 2020; Gokuldass et al., 2021). The *Swift*-XRT light curve for GRB 201216C has been rebinned into five minute bins. The inset shows a clearer view of the radio dataset.

The 1.3 GHz MeerKAT light curve (the purple stars in Figure 4.6) starts with a very steep rise ($\alpha_{1.3\,\mathrm{GHz}} \gtrsim 5$) from a 3σ upper limit of 29μJy to a detection of 95μJy over 6 days. The next three data points show a flat light curve ($\alpha_{1.3\,\mathrm{GHz}} = 0.1 + /{-0.2}$) to 130μJy in the final epoch. The sharpest rise possible for the standard forward shock model is $t^{1.75}$, which is far shallower than the observed rise, comes from optically thick synchrotron from a forward shock propagating through a stellar wind environment in the regime where $\nu_{\mathrm{m}} < \nu_{obs} < \nu_{\mathrm{SA}}$ (Granot & Sari, 2002).

Due to the jet's compactness, radio observations of GRB afterglows are susceptible to scintillation, which can cause significant spectral and temporal variability, especially at early times. It should be noted that scintillation timescales are also frequency dependent and that the observations sample variability on different timescales with the different interferometers due to differing observation lengths. ISS may be the cause of the inter-observation variability seen with the VLA. Intra-observation variability is searched for within the VLA data, as shown in Figure 4.7. Some low-level variability, ~10-20% (using equation 10 from Vaughan et al., 2003), is observed in VLA epochs one and three. VLA epochs two and four show no such variability (see Figure 4.7). The flux densities of the last two observations are too low to search for variability.

The two *e*-MERLIN detections, which are six hours long each, are split into four-90 minute segments. The left hand panel of Figure 4.8 shows that for the first epoch, radio emission was only detected in two of the four segments. In the final epoch, radio emission is only detected for 90 minutes out of six hours.

The MeerKAT data set shows no evidence of intra-observation variability on a timescale of tens of minutes. The implications of the observed variability are discussed further in Section 4.4.3.

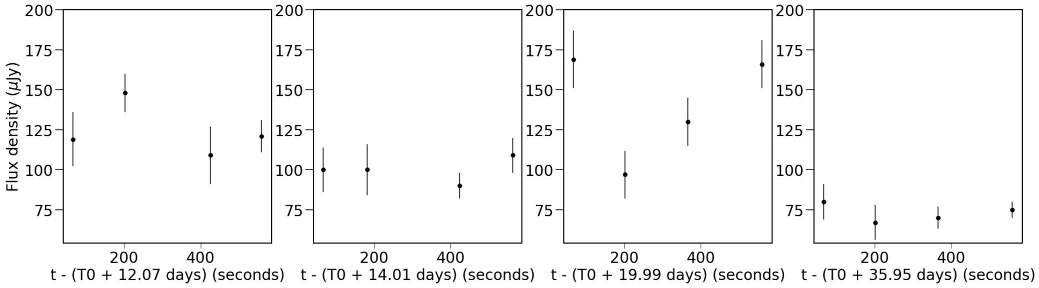

Figure 4.7: Intra-observation light curves to show short term variability in the VLA 10 GHz data set. The first four 10 minute epochs are sub-divided into four-2.5 minute sub-integrations. Only the first four observations are used as these are the brightest four where the source is reliably detected on short timescales.

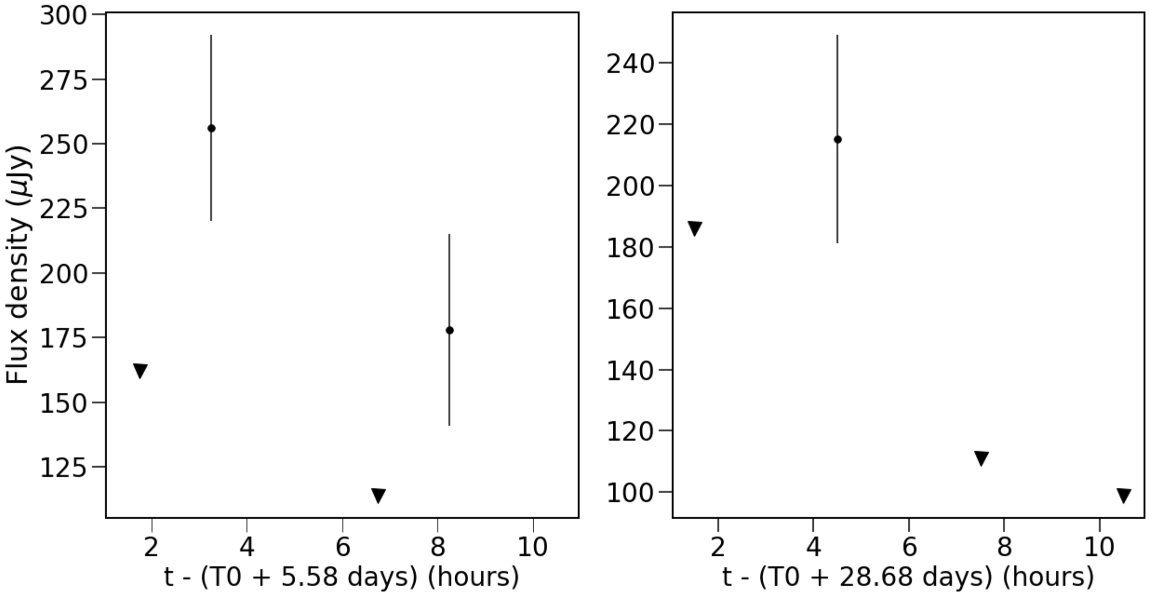

Figure 4.8: Short term variability observed in the first and third *e*-MERLIN epochs. Each six hour observation was split into four sub-integrations. In the first observation made 6 days post burst, radio emission was detected in two of the four sub-integrations. In the third observation, made at 28 post burst, the source was only detected in one of the four sub-integrations.

Light curves: Optical

An optical counterpart to GRB 201216C was detected with the Liverpool telescope and the VLT (red and orange squares in Figure 4.6, respectively; Shrestha et al., 2020; Izzo et al., 2020b). Within a couple of hours, the source had faded below detection limits. The r'-band light curve follows a $\alpha_r = -0.83 \pm 0.01$ decay from a few minutes post burst (Belkin et al., 2020; Gokuldass et al., 2021). Such a decay rate is consistent with optically thin synchrotron radiation in an ISM environment which gives p = 2.11±0.01 (from ($\alpha = 3(1-p)/4$, Granot & Sari, 2002). An optically thin forward shock in an wind environment would decay more rapidly (for p = 2, $\alpha = -1.25$), however, with only a handful of detections it is impossible to determine whether the measured decay rate could be due to a combination of a frequency break passing through the optical observing band and a stellar-wind-like environment. Such a combination would result in the optical light curve appearing shallower.

Light curves: X-ray

The XRT light curve (black circles in Figure 4.6) consists of a significant number of detections early on (t < one day) and one further detection around 25 days post burst. The photon-counting mode light curve has been rebinned to reduce any bias towards the earlier detections when fitting a power law decay to the light curve. Using either five or ten minute bins, the light curve has a decay rate of $\alpha_{X-ray} = -1.9 \pm 0.3$. The final detection is slightly above the predicted flux density given the above decay rate as shown in Figure 4.12.

There are many scenarios in which the X-ray light curve agrees with theoretical predictions. (1) Synchrotron radiation from a forward shock above $\nu_{\rm C}$ in either a homogeneous or wind environment, $\alpha = (2-3p)/4$, giving p = 3.2±0.4; (2) optically thin forward shock synchrotron emission below ν_C in a stellar wind environment, $\alpha = (1-3p)/4$, p = 2.9±0.4 (Granot & Sari, 2002); (3) optically thin forward shock emission below ν_C in a homogeneous environment, $\alpha = 3(1-p)/4$: p = 3.5±0.4, and (4) the early X-ray light curve is also consistent with a jet break with no significant lateral spreading, i.e. only edge effects are considered. In a homogeneous environment, emission above the cooling break should decay as $\alpha = -(1+3p)/4$, where p = 2.2±0.2, and below the cooling break $\alpha = -3p/4$, where p = 2.5±0.2. In a stellar wind environment, emission below the cooling break should decay as $\alpha = -(1+3p)/4$, where p = 2.2±0.2, and above the cooling break $\alpha = -3p/4$, where p = 2.5±0.2 (Gao et al., 2013). The degeneracy between the different potential scenarios can be broken by considering the X-ray spectral index measurements and light curves in other wave bands to form a broadband model.

4.4.3 Short timescale radio variability

As well as the long term evolution, the radio observations also show evidence of short timescale (inter- and intra-epoch) variability as a result of ISS.

Diffractive scintillation

DISS causes narrow-band fluctuations of order unity on a range of timescales and therefore, can affect radio observations dramatically. The *e*-MERLIN observations show evidence of short timescale variability, a feature that is inconsistent with the smooth power law variations expected from GRB afterglows. It is possible to explain the variability observed as a result of small scale inhomogeneities in the local ISM which causes multi-path propagation (DISS) of the radio waves from GRB 201216C (Goodman, 1997). For simplicity, the region of the ISM causing the scattering is collapsed into a screen as some distance along the line of sight (Walker, 1998).

I placed a lower limit on the intra-observation temporal variability of 30% for the *e*-MERLIN data set (Vaughan et al., 2003). If the observed variability is due to DISS, one would expect to see narrow-band flux modulations up to one on the timescale of an hour (Goodman, 1997; Walker, 1998). Due to signal to noise limitations, it is not possible to search for shorter timescale variability. I also searched for variability in the spectral domain by dividing the two detection epochs into 4 sub-bands (centred at 4.8, 4.9, 5.1 and 5.2 GHz), another sign of DISS since it is a narrow-band phenomenon. In the first *e*-MERLIN epoch, radio emission is only detected in the sub-band centred at 4.8 GHz, at $300\pm30\mu$Jy. In the bands centred at 4.9, 5.1 and 5.2 GHz, 3σ upper limits of 156, 144 and 195μJy, respectively, are placed. A high level significance detection in a single, narrow frequency band implies that DISS is most likely the origin of the variability at 5 GHz. In the final *e*-MERLIN epoch, the low flux density prevents the source from being detected in any of the sub-bands.

Under the assumption that the *e*-MERLIN variability is caused by DISS, it is possible to place constraints on the location of the scattering screen between the Earth and the position of the GRB. Assuming that the screen is located within the Milky Way, by integrating the free electron distribution along the line of sight using the NE2001 model (Cordes & Lazio, 2002), I calculate a scattering measure $\mathrm{SM}_{\text{-}3.5} = 0.69$ where $\mathrm{SM}_{\text{-}3.5} = \mathrm{SM}/(10^{-3.5}\,\mathrm{kpc\ m}^{-20/3})$, defined as the characteristic angle that incoming radio waves are scattered by whilst propagating through the ISM corresponds to a transition frequency of 8.8 GHz in the direction of the GRB. Observations below 8.8 GHz are in the regime where it is possible to observe strong scattering, consistent with the conclusion that the variability at 5 GHz is produced by DISS. This scattering measure and transition frequency correspond to a scattering screen at a distance (d_{scr}) of ~0.9 kpc. I obtain the same value for d_{scr} using the method presented in Goodman (1997).

DISS is heavily dependent on the angular size of the GRB. Once the size of the jet projected on the sky has expanded above a critical size on the sky, the effects of DISS will no longer will observable. This critical size is determined by the distance to the scattering screen, observing frequency, and the scattering measure (Goodman, 1997):

$$\theta_s < 2.25\nu_{10}^{6/5}(SM_{-3.5})^{-3/5}d_{\mathrm{scr,\,kpc}}^{-1}\mu\mathrm{as}$$

given that the radio emission observed is still affected by DISS 29 days post burst, based on the short timescale variability observed in the last *e*-MERLIN observation (Figure 4.8).

Therefore, at 29 days post burst the angular size of the jet associated with GRB 201216C must be less than 1μas. At a redshift of 1.1, the distance to GRB 201216C, 1μas is $\sim 1 \times 10^{17}$cm. This size upper limit is consistent with size measurements of other long GRBs made at around 30 days (see figure 7 of Alexander et al., 2019; Taylor et al., 2004). It is likely that if subsequent observations at 5 GHz were made, they would most likely not have been affected by DISS.

According to the thin screen scattering model, at 1.3 GHz (the MeerKAT observing band), one would expect to see variability on timescales of ten minutes with a modulation index of one. There is no intra-observation or narrow-band variability in the MeerKAT data. This indicates that by 29 days post burst, the angular size of the jet has grown larger than the 0.3μas (0.3×10^{17}cm).

Refractive scintillation

The presence of DISS at 5 GHz also implies the presence of RISS. RISS produces variability on longer timescales. At 1.3 and 5 GHz, the variability is expected to be at a level of about 30 and 70% on timescales of over 5 days and ~7 hours, respectively (Walker, 1998). It is possible to use RISS to also constrain the source size:

$$\theta_{\rm S} < 8\nu_0^{17/10}\nu^{11/5}{\rm d}_{\rm scr,kpc}^{-1/2}$$

where ν_0 and ν are the transition and observing frequency. respectively.

The observations at 5 GHz are dominated by the effects of DISS, and due to the sparse cadence, days between each epoch, it is not possible to observe the effects of RISS. In the MeerKAT band, the increase in flux density between days 23 and 29 is greater than a factor of three, far higher than the predicted RISS flux modulations of 30%. The observations in which the source detected shows a smooth increase in flux density across the three epochs in which the source is detected. The spacing between each epoch is too large to infer whether the increase in flux density is due to RISS. Therefore, I cannot confidently attribute the

MeerKAT flux variations to RISS.

Weak Scintillation

Weak scintillation often affects the data at a level similar to that of the calibration uncertainties ($\sim 5 - 10\%$); although it can be significantly higher for observing frequencies close to the transition frequency). The VLA observations at 10 GHz, which is above the transition frequency (8.8 GHz), show clear inter-observation variability (the blue stars in Figure 4.6), as well as at the $\sim$10% level on the timescale of minutes in the two of the first four epochs, see Figure 4.7. The flux density of the radio counterpart in the last two VLA epochs are too low to search for intra-observation variability. As a result, it is not possible to tell if the effects of weak scintillation have faded as the jet grows on the sky.

With a transition frequency of 8.8 GHz, the majority of the VLA observing band falls within the weak scattering regime. However, the VLA's wide bandwidth means that some effects of DISS and RISS are still observed. DISS, RISS and weak ISS are expected to cause variation on timescales of two to three hours across the VLA band with a modulation index as high as one (Walker, 1998; Granot & Van der Horst, 2014). Such high variability levels are to be expected because the VLA observations are so close to the transition frequency, although the amplitude of the flux modulation is expected to drop rapidly towards high frequencies. Therefore, it is most likely that the variability observed in the VLA band is a combination of DISS and weak scintillation.

Spectra

Spectra: Radio

The right-most column of Table 4.3 shows all the in-band radio spectral index measurements calculated using the individual observing bands for epochs where the source was bright enough. Of the three *e*-MERLIN observations, only the first epoch was bright enough to obtain an in-band spectral index. The scintillation dramatically affects the *e*-MERLIN spectra as it does the intra-epoch light curves. At 5 days post burst, the only time where the source is bright enough to split the band in two, the 4.8 – 5.3 GHz spectral index is 7±4. The large uncertainties mean that such a steep result is still compatible with the steepest branch of the synchrotron spectrum in the GRB afterglow scenario ($\nu^{\frac{5}{2}}$), caused by synchrotron self-absorption.

The radio emission at 10 GHz (VLA) is only bright enough in the first three epochs to split the 4 GHz bandwidth into two-2 GHz subbands. In each of these three epochs, the 8-12 GHz spectral index is consistent with being spectrally steep or fairly flat ($\beta_{10\,\mathrm{GHz}} \geq 0$). Over the course of the three observations, the VLA in-band spectral index slowly flattens (see Table 4.3). The wide VLA observing band smears out any narrow-band effects of DISS. In the context of the fireball model, the observations made at 12 and 14 days post burst are too steep to be in the regime where $\nu_{\mathrm{SA}} < 10\,\mathrm{GHz} < \nu_{\mathrm{m}}$ ($\beta = 1/3$). Instead, they are more consistent with $10\,\mathrm{GHz} < \nu_{\mathrm{SA}}, \nu_{\mathrm{m}}$ ($\beta = 2$) or $\nu_{\mathrm{m}} < 10\,\mathrm{GHz} < \nu_{\mathrm{SA}}$ ($\beta = 2.5$, Granot & Sari, 2002).

The 1.0-1.7 GHz spectral index is calculated for the three MeerKAT observations where radio emission is detected (values are also given in Table 4.3). At 28 days post burst, radio emission is only detected in the upper half of the band, which gives a lower limit on the spectral index of >-0.3. The final two epochs show a spectral index of $\beta_{1.3\,\mathrm{GHz}}<0$, consistent with optically thin synchrotron: ν_{m}, $\nu_{\mathrm{SA}} < 1.3\,\mathrm{GHz}$. The three MeerKAT detections are made after the epochs where the 8-12 GHz spectral indices are calculated, meaning that over the course of the radio campaign, the emission evolves from being optically thick to optically thin.

Spectra: X-ray

The *Swift*-XRT spectra in the range of 0.3-10 keV are each fitted with a power law parameterised by the photon index: Γ, where $\beta_X = 1 - \Gamma$. There are no significant variations in Γ over the observing period implying that no break frequency passes through the XRT band.

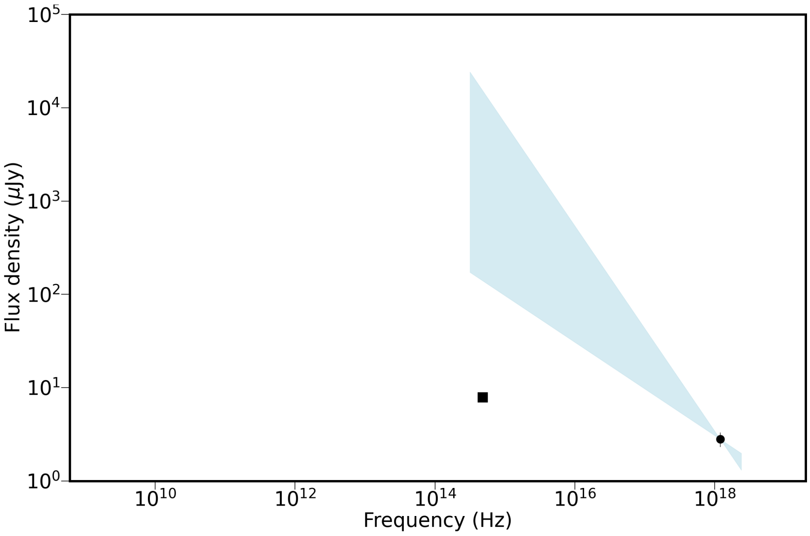

Figure 4.9: Optical and X-ray detections from 2 hrs post burst. The blue shaded region corresponds to the range in predicted spectra assuming that ν_C falls between the optical and X-ray bands. Comparison of the faint optical detection and the hypothetical synchrotron spectrum shows that GRB 201216C is a dark GRB.

The data taken in photon counting mode result in $\Gamma = 2.0 \pm 0.1$ (β_X = -1.0±0.1). As with the X-ray light curve, β_X, emission both below (p = 3.0±0.2) and above (p = 2.0±0.2) ν_C. The spectral index does not change in the event of a jet break, unlike the light curves.

Spectra: Broadband spectra

There are three epochs in which broadband spectra are constructed. Figure 4.9 shows the optical and X-ray data detections (black circle and square), approximately two hours post burst. The blue shaded region denotes the range of possible predicted flux densities under the assumption that ν_C falls between the optical and X-ray bands at the time of the observations. The range is calculated assuming that β_{O-X} is between $\beta_X + 0.5$ and β_X i.e. ν_C is at 0.3 keV and in the r'-band, respectively. It is clear from the blue shaded region that the measured spectral index ($\beta_\mathrm{O\text{-}X} = -0.13 \pm 0.02$) is significantly flatter than expected from the synthesised synchrotron spectrum. Given that $\beta_X = -1.0 \pm 0.2$ at this time, if ν_C falls between the optical and lower end of the X-ray band, it can be inferred that β_{O-X}should be $-\ 0.5 \pm 0.2$ ($\beta_{O-X} = \beta_X + 0.5$), much steeper than our measured $\beta_\mathrm{O\text{-}X}$ (Van

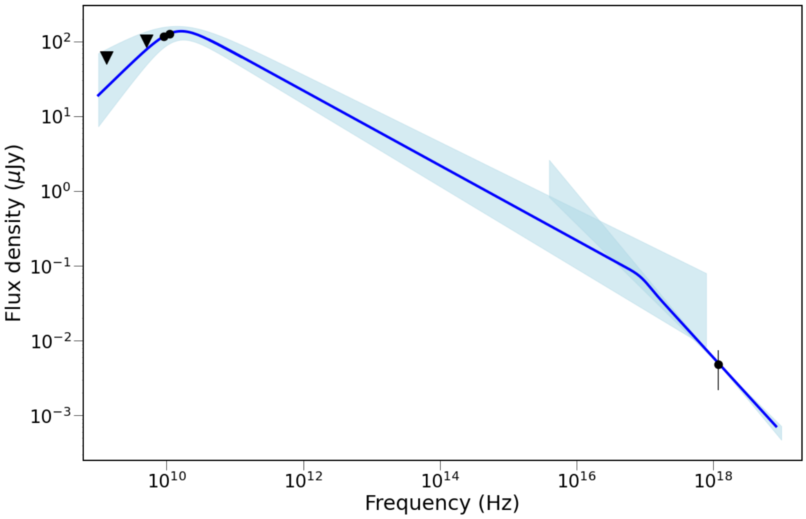

Figure 4.10: Broadband spectrum from 0.9 GHz to 10 keV using data from MeerKAT, *e*-MERLIN, VLA and *Swift*-XRT made between 20 and 24 days. The *Swift*-XRT spectral index is used to calculate p, which is then applied to construct the spectrum above the peak frequency. A power law is fit to the radio data ($\beta_{\rm rad}$ = 0.9 ± 0.4), assuming that the peak of the spectrum is at/above the VLA band. The shaded regions reflect the 1σ uncertainties on the spectral indices. The spectrum shows that $\nu_{\rm C}$ is between $8{\times}10^{15}$ and $8{\times}10^{17}$ Hz and that the peak of the spectrum at 13±9 GHz. $F_{\nu,\,\rm max}$ is 130±30 μJy.

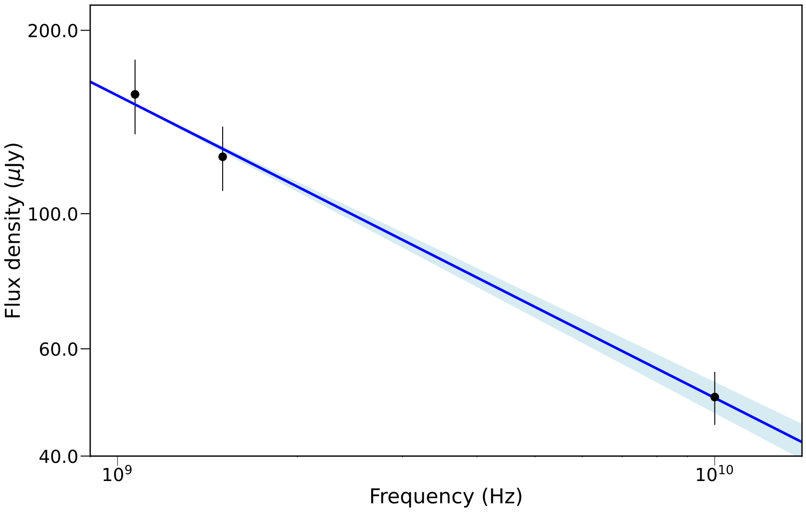

Figure 4.11: Radio spectrum from 0.9 to 12 GHz using observations from MeerKAT and VLA at ~54 days post burst.

der Horst et al., 2009). This classification is discussed further in section 4.4.4.

Figure 4.10 shows a 1.3 GHz to 10 keV broadband spectrum constructed between 20 and 24 days post burst. Around 20 days, $\beta_{10\,\mathrm{GHz\text{-}X}} = -0.6$, which differs from $\beta_X = -1.0 \pm 0.1$ at a 4σ level indicating that it is likely that ν_C is below the XRT band. Using the value of p (2.0±0.2) derived from the X-ray spectrum and constrain the location of the cooling break at 20 days is constrained to be between $8{\times}10^{15}$Hz < ν_C < $8{\times}10^{17}$Hz. The position of the peak of the spectrum and the corresponding flux density is 13±9 GHz and 130±30 μJy, respectively. The resulting broadband spectrum from around 20 days post burst can be well described with a series of three power laws, as shown in Figure 4.10: (1) a low frequency steep spectral component, (2) an optically thin branch where β=-0.5 between $\nu_\mathrm{peak} < \nu < \nu_\mathrm{C}$, and (3) the final branch above the cooling break where β=-1.0±0.1. The shaded regions denote the uncertainties (for the optically thin and cooling branches) or variations in possible spectral indices (low frequency optically thick branch).

At 54 days post burst, the broadband radio spectrum is best described by a single power law component (Figure 4.11) with a spectral index of $\beta_\mathrm{rad} = -0.50 \pm 0.02$, most likely from the optically thin branch of the spectrum below ν_C where p = 2.00±0.04. This means that by 54 days post burst the peak of the synchrotron spectrum is below 0.9 GHz.

4.4.4 GRB 201216C as a dark GRB

Early time optical observations either placed deep upper limits on any optical emission or obtained very faint detections of the afterglow with respect to the X-ray fluxes, see e.g. Figure 4.9. Furthermore, the optical spectrum observed by the VLT was very steep, which provided concrete evidence that GRB 201216C is a dark GRB (Vielfaure et al., 2020).

From the optical and X-ray light curves, as well as the broadband and optical spectra, I can infer that ν_C is between the optical and X-ray observing bands from 0.05 to ~1 day post burst. The final X-ray data point is now considered because it is a low significance detection. This information is used to place limits on the r'-band flux density if GRB 201216C was not heavily affected by extinction as described in Section 4.4.3. By comparing the inferred and measured optical flux densities, the extinction is estimated to be between 5.3 and 8.6 magnitudes (r'-band); values far in excess of the the galactic extinction contribution: $A_R = 0.12$ mag (E(B-V) = 0.05; Schlegel et al., 1998; Fitzpatrick, 1999).

Using the empirical relations between extinction and neutral hydrogen column density: $N_H \approx 2\times10^{21}$ cm$^{-2}A_V$, (Predehl & Schmitt, 1995; Güver & Özel, 2009), one can determine whether or not the line of sight hydrogen column density is consistent with the attenuated optical flux densities. For $N_H = 5.07\times10^{21}$ cm^{-2}, from X-ray spectra, $A_V \approx 3$ mag ($A_R \approx 2$ mag) given by the above relation. Therefore, an additional source of optical extinction is required. From the observed extinction range, N_H is 1-3$\times10^{22}$ cm^{-2}, obtained from the X-ray spectra, which is at least a factor of two higher than the measured N_H value.

Given that GRBs occur in regions of high star formation, increased dust in the vicinity of the GRB site is expected, so optically dark GRBs should not be uncommon (Fruchter et al., 2006). Studies of the host galaxies of dark GRBs have shown that the dust distribution is non-uniform, further agreeing with the previous statement that dark GRBs occur in highly obscured regions (Perley et al., 2009b). Giant molecular clouds could also be a contributing factor to increased amounts of dust in the vicinity of long GRBs, but would also result in higher measured N_H values (Solomon et al., 1987).

The fact that such a high N_H is not observed may also be a result of the A_V-N_H correlation varying from galaxy to galaxy, especially at high redshift ($z > 1$) where the star formation rate is much higher than in local galaxies. The above calculation assumes a universal A_V-N_H relation, and so is not necessarily correct for GRB 201216C's host galaxy. GRB 110709B's optical darkness was similarly under predicted by the measured hydrogen column density (Penacchioni et al., 2013; Zauderer et al., 2013). On the other hand, the optical extinction for many GRBs is *over* estimated, again implying a clear deviation from the Galactic and Magellanic Cloud relations (Perley et al., 2009b; Krühler et al., 2011).

Of the four other VHE GRBs detected so far, GRBs 190829A and 190114C have also shown increased optical extinction (Campana et al., 2021; Zhang et al., 2021). Zhang et al. (2021) measured an absorption *E(B-V)*=0.757 for GRB 190829A and Campana et al. (2021) obtained *E(B-V)*=0.83 for GRB 190114C (GRB 180720B requires *E(B-V)*=0.037. Such high extinctions in the most well studied VHE GRBs could suggest a potential connection between high density/dusty environments and the presence of VHE emission. Significant dust presence would imply strong infrared radiation fields which could be the source of the photons for an EIC explanation of the VHE spectral component. The optical light curve of the jetted tidal disruption event *Swift* J164449.3+573451: reduction in the optical emission was interpreted as inverse Compton up-scattering (Kumar et al., 2013). Dusty environments could result in strong infrared radiation fields following the reprocessing of optical emission. The infrared radiation could be up-scattered to VHE energies in the presence of electrons with sufficiently high Lorentz factors ($\gamma_e \sim 10^6$). I plan to continue to explore the idea in a future project searching for differences in the afterglows of long GRBs with and without VHE components.

4.4.5 Discussion

Single forward shock model

The most simple description of the multi-frequency data would be a single forward shock which is produced as the jet decelerates in the circumburst medium. Using the constraints on the positions of the break frequencies and the peak flux from the broadband spectra combined with well established analytical afterglow models (e.g. Granot & Sari, 2002), it is possible to determine if a single forward shock describes our data well.

In Section 4.4.3, the spectrum showed that the location of ν_C at 20 days post burst was between $8{\times}10^{15}$ and $8{\times}10^{17}$ Hz. Given that no statistically significant breaks are observed in the light curve before day 20, the X-ray emission, until day 20, must originate from above ν_C. For an X-ray decay of $\alpha_X = -1.9 \pm 0.2$, using the binning shown in Figure 4.6, p = 3.2±0.3, which is steeper than p derived from the X-ray spectra (2.0±0.4) at nearly

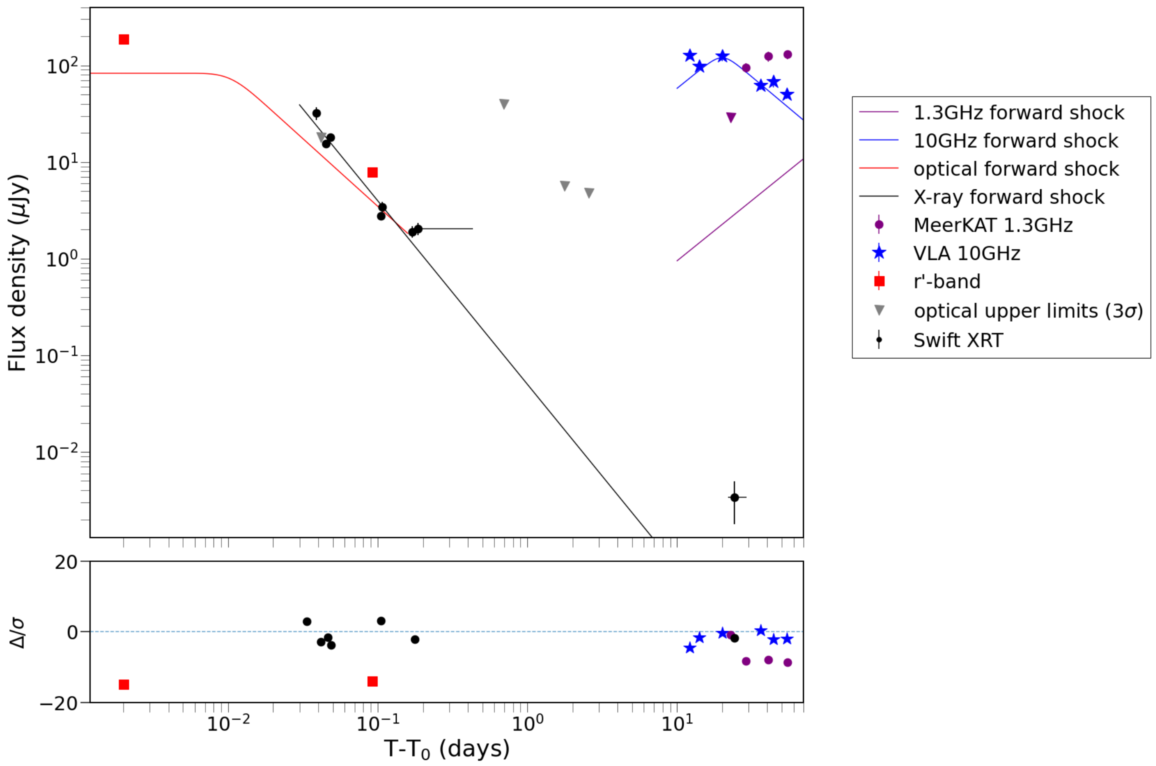

Figure 4.12: *Top panel:* X-ray, optical, 10 GHz and 1.3 GHz data for GRB 201216C. Overlaid is a simple single forward shock model. For the optical light curve, an optical extinction between 4.3-4.6 magnitudes is required, this is far outside the range of inferred extinction and so the light curve is modelled with an extinction of 5.3 magnitudes: the lowest value in our inferred range. *Bottom panel:* the normalised residuals, the ratio of 'Δ' (the difference between each observed flux density and the model at that time) to σ (the uncertainty on each measured flux density).

2σ. These p values are independent of the circumburst medium. Despite the light curve slope being same, the movement of ν_C changes depending on the environment. In a stellar wind environment $\nu_C \propto t^{\frac{1}{2}}$ and in a homogeneous medium $\nu_C \propto t^{-\frac{1}{2}}$. Given the inference that ν_C is only just below the XRT band at day 20; if the jet was propagating through a homogeneous environment, a break in the X-ray light curve due to ν_C would be expected at some time before day 20. Therefore, the XRT emission is most likely a result of a stellar-wind environment where ν_C moves from lower to higher frequencies with time, i.e. towards the XRT band.

The model X-ray light curve is shown as the black line in Figure 4.12. From either the X-ray light curve or spectra, it is impossible to determine the location of ν_C with respect to the 0.3-10 keV band. However, when combining the two with the broadband spectrum at 20 days, there is good evidence for a jet is propagating through a stellar wind environment. Figure 4.13 shows the movement of ν_C with time according to our stellar wind model (solid purple line). The shaded purple region around the line represents the uncertainty on the location of ν_C at a given time, derived from the broadband spectrum constructed around day 20 (Figure 4.10).

The intrinsic brightness of the optical emission is heavily absorbed, but it is likely that the decay rate ($t^{-0.83\pm0.01}$) observed is unaffected by the material causing the absorption. For a wind environment, such a decay is too shallow to be produced by optically thin synchrotron in which the r'-band is below ν_C. The decay, $\alpha_{\rm opt}$, should follow $-2.0 < \alpha_{\rm opt} < -1.3$, using an optically thin decay in a stellar wind environment for $2 < p < 3$. The shallower decay could be a result of $\nu_{\rm m}$ passing through the optical observing band within a few hours of the burst (as previously mentioned in Section 4.4.2). This is used to constrain the position of ν_m at early times as the purple dotted line in Figure 4.13. The red line in Figure 4.12 shows the model light curve for a forward shock where $\nu_{\rm m}$ causes the break around 0.01 days. The best fit to the optical data, requires ~5.3 magnitudes of optical extinction, the lowest value in the extinction range calculated in Section 4.4.4. Figure 4.12 shows that our forward shock

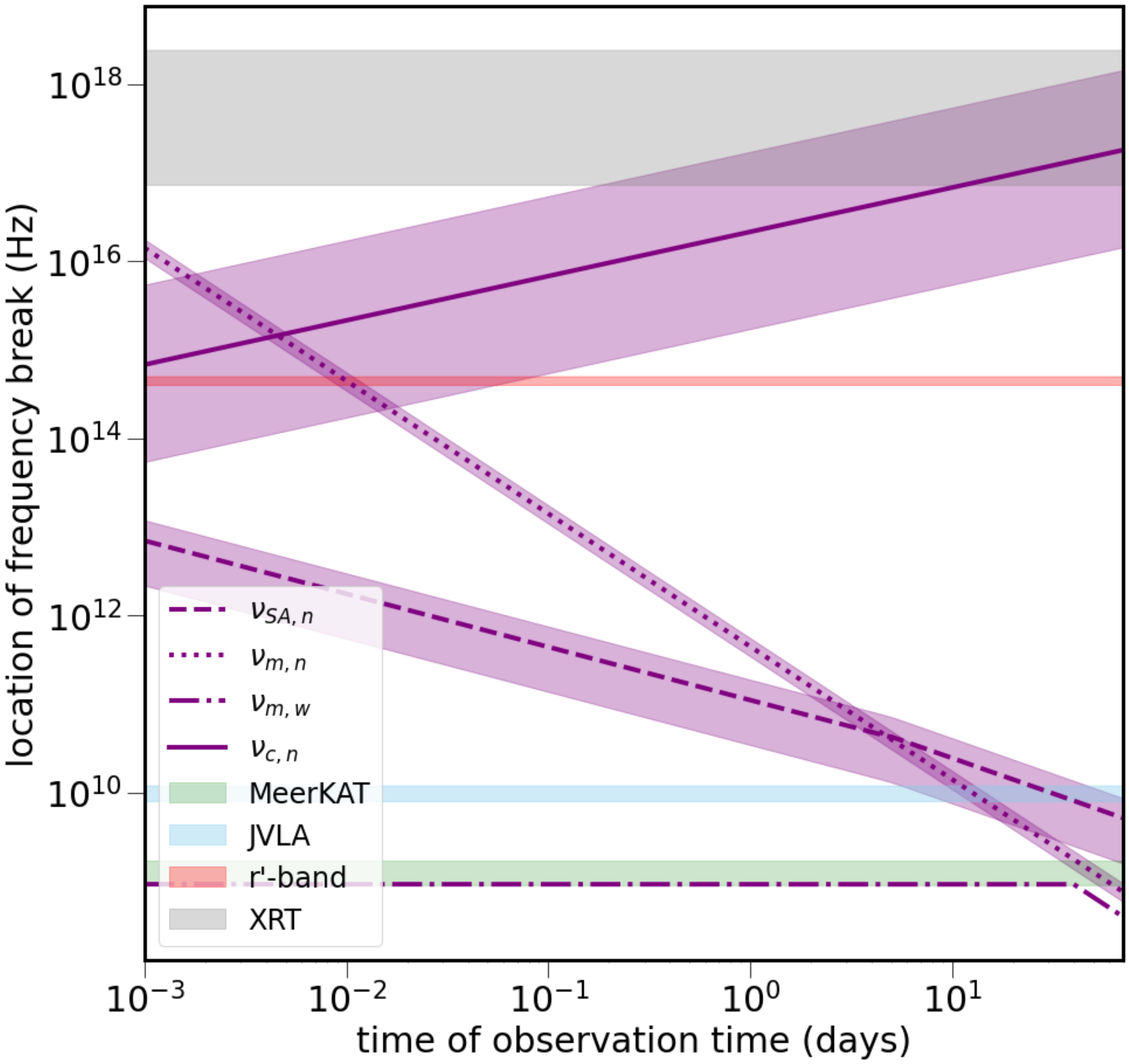

Figure 4.13: A plot showing the evolution of the break frequencies for both the narrow and wide components from Peng et al. (2005)'s two component afterglow model, adapted for a stellar-wind environment applied to the dataset. The purple dashed, dotted and solid region denotes the movement of ν_{SA}, ν_{m} and ν_{C} from the narrow jet, respectively. The dotted-dashed line shows the evolution of ν_{m} from the wide component viewed off-axis. The purple shaded regions denote the uncertainties in the location of each frequency break. Overlaid in green, blue, red and grey are the MeerKAT, VLA, optical and XRT observing bands, respectively.

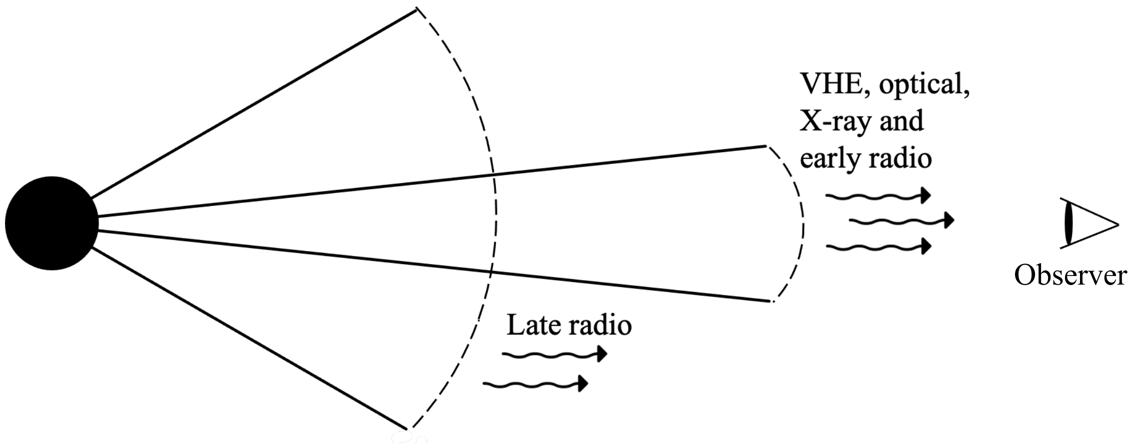

Figure 4.14: A schematic of the geometry of VHE GRB 201216C. The narrow core component is the origin of the VHE, optical, X-ray and early (< 25 days) radio data. The wider cocoon component produces the late-time radio emission.

model does not fit the optical data well.

The similar flux densities, to within an order of magnitude, are observed by both XRT before 0.1 days post burst and at the beginning of the VLA observing campaign. Figure 4.13 shows that the peak of the spectrum should be in the optical band around 0.01 days. Figure 4.12 shows that at 0.1 days, the most optical and X-ray flux densities are approximately the same. When the extinction calculated in Section 4.4.4 is considered, it is clear that $F_{\nu,\,\mathrm{max}}$ should be significantly higher at this time. The VLA observations, which start at day 20 and show flux densities similar to that measured by XRT 0.04 days post burst, show evidence of the spectral peak passing through the 10 GHz band, meaning that $F_{\nu,\,\mathrm{max}}$ must have decayed from 0.01 to 20 days post burst to show similar X-ray and radio flux densities. If an ISM environment is assumed $F_{\nu,\,\mathrm{max}}$ would be constant with time and would not describe the data at all. Instead, this can be attributed to either a jet break or a stellar-wind environment. A jet break can cause $F_{\nu,\,\mathrm{max}}$ to decay rapidly as a result of the jet expanding laterally ($F_{\nu,\,\mathrm{max}} \propto t^{-1}$, Sari et al., 1999b). A stellar wind environment means that $F_{\nu,\,\mathrm{max}}$ will decay with time as $F_{\nu,\,\mathrm{max}} \propto t^{-0.5}$ when $\nu_\mathrm{m} > \nu_\mathrm{SA}$, and $F_{\nu,\,\mathrm{max}} \propto t^{-\frac{4p+1}{2(p+4)}}$ ($t^{-(0.75-0.93)}$ for 2<p<3) when $\nu_\mathrm{SA} > \nu_\mathrm{m}$ (Granot & Sari, 2002).

The VLA in-band spectral indices of the first three observations are steep (see Table

4.3). Such values further imply that the peak of the synchrotron spectrum is above 12 GHz until at least 20 days post burst (see the upper panel of Figure 4.10). As explained in Section 4.4.2, if the peak of the spectrum was caused by $\nu_{\rm m}$ the expected spectral index is $\beta = 1/3$. The steepness of the spectral indices implies that either $\nu_{\rm SA}$ and $\nu_{\rm m}$ or just $\nu_{\rm SA}$ must be above the VLA observing band. The third VLA epoch is more consistent with a flat spectrum, i.e. $\beta = 1/3$ or the peak of the spectrum being at the observing frequency. Combined with the decaying flux density of the final three epochs, the peak of the synchrotron spectrum must have passed through the 8-12 GHz band between 20 and 36 days post burst. The most simple scenario for the decay is if only one spectral break is above the VLA band, which moves towards lower frequencies with time, causing the emission above the break to decay with time. In the regime where $\nu_{\rm m} < \nu_{\rm SA}$, $\nu_{\rm SA} \propto t^{-\frac{3(p+2)}{2(p+4)}}$ ($t^{-(1.0-1.1)}$ for 2<p<3, Granot & Sari, 2002), and so the peak is caused by ν_{SA}.

At 10 GHz, the forward shock model would show a broken power law, with a rise following $t^{\frac{5}{4}}$ to a peak around day 20 followed by a decay of $\alpha_{10\,\rm GHz} = \frac{(1-3p)}{4}$ ($t^{-(1.3-2.0)}$ for $2 < p < 3$) as $\nu_{\rm SA}$ moves through the observing band (Granot & Sari, 2002). The theoretical 10 GHz light curve is shown (where p = 2.0) with the blue line in Figure 4.12. The optically thick to thin transition provides a reasonable fit to the 10 GHz light curve. Please note that the variability due to weak scintillation increases the residuals as shown in the lower panel of Figure 4.12.

Figure 4.11 shows that by 54 days post burst, the 1.3 and 10 GHz light curves are on the same, optically thin branch, of the synchrotron spectrum, with p = 2.00±0.05. The MeerKAT in-band spectral index is also similar at day 41 post burst indicating that by 41 days post burst, 1.3 GHz is above $\nu_{\rm SA}$ and $\nu_{\rm m}$. In order for $\nu_{\rm SA}$ to be below the MeerKAT band at 41 days post burst, $\nu_{\rm SA} \propto t^{-3.5}$, which is significantly faster than the theoretical movement where for $p \approx 2$, $\nu_{\rm SA} \propto t^{-\frac{3(p+2)}{2(p+4)}} = t^{-0.8}$ (Granot & Sari, 2002). The measured $\nu_{\rm SA}$ movement is unphysical when compared to analytical models.

The unphysical movement for $\nu_{\rm SA}$ complicates the 1.3 GHz model light curve. Using

$\nu_{\mathrm{SA}} \propto t^{-0.8}$, the model light curve would consist of a single power law component with $\alpha_{1.3\,\mathrm{GHz}} = \frac{5}{4}$. The light curve would turn over at 200 days as a result of ν_{SA} entering the observing band if ν_{SA} moved as given in Granot & Sari (2002). During the rise, a spectral index $\beta_{1.3\,\mathrm{GHz}} = \frac{5}{2}$ is expected, not ~-1 as measured. Furthermore, the peak flux density, according to the single shock model would continue to decay as $\mathrm{F}_{\nu,\,\mathrm{max}} \propto t^{-\frac{4p+1}{2(p+4)}} = t^{-0.75}$ for p = 2, so by the time ν_{SA} (the peak of the spectrum) reaches the MeerKAT band, $\mathrm{F}_{\nu,\,\mathrm{max}} \approx 20\,\mu$Jy, which is a factor of 7 fainter than the observed 1.3 GHz flux density. When compared to the MeerKAT data points (purple circles and downwards facing triangle), the 1.3 GHz model light curve (the purple line) in Figure 4.12 show a clear deviation away from the forward shock model. At all times, the model light curve falls far below the observed data. Even if the unphysical movement of ν_{SA} is used, $\mathrm{F}_{\nu,\,\mathrm{max}}$ still decays with time meaning that the modelled 1.3 GHz light curve is predicted to be much fainter than the observed emission.

The late-time change in the evolution of $\mathrm{F}_{\nu,\,\mathrm{max}}$ and ν_{SA} could be a result of a change in the circumburst environment. A varying circumburst density distribution, i.e. a deviation from $\rho \propto r^{-2}$, where ρ and r are the density and radius for the burst site, could occur as a result of the progenitor star having fluctuating mass loss rates towards the end of its life. In order to reproduce the observations, the circumburst environment must change from $\rho \propto r^{-2}$ to $\rho \propto r^{0}$: an homogeneous environment. Such a change seems unlikely to reflect the mass loss history of the progenitor. Furthermore, this cannot explain the MeerKAT light curve or the discrepancy in p derived from the X-ray light curve and spectra.

In conclusion, Figure 4.12 shows the results of a single forward shock component model overlaid on the X-ray, optical, 10 GHz and 1.3 GHz light curves. The *e*-MERLIN 5 GHz data points are not used in the model as they are heavily affected by DISS. The bottom panel of Figure 4.12 shows the normalised residual values for the forward shock model with respect to the data. The X-ray and VLA light curves are reproduced reasonably well. The inter-observation variability increases the residuals of the VLA data with respect to the model. However, it is clear from the large residuals for optical and MeerKAT light curves that a single forward shock model is not a good fit. In a single shock scenario, any variation in $F_{\nu,\,\mathrm{max}}$ is expected to be dictated by the movement of ν_{SA} and ν_{m}. I acknowledge that the understanding of how $F_{\nu,\,\mathrm{max}}$ evolves with time early on is poorly constrained because of the faint optical emission. By inferring the range of optical flux densities from the X-ray data, it is clear that a steeper $F_{\nu,\,\mathrm{max}}$ decay than the afterglow models provide is required (Granot & Sari, 2002). On the other hand, by the time the radio campaign begins, $F_{\nu,\,\mathrm{max}}$ appears to be constant in time. The rapid decay of $F_{\nu,\,\mathrm{max}}$ until day ~20 followed by a transition to a constant $F_{\nu,\,\mathrm{max}}$ for the rest of the observing campaign is too complex to be attributed to a single jet component.

Multiple shock component model

It is possible that the discrepancies the light curves could be explained with the addition of an extra shock component. Unfortunately, the light curves in any one observing band are too sparse to search for reverse shock emission. For example, optically thin reverse shock emission decays far steeper than the optical light curve. It must be noted that two data points are not constraining enough to fully eliminate the possibility of reverse shock contribution. Unfortunately, because the first data point from *e*-MERLIN at 5 days post burst is dominated by RISS, it is not possible to know the intrinsic flux density value at this time and so cannot determine if there is any reverse shock contribution. The full 5 GHz flux density in the absence of RISS (double/half the observed flux density assuming order of unity variability) is not constraining enough to confirm or reject the presence of reverse shock emission.

The MeerKAT and VLA bands are less affected by ISS and therefore are more appropriate to search for reverse shock emission. I applied a similar methodology to that in Rhodes et al. (2020) in order to determine whether the reverse shock makes a significant contribution to the 1.3 GHz light curve despite not being detectable at 10 GHz. If the reverse shock has faded at 10 GHz by 12 days post burst, then by 29 days, whilst the peak of the reverse shock might be in the MeerKAT observing band, $F_{\nu,\,\mathrm{max}}$ corresponding to the reverse shock will be significantly fainter than the observed MeerKAT flux densities at this time. The strongest evidence against reverse shock emission in the MeerKAT band is that the sharp rise between 22 and 29 days post burst, inconsistent with the reverse shock scenario.

An additional forward shock component could instead explain the large residuals between the data and the single shock model for the later observations at 1.3 GHz. In order to determine whether an additional forward shock could explain the discrepancies found in Section 4.4.5, I used the two component jet model presented in Peng et al. (2005) adapted for a stellar wind environment (Chevalier & Li, 1999) to better interpret the GRB 201216C data, similar to that applied to GRB 130427A by Van der Horst et al. (2014). Structured jets encompass a broad range of geometries and multiple jet components have been invoked in previous GRB afterglow data sets (e.g. Resmi et al., 2005; Racusin et al., 2008). The afterglow from gravitational wave event GW 170817 was inferred to have an ultra-relativistic core surrounded by lower velocity wings (Margutti et al., 2018). In GRB 080319B, the presence of two distinct outflow components was inferred, but the wider component was still more collimated than what inferred for the narrow jet of GRB 201216C (Racusin et al., 2008). The presence of a wider component is strongly supported by simulations (e.g. Morsony et al., 2007), although observations of such a component span a broad range of energetics and opening angles.

To interpret the afterglow emission, the model consider a narrow, ultra-relativistic jet launched at a Lorentz factor, $\Gamma_{0,n} > 100$, like with the single shock scenario, but with the addition of a wider outflow with $\Gamma_{w,0} \sim 10$ (the subscripts n and w refer to *narrow* and *wide*, respectively). It is possible for the wider outflow to be non-relativistic, but I find that a relativistic outflow is more likely given the high luminosity and light curve behaviour. The possibility of supernovae emission can be ruled as the origin of the late time radio detections: the radio luminosities are an order of magnitude higher than the next most

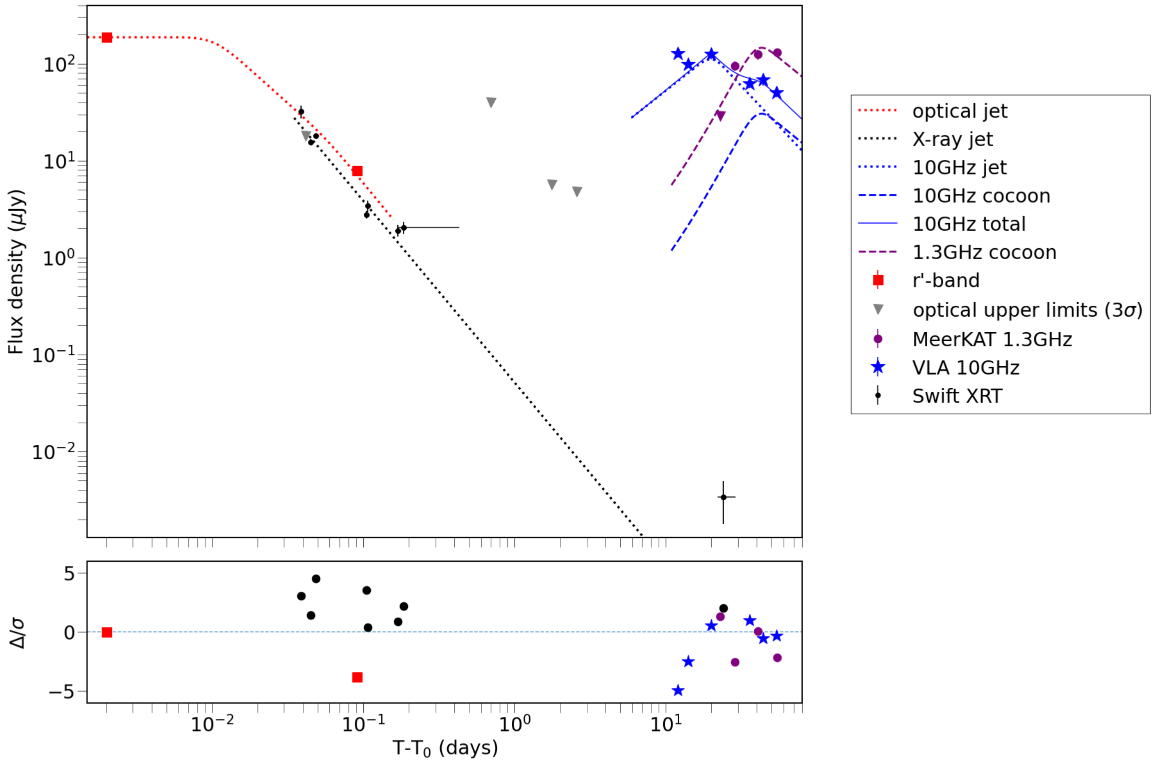

Figure 4.15: *Top panel*: X-ray, optical and radio data. Overlaid are the model light curves corresponding to the two jet component scenario. In this scenario, a range of optical extinction between 7.4-8.0 magnitudes is required. *Bottom panel*: the normalised residuals, the ratio of 'Δ' (the difference between each observed flux density and the model at that time) to σ (the uncertainty on each measured flux density).

luminous type Ib/c broad-line supernova (Bietenholz et al., 2021).

Each component is uniform within some opening angle $\theta_{j,n}$, $\theta_{j,w}$. The two components do not interact with each other. In the event of a jet break, only consider edge effects are considered, not lateral spreading. An on-axis observer would see that the narrow jet dominates at early times. The wider component becomes visible only in systems with favourable geometries and energetics. Figure 4.14 shows the geometry of such a system, which undergoes a jet break early on (~0.05 days) allowing the wider outflow to be visible later on.

Multiple shock component: Narrow jet

In Section 4.4.5, it was noted that the evolution of $F_{\nu,\,\mathrm{max}}$ is inconsistent with a single forward shock. A steep decay of $F_{\nu,\mathrm{max}}$ can be explained along with the X-ray light curve if the narrow component undergoes a jet break before the first X-ray data points at around 0.05 days post burst. As with the single jet scenario, the X-ray light curve follows a single power law decay. For a jet break scenario in a wind environment, $p = 2.2\pm0.2$, which agrees with p from the X-ray spectra ($p = 2.0\pm0.4$) at a 1σ level, slightly better than in the single shock scenario where $p = 3.2\pm0.4$ (Section 4.4.2).

Figures 4.9 and 4.13 show that at two hours post burst: $3 \lesssim F_{\nu,\,\mathrm{max}} \lesssim 15$ mJy. By 20 days, $F_{\nu,\,\mathrm{max}} = 0.13\pm0.03$ mJy (Figure 4.10). The best explanation of the steep decay of $F_{\nu,\mathrm{max}}$ is a combination of the jet break and the wind environment. The combination creates a steeper decay of $F_{\nu,\,\mathrm{max}}$ compared to a stellar wind-only decay as used in the single shock scenario. The steepening of the light curves due to a jet break is a correction factor of 0.75 (Panaitescu et al., 1998). Once the optical extinction is considered, the inferred optical flux density from the model can be matched with observed optical flux densities. I use the spectral evolution to explain the optical detections here as in Section 4.4.5: ν_m passing through the band resulting in an apparent flattening of the optical light curve. The dotted red line in Figure 4.15 shows a broken power law where the break is a result of ν_m passing through the band, in addition to the jet break at 0.05 days. The optical emission is best fit with an extinction range between of 7.4-8.0 magnitudes which is within the extinction range inferred from the X-ray observations (5.3-8.6 magnitudes). For the multiple component jet model, a larger extinction value is required to fit the optical light curve well because at earlier times $F_{\nu,\mathrm{max}}$ is brightest compared to the single shock model. The lower panel of Figure 4.15 shows that this optical model fits the data significantly better, compared to in Figure 4.12 where in order to get the best fit the assumed extinction was outside the inferred range.

In terms of the radio data, the narrow jet dominates the early VLA light curve. The narrow jet contribution to the measured 10 GHz emission is shown with the blue dashed line in Figure 4.15. The 10 GHz narrow component light curve follows a sharp rise, $\alpha_{10\,\mathrm{GHz}} = \frac{5}{4}$, followed by a decay as $\alpha_{10\,\mathrm{GHz}} = -\frac{3p}{4} = -1.7$ for p = 2.2. After the peak, the 10 GHz emission decays rapidly giving way to a wider component. Both the rise and the decay are steeper than in the single shock scenario because by the first VLA epoch the narrow jet component has already undergone a jet break. The first two VLA spectra show that the narrow component is self-absorbed. Therefore, the 1.3 GHz narrow jet would peak at around 2μJy, and therefore the 1.3 GHz contribution to the narrow component is not shown.

Despite GRB 201216C having a VHE counterpart, the modelling of the afterglow considers only synchrotron emission. Unfortunately, it is not possible to model the SSC emission for GRB 201216C given the sparse sampling in the X-ray energy range and the lack of public VHE data. However, the low value of ϵ_B derived from the afterglow modelling of the narrow jet implies that the narrow jet is in a regime where SSC cooling dominates over synchrotron cooling at least at early times when there is a high fraction of electron energy lost due to radiation (Sari & Esin, 2001). In future studies, I plan to use new tools such as detailed modelling code by Jacovich et al. (2021) which consider SSC cooling.

The optical light curve, VLA in-band spectral indices and broadband spectrum at 20 days, allow us to constrain the locations of ν_{SA}, ν_{m} and ν_{C} for the narrow jet. Combining analytical models for the movement of the frequency breaks (Figure 4.13) along with the decay of $\mathrm{F}_{\nu,\,\mathrm{max}}$, and extract physical parameters from this dataset: $\mathrm{E}_{\mathrm{K,ISO,n}}$, A_*, ϵ_{e} and ϵ_{B} (assuming p=2.2 from the X-ray data). These ranges of derived values for those paramters are given in Table 4.4. A jet break at 0.05 days corresponds to an opening angle of ~1-9° (Chevalier & Li, 2000).

The stellar wind environment inferred from this data set is characterised by the parameter A_*. Chevalier & Li (1999) relates A_* to the density profile $\rho = Ar^{-2}$ where A = $\dot{M}/4\pi v_w$ = $5\times10^{11}\mathrm{A}_*$ g cm^{-1}. If v_w = 1000 km s^{-1}, the progenitor mass loss rate ($\dot{\mathrm{M}}$) of (0.6-

Parameter	Narrow	Wide
$E_{ISO,K}$ (erg)	$(0.6\text{-}10)\times10^{52}$	$(0.02\text{-}50)\times10^{48}$
A_*	0.6-200	0.6-200
ϵ_e	0.04-0.1	0.1
ϵ_B	5×10^{-8} - 4×10^{-3}	0.01
p	2.0-2.4	2.0
θ_j	1-9°	-

Table 4.4: The physical parameters extracted from the GRB 201216C dataset using Peng et al. (2005)'s two component model. For the wider outflow, there is reduced coverage and therefore I assume the same range of values for A_* and use fiducial values of $\epsilon_e = 0.1$ and $\epsilon_B = 0.01$.

200)$\times10^{-5}M_\odot$/yr. Winds of massive stars are heavily dependent on metallicity and GRBs are expected to occur in low metallicity environments. If the metallicity is too high, the mass loss rate would also be too high resulting an increased loss of angular momentum which inhibits the formation of the GRB. Furthermore, the stellar wind is expected to have a non-spherical distribution with the majority of the material concentrated around the equator. Therefore, at the poles, a less distinct stellar wind profile is expected compared to an equatorial view. The inferred range of mass loss rate for GRB 201216C from the two component model is within the range of expected values (Vink & De Koter, 2005; Aguilera-Dena et al., 2018).

The $\dot{M}$ range derived from the afterglow modelling can be used to infer limits on the progenitor mass (Langer, 1989; Tramper et al., 2016; Yoon, 2017). The upper end of the $\dot{M}$ range is pushing the boundaries for the progenitor to be a Wolf-Rayet star, independent of metallicity. Low metallicities alongside with high stellar masses would be required to begin to reach such high mass losses, combined with inciting gravity waves (Fuller & Ro, 2018) or if the star is reaching the Eddington luminosity (Langer et al., 1994). At the lower end of the inferred $\dot{M}$ range, the progenitor could be a Wolf-Rayet star of $10\dot{M}_\odot$ at solar metallicity or even 20-25 $M_\odot$ at sub-solar metallicity. Since GRBs tend to occur in low metallicity environments, the progenitor mass is likely to be between 12-25 $M_\odot$.

Multiple shock component: Wider outflow

The decay of the narrow component allows the wider outflow to be detected. The wider outflow is the origin of the observed 1.3 GHz emission: the MeerKAT light curve shows a sharp rise from 22 days, best described as emission from such a second jet component. Using the behaviour of ν_{m} and $\mathrm{F}_{\nu,\,\mathrm{max}}$ for off-axis jets in a stellar wind environment (Peng et al., 2005; Chevalier & Li, 1999), the time at which the outflow comes into the observers line of sight (t_{on}) can be constrained from both the light curve and the spectra. For $\mathrm{t} < \mathrm{t}_{\mathrm{on}}$, $\nu_{\mathrm{m}} \propto t^{0}$, and for $\mathrm{t} > \mathrm{t}_{\mathrm{on}}$, $\nu_{\mathrm{m}} \propto t^{-\frac{3}{2}}$. The dotted-dashed purple line at the bottom of Figure 4.13 shows the movement of ν_{m} in the wide jet component. Comparison of the spectral index measurements between day 28 ($\beta_{1.3\,GHz} > -0.3$) and 41 ($\beta_{1.3\,GHz} = -1.1 \pm 0.6$, see also Figure 4.11) shows that there is some movement of ν_{m} between the two epochs. Therefore t_{on} must occur before day 41. The deceleration time can be further constrained by looking at the evolution of $\mathrm{F}_{\nu,\,\mathrm{max}}$: for $\mathrm{t} < \mathrm{t}_{\mathrm{on}}$, $\mathrm{F}_{\nu,\,\mathrm{max}} \propto t^{3}$, for $\mathrm{t} > \mathrm{t}_{\mathrm{on}}$, $\mathrm{F}_{\nu,\,\mathrm{max}} \propto t^{-\frac{1}{2}}$, meaning t_{on} occurs around ~40 days (Peng et al., 2005).

The later epochs do not have such broadband coverage and as a result the same detailed modelling is not applied as presented in section 4.4.5. By assuming the same range of A_{*} as for the narrow component and assuming that ϵ_{e} and ϵ_{B} are 0.1 and 0.01, respectively. $\mathrm{E}_{\mathrm{K,\,ISO,\,w}}$ in the wider outflow is calculated to be $(0.02\text{-}50)\times10^{48}$erg. These values are also summarised in Table 4.4. The isotropic equivalent kinetic energy present in the wide outflow is two and seven orders of magnitude lower than in the narrow component for the same stellar wind profile. It should be noted that the inferred range of kinetic energies for the cocoon is dependent on the assumed values of ϵ_{e} and ϵ_{B}. With the assumed microphysical parameters, the kinetic energy of the cocoon can be considered as mildly to non-relativistic when compared to other radio transients, similar to radio-detected supernovae (e.g. figure 5 of Coppejans et al., 2020). However the rapid rise and high luminosity are inconsistent with type Ib/c supernovae (those associated with long GRBs) and so the outflow is more likely to be mildly relativistic.

Figure 4.15 shows the wide jet contribution to the 1.3 GHz and 10 GHz light curves as the purple and blue dashed lines, respectively. The total 10 GHz model from both jet components is the solid blue line. The wide component of the jet is expected to make some contribution of the total X-ray flux observed by XRT at the time of our final observation which would make the model closer to the observed flux density. The contribution of wide jet component to the total X-ray flux is unknown because the location of ν_C with respect to the XRT observing band is also unknown.

In comparison to the single shock scenario, the normalised residual values are much lower denoting a better fit (shown in the lower panel of Figure 4.15). There are still some increased residual values early on in the 10 GHz light curve, although this may be due to weak interstellar scintillation which cannot be modelled. A much wider outflow makes for a much better fit to the MeerKAT light curve as well as the later VLA data points. I can better quantify whether the more complex, multiple jet component model is a better fit compared to the single forward shock model by performing an F-test. The single jet model has four parameters and the two component model has only one additional free parameter originating from the wider component, the kinetic energy. The results show that the more complex model is favoured at greater than 4σ significance.

4.5 Comparison with other GRBs

With five VHE GRBs, the community is beginning to be able to consider the population as a whole. Here, I compare the radio data for the three GRBs in two ways: examining the measured flux values at different bands and comparing the luminosities to a sensitivity-limited selection of the GRB population.

4.5.1 Radio light curves of the VHE GRBs

Figure 4.16 shows a comparison between H.E.S.S. GRBs 190829A and 180720B, and MAGIC GRBs 190114C, 202015A and 201216C. The upper panel shows the low frequency light curves for all five VHE GRBs (MAGIC Collaboration et al., 2019b; Monageng et al., 2021). The lower panel shows high frequency data for all events except 201015A (the GRB 190114C fluxes have not been host galaxy-corrected, Tremou et al., 2019).

The low frequency light curves all rise both a rise and decay with the exception of 201216C, which, as shown in Section 4.4, originates from a cocoon and not the jet. The comparative similarities in the low frequency light curves for the remaining four events show that, despite the broad range of parameters that can be inferred from the afterglows they still show a similar evolution.

The higher frequency light curves all show a decay with some inter-epoch variability overlaid. The variability may arise from scintillation (Granot & Van der Horst, 2014). Only GRB 190829A shows a reverse shock component, the afterglows from the four other events consider only forward shock emission.

4.5.2 Energetics and environment

The isotropic equivalent kinetic energy of the VHE GRBs spans at least four orders of magnitude from $\sim 5\times10^{50}$ to $\sim 4\times10^{54}$ erg (Fraija et al., 2019). Such a broad range of kinetic energies have also been inferred in large samples of long GRBs without GRB observations from either multi-wavelength modelling or the X-ray light curves (Zaninoni et al., 2016; Aksulu et al., 2022). The environments derived from the afterglow observations of the events presented in this Chapter are more varied then the energetics. The observations of GRB 201216C appear consistent with a very high density stellar wind environment so dense it is bordering on unphysical. At the other end of the scale, the environment I infer from GRB 190829A is so diffuse that it is lower than the average ISM environment. It is not always possible to detect evidence of a stellar wind environment. This could be a result of the non-spherical nature of the wind, or the GRB progenitor being in a binary system and therefore the stellar winds of both stars would result in a relatively constant density profile, or if the observing campaign does not last long enough to infer the effects of the decrease in density due to the stellar wind profile. As a result a homogeneous environment may be a better fit to observations instead. An alternative explanation could be that variations in $\dot{\mathrm{M}}$ at the end of the progenitor's life mass change the inferred density profile significantly.

From the energetics and environments, there appear to be no differences between GRBs with and without VHE detections. In order to be more confident in the previous statement, the afterglow parameters derived from the VHE component need to be compared to those from the synchrotron afterglow to determine at what point the synchrotron-only models are no longer appropriate in our modelling.

4.5.3 Comparison to a flux-limited sample

I have also compared the spectral radio luminosities of the three GRBs with each other and a sensitivity-limited, redshift-selected ($z < 1.5$) sample of radio detected GRB population using the AMI-LA GRB catalogue (Anderson et al., 2018; Bright et al., 2019; Rhodes et al., 2021a). The luminosities are calculated using $L = 4\pi F_\nu D_L^2 (z+1)^{\alpha-\beta-1}$ where F_ν is the measured flux, D_L is the luminosity distance, α and β are the temporal and spectral indices, set to 0 and $\frac{1}{3}$, respectively, according to Chandra & Frail (2012). Figure 4.17 shows a direct comparison of the radio luminosity light curves between the VHE GRBs and the AMI-LA GRB catalogue.

The radio luminosities of GRBs 190829A and 201015A are two orders of magnitude lower than the two other VHE GRBs. Alone, they could lead one to believe that VHE GRBs are less luminous than their non-VHE counterparts. However, GRB 190829A and 201015A are approximately the same luminosity as GRB 200826A and GRB 130702A (Rhodes et al., 2021a). There is no evidence in the literature if these events were targets for IACTs and so it is impossible to know if they would have had detectable VHE emission. The luminosities for GRBs 180720B, 190114C and 201216C sits firmly within the bulk of the GRB sample. As a population, there appears to be no difference in the radio luminosities between the VHE and non-VHE GRBs. Despite the range of luminosities of the VHE GRBs in Figure 4.17, none stand out with respect to this sensitivity limited sample of radio detected GRBs.

I have shown that in terms of the radio luminosities, in the same way as the energetics, VHE GRBs with radio detections are very to other GRBs with observed radio afterglows. As a result, one may expect more VHE counterparts to have been detected for events at z = 1.5 and below, and those where an IACT could be on source within minutes. There are GRBs, with z<1.5, that show no evidence of VHE counterparts, such as GRB 100621A (H. E. S. S. Collaboration et al., 2014). In the same way that no all GRBs have detectable radio counterparts, it may be possible that the range of luminosities of GRBs at VHE energies are such that IACT observations are sensitivity limited and so many VHE counterparts are undetectable with the current instrumentation.

4.6 Conclusions

In this chapter, I have presented detailed results on VHE GRBs 180720B, 190829A and 201216C. From nearly 200 days of radio and X-ray observations of H.E.S.S. GRB 190829A, MeerKAT 1.3 GHz and *Swift*-XRT light curves appear to be dominated by forward shock emission while the AMI-LA data at 15.5 GHz originates from a reverse shock up to at least 50 days. I have shown that neither shock component significantly contributes to the light curve at the other radio frequency. In addition to emission from the GRB, the host galaxy is also detectable in both bands, at 1.3 GHz the galaxy spatially resolved from the GRB position and at 15.5 GHz the host galaxy dominated the light curve after 70 days post-burst. Applying a standard fireball model to the data, it can be concluded that the circumburst medium is homogeneous. Assuming fiducial values for the fraction of energy in the electrons (0.1), the density of the homogeneous environment was inferred to be

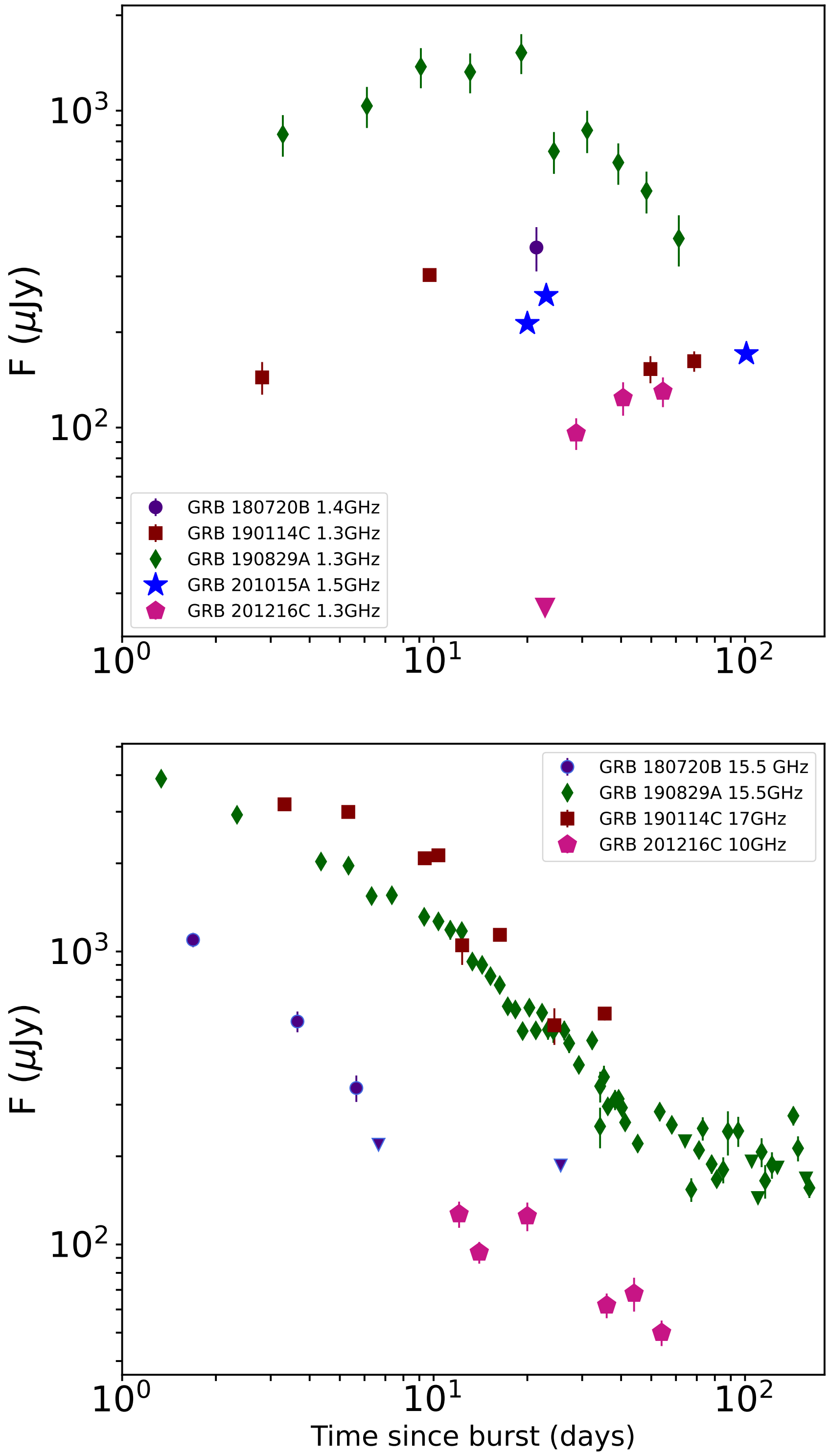

Figure 4.16: High and low frequency light curves from the MAGIC GRBs 190114C, 201015A and 201216C, and H.E.S.S. GRBs 180720B and GRB 190829A. *Upper panel*: shows the low frequencies (~1 GHz) light curves for all five VHE GRBs (Chandra et al., 2018; Misra et al., 2021). *Lower panel*: shows the high frequency light curves for VHE GRB 1908720B, 190114C, 190829A and 201216C (Fraija et al., 2019).

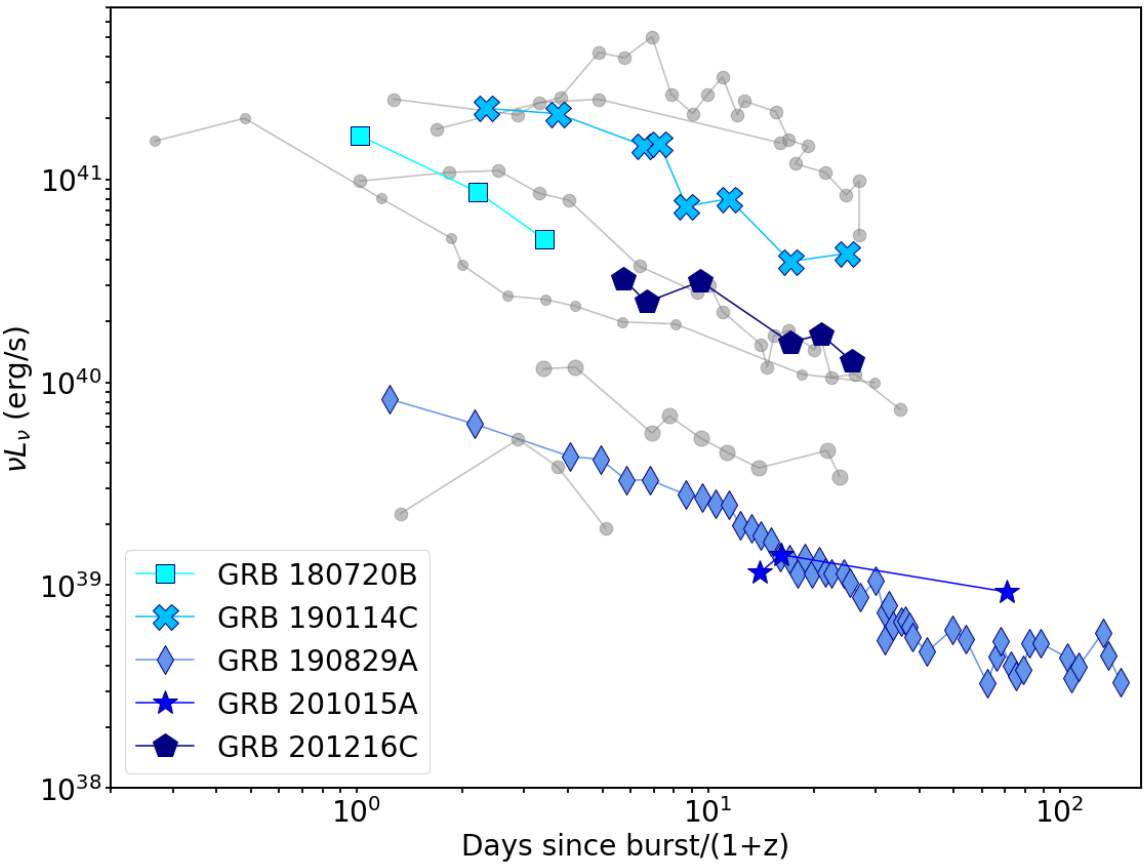

Figure 4.17: Comparison of data from all five VHE GRBs with a sample of the GRB population as detected by AMI-LA and e-MERLIN (below z<1.5, Anderson et al., 2018; Bright et al., 2019; Fraija et al., 2019; Rhodes et al., 2021a). The GRBs from the AMI-LA catalogue are given as grey circles. The VHE GRBs are the blue symbols with navy edges.

very low: (1-3)$\times10^{-5}$ cm^{-2}. The isotropic kinetic energy of the burst is also low around (5-8)$\times10^{50}$erg, of which a fraction: (5-9)$\times10^{-4}$ is given to the magnetic fields. The lack of jet break in the MeerKAT light curve allows a constraint to be placed on the opening angle of the jet: given the inferred density and energy the opening angle should be greater than 9°.

I have also presented previously unpublished AMI-LA observations of GRB 180720B, the first GRB with a VHE detection. The VHE counterpart was not made public at the time of the detection and so this event does not have the dedicated counterpart that the follow up campaigns like with the other events. From the limited data, I was able to infer that the observed emission is from a forward shock propagating into a homogeneous environment.

Finally, I have presented multi-wavelength observations of the fifth VHE GRB. Spectra of the host galaxy confirmed GRB 201216C to be the highest redshift VHE GRB so far ($z = 1.1$), close to the theoretical distance limit beyond which pair-production due to the EBL would prevent the detection of any VHE photons. The faint early optical detections defined this event as a dark GRB where I show that the optical emission is attenuated by at least 5 magnitudes. Such attenuation is at least two magnitudes greater than that derived from galactic A_V-N_H relations. Such high extinction could be due to a high dust density in the vicinity of the long GRB, for instance if the stellar progenitor did not travel far from its formation site in the centre of a giant molecular cloud. It could also be a result of inverse Compton up-scattering of optical photons to VHE. At radio frequencies, I obtained MeerKAT (1.3 GHz), *e*-MERLIN (5 GHz) and VLA (10 GHz) observations covering 5 to 55 days after the burst. The *e*-MERLIN epochs show evidence of DISS up to 29 days post-burst corresponding to an upper limit on the emitting size region of $<1\times10^{17}$ cm (Goodman, 1997).

The best interpretation of the data uses a jet-cocoon geometry where the earlier emission is dominated by a narrow ultra-relativistic jet which undergoes a jet break at 0.1 days. The later time emission is dominated by a wide-angled, slower moving outflow: a cocoon. The additional component allows for fixing the problems regarding the rapid decay of $F_{\nu,\,\mathrm{max}}$ early on, produced by the jet break, and then the flattening occurs as the radio observations are now viewing the cocoon as a separate synchrotron component. The cocoon also addresses the unphysical movement of ν_{SA}. The jet-cocoon scenario shows the afterglow to be moving through a stellar wind environment of a density similar to that modelled for massive stellar-winds with energies of $(0.6\text{-}10)\times10^{52}$ and $(0.02\text{-}50)\times10^{48}$ erg for the jet and cocoon respectively. The opening angle of the ultra-relativistic jet is between $1-9^{\circ}$. Deeper, more late-time observations are required moving forward in order to better understand and constrain cocoon emission in long GRB events.

Comparison of the radio luminosity light curves of the give VHE GRBs and a sample of long GRBs without detected VHE emission or observations show no significant differences. This is consistent with the VHE GRBs being drawn from the same parent population as the other radio-detected long GRBs. Despite this, the range of environments and jet energetics inferred are varied and span orders of magnitude.

The VHE GRBs are an excellent dataset to test the limits of afterglow models. Combined with the increased sensitivity of the new generation of radio interferometers, I have shown it is possible to detect new emission components and begin to explore the possibility of different origins of the VHE emission.

Chapter 5

Radio monitoring of Neutron Star X-ray Binary *Swift* J1858.6-0814

The work in this chapter is based on the paper Rhodes et al. (2022b).

5.1 Introduction

Approximately half of all stars are thought to be born in binary systems (Duchêne & Kraus, 2013). In a very small fraction of binaries, on of the stars will be of high enough mass that it undergoes supernova leaving a black hole or neutron star behind. If the binary system is not disrupted, this leaves a compact object and main sequence star orbiting each other, allowing the main sequence star to evolve. As the low mass star evolves, it begins to fill its Roche Lobe. Both objects in the binary have their own gravitational potentials that connect at the inner Lagrange point (L1). Inside the Roche lobe, the material is still gravitationally bound to the star. Material from the star can pass through L1 via Roche lobe overflow so that is then within gravitational potential of the compact object. Low mass X-ray binaries (XRBs) are systems which contain a low mass star and a compact object - either a neutron star or stellar mass black hole - orbiting each other.

Material is transferred onto the compact object via an accretion disc. The disc is approximated to be optically thick and geometrically thin (Shakura & Sunyaev, 1973; Novikov & Thorne, 1973). The material orbits the compact object in approximately circular paths, in order for it in the disc to move inwards towards the compact object angular moment moves outwards. Emission from the disc can be approximuated as a multi-temperature black-body (e.g. Mitsuda et al., 1984).

On long timescales, the accretion rate onto the compact object remains fairly constant. Hydrogen ionisation instabilities within the disc can cause an increase in the accretion rate, and therefore X-ray luminosity, and the system goes into an 'outburst' (Narayan & Yi, 1995; Lasota, 2001). In general, black hole XRBs in outburst follow a similar evolution: a q-shaped path on a hardness-intensity diagram (HID, Figure 5.1). An HID is a plot of X-ray hardness (ratio of hard X-ray colour to soft X-ray colour) against X-ray flux.

Whilst in quiescence (position *a* in Figure 5.1), the X-ray colour is very hard, i.e. a relatively high hard X-ray photon count. As the outburst begins, the X-ray flux increases whilst the colour remains hard. During this time the system is said to be in the *hard state* and the X-ray spectrum is characterised by a power law called the photon index (Γ, position *b* in Figure 5.1). The hard X-ray emission is thought to be produced by inverse Compton scattering of disc photons to higher energies by a corona. The exact nature/geometry of the corona is unknown but in some popular models, it is described as a geometrically thick inner disc region or the base of a jet (Galeev et al., 1979; Miyamoto & Kitamoto, 1991; Fender et al., 1999a).

As well as X-ray emission, during the hard state there is also significant non-thermal radio emission. The radio flux is usually steady and has an optically thick/flat spectrum ($S_\nu \propto \nu^\alpha$ where $\alpha \geq 0$, Fender, 2001; Migliari et al., 2003). This emission is most consistent with a canonical jet (see Figure 1.5 in Chapter 1), where the flat spectrum arises from a superposition of many optically thick spectra from different emission regions resulting in different peak frequencies. The radio emission is thought to be a result of the accretion process launching compact steady jets (Fender et al., 2004a). The black circles in Figure

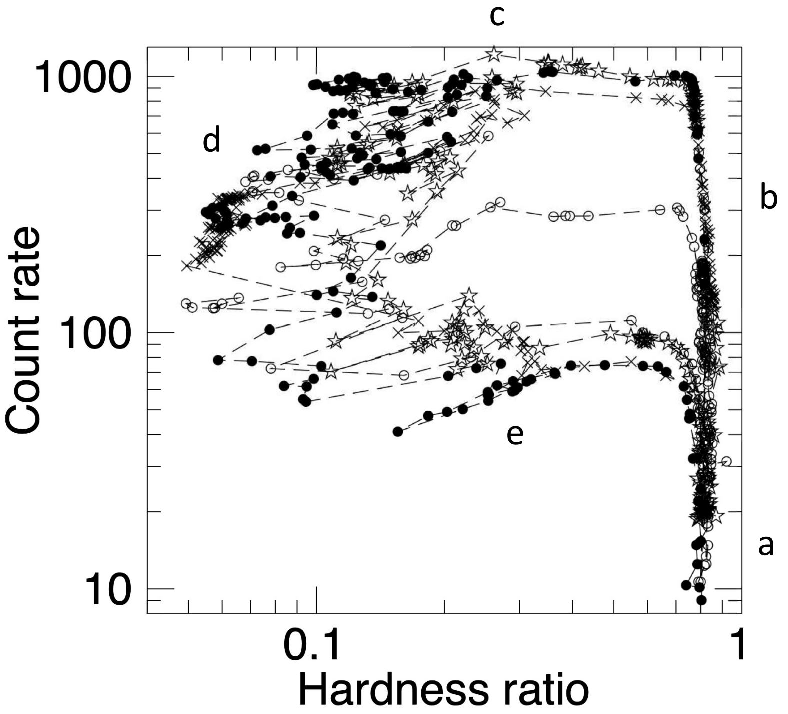

Figure 5.1: An example of a hardness intensity diagram from Belloni & Motta (2016) for black hole low mass XRB GX 339-4. Black hole XRBs follow the q-shaped path around in the HID in an anti-clockwise direction (a -> b -> c -> d -> e). Higher hardness values correspond to the system being in the hardness with a compact radio jet is present. Lower hardness values (the left hand side of the figure) correspond to the soft state with the jet is quenched.

5.3 show the radio and X-ray luminosities of hard state black hole XRBs.

As the outburst evolves, the mass accretion rate, and consequent X-ray flux, increase so the XRB transitions from the hard state to the *soft state*. In doing so it passes through the *intermediate state*. During the intermediate state, the radio emission shows sharp, bright flares. This is thought to be due to the ejection of plasmoids or blobs of relativistic ejecta that propagate into the surrounding ISM. Such ejections have been observed in several black hole XRB systems (e.g. Mirabel & Rodríguez, 1994; Hjellming & Rupen, 1995; Miller-Jones et al., 2012; Belloni & Motta, 2016).

The soft state is a higher luminosity (accretion rate) state (position *d* in Figure 5.1). Here, the X-ray spectrum is dominated by soft photons produced by the disc of some black body temperature (parameterised by k_BT). The power law component from the corona is no longer present. In the soft state, radio emission in black hole XRBs is quenched by at least 3.5 orders of magnitude (Fender et al., 1999b; Russell et al., 2011, 2019; Carotenuto et al., 2021; Bright et al., 2020).

Before returning to quiescence, the XRB transitions back to the hard state at a lower flux density (position *e* in Figure 5.1), following a hysteresis pattern (Fender et al., 2009; Belloni & Motta, 2016, for a recent review). Outbursts can last between days and months.

5.1.1 Neutron star X-ray binaries

All low mass neutron star XRBs are thought to have low magnetic fields ($\sim 10^9$ G, e.g. Degenaar et al., 2016; Ludlam et al., 2019). Based on their X-ray properties, they fall into two separate classes: Atoll and Z sources (Figure 5.2). Studies of XTE J1701-462 have shown that the apparent separation is a result in changes in mass accretion rate (Homan et al., 2010). The unusual young neutron star XRB circinus X-1 also shows intermittent periods of Z source behaviour (Shirey et al., 1999).

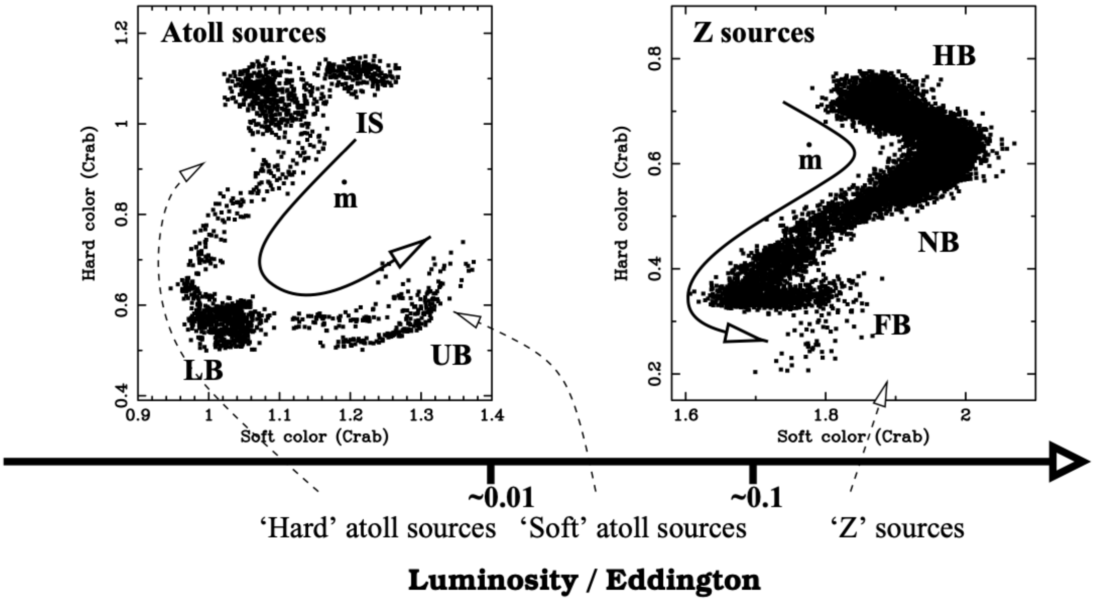

Figure 5.2: An example of hard vs soft colour plots for an Atoll (left) and Z (right) source from Migliari & Fender (2006). Also labelled are the inferred directions of increasing mass accretion rate ($\dot{m}$) and the direction of increasing Eddington luminosity.

Atoll sources

Atoll sources share some characteristics with black hole XRBs: they have similar X-ray spectra and timing properties (Van der Klis, 1994; Remillard & McClintock, 2006; Muñoz-Darias et al., 2014). The X-ray states are often referred to as the island and banana states (IS, and LB/UB in the left hand panel of Figure 5.2), instead of the hard and soft states, respectively. The names originate from the paths they track on the colour-colour diagram (a plot to study the apparent X-ray colour of XRB by comparing the number of counts in harder and softer X-ray bands - Figure 5.2 e.g. Van der Klis, 1989). In all states, neutron star XRB spectra may also contain an additional component originating from the neutron star's surface (Mazzola et al., 2021).

Radio emission from atoll systems is far less luminous than from black hole XRBs (Gallo et al., 2018). In a similar manner to black hole XRBs, steady radio emission is detected during the hard state and variable, flaring emission may be observed during state transitions (Migliari et al., 2003). A sample of hard state neutron stars are shown as blue squares in

Figure 5.3. Whilst in the soft state, it appears that neutron star XRBs have a more complex jet quenching process. Some systems have shown clear evidence of strong quenching e.g. Aquila X-1 and 1RXS J180408.9-342058 (Miller-Jones et al., 2010; Gusinskaia et al., 2017, respectively). Instead, 4U 1820 - 30 shows lower levels of reduction in radio flux density and change in spectral index consistent with a quenching of the compact jet and possible launch of transient ejecta (Migliari et al., 2004; Russell et al., 2021).

Z sources

Z sources evolve through sequences of different accretion states much faster. They traverse their colour-colour diagram in hours-days (the right hand panel of Figure 5.2), thought to be caused by variations in mass transfer rate, which is usually near the Eddington limit (Hasinger & Van der Klis, 1989). There is some evidence of a correlation between radio flux density and X-ray hardness, similar to black hole XRBs (Penninx et al., 1988). Z sources are more radio- and X-ray-luminous than atoll sources (purple crosses in Figure 5.3). Both the X-ray and radio emission varies rapidly along with transient ejections (e.g. Fomalont et al., 2001; Fender et al., 2004b).

5.1.2 Radio-X-ray correlation

Multiple XRB systems have shown a non-linear correlation between the radio and X-ray flux whilst in the hard state (Corbel et al., 2000, 2003; Gallo et al., 2003). Figure 5.3 shows an example of the radio-X-ray correlation by Bahramian et al. (2018). The black dotted line in Figure 5.3 shows the correlation for black hole XRBs $L_{\text{radio}} \propto L_{\text{X-ray}}{}^{\sim 0.6}$ (where $L_{\text{X-ray}}$ and L_{radio} are the X-ray and radio luminosities, respectively). For neutron star systems the relationship appears to be correlated differently $L_{\text{radio}} \propto L_{\text{X-ray}}{}^{\sim 0.4}$ (Gallo et al., 2018). However, there are hints that the neutron star correlation will end up being the same to that for black holes (Deller et al., 2015). The correlation between the luminosities in the two bands suggests a connection between the accretion flow and the compact jets. There is a

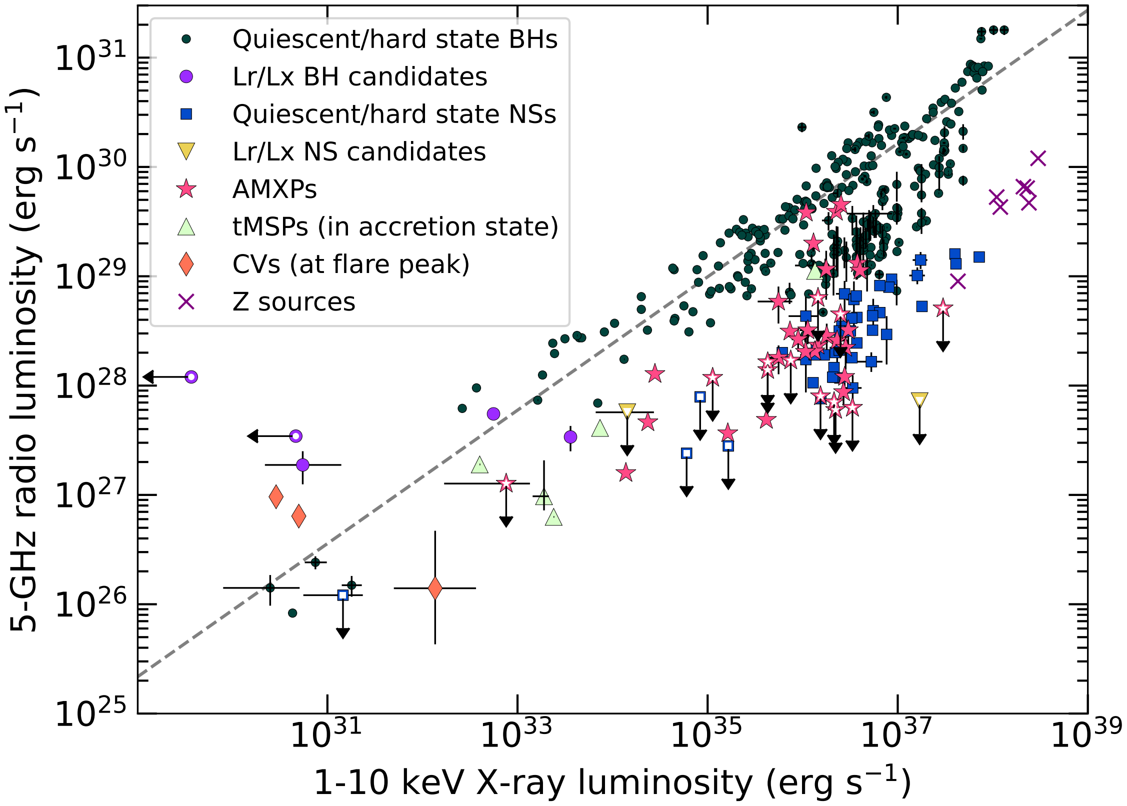

Figure 5.3: From Bahramian et al. (2018), an compilation of radio and X-ray luminosities of hard state (or equivalent) black hole and neutron star XRBs, CVs, among other accreting variables.

sub-sample of black hole XRBs which fall below the dotted line. The track along which these lower radio luminosity systems evolve is referred to as the radio quiet branch (e.g. Corbel et al., 2004). The separation of the main track and the radio-quiet track are not statistically significant.

The radio-X-ray correlation shows that different accreting systems occupy different areas of luminosity parameter space (Figure 5.3). This allows one to tentatively classify an unknown accretor based on its radio and X-ray luminosity. For a given X-ray luminosity, atoll sources are about a factor of 27 times radio less luminous than black holes (Gallo et al., 2018). On the other hand, Z sources are about an order of magnitude more X-ray luminous than the most luminous black hole XRBs for a given radio luminosity. Cataclysmic variables are the least radio- and X-ray-luminous sources in a similar region of space to quiescent black hole XRBs (e.g. Hewitt et al., 2020).

5.1.3 Swift J1858.6-0814

Swift J1858.6-0814 (hereafter J1858) is a newly discovered XRB that was first reported as going into outburst by the Neil Gehrels *Swift* Observatory (hereafter *Swift*) - Burst Alert Telescope (BAT) on MJD 58416 (2018 October 25) (Krimm et al., 2018). The reported position was RA: 18h 58m 34.96s, dec: -08d 14' 16.4" with an uncertainty of 2.2 arcseconds (Kennea & Krimm, 2018).

A number of multi-wavelength monitoring campaigns of this outburst have been conducted, including radio (presented in this work), optical (Saikia et al., 2020) and X-ray (Van den Eijnden et al., 2020; Buisson et al., 2021). All sky X-ray monitors also observed this source (Matsuoka et al., 2009; Krimm et al., 2013)[1][2]. There have also been many targeted, short term studies which provide in-depth, short timescale information on J1858. For the first ~18 months of the outburst, there were reports of J1858's X-ray spectra being

---

[1] https://swift.gsfc.nasa.gov/results/transients/weak/SWIFTJ1858.6-0814/

[2] http://maxi.riken.jp/top/lc.html

best fit with a power law, indicative of the source being in the hard/extreme island state. However the power law index of the individual spectra varied between 0.22 and 2.2 (Kennea & Krimm, 2018; Bozzo et al., 2018). There was also evidence of strong variability and soft flares on timescales of 10-100 seconds along with variable absorption centred around $N_H = 2 \times 10^{21} cm^{-2}$ (Ludlam et al., 2018; Hare et al., 2020). Despite the fact that a power law was the best spectral fit on many occasions, the varied behaviour has made it hard to conclusively say that J1858 was in the hard state, unlike many other black hole/ atoll XRBs (Hare et al., 2020).

Buisson et al. (2020b) reported that J1858 had made a state transition to the soft state from at least MJD 58897 (after ~18 months in a hard state) evidenced by a significantly brighter soft X-ray flux with NICER (MJD 58897). Shorter, more details studies of J1858 with NICER and NuSTAR were performed after the state change. Firstly, they determined that the compact object is a neutron star via the detection of Type I X-ray bursts (Buisson et al., 2020c). The subclass of type I X-ray bursts observed from J1858 are thought to be evidence of photospheric radius expansion occurring when the X-ray flux observed corresponds to the Eddington luminosity. As a result these events can be considered to be standard candles (Tawara et al., 1984; Lewin et al., 1984). The distance calculated from the detection of Type I X-ray bursts is $12.8^{+0.7}_{-0.6}$kpc, Buisson et al. (2020a) notes that the distance is metallicity and inclination dependent where a higher hydrogen mass fraction and inclinations favours lower distances. Secondly, NICER detected the presence of X-ray eclipses allowing for the calculation of the orbital period (~0.83 days) as well as implying that J1858 has a high inclination (>75°, Buisson et al., 2021). Such a high inclination could impact observing the inner regions of the accretion disc, which would explain the increased and highly variable absorption that has been observed (Hare et al., 2020).

Even with a state change, they report that the increased soft X-ray flux is not enough to conclude that J1858 has definitely transitioned into a canonical soft state. It may be that J1858 follows the established hard/soft state evolution as seen in other atoll systems

(Muñoz-Darias et al., 2014), but the obscuration and variability observed at X-ray energies makes it difficult to conclusively determine J1858's long term X-ray state evolution.

Optical variability has also been observed (Paice et al., 2018) in addition to detections of optical P-Cygni profiles, a signature ascribed to out-flowing material (Muñoz-Darias et al., 2019). Combining the optical and X-ray observations has led to comparisons to V404 Cygni and V4641 Sgr, which showed similar variability and absorption features (Buisson et al., 2020a; Muñoz-Darias et al., 2020). Van den Eijnden et al. (2020) also observed minute-timescale radio variability with the Karl G Jansky Very Large Array (VLA) and the Australia Telescope Compact Array (ATCA). In conjunction with multi-wavelength observations of J1858, the ThunderKAT collaboration, of which I am part of, commenced a long term radio monitoring campaign with with the Arcminute Microkelvin Imager - Large Array (AMI-LA) and MeerKAT. Observations commenced on MJD 58424 and MJD 58432 with AMI-LA and MeerKAT, respectively. The initial radio detection with AMI-LA was reported in Bright et al. (2018b).

In order to relate the radio and X-ray behaviour throughout the rest of the paper, I refer to the period between MJD 58416 and 58897 as the 'hard state' and between MJD 58897 and 58928 as the 'soft state' (Buisson et al., 2020b). After MJD 58928, J1858 transitioned into quiescence (Saikia et al., 2020).

In Section 5.2, I describe the observations and data reduction process for both the AMI-LA and MeerKAT as part of the ThunderKAT Large Survey Project (Fender et al., 2016). I combined this with *Swift*-BAT data taken as part of the hard X-ray transient monitoring program (Krimm et al., 2013). In Section 5.3, I present the results of the observing campaign and in Section 5.4, I place J1858 in the context of other neutron star XRBs.

5.2 Observations and Data Analysis

5.2.1 Arcminute Microkelvin Imager - Large Array

Observations of J1858 started with the Arcminute Microkelvin Imager (AMI-LA) on MJD 58424 (2018 November 2) for 2 hours (8 days after the outburst began). The observations were made at 15.5 GHz with a bandwidth of 5 GHz, binned to 8 channels (Zwart et al., 2008; Hickish et al., 2018). All AMI-LA data were reduced using a custom pipeline: REDUCE_DC, which flags the data, performs a primary calibration (using 3C 286), and applies phase corrections, using J1846−0651 as a secondary calibrator (Perrott et al., 2013). J1846−0651 was observed for 60-90 seconds every 10 minutes. The data were cleaned and imaged in CASA (Version 4.7.0 McMullin et al., 2007b).

In the initial 2 hour observation, J1858 was detected with a flux density of 310±50 μJy. In the first week, five observations were made. Following that, J1858 was observed once every one to two weeks for the rest of the outburst; 59 observations in total over 18 months.

The colour map in Figure 5.4 shows the central region of the AMI field. The source labelled *1* is J1858. There is an additional, steady, ~200 μJy source within 70" of the phase centre, labelled *2*.

Some images of J1858 made with AMI-LA had an elliptical beam as a result of the source's equatorial declination. The elliptical beam produced issues in some epochs where the position angle of the AMI-LA clean beam is such that both source *1* and *2* were unresolvable. In three of the epochs where J1858 and the second source were unresolvable, a point source model was generated and performed a *uv*-subtraction in CASA, using the task *uv-sub*, to subtract emission due to the secondary source (assuming a flux density of 200μJy). The resulting flux density measurements of J1858 are denoted by unfilled black circles in Figure 5.5 and 5.6. Even after *uv*-subtraction, there may be some contamination from the secondary source, if the secondary source is variable, hence the brighter than average flux densities in these epochs. Please note that it was not possible to successfully perform *uv*-subtraction for all epochs where the J1858 and source *2* were unresolved. For these observations I have provided upper limits. AMI-LA observations ceased March 2020 due to the COVID-19 pandemic, the final epoch was on MJD 58924. Table C.1 gives a full list of all observing dates, durations, the flux density measurements and upper limits from the AMI-LA observing run.

5.2.2 MeerKAT

Monitoring of J1858 with MeerKAT was performed as part of the large survey project ThunderKAT (Fender et al., 2016). Weekly observations of J1858 with MeerKAT commenced on the MJD 58432 (2018 November 10), 16 days after the outburst was initially reported) and ceased on MJD 58488 (2019 January 5).

Weekly monitoring restarted on MJD 58530 (2019 February 16), as J1858 was no longer sun constrained and new optical observations showed that the source was still in outburst, and continued until MJD 58632 (May 25) (Rajwade et al., 2019). Regular monitoring stopped after another series of three non-detections. Two further, isolated observations were made: the first (MJD 58700) was part of a multi-wavelength campaign (Castro Segura et al., 2022), the second was after a report of an X-ray state change (MJD ~58900, Negoro et al., 2020; Buisson et al., 2020c).

The MeerKAT observations were made at a central frequency of 1.28 GHz with a bandwidth of 856 MHz split into 4096 channels. Each observation consisted of 10 minutes observing the bandpass and flux calibrator, PKS B1934−638 (J1939−6342), 2 minutes observing the phase calibrator, PKS J1911−2006, both before and after J1858, combined with 15 minutes on J1858. Reduction of the MeerKAT data was performed using a set of python scripts, `OxKAT`, allowing for semi-automatic processing (Heywood, 2020). Persistent RFI was removed from the calibrator fields before performing bandpass calibration and flux density scaling using J1939−6342. The complex gains were solved for on both J1939−634 and J1911−2006 and applied to the target field, which was flagged using TRICOLOUR[3]. Imaging was performed with WSCLEAN (Version 2.5, Offringa et al., 2014), using a Briggs weighting with a robust parameter of -0.7. A single round of phase-only self calibration was performed after which the target field was re-imaged.

The contours in Figure 5.4 show the central region of the MeerKAT J1858 field. Compared to the AMI field, the sources labelled *1* and *2* in Figure 5.4 are clearly resolved in MeerKAT image. Table C.2 shows a full list of the observation made with MeerKAT, the flux density and uncertainty for each epoch.

5.2.3 *Swift*-BAT

Swift-BAT first triggered on the outburst of J1858 on MJD 58416 (Krimm et al., 2018). The first public data point is 6 days later, on MJD 58422. BAT tracked the X-ray emission from J1858 between 15 and 50 keV, until MJD 58935 when the source returned to quiescence (Saikia et al., 2020). The third panel in Figures 5.5 and 5.8 shows the X-ray light curve from the *Swift*-BAT hard transient monitoring program. The flux levels for J1858 are very faint, therefore, only the epochs in which the detection is at 3σ significance or higher is plotted. The significance of the detection is calculated by assuming that the flux uncertainty is representative of the rms noise. A 3σ detection would be at least as bright as three times the uncertainty on the detection.

In order to compare J1858 to other hard state XRBs, I converted the 15-50 keV count rate to a 1-10 keV luminosity. First, the 15-50 keV flux is extrapolated to a 1-10 keV unabsorbed flux using a range of photon indices (Γ) within `WebPIMMS`[4]. The use of 15-50 keV count rates is discussed further in Section 5.4. Two Γ values are used: 1.4 and 2.2 (Kennea & Krimm, 2018; Bozzo et al., 2018). X-ray spectra of J1858 have been fit with a broader range of Γ, between 0.22 and 2.2 however anything below 1.4 becomes nonphysical due

---

[3] https://github.com/ska-sa/tricolour

[4] https://heasarc.gsfc.nasa.gov/cgi−bin/Tools/w3pimms/w3pimms.pl

to the nature of the Comptonization of soft photons from the disc (Done et al., 2007). It should be noted that the unabsorbed flux is used because at low energies the X-ray photons are susceptible to absorption or scattering. Therefore, a better estimate of the accretion is gained by extrapolating from higher X-ray energies. From there, the unabsorbed fluxes were converted to luminosities which are used in Figure 5.9.

5.2.4 MAXI/GSC

To monitor the soft X-ray emission from J1858, I used the data between 4 and 10 keV from the Monitor of All-sky X-ray Image mission (MAXI/GSC, Matsuoka et al., 2009). The daily count rate is shown in the bottom panel of Figure 5.5 and 5.8.

To compare the radio and X-ray luminosities of J1858 during the 'soft' and 'hard' states, I also converted the average 4-10 keV count rate to a 1-10 keV luminosity for the period where there is a significant increase in soft X-ray flux using a black body temperature of 2.0 keV (Buisson et al., 2020b). The same N_H value that was used to convert the BAT count rates was used here to calculate the unabsorbed fluxes as well. Both the BAT and MAXI/GSC converted luminosities are used in Figure 5.9. It should be noted that both the MAXI/GSC and BAT luminosities are subject to increased uncertainties due to variable N_H measured throughout the outburst.

5.3 Results

5.3.1 Radio Light Curves

The upper panel of Figure 5.5 shows the MeerKAT 1.3 GHz (grey circles) and AMI-LA 15.5 GHz (black circles) light curves from MJD 58424 to 58924 (November 2018 to March 2020). The errorbars associated with the AMI-LA and MeerKAT data points are calculated by adding the fitting error and calibration error in quadrature. A 5 and 10 per cent calibration

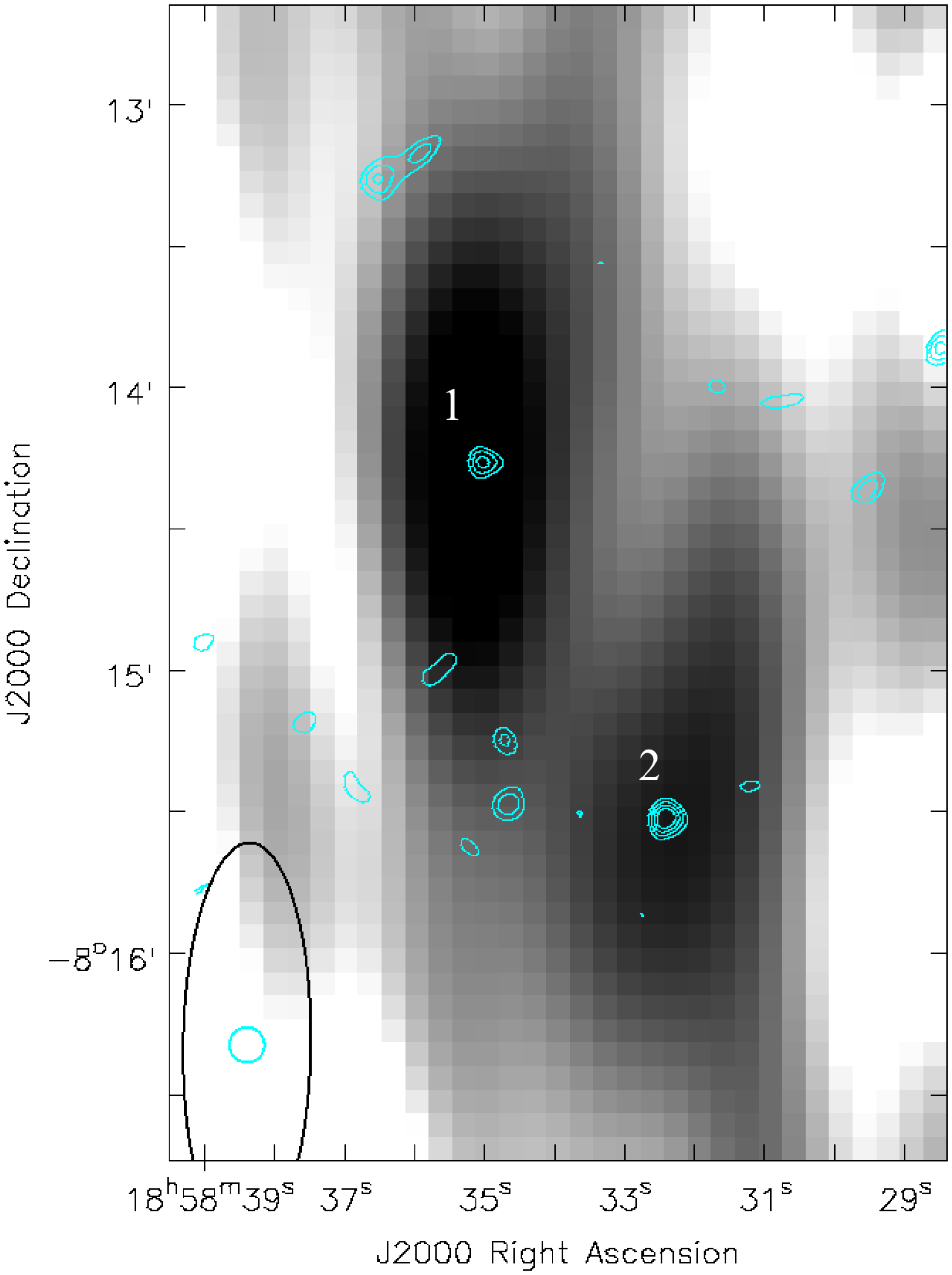

Figure 5.4: The J1858 field at radio frequencies. The background colour map shows an AMI observation in which J1858 and the south-west source are separated. At some epochs, the synthesised beam position angle resulted in J1858 (source 1) and source 2 being blended in the image. The cyan contours show an example of the MeerKAT field. The contours are at 3, 4, 5 and 6 sigma times an rms noise of 22μJy. The source labelled (1) is J1858, also labelled is the second source (2) which has created issues in some AMI observations.

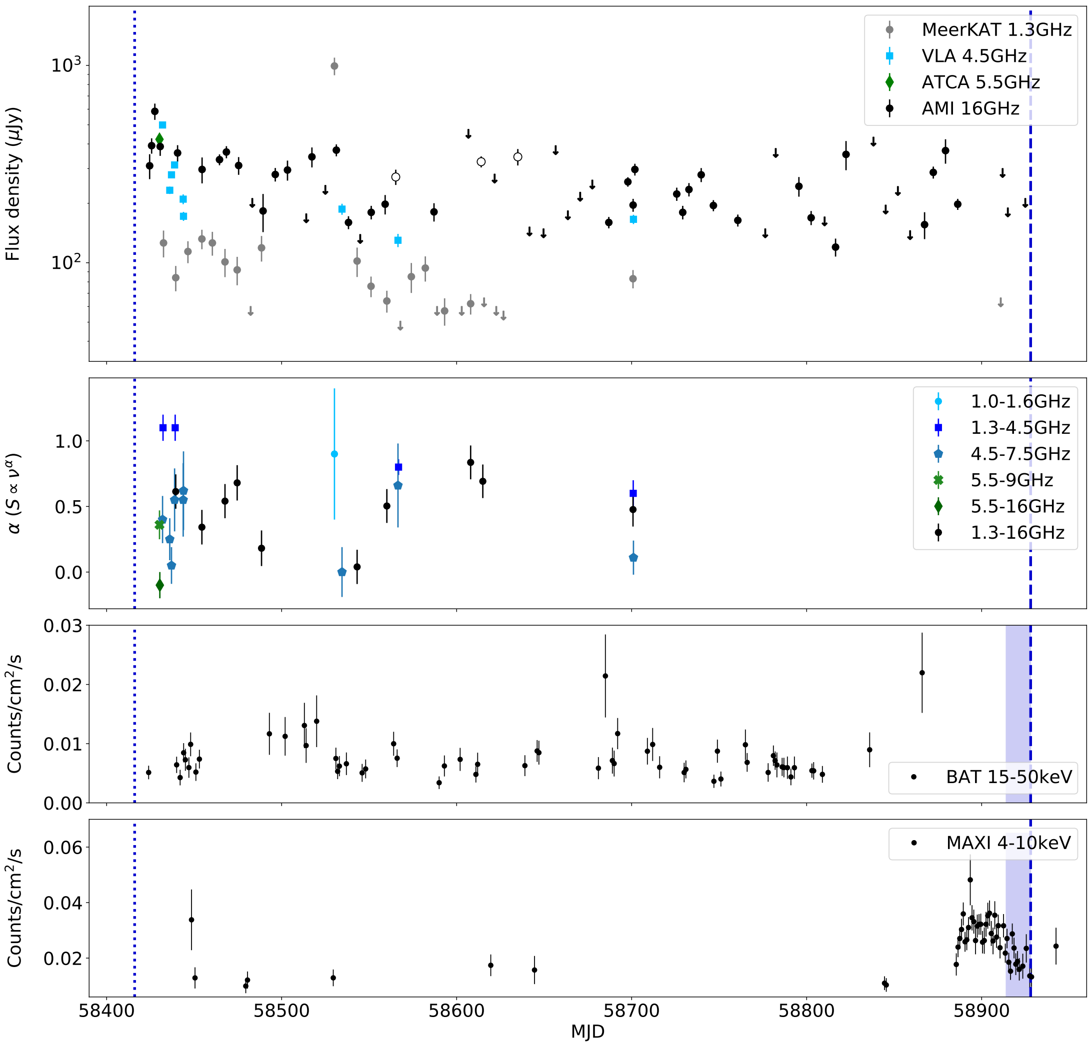

Figure 5.5: Caption on the following page.

Figure 5.5: The upper panel of this plot shows the light curve for all AMI-LA and MeerKAT radio observations. MeerKAT detections are denoted by grey circles and AMI detections are black circles. There are three AMI detections denoted with black unfilled circles denoting epochs where uv-subtraction was performed to remove emission from a contaminating source as described in 5.2.1. Three sigma upper limits are marked with downwards facing triangles in black and grey for MeerKAT and AMI-LA respectively. The light blue squares and green diamonds are the VLA and ATCA data points from Van den Eijnden et al. (2020). The second panel shows the spectral indices for all quasi-simultaneous observations. Quasi-simultaneous observations are defined where the observations in the two bands are within 24 hours of each other. I only calculated spectral indices where there is a detection in at least one of the bands. The errors are calculated following Espinasse & Fender (2018). There is a flat/ inverted optically thick spectrum in all epochs. The lower two panels show the daily count rate from BAT (15-50 keV) and MAXI/GSC(4-10 keV), respectively. I only plotted the data points where I obtain 3σ detections. Despite MAXI/GSC monitoring the position of J1858 pre-outburst, no detection is made until the outburst begins. The MAXI/GSC light curve clearly shows a count rate increase around MJD 58880 indicates a state transition which was also seen by NICER (Buisson et al., 2020b). The vertical dotted and dashed lines denotes the beginning and end of the outburst, respectively (Krimm et al., 2018; Saikia et al., 2020). The dotted-dashed line indicates the time at which the state transition was observed by NICER on MJD 58901 (Buisson et al., 2020b). The shaded region is the time over which Type I X-ray bursts were detected (Buisson et al., 2020a). Figures 5.6 and 5.8 show the periods MJD 58420 to MJD 58447 and MJD 58510 to 58550 for clarity.

error is applied to the AMI-LA and MeerKAT data points, respectively. Three sigma upper limits are indicated with downwards facing arrows in the same colours as the detections for each telescope. I have also added VLA (4.5 GHz) and ATCA (5.5 GHz) data points from Van den Eijnden et al. (2020), shown as blue squares and green diamonds, respectively. Also shown is the radio light curve and spectral indices between MJD 58420 and 58450 in Figure 5.6, where the radio coverage is denser earlier on in the outburst.

The first AMI-LA observation took place eight days after the outburst started (blue dashed line in Figure 5.5 and 5.6, Krimm et al., 2018). The AMI-LA light curve shows an initial flare that reached a peak flux density of almost 600μJy at MJD 58427, seen more clearly in Figure 5.6. A flare is defined as a sudden, short period of increased radio flux density compared to the average level measured throughout the outburst. At the peak of the flare, I searched for shorter term variability by splitting the epoch into four one-hour long sections. J1858 showed ~25% variability on hour long timescales spanning between

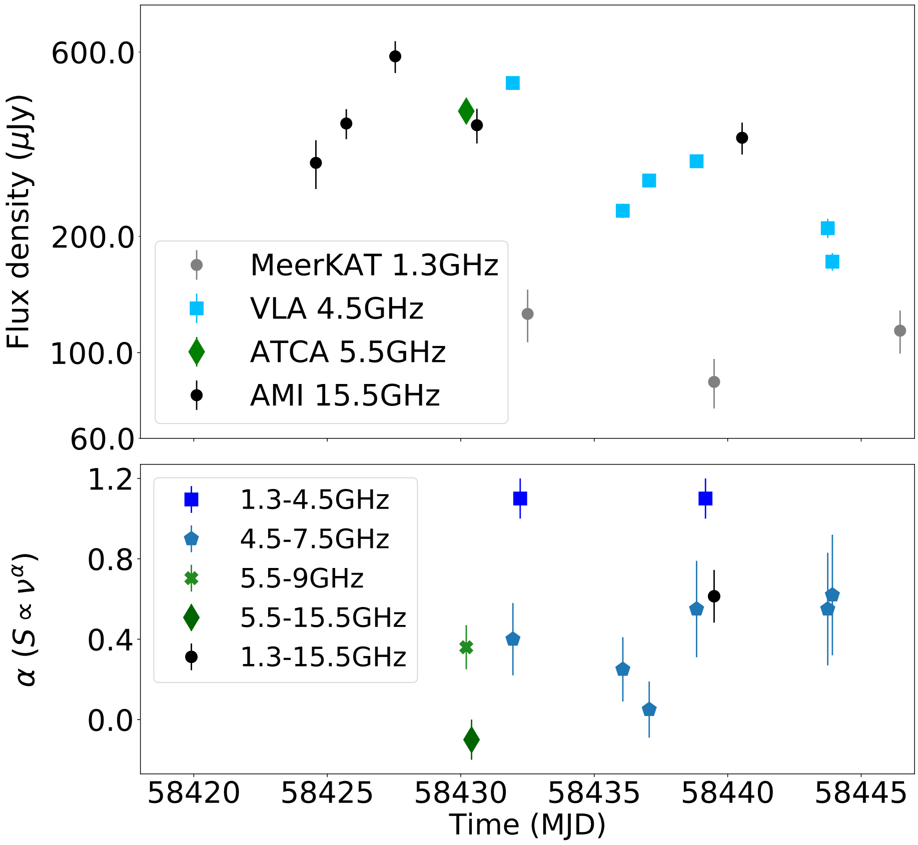

Figure 5.6: Subset of the top two panels of Figure 5.5 between MJD 58420 and 58447 shown to demonstrate, more clearly, the epoch to epoch radio variability observed early on in the outburst.

450 and 800μJy. Due to sensitivity constraints, I was unable to search for variability on timescales of less than one hour, like that seen in Van den Eijnden et al. (2020). For the rest of the outburst, the radio emission at 15.5 GHz is seen to be variable on a timescale of weeks with a series of detections and non-detections all around 300μJy.

Due to the delayed start time of the monitoring program with MeerKAT, there is no coverage of the initial flare at 1.3 GHz. Like AMI-LA, the MeerKAT light curve shows slow flux variability on the week-time-scales, but at a lower flux level, around 100μJy, except for a second flare observed at MJD 58530, which reached 1mJy at 1.3 GHz. It is likely the peak of the flare was missed with MeerKAT given that observations of J1858 lasted 15 minutes once a week, as a result the peak could have been much higher. I divided the MeerKAT epoch into shorter (five 3 minute) sections in order to search for short timescale variability, the flux density is consistent wit being constant across the epoch. During the period of the MeerKAT flare, there is no change in flux density the AMI-LA light curve. The flare seen with MeerKAT is discussed further in section 5.4.1.

Following the second flare, the flux densities measured at 1.3 GHz are fainter than at the beginning of the outburst and are all below 100μJy. From MJD 58588, there were more 3σ upper limits than detections and so on MJD 58626, weekly monitoring of J1858 with MeerKAT stopped. On MJD 58700, J1858 was observed for one hour as part of a multi-wavelength observing campaign. The signal to noise in the observation was high enough signal to split the observation into shorter integrations to search for short term variability. The resulting light curve is shown in the top panel of Figure 5.7. During the 60 minute observation, two flares were detected, the first lasting only two minutes, the second, about 30 minutes.

Our final radio detection was made on MJD 58886 with AMI-LA, around the same time as observations made with NICER and MAXI/GSC reported an increase in soft X-ray flux (see the bottom panel of Figure 5.5) and a state transition (Buisson et al., 2020b). After the transition, only 3σ upper limits are measured at around the same flux level or higher than when J1858 was in the hard state. I have concatenated the final three AMI-LA upper limits, to place deeper constraints on any soft state jet quenching with respect to the hard state. Combining the last three data points gives a 3σ upper limit of 70μJy.

By MJD 58928 (20 March 2020), optical monitoring of J1858 suggested that the source was entering quiescence (blue dashed line in Figure 5.5) and was further confirmed by multiple *Swift*-X-ray Telescope (XRT) observations showing continued low count rates (Saikia et al., 2020; Parikh et al., 2020).

5.3.2 Radio Spectrum

The second panel of Figure 5.5 shows radio spectral index measurements, where the spectral index α is defined as Flux density $S_\nu \propto \nu^\alpha$ (ν is the observing frequency, see lower panel

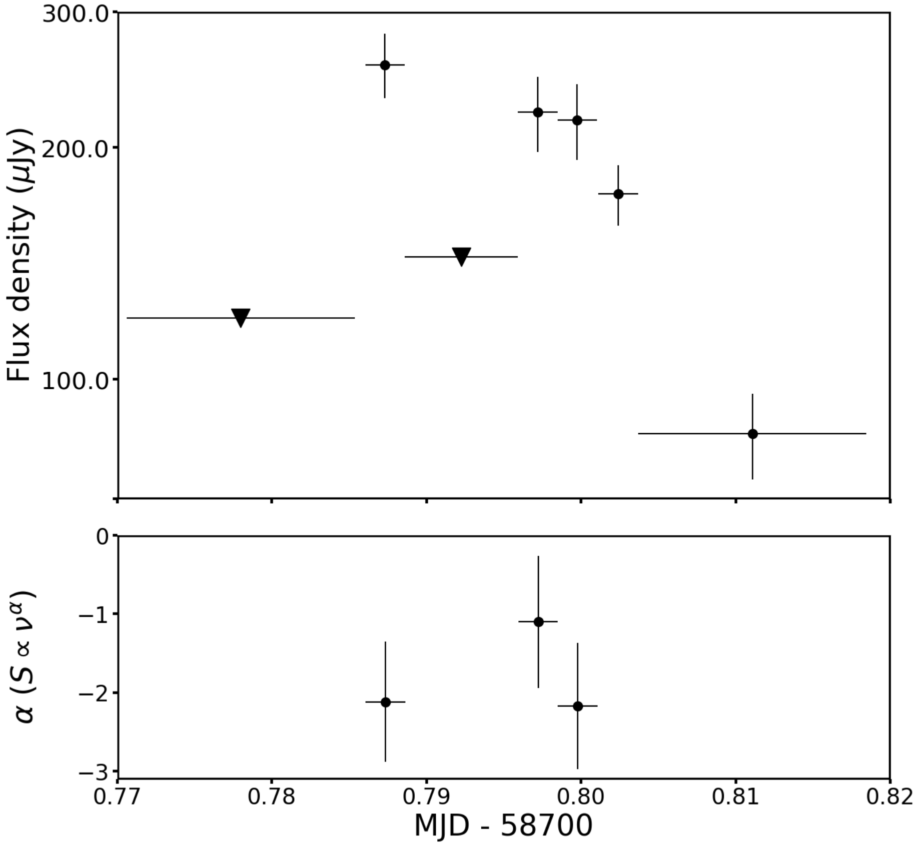

Figure 5.7: Data from an hour long observation with MeerKAT made as part of a multi-wavelength campaign including the Hubble Space Telescope (Castro-Segura et al, *in press*). The top panel shows the 1.3 GHz light curve for the observation. There is variability on timescales of minutes, similar to that seen by Van den Eijnden et al. (2020). The bottom panel shows the in-band spectral index for the sub-integrations where the J1858 was bright enough to detect in both halves of the band. In both panels the horizontal error bars correspond to the duration of the integration. The vertical errorbars are the same as in Figures 5.5, 5.6 and 5.8.

of Figure 5.6 for spectral index measurements between MJD 58420 and 58450). The errors (1σ) were calculated using the following:

$$err(\alpha) = \frac{1}{\ln(\nu_1/\nu_2)}\sqrt{\left(\frac{err(F_1)}{F_1}\right)^2 + \left(\frac{err(F_2)}{F_2}\right)^2}$$

where α is the spectral index, $\nu_{1,2}$, $F_{1,2}$ and $err(F_{1,2})$ are the observing frequency, flux density and associated uncertainty in the lower(1) and upper (2) halves of the band, respectively (Espinasse & Fender, 2018). I have calculated the spectral indices where the two observations in different bands are made within 24 hours of each other and the source is detected in at least one of the bands. The black circles are the spectral index measurements between MeerKAT and AMI-LA (1.3-15.5 GHz), the blue squares are for MeerKAT-VLA (1.3-4.5 GHz) and the dark green diamonds are for ATCA-AMI-LA (5.5-15.5 GHz).

Van den Eijnden et al. (2020) published the measured radio flux densities in the two halves of the observing band for both the VLA (4.5-7.5 GHz, turquoise hexagons) and ATCA (5.5-9 GHz, green crosses), allowing for in-band spectral index measurements. An inband 1.0-1.6 GHz spectral index is calculated for a single MeerKAT epoch (MJD 58530) where the source reached 1 mJy (light blue circle). All calculations show the radio emission from J1858 to be consistent with being either inverted or flat, i.e. $\alpha \geq 0$.

The only time where the radio spectral index followed $\alpha \leq 0$ was on MJD 58700. The bottom panel of Figure 5.7 shows the in-band spectral indices for the MeerKAT observation on MJD 58700 for the periods where J1858 was bright enough in both halves of the band. The negative spectral index measurements were obtained only on timescales of less than 15 minutes. Van den Eijnden et al. (2020) also measured variable spectral indices on short timescales with rapid changes with $\alpha \leq 0$ and $\alpha \geq 0$.

5.3.3 X-ray Light Curve

The bottom two panels of Figure 5.5 show the daily average count rate from *Swift*-BAT, between 15 and 50 keV, and MAXI/GSC, between 4 and 10 keV, respectively, for all detections that are 3σ or greater.

The BAT X-ray light curve shows repeated, low-level, hard X-ray detections from the beginning of the outburst, MJD 58422 until 58800. When combined with quasi-persistent, self-absorbed radio detections, the detections from BAT imply that J1858 is in the hard state. There are two periods during the outburst: MJD 58470 to 58520, and 58830 to ~58880, where J1858 was close to the Sun. During this period, BAT and MAXI/GSC, which scan large portions of the sky, were still able to observe but the resulting data points have larger associated uncertainties. Our final BAT detection is on MJD 58866.

From MJD 58880 onwards, after the final BAT detection, MAXI/GSC regularly detects J1858. The bottom panel of Figure 5.5 shows a sharp increase in soft X-ray flux (bottom panel of Figure 5.5) that lasts until around MJD 58940. The observed flux increase is consistent with the NICER and MAXI observations made on MJD 58897 reporting a change in X-ray spectral state (Buisson et al., 2020b; Negoro et al., 2020). After reaching a peak around MJD 58900, the MAXI/GSC light curve shows a gradual decay as J1858 returns to quiescence (the blue dashed line in Figure 5.5 Saikia et al., 2020). Previous to the state transition, the regular BAT detections are indicative of J1858 being in the hard state. Between the soft state and quiescence, there are no further hard X-ray detections. However, it is possible to conclusively say that J1858 did not return to the hard state. When XRBs return to the hard state before quiescence, it may be at a lower flux level than when the system first enters the outburst (Fender & Belloni, 2004). It is possible that the hard state emission was too faint for BAT to detect.

5.4 Discussion

I have monitored the newly discovered neutron star XRB J1858 throughout its outburst, lasting from MJD 58242 to 58924 (late 2018 to early 2022). The radio observations show faint emission consistent with a quasi-persistent (but variable), self-absorbed jet. X-ray monitoring with both BAT and MAXI/GSC show little evidence of strong variability on day-long timescales. On two separate occasions the light curves show evidence of flares, one with AMI at the beginning of the outburst and a second with MeerKAT around MJD 58530. Here, I place our observations in the context of the wider XRB population.

5.4.1 Jet emission

J1858 was detected in approximately 60% of our observations with AMI-LA, with flux densities in a range between 150 and 350μJy (with the exception of the flare around MJD 58430). It should be noted that several non-detections obtained with AMI-LA are not particularly constraining given they correspond to flux densities higher than in the narrow range over which J1858 is detected. Combined with the positive spectral index measurements (with the exception of MJD 58700), the radio detections point towards radio emission produced by a compact, self-absorbed jet (Migliari et al., 2003). I was only able to search for short (minute) timescale variability, like that found by Van den Eijnden et al. (2020), in a single epoch: MJD 58700, see Figure 5.7. Some of the VLA and ATCA epochs overlap with the AMI/MeerKAT observations. Those observations show short term variability whereas our observations do not, mainly due to lack of signal to noise. The short term variability is accompanied by changing, often negative, spectral indices (Van den Eijnden et al., 2020). It may be the case that for most of the outburst where the observations last for 15 minutes or longer, any short time-scale variability and change in spectral index may average out as a relatively steady and self-absorbed jet.

Similar radio properties have been observed in V404 Cygni, a black hole XRB that J1858 has been compared to previously due to similar X-ray signatures (Ludlam et al., 2018). In V404 Cygni, the time averaged spectrum showed a self-absorbed component similar to what is shown in the second panel of Figure 5.5, but on shorter timescales (minutes) there are transitions from optically thick to thin like seen in Figure 5.7. In V404 Cygni, it was suggested that the rapid spectral variability arose from intrinsic fluctuations in the accretion flow (Rana et al., 2016).

Very few other neutron star XRB outbursts have had comparable, long term, radio observing campaigns with such high signal to noise ratios so that the short timescale spectral index and flux density variability can be studied. Observations of neutron star XRB Scorpius X-I, a Z source, by Fomalont et al. (2001) showed ~hour timescale variability in both flux density and spectral index. This is perhaps the most similar behaviour to that observation in J1858. Regular radio observations of GRS 1747-312 showed strong swings in spectral index, on longer timescales: over a period of three months (Panurach et al., 2021). One the other hand, XTE J1701-462 was observed every three days for three months with ATCA in 2006 and showed a steady flat/ inverted spectral index, similar what has been observed in J1858 (Fender et al., 2007).

Persistent radio jets and power law components in the X-ray spectra are clear signatures of hard state XRBs. As mentioned in Section 5.1.3, observations of J1858 at X-ray energies shows that the source does not appear to have a canonical hard X-ray state, instead, the X-ray emission is highly variable with hard emission interspersed with soft flares (Hare et al., 2020). The quasi-persistent, self-absorbed radio emission observed on long timescales is perhaps the best indication that J1858 is in the hard state.

The final radio detection is on MJD 58886. Around the same time, our BAT light curve shows no further detections, and there is a significant increase in flux in the MAXI 4-10 keV light curve, as shown in the lower two panels of Figure 5.5. Such a change indicates that J1858 transitioned to a state that is dominated by soft X-ray photons. Similarly to when in the hard state, Buisson et al. (2020b)'s NICER observations between 0.6 and 12 keV demonstrates that J1858 also does not show a canonical soft state, however, the spectrum can no longer be described using a single power law, a soft component (from a disc) is also required, thus indicating a potential state change.

The final radio detection with AMI-LA on MJD 58886 is fainter by a factor of two compared to the detection a week earlier, hinting at a possible jet quenching during the transition to the softer state. I concatenated the final three AMI-LA non-detections and obtain a much deeper 3σ upper limit of 70μJy. In comparison to the average AMI-LA flux density measured whilst J1858 was in the hard state, the jet emission from J1858 was quenched by at least a factor of four upon entering the softer state, if the reduction in observed radio flux density is due to quenching from a state transition. Evidence of jet quenching has been observed in some other neutron star XRBs, but there are also cases where bright radio emission has been detected in the soft state indicating that jet quenching is not a global phenomena in neutron star systems (Migliari et al., 2004; Gusinskaia et al., 2017). Further observations of neutron star systems in both hard and soft states are required to better understand any jet quenching.

Optically-thick flare

The radio emission associated with J1858 has been fairly constant on long (weeks-months) timescales at faint flux ($\sim$100 μJy/beam) density level, similar to other self-absorbed compact jets observed in other neutron star XRBs. During J1858's outburst, there were two occasions where the radio emission deviated from this pattern in the form of optically thick flares (MJD 58430 and 58530). Radio flares are usually associated with state transitions in both black hole and some neutron star XRBs, tracking the evolution of the flares show an transition from optically thick to thin synchrotron emission (Mirabel & Rodríguez, 1994; Fender et al., 2004b; Fomalont et al., 2001). During the transition, flares are thought to occur when discrete blobs of synchrotron emitting plasma are ejected from the accreting compact object. Depending on the how quickly the transition occurred, one may also ex-

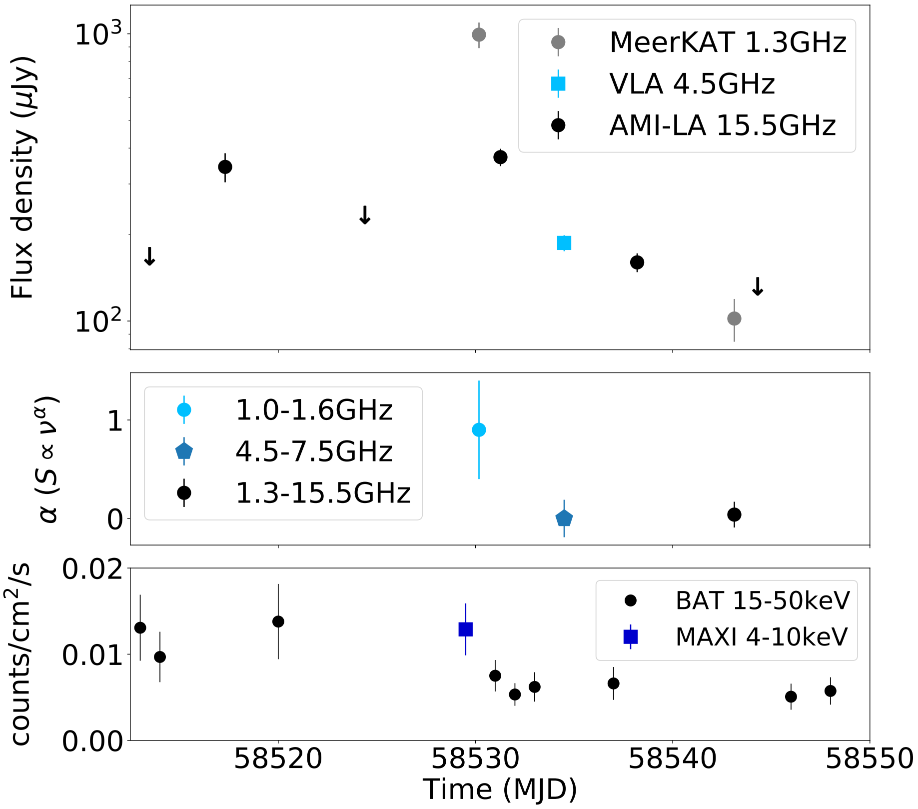

Figure 5.8: A subsection of Figure 5.5 showing the radio and X-ray light curves for 20 days either side of the 1 mJy flare observed with MeerKAT. Combining observations from 3 different observing frequencies there is a sharp rise and a decay. Also shown are the radio spectral index measurements for the same period. The X-ray light curve remains fairly consistent during the period of the flare.

pect to see a drop in the hard X-ray flux, due to the transition to a softer X-ray spectral state. Figure 5.8 shows the radio and X-ray light curves, as well as the radio spectral index measurements for the period 20 days either side of the optically thick flare observed with MeerKAT. There is a single soft X-ray detection during the 40 days (bottom panel of Figure 5.8), just before the flare that was observed with MeerKAT. BAT detects J1858 repeatedly during this period (MJD 58510 - 58550), with a BAT count rate that is approximately the same either side of the flare (also see panel three of Figure 5.5). It may be likely that a fast transition occurred and could have easily been missed given how faint J1858 is.

On MJD 58530, the flux density of J1858 observed with MeerKAT reached 1.0±0.1 mJy, about an order of magnitude brighter than the average MeerKAT flux density for the rest of the outburst. The 1.0-1.6 GHz spectral index of the flare was $\alpha = 0.9 \pm 0.5$ (consistent with optically thick emission, see middle panel of Figure 5.8). By observing an optically thick flare, I have been able to place lower limits on the size of ejecta at the peak of the flare, infer the minimum energy, magnetic field associated with the minimum energy and the brightness temperature (Fender & Bright, 2019). At a distance of $12.8^{+0.7}_{-0.6}$ kpc, (Buisson et al., 2020a), a peak flux of 0.99 mJy at a frequency of 1.3 GHz corresponds to a brightness temperature of 5×10^{10}K and energy of 5×10^{37} erg. The magnetic field associated associated with the minimum energy is 0.2 G. At the peak of the flare, the emission region size is 10^{13} cm. These results are at a similar order of magnitude or slightly lower than those calculated for black hole XRBs V404 Cygni, Cygnus X−3, GRS 1915+105 and MAXI J1631−472 (Fender & Bright, 2019; Monageng et al., 2021). I obtained a minimum energy four orders of magnitude higher compared to that observed in cataclysmic variable SS Cygni (Fender et al., 2019). Placing J1858 in the context of other transient compact systems: the radio flares observed in black hole and neutron star XRBs correspond to ejections of similar sizes and energies, independent of the nature of the compact object. Cataclysmic variables, on the other hand, launch much less powerful ejections. However, this comparison is based on a limited sample size.

Despite observing the radio flare, there is observe no evidence of movement of the radio source associated with J1858 in the MeerKAT images subsequent to the 1 mJy flare. Such motion would imply the ejection of plasma of a similar energy and duration as that observed in multiple black hole systems by MeerKAT (Bright et al., 2020; Carotenuto et al., 2021). However, given the large distance to J1858, combined with the large MeerKAT beam size (~ 7"), it is not surprising that there is no movement of the radio source in the MeerKAT images. In order to resolve any proper motion, VLBI would be required. In the AMI-LA and MeerKAT observations made the following week, the optically thick jet feature had returned with a flux level ~ 100μJy fainter than before the flare. The return of the compact jet component indicates that any transition to the soft state occurred on a timescale of days.

5.4.2 Radio X-Ray Correlation

Using the detections of self-absorbed radio emission as an indication that J1858 is in the 'hard state', these detections can be combined with hard X-ray detections and compare J1858 to other hard state XRBs. Figure 5.9 shows the 5 GHz radio and 1-10keV X-ray luminosities for a compilation of hard state neutron star (downwards facing blue triangles) and black hole XRBs (black circles, Bahramian et al., 2018). I have also plotted a selection of Z sources from Migliari & Fender (2006, purple crosses). The red circle denotes the radio and X-ray luminosities of XTE J1701−462, an interesting neutron star system which has shown both Atoll and Z-source-like phases (Fender et al., 2007). Overlaid are the radio and X-ray luminosities for every epoch with quasi-simultaneous radio and BAT detections.

The very high and varying column density in J1858, (Hare et al., 2020), makes estimating the intrinsic X-ray luminosity difficult. Van den Eijnden et al. (2020) showed that the XRT fluxes under-represent the intrinsic emission by a factor of 2-4 due to significant absorption along the line of sight. The use of NuSTAR, which observes at a higher energy range than XRT allowed for the calculation of the ionizing X-ray luminosity at 2×10^{38}erg s^{-1}, (Buisson et al., 2020a), which is approximately 30 times higher than the luminosities derived from

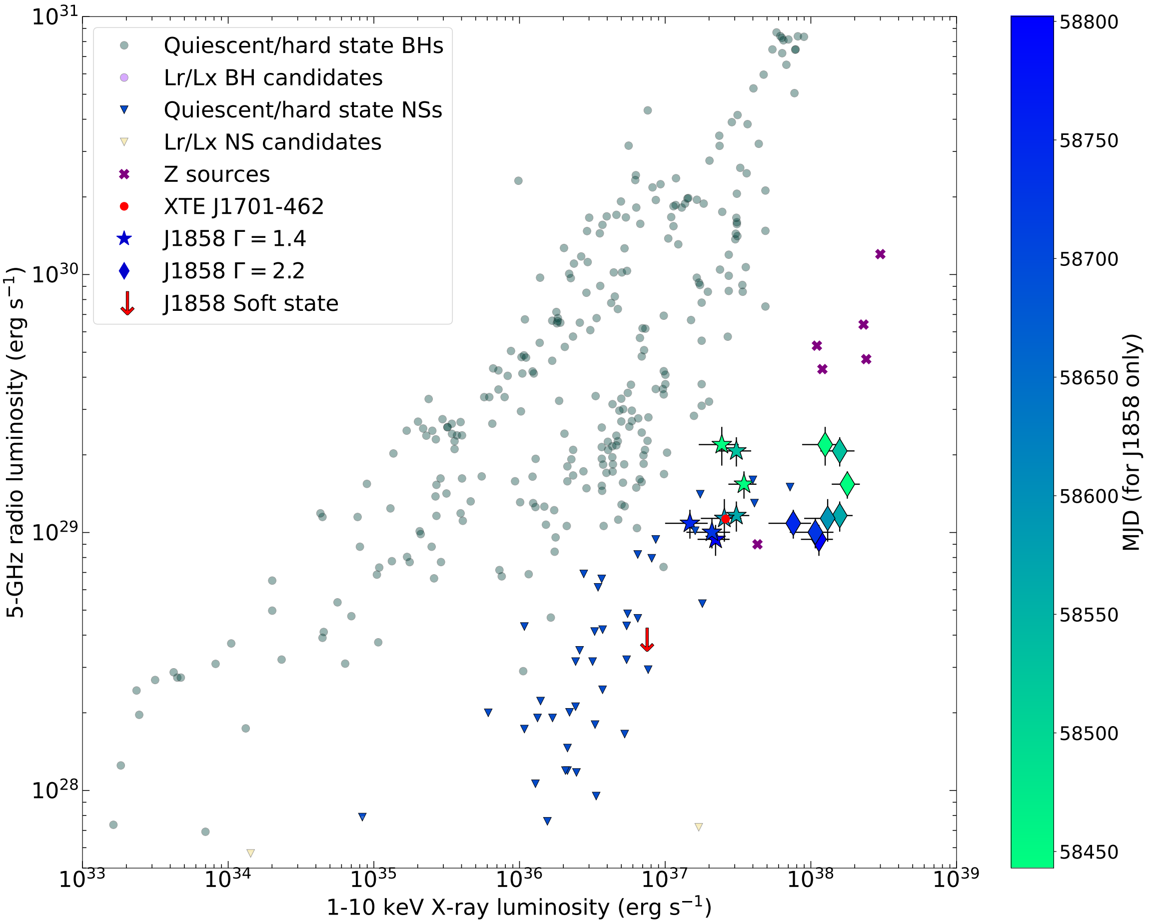

Figure 5.9: Caption on the next page.

Figure 5.9: Radio/X-ray luminosity plane for a range of black hole and neutron star XRBs in the hard state (or equivalent) (Bahramian et al., 2018). I have also added a sample of Z sources from Migliari & Fender (2006), shown with purple crosses as well as XTE J1701−462, a neutron star XRB that has shown both Atoll and Z source phases (red circle Fender et al., 2007). Using a distance of $12.8^{+0.7}_{-0.6}$ kpc, I calculated the 5 GHz and 1-10keV luminosities for every quasi-simultaneous observation between *Swift*-BAT and MeerKAT, VLA or AMI-LA (Buisson et al., 2020a). I have calculated the 5 GHz luminosity by assuming a spectral index of $\nu^{0.5}$, the average spectral index calculated from our observing campaign. The X-ray luminosities are calculated using two different photon indices, 1.4 and 2.2 (diamonds and stars, respectively), to reflect the range of values measured throughout the outburst (Bozzo et al., 2018). The errorbars on the X-ray luminosities consider the count rate and distance uncertainties, no uncertainty induced by the variable absorption is considered because in the *Swift*-BAT observing band (15-50keV, where the X-ray data points were obtained), the variable N_H affects are negligible. The colour gradient shows the movement of J1858 on the radio/X-ray plane as the outburst evolved. Three AMI-LA observations took place after J1858 transitions in to a softer state. I have concatenated these observations and combined with MAXI/GSC observations made in the same period to produce the downwards facing red arrow.

the XRT observations. This shows that absorption cannot fully explain the flux discrepancy found between BAT and XRT. A large fraction of the emission is scattered out of our line of sight, which may be due to the high inclination of the source (>70°, Buisson et al., 2021). The BAT fluxes are less affected by the significant absorption and scattering, so the luminosities obtained are similar to that obtained by Buisson et al. (2020a). Therefore, in Figure 5.9, I have extrapolated the BAT fluxes measured between 15-50 keV to 1-10keV using two different photon indices to reflect the varying spectrum that has been reported: 1.4 and 2.2, shown as diamonds and stars, respectively.

To calculate the radio luminosity, I have scaled the radio detection to 5 GHz using a spectral index of 0.5, the average spectral index measured throughout the outburst. A flat spectral index is usually assumed when scaling radio luminosities to 5 GHz both to consider the difference in radio spectral index measurements on the radio loud and quiet black hole branches and when a spectral index is not available (Espinasse & Fender, 2018). Using a flat spectral index would result in MeerKAT luminosities that would be about a factor of two lower and the luminosities from our AMI-LA data points would about a factor of two higher.

The colour gradient in Figure 5.9 shows how J1858 moves across the radio/X-ray correlation throughout the outburst. For a given photon index, the source follows an approximately semi-circular path on the radio/X-ray plane, becoming less radio-luminous by about a factor of three as the outburst progresses. Unlike the radio luminosity, the 1-10 keV luminosity remains fairly constant. However, this is all under the assumption that the X-ray photon index is constant across all epochs. It is most likely that the X-ray luminosity and photon index varies significantly throughout the outburst. J1858 can be used to potentially sample new luminosity parameter space between the hard state neutron stars and Z sources in Figure 5.9.

J1858 sits between the atoll and Z sources in terms of both X-ray and radio luminosities in Figure 5.9. It is at the low luminosity end of the Z source distribution but also at the high luminosity end of the atoll group. The long term radio light curve shows emission consistent with a compact self-absorbed jet, similar to those observed in other atoll sources. However, on short timescales, there is some rapid flaring (Figure 5.7), which is Z source-like behaviour, the flaring is only observed for a short period and it is not possible to be certain that such behaviour is present through the outburst. If one assumes $\Gamma = 1.4$, J1858 also overlaps perfectly with the position of XTE J1701-462. XTE J1701-462 is a neutron star XRB that was initially classified as a Z source (Homan et al., 2006). Subsequent analysis of RXTE observations that covered the duration of the outburst showed that XTE J1701-462 evolved from a Z source to an atoll source (Homan et al., 2007). Radio observations showed a fairly constant (few 100μJy) point source with a inverted spectral index in almost all epochs except when at the highest accretion rate, similar to what has been observed from J1858 (Fender et al., 2007). Therefore, despite the wealth of observations and data, it is not possible to determine whether J1858 is an atoll or Z source.

I have also placed the deep radio upper limit on Figure 5.9 corresponding to the time after the spectral state change (around MJD 58900, Buisson et al., 2020b). The resulting data point is shown as a red downwards facing arrow. As J1858 moves into the soft-state, the radio luminosity continues to drop reaching an 3σ upper limit of ~4×10^{28}erg s^{-1}. The radio luminosity in the soft-state is about a factor of four fainter than the average flux density measured with AMI-LA throughout the outburst. The X-ray luminosity also decreases by at least an order of magnitude (Γ-dependent).

5.5 Conclusions

I have presented near weekly radio observations of the outburst of neutron star XRB J1858.6-0815 that started in October 2018. The radio observations show self-absorbed emission, consistent with a quasi-steady compact jet as expected in the hard X-ray spectral state, despite J1858 not appearing to be in a canonical hard state. The radio light curves show little significant long term variability, with the exception of MJD 58427 and 58530, where there are two flares. During these periods, there is no evidence of a link between the radio flares and any X-ray behaviour. On shorter timescales, MJD 58700, there is significant variability in terms of flux density and spectral index (also shown in Van den Eijnden et al., 2020). Comparing J1858 to other XRBs on the radio/X-ray correlation, at a distance of $12.8^{+0.7}_{-0.6}$kpc, J1858 appears to be a very radio luminous atoll-type or faint Z source neutron star binary yet placed in the radio/X-ray plane, and therefore of fundamental importance in establishing the slope and normalisation of the correlation for neutron stars. This allows for a better understanding into to the differences between accretion and jet production in neutron stars and blacks holes.

Chapter 6

Conclusions and Future Outlook

In this thesis, I have presented observations of transient radio jets from stellar mass compact objects. These jets are interpreted using a series of different of models from persistent, compact jets (Blandford & Königl, 1979) to ultra-relativistic fireballs (Blandford & McKee, 1976). The research I have performed on GRBs to date has demonstrated that our understanding of the afterglow of GRBs is far from complete. With increasingly sensitive observing facilities, more questions are being asked than answered. As shown in Chapter 3, it is beginning to become evident that the classification system of short vs long GRB that has been in place since the early 1990s (Kouveliotou et al., 1993) cannot be used for all events. GRB 200826A, an apparent short GRB, was shown to be from a jet propagating through a stellar wind environment incompatible with a binary neutron star progenitor. Another demonstration in the incompleteness of understanding into GRB afterglows is the detection of a VHE counterpart to five long GRBs (Chapter 4). I have shown that VHE GRB afterglows are just as varied as the rest of the long GRB population. Looking forward, I plan to study these events further and compare them to non-VHE GRBs to determine if there is a possibility of VHE GRBs being a separate population. Many of the GRB data sets I have presented in this thesis have been collated from the AMI-LA radio telescope. Such observing campaigns have allowed me to constrain and test GRB afterglows models (e.g.

GRB 190829A) as well as establish how these campaigns can be more effective in the future. I have demonstrated (yet again) that the AMI-LA telescope is an excellent facility for long term campaigns of other transients such as neutron star X-ray binary *Swift* J1858.6-0814 twice a week throughout the 18 month outburst. Similar facilities to AMI-LA will be vital in the future if we are to continue studying radio transients in such detail.

6.1 Applying blast wave models to X-ray binary jets

The van der Laan model (Section 1.3.1) assumes that the radio of the fraction of kinetic energy in the jet that go into the electrons and magnetic fields is constant at all times (van der Laan, 1966). Identification of the synchrotron self-absorption frequencies allows one to make estimates of the magnetic field strength, emitting size region and bulk Lorentz factor of the jet (Fender et al., 2019). Traditionally, such models have been limited in their applications to X-ray binary systems such as I have shown in Chapter 5. Barniol Duran et al. (2013) demonstrated that the assumption of equipartition can also be used to extract parameters from relativistic outflows such as GRBs. In Chapter 3, I applied Barniol Duran et al. (2013)'s model to the radio afterglow from GRB 200826A.

However, GRB afterglow models do not assume equipartition, in fact they are assumed to be very far from it. The fraction of energy that goes to the electrons and magnetic fields can even vary with time (Misra et al., 2021). Applications of blast wave models to afterglow data sets, such as that in Chapter 4 (GRB 201216C), demonstrate that in some cases 1000 times more energy goes into the electrons compared to the magnetic field (Rhodes et al., 2022a). Particle-in-cell simulations have also demonstrated that the fraction of energy given to the magnetic fields is actually differential across the shell with a higher fraction closer to the shock front and a lower fraction upstream (Keshet et al., 2009). As a result, it may be possible that for jets that can be approximated as a blast wave (i.e. GRBs), the system may be closer to equipartition as assumed in x-ray binary jets.

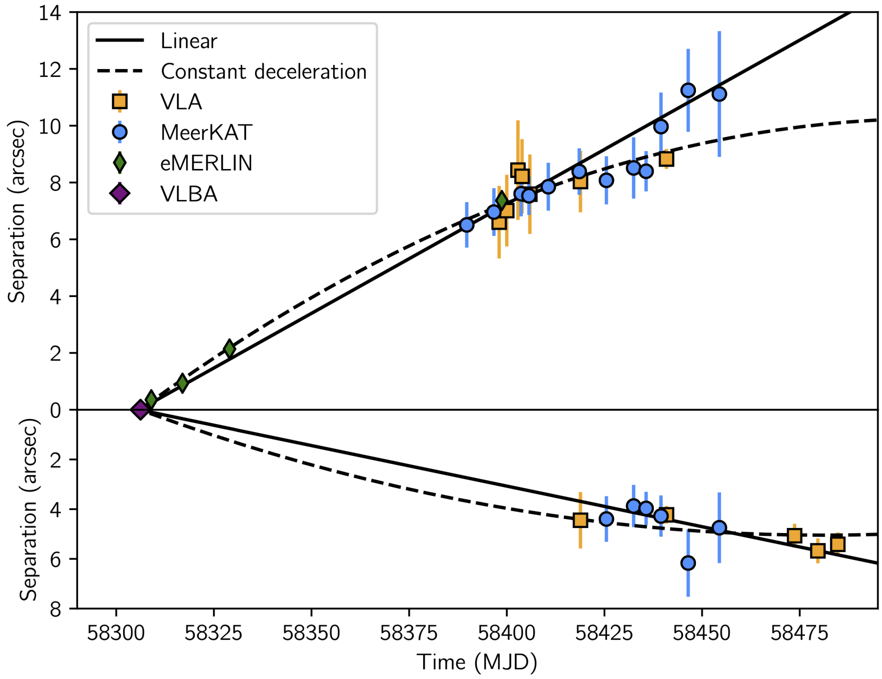

Figure 6.1: Angular separation as a function of time for both the approaching and receding ejecta components from the black hole X-ray binary MAXI J1820+070 (Bright et al., 2020).

Over the next three years, I will begin to explore the question: *are X-ray binary transient ejecta low energy/Lorentz factor analogues of GRB jets?* Compared to van der Laan models, GRB afterglow models have more freedom and a wider range of parameter space. Multiple sets of X-ray binary observations with MeerKAT have shown evidence of high proper motion jets that appear to decelerate (see Figure 6.1 for an example). Initial studies indicate that the motion observed from these ejecta could be explained using a decelerating blast wave model where the turnover occurs around $\Gamma \approx 2$ (Fender & Rhodes, in prep). Combining the separation vs time plots with light curves and spectral evolution, I will be able to test the validity of GRB afterglow models on the more densely sampled X-ray binary data sets in order to determine whether or not their deceleration and trajectory can be described as a low energy GRB analogue.

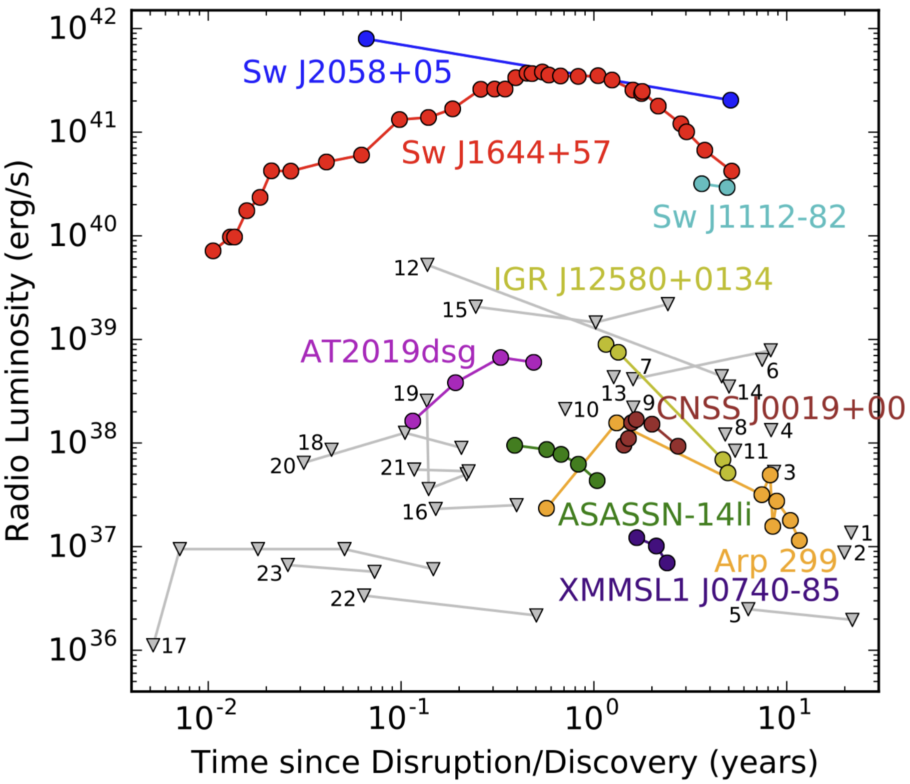

Figure 6.2: A compilation of TDE radio light curves from (Alexander et al., 2020a). The events with luminosity above 10^{40} erg/s are categorised as relativistic TDEs where the emission is modelled as a GRB-like jet.

6.2 ZTF22aaajecp/AT2022cmc: a new relativistic TDE

This thesis has considered only radio transients from stellar mass compact objects. There are also a class of radio transients from supermassive black holes: tidal disruptions events (TDEs). A handful of TDEs have been called *relativistic* TDEs, their radio emission is very luminous (above 10^{40} erg/s, see Figure 6.2). Relativistic TDEs are rare with only one well-studied event to date: *Swift* J1644+57 (the red light curve in Figure 6.2, Zauderer et al., 2011). The radio emission has been interpreted using external shocks with the circumnuclear medium and inverse Compton cooling (Metzger et al., 2012; Cao & Wang, 2012; Kumar et al., 2013).

Events like *Swift* J1644+57 are rare, with a detection rate of approximately one per decade. In February 2022, the Zwicky Transient Facility discovered a new transient, ZTF22aaajecp/AT2022cmc (hereafter AT2022cmc Andreoni et al., 2022a), which was fading too rapidly to be a supernova and had no evidence of a host galaxy (Andreoni et al., 2022b). Multi-wavelength follow up determined that AT2022cmc was a relativistic TDE at $z = 1.12$ (Tanvir et al., 2022), four times more distant than *Swift* J1644+57.

Through guaranteed time, successful DDT and open time calls, I have been performing regular radio follow up of AT2022cmc. To date, the radio emission from AT2022cmc is optically thick and following a steady plateau (Figures 6.3 and 6.4). Given that *Swift* J1644+57 has been detectable for nearly a decade, I expect that we shall be observing the radio counterpart to AT2022cmc for many years to come. These observations will be an ideal test bed to explore the possibility and applicability of blast wave models to transients from supermassive black holes. If the radio emission is from a jet, my high cadence observing campaigns will help to track the deceleration and evolution of the blast wave. It will also provide an opportunity to understand the environment in the vicinity of the burst.

The production of jets is ubiquitous in astrophysics. Jetted transients are some of the most powerful events in the Universe. To have so much power, they must occur in highly relativistic but compact environments. Their association with compact objects across all

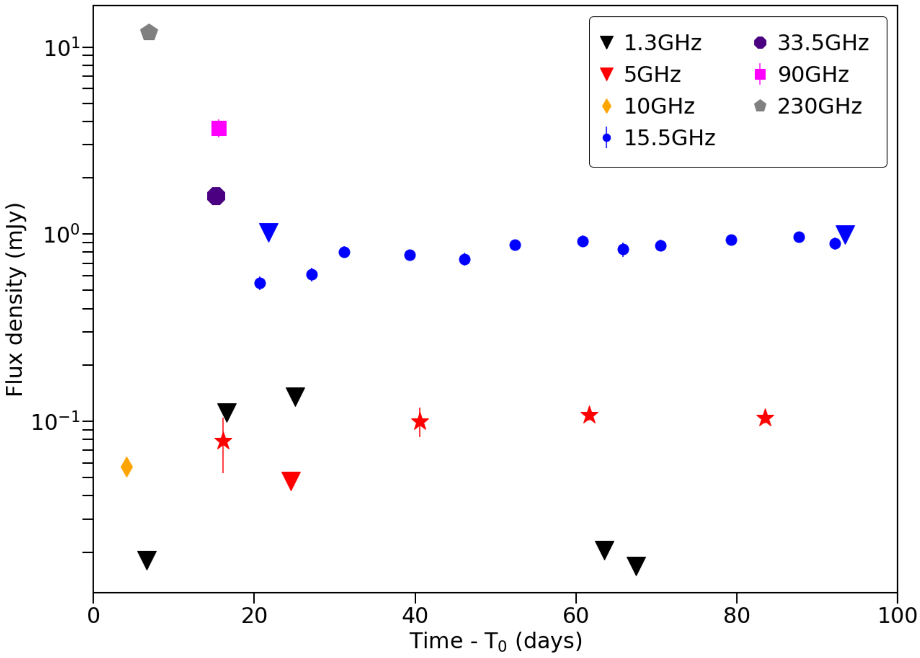

Figure 6.3: Multi-frequency radio light curve of the newly-discovered relativistic TDE AT2022cmc. The light curves showed an initial short rise followed by a plateau overlaid with variability on ~day times scales. T_0 is the time of optical discovery (Andreoni et al., 2022a).

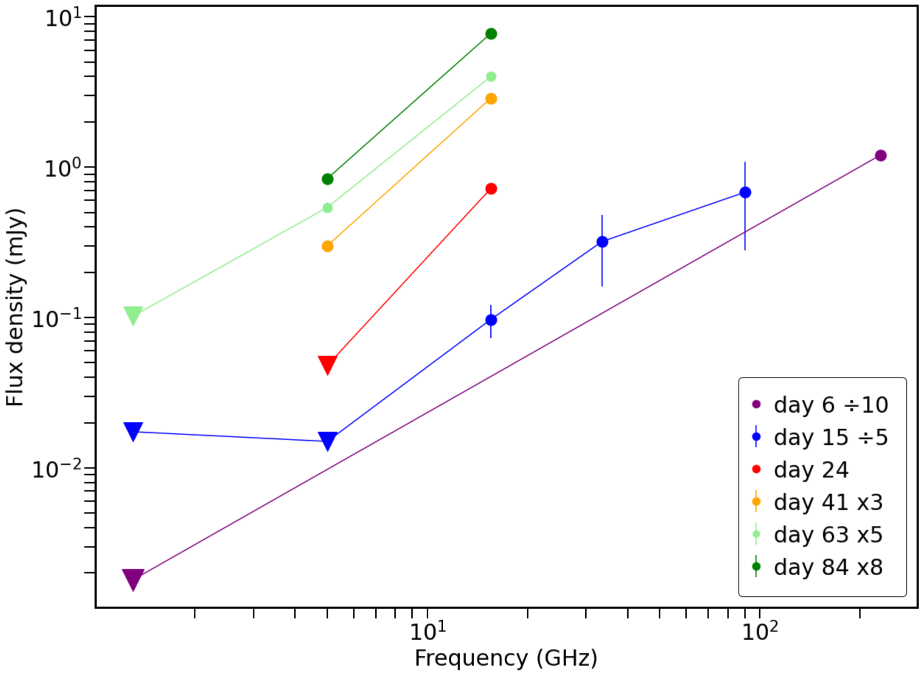

Figure 6.4: Broad band radio spectra over six epochs from day six to 84 post-discovery. In all epochs, the radio spectra are consistent with being self-absorbed.

mass scales allows us to better understand the extreme physics associated with accretion-outflow connection. Furthermore, as demonstrated in this thesis, they provide an excellent probe to study not only jet physics, but compact objects, the interstellar medium and stellar evolution.

Appendix A

GRB follow up data

Table A.1: A summary of the GRB observations obtained with AMI-LA during my DPhil. T_0 refers to the start time of the observation and ΔT is the observation duration.

GRB	Date	T_0 (UTC)	RA	Dec	Flux density (μJy)	Noise (μJy)	ΔT (hrs)
190424A	24/04/19	14:19:12	03h 14m 43s	+20d 14’ 00"	N/A	70	2
190427A	27/04/19	08:45:19	18h 40m 51s	+40d 19’ 20"	N/A	170	0.5
190427A	28/04/19	01:29:33	"	"	N/A	99	2
190515A	16/05/19	17:17:00	09h 10m 32.13s	+29d 20’ 43.0"	204±16	60	2
190515A	17/05/19	17:24:02	"	"	N/A	43	4
190515B	15/05/19	16:06:24	06h 35m 22.67s	+52d 17’ 06.13"	493±46	89	2
190610A	11/06/19	06:38:14	03h 05m 09s	-07d 39’ 57"	N/A	127	4
190630B	30/06/19	15:02:13	14h 54m 40.6s	+41d 13’ 30"	N/A	900	2
190701A	01/07/19	09:48:08	01h 52m 15s	+58d 54’ 22"	N/A	200	2
190719C	19/07/19	15:00:18	16h 00m 50s	+12d 58’ 39"	N/A	130	2
190826B	28/08/19	14:32:25	16h 47m 16.4s	+27d 14’ 12"	N/A	150	3.8
190829A	31/08/19	02:29:35	02h 58m 10.6s	-08d 57’ 31.9"	3889±31	60	3
190829A	01/09/19	02:34:36	"	"	2928±22	50	3
190829A	03/09/19	03:22:32	"	"	2028±16	60	2
190829A	04/09/19	02:24:48	"	"	1963±48	192	3

190829A	05/09/19	02:15:54	"	"	1546±16	54	3
190829A	06/09/19	02:46:51	"	"	1556±30	47	3
190829A	08/09/19	01:52:08	"	"	1313±15	40	4
190829A	09/09/19	03:40:54	"	"	1267±30	64	2
190829A	10/09/19	02:36:07	"	"	1186±66	73	2
190829A	11/09/19	01:40:21	"	"	1174±33	80	4
190829A	12/09/19	01:36:25	"	"	924±18	61	4
190829A	13/09/19	01:37:27	"	"	895±26	47	4
190829A	14/09/19	01:28:34	"	"	834±27	41	4
190829A	15/09/19	01:24:36	"	"	768±18	41	4
190829A	16/09/19	01:20:40	"	"	650±25	65	4
190829A	17/09/19	01:16:46	"	"	634±23	43	4
190829A	18/09/19	01:50:43	"	"	535±13	42	3.3
190829A	19/09/19	01:08:54	"	"	643±9	42	4
190829A	20/09/19	01:04:59	"	"	538±22	47	4
190829A	21/09/19	01:09:59	"	"	624±11	49	4
190829A	22/09/19	01:24:01	"	"	540 ± 33	60	3.5
190829A	23/09/19	00:53:09	"	"	536±40	73	2

190829A	24/09/19	03:15:48	"	"	N/A	162	1.5
190829A	25/09/19	00:45:17	"	"	551± 31	84	4
190829A	26/09/19	00:41:21	"	"	486 ± 26	122	2
190829A	27/09/19	00:37:26	"	"	410±10	45	4
190829A	28/09/19	00:33:31	"	"	497±23	56	4
190829A	01/10/19	02:14:23	"	"	347±38	83	2
190829A	03/10/19	01:24:39	"	"	253±38	61	2
190829A	04/10/19	00:15:53	"	"	373 ± 29	107	3
190829A	05/10/19	00:05:58	"	"	296 ± 11	47	4
190829A	06/10/19	00:02:03	"	"	N/A	600	4
190829A	06/10/19	23:58:07	"	"	312 ± 19	49	4
190829A	08/10/19	01:48:53	"	"	314 ± 9	65	2
190829A	08/10/19	23:50:14	"	"	293± 9	43	4
190829A	09/10/19	23:46:19	"	"	261±6	48	3
190829A	13/10/19	23:36:35	"	"	221 ± 10	38	4
190829A	21/10/19	23:58:58	"	"	284 ± 15	53	3
190829A	26/10/19	23:31:20	"	"	256 ± 11	39	3
190829A	01/11/19	22:17:53	"	"	N/A	75	4

190829A	04/11/19	22:56:57	"	"	154± 12	39	3
190829A	08/11/19	21:57:20	"	"	210±10	40	4
190829A	10/11/19	21:40:31	"	"	249±19	59	4
190829A	15/11/19	21:20:49	"	"	189±10	58	4
190829A	18/11/19	21:09:02	"	"	167±4	35	4
190829A	22/11/19	20:53:19	"	"	180±16	55	4
190829A	25/11/19	20:41:31	"	"	234±40	68	4
190829A	02/12/19	20:14:00	"	"	244±26	78	4
190829A	12/12/19	19:41:40	"	"	N/A	64	4
190829A	17/12/19	19:15:01	"	"	N/A	48	4
190829A	20/12/19	19:03:13	"	"	207 ± 21	58	4
190829A	23/12/19	18:51:25	"	"	165 ± 20	45	4
190829A	29/12/19	18:27:49	"	"	187 ± 17	56	4
190829A	03/01/20	18:08:10	"	"	N/A	61	4
190829A	10/01/20	17:40:39	"	"	131±7	38	4
190829A	19/01/20	17:05:16	"	"	275±15	72	4
190829A	24/01/20	16:45:35	"	"	213±18	58	4
190829A	02/02/20	16:25:10	"	"	N/A	168	4

190829A	06/02/20	15:54:30	"	"	156±9	52	4
190829A	28/02/20	14:27:59	"	"	N/A	104	4
190926A	27/09/19	05:46:35	06h 42m 23.74s	+59d 30’ 40"	N/A	36	2
191016A	18/10/19	02:23:17	02h 01m 10.9s	+24d 30’ 03"	N/A	113	2
191031D	11/01/19	13:43:18	18h 53m 06.0s	+47d 38’ 19.3"	N/A	144	4
191031D	11/05/19	12:16:44	"	"	N/A	45	4
191031D	31/10/19	21:33:12	"	"	N/A	137	0.5
191031D	06/11/19	13:01:41	"	"	N/A	61	2
191031D	07/11/19	16:44:08	"	"	N/A	59	3
191031D	11/11/19	15:39:32	"	"	N/A	63	2
191031D	12/11/19	11:59:11	"	"	N/A	70	2
191031D	14/11/19	12:52:10	"	"	N/A	53	2
191031D	21/11/19	11:56:43	"	"	N/A	74	2
191031D	24/11/19	11:27:00	"	"	N/A	70	2
191031D	11/12/19	12:58:42	"	"	N/A	50	2
191031D	15/12/19	11:10:14	"	"	N/A	51	2
191031D	23/12/19	09:17:01	"	"	N/A	41	2
191031D	29/12/19	11:18:59	"	"	N/A	75	1.5

191031D	05/01/20	08:17:54	"	"	N/A	98	1.5
191101A	11/02/19	08:42:26	16h 47m 22s	+43d 44’ 31"	N/A	56	1
191101A	11/05/19	10:14:05	+16h 47m 22s	+43d 44’ 31"	N/A	62	2
191106A	06/11/19	15:03:22	17h 57m 23.9s	+46d 03’ 06.5"	N/A	40	2
191123A	27/11/19	09:57:23	14h 21m 03s	+22d 50’ 30"	N/A	51	2
191220A	20/12/19	13:31:22	18h 45m 79s	+26d 40’ 02"	N/A	85	2
200115	15/01/20	20:16:31	03h 45m 48.9s	+05d 36’ 46.1"	130±9	34	2
200119	19/01/20	09:06:33	18h 58m 34.96s	-08d 14’ 16.4"	156±23	48	4
200122A	22/01/20	01:42:14	13h59m55.40s	+27d 33’ 55"	N/A	130	2
200127A	27/01/20	14:46:22	19h 40m 49.08s	+44d 54’ 34.6"	N/A	182	2
200131A	25/02/20	12:57:05	00h 12m 22.90s	+51.07.25.00"	N/A	55	2
200215A	25/02/20	14:59:44	02h 16m 19.05s	+12d 46’ 13.6"	N/A	70	2
200215A	02/03/20	15:18:01	"	"	N/A	57	2
200216B	26/02/20	00:13:14	10h 41m 44.23s	+19d 28’ 32.4"	N/A	62	2
200219C	15/03/20	06:30:13	17h 30m 02.30s	+10d 32’ 22.2"	N/A	169	4
200219C	05/03/20	04:33:58	"	"	618±27	56	4
200224A	25/02/20	07:56:54	16h 35m 04.14s	+41d 36’ 42.3"	N/A	55	2
200227A	27/02/20	11:59:36	03h 45m 44.62s	+09d 29’ 27.2"	N/A	264	1.5

200306C	06/03/20	22:52:17	13h 14m 18.6s	+11d 15’ 47.7"	N/A	49	2
210104A	18/03/21	17:16:34	07:48:19.30	+11d 24’ 34.2"	N/A	95	4
210321A	21/03/21	18:50:29	05h51m29.69s	+70d 07’ 09.5"	N/A	59	2
210321A	26/03/21	14:36:28	"	"	N/A	42	4
210321A	31/03/21	13:20:58	"	"	N/A	64	4
210323A	24/03/21	07:51:27	21h 11m 48.58s	+25 22m 40.4"	N/A	50	5.2
210323A	25/03/21	08:16:26	"	"	N/A	40	4.5
210323A	27/03/21	05:47:59	"	"	N/A	43	4
210323A	31/03/21	08:41:43	"	"	N/A	75	4
210323A	01/04/21	09:29:39	"	"	N/A	54	2
210413B	16/04/21	18:31:02	12h 10m 13.92s	+55d 57m 54.0"	N/A	56	4
210420B	23/04/21	02:08:08	16:57:17.90	+42d 34’ 12.7"	N/A	30	4
210420B	29/04/21	23:02:04	"	"	199±17	27	4
210420B	01/05/21	22:56:10	"	"	N/A	45	4
210420B	02/05/21	22:14:21	"	"	264±27	55	4
210420B	12/05/21	00:42:27	"	"	N/A	69	4
210420B	12/05/21	22:41:52	"	"	N/A	101	4
210420B	13/05/21	21:24:06	"	"	N/A	225	4

210420B	16/05/21	00:26:43	"	"	N/A	52	4
210420B	17/05/21	22:47:07	"	"	230±29	47	4
210420B	20/05/21	00:34:56	"	"	N/A	85	4
210420B	24/05/21	23:38:23	"	"	N/A	59	4
210420B	26/05/21	20:58:56	"	"	N/A	39	6
210420B	31/05/21	20:27:18	"	"	N/A	94	4
210527A	27/05/21	15:33:52	11h 29m 25.10s	+31d 37’ 05.5"	N/A	100	4
210610A	10/06/21	17:40:20	11h 23m 45.86s	+00d 48’ 46.5"	N/A	47	4
210610A	11/06/21	16:18:37	"	"	N/A	45	4
210610A	12/06/21	16:36:37	"	"	N/A	63	4
210610A	13/06/21	17:31:32	"	"	N/A	100	4
210610A	14/06/21	16:13:48	"	"	N/A	62	4
210610A	15/06/21	16:36:48	"	"	N/A	71	4
210610A	17/06/21	16:45:52	"	"	N/A	124	4
210610A	23/06/21	15:54:22	"	"	N/A	56	5
210610A	01/07/21	15:41:52	"	"	N/A	77	4
210610B	10/06/21	22:14:35	16h 15m 40.52s	+14d 23’ 55.7"	N/A	84	2
210610B	11/06/21	20:51:52	"	"	604±30	42	2

210610B	12/06/21	21:32:50	"	"	470±56	72	4
210610B	13/06/21	22:27:43	"	"	357±27	52	4
210610B	14/06/21	21:09:59	"	"	360±31	62	4
210610B	15/06/21	21:33:00	"	"	271±17	50	4
210610B	17/06/21	21:55:03	"	"	N/A	173	4
210610B	22/06/21	18:14:55	"	"	142±13	43	4
210610B	23/06/21	21:28:26	"	"	N/A	45	4
210610B	24/06/21	18:15:02	"	"	N/A	51	4
210618A	18/06/21	18:43:37	15h 43m 16.87s	+46d 02’ 35.9"	N/A	256	2
210619B	25/06/21	04:12:24	21h 18m 52.39s	+33d 51’ 01.6"	N/A	132	4
210619B	05/07/21	03:51:02	"	"	N/A	543	1
210619B	11/07/21	00:08:59	"	"	N/A	60	4
210619B	13/07/21	00:08:59	"	"	N/A	64	4
210619B	01/08/21	00:31:07	"	"	N/A	87	4
210706A	08/07/21	00:57:41	20h 47m 58.70s	+13d 19’ 01.3"	N/A	133	4
210706A	13/07/21	00:57:58	"	"	N/A	310	4
210706A	29/07/21	22:50:18	"	"	N/A	240	4
210706A	02/08/21	21:30:44	"	"	N/A	105	4

210708B	08/07/21	14:41:26	09h 30m 19s	+14d 28’ 16"	667±20	108	2
210726A	28/07/21	13:52:43	12h 53m 09.7s	+19d 11m 24.6"	N/A	87	0.5
210726A	30/07/21	16:12:27	"	"	N/A	67	4
210726A	02/08/21	15:28:44	"	"	N/A	54	4
210726A	04/08/21	15:56:46	"	"	N/A	93	4
210726A	10/08/21	14:21:22	"	"	N/A	65	4
210726A	20/08/21	12:40:13	"	"	181±23	46	4
210726A	22/08/21	12:54:18	"	"	N/A	51	4
210726A	24/08/21	10:52:45	"	"	N/A	41	5
210726A	27/08/21	10:43:57	"	"	N/A	52	6
210726A	27/08/21	22:24:01	"	"	N/A	52	4
210726A	30/08/21	10:40:09	"	"	N/A	67	6
210726A	31/08/21	11:03:07	"	"	N/A	85	5
210726A	03/09/21	10:11:25	"	"	N/A	33	6
210726A	10/09/21	09:42:54	"	"	N/A	172	5
210726A	17/09/21	09:41:20	"	"	N/A	56	5
210726A	21/09/21	09:02:40	"	"	N/A	131	5
210730A	30/07/21	11:38:12	09:58:16.8	+69d 42’ 10.8"	N/A	82	4

210730A	03/08/21	09:16:49	"	"	N/A	251	4
210807A	10/08/21	04:11:03	05:06:43.90	+58d 14’ 59.2"	N/A	74	4
210807A	13/08/21	07:20:41	"	"	N/A	100	4
210807A	14/08/21	07:37:44	"	"	N/A	97	4
210807A	17/08/21	07:13:56	"	"	N/A	203	4
210820A	22/08/21	23:46:30	01h 22m 33.48s	+04d 36’ 28.2"	N/A	75	4
210820A	26/08/21	03:34:04	"	"	N/A	219	4
210820A	28/08/21	02:26:22	"	"	N/A	136	4
210822A	24/08/21	20:41:08	20h 17m 45.01s	+05° 17’ 00.5"	N/A	140	4
210822A	26/08/21	20:33:17	"	"	N/A	87	4
210822A	29/08/21	19:21:38	"	"	N/A	127	4
210912A	16/09/21	05:24:59	08h 39m 34.27s	+79d 13’ 17.1"	N/A	88	4
210912A	20/09/21	05:22:13	"	"	N/A	77	4
210912A	26/09/21	04:55:37	"	"	N/A	119	4
210919A	24/09/21	06:44:12	05h 20m 55s	+01d 16’ 27.1"	N/A	318	4
210919A	02/10/21	03:35:12	"	"	N/A	76	4
210930A	01/10/21	12:41:37	13h 09m 39.6s	+48d 37’ 48.0"	N/A	106	2
211023B	25/10/21	07:45:50	11h 21m 14s	+39d 08’ 07"	N/A	95	4

211023B	03/11/21	06:20:36	"	"	N/A	71	4
211023B	11/11/21	04:03:25	"	"	N/A	60	4
211024B	26/10/21	07:39:53	10h 18m 51s	+24d 34’ 06"	N/A	84	4
211024B	02/11/21	05:24:39	"	"	N/A	76	4
211024B	10/11/21	04:41:14	"	"	N/A	128	4
211025A	26/10/21	09:40:34	10h 49m 32s	+31d3 0’ 44.4"	N/A	92	2
211221A	21/12/21	22:25:41	05h 15m 35.39s	+00d54’52.4"	N/A	78	2
220101A	13/01/22	13:43:26	00h 05m 25.46s	+31d 46’ 12.7"	262±16	41	4
220101A	15/01/22	13:18:37	"	"	237±19	47	3.5
220101A	17/01/22	12:34:51	"	"	249±15	30	4
220101A	20/01/22	15:34:31	"	"	173±23	33	4
220101A	22/01/22	15:13:42	"	"	200±19	44	4
220101A	24/01/22	15:34:46	"	"	232±43	51	4
220107A	13/01/22	00:21:38	11h 19m 14s	+34d 10’14.3"	N/A	41	4
220118A	19/01/22	04:52:13	12h 49m 06s	+22d 54’ 33"	N/A	78	4

Table A.3: A summary of the observations obtained with *e*MERLIN during my DPhil. T_0 refers to the start time of the observation and ΔT is the observation duration.

GRB	Date	T_0 (UTC)	RA	Dec	Flux density (μJy)	Noise (μJy)	ΔT (hrs)
200826A	30/08/20	20:45:00	00h 27m 08.54s	+34d 01' 38.37"	89±9	18	12
"	31/08/20	21:50:00	"	"	N/A	19	11
"	01/09/20	22:00:00	"	"	N/A	34	10
"	02/09/20	15:00:00	"	"	N/A	22	10
"	03/09/20	16:38:00	"	"	N/A	14	20
"	04/09/20	18:00:00	"	"	N/A	16	19
200907B	08/09/20	20:45:00	05h 56m 04.5s	+06d 54' 38"	N/A	25	16
201015A	04/11/20	21:25:04	23h 37m 16.39s	+053d 24; 56.44"	213± 13	34	8.5
"	07/11/20	22:00:03	"	"	261±12	40	11.75
"	24/01/21	08:55:49	"	"	211±16	57	16.5
201216C	22/12/20	13:00:03	01h 05m 28.88s	+16d 30' 58.00"	180±15	29	6
"	07/01/21	17:15:03	"	"	N/A	34	6
"	14/01/21	13:30:03	"	"	76±8	20	6
210323A	25/03/21	04:35:03	21h 11m 48.58s	+25d 22m 40.40s	N/A	16	8.5
"	26/03/21	02:00:04	"	"	N/A	16	14
"	27/03/21	02:00:04	"	"	N/A	14	14
"	28/03/21	02:00:04	"	"	N/A	19	14
"	29/03/21	12:20:04	"	"	N/A	23	7.3
"	02/04/21	03:00:03	"	"	N/A	32	2.66
"	03/04/21	03:00:03	"	"	N/A	25	2.66
210726A	28/07/21	11:40:40	12h 53m 09.7s	+19d 11m 24.6s	N/A	28	11
"	29/07/21	11:48:13	"	"	N/A	19	11
"	31/07/21	12:00:00	"	"	N/A	29	11
"	02/08/21	11:05:30	"	"	N/A	23	12
"	04/08/21	17:50:03	"	"	N/A	46	4.5
"	05/08/21	09:30:04	"	"	N/A	29	13
"	06/08/21	09:36:04	"	"	N/A	23	13
"	04/09/21	08:15:04	"	"	N/A	20	11
"	23/09/2021	07:30:11	"	"	N/A	27	11

Table A.5: A summary of the GRB observations obtained with MeerKAT during my DPhil. T_0 refers to the start time of the observation and ΔT is the observation duration.

GRB	Date	T_0 (UTC)	RA	Dec	Flux density (μJy)	Noise (μJy)	ΔT (hrs)
181126A	28/11/18	03:32:58	10h 09m 22.6s	-29d 41’ 15"	N/A	29	0.75
190829A	02/09/19	02:10:25	02h 58m 10.6s	-08d 57’ 31.9"	840±130	10	1.33
"	04/09/19	22:20:05	"	"	1040±150	17	0.72
"	06/09/19	22:11:09	"	"	1380±200	17	0.72
"	11/09/19	22:12:36	"	"	1330±190	17	0.72
"	17/09/19	22:51:59	"	"	1520±220	22	0.27
"	23/09/19	04:12:13	"	"	740±110	23	0.47
"	28/09/19	22:48:18	"	"	870±130	22	0.27
"	08/10/19	00:06:32	"	"	690±100	17	0.57
"	17/10/19	02:12:48	"	"	560±80	33	0.38
"	30/10/19	02:42:06	"	"	400±70	20	0.42
200219A	19/02/20	14:31:46	22h 50m 33.02s	-59d 07’ 11.8"	N/A	14	4
"	23/02/20	12:07:20	"	"	N/A	10	4
"	21/03/20	12:28:43	"	"	N/A	7	4
200411A	12/04/20	07:19:52	03h 10m 39.40s	-52d 19’ 03.5"	46±3	6	4

"	14/04/20	11:31:27	"	"	37±4	6	4
"	18/04/20	07:27:42	"	"	37±2	5	4
200522A	23/05/20	06:56:45	00h 22m 43.6s	-00d 16’ 57.8"	N/A	22	4
"	24/05/20	06:01:17	"	"	N/A	28	4
"	29/05/20	02:11:21	"	"	N/A	19	4
"	06/06/20	02:01:22	"	"	N/A	19	4
200907B	08/09/20	01:03:55	05h 56m 03s	+06d 54’ 38"	N/A	8	4
"	10/09/20	01:47:20	"	"	N/A	6	4
"	14/09/20	01:36:00	"	"	N/A	14	4
"	25/09/20	02:17:20	"	"	N/A	10	4
201216C	08/01/21	17:17:26	01h 05m 28.9s	+16d 30’ 58.0"	N/A	9.5	2
"	14/01/21	14:17:49	"	"	95±6	16	2
"	26/01/21	12:42:45	"	"	124±9	15	2
"	09/02/21	12:05:32	"	"	130±5	15	2
210726A	28/07/21	14:24:57	12h 53m 09.8s	+19d 11’ 15.1"	N/A	8	3.4
"	01/08/21	12:28:24	"	"	N/A	9	4
"	07/08/21	12:20:10	"	"	19.4±3.4	6	4
"	19/08/21	12:18:15	"	"	24±1	6	4

"	06/09/21	11:51:06	"	"	21±1	6	4
"	26/09/2021	09:48:16	"	"	N/A	6	4
"	27/12/2021	03:01:07	"	"	N/A	7	4
210928A	30/09/2021	17:07:48	16h 22m 02.66s	-17d 56’ 52.4"	214.6±6.3	16	0.25

Table A.7: A summary of the GRB observations obtained with VLA during my DPhil. T_0 refers to the start time of the observation and ΔT is the observation duration.

GRB	Date	T_0 (UTC)	RA	Dec	Flux density (μJy)	Noise (μJy)	ΔT (hrs)
201216C	29/12/20	00:52:48	01h 05m 28.88s	+16d 30' 58.00"	127 ±12	10	0.17
"	30/12/20	23:26:32	"	"	98±6	10	0.17
"	05/01/21	22:57:00	"	"	130±10	14	0.17
"	22/01/21	21:58:18	"	"	62±5	10	0.17
"	29/01/21	23:39:44	"	"	68±8	14	0.17
"	08/02/21	22:18:24	"	"	50±4	11	0.17

Appendix B

GRB 200826A: MCMC corner plots

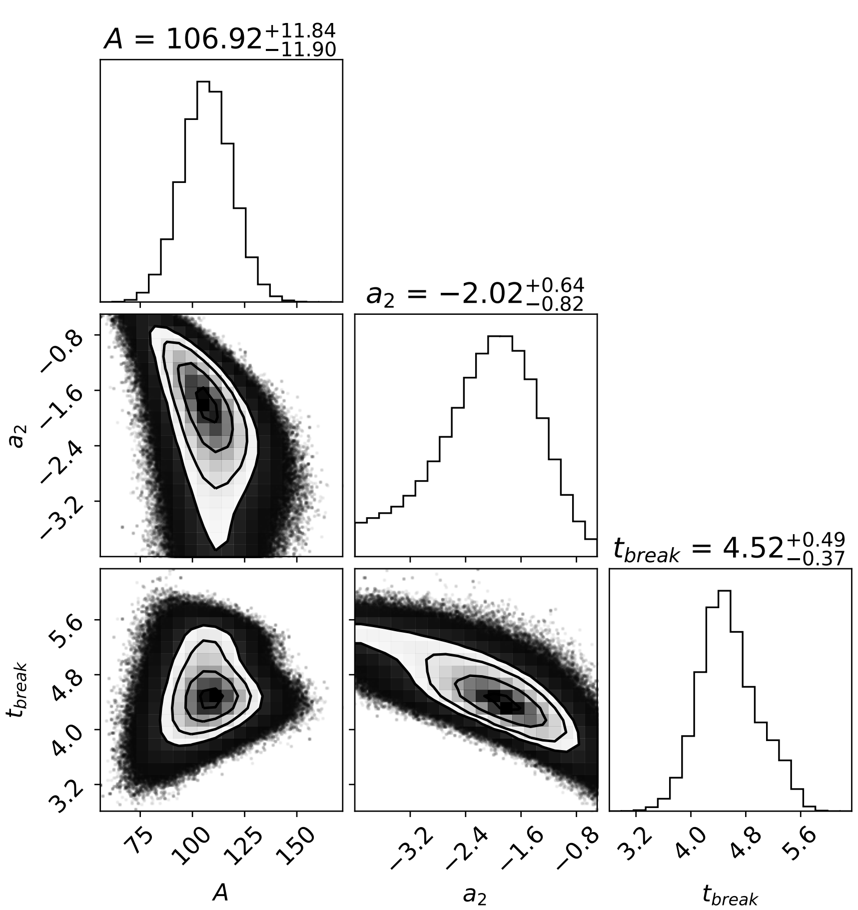

Figure B.1: Result of fitting a broken power law with a fixed rise of $t^{1.75}$ using EMCEE to the eMERLIN light curve. The value α_1 is the exponent of the power law and A is the flux density at the peak of the light curve: time $\mathrm{t_{break}}$.

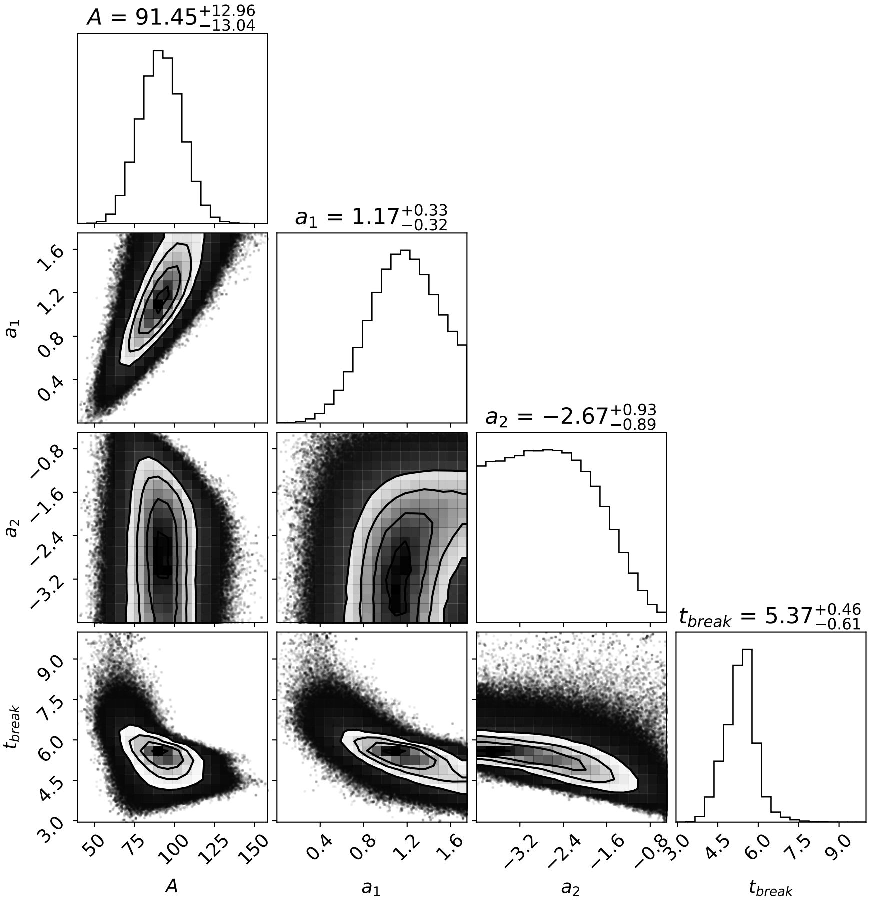

Figure B.2: Result of fitting a broken power law to the eMERLIN and VLA data points. A is the flux density at the peak of the light curve: time t_{break}. α_1 and α_2 are the power law exponents.

Appendix C

GRB 190829A: flux density tables and MCMC corner plots

T-T$_0$ (days)	Flux Jy/beam)	Duration (hrs)
1.34	3890±200	3
2.34	2930±150	3
4.35	2030±100	2
5.33	1960±110	3
6.33	1550±80	3
7.35	1560±80	3
9.33	1310±70	4
10.36	1270±70	2
11.32	1190±90	2
12.32	1170±70	4
13.32	920±50	4
14.32	900±50	4
15.23	830±50	4
16.31	770±40	4

17.31	650±40	4
18.31	630±40	4
19.32	540±30	3.3
20.30	640±30	4
21.30	540±40	4
22.30	620±30	4
23.30	540±40	3.5
24.25	540±50	2
27.24	550±40	1.5
28.28	490±40	4
29.28	410±20	2
32.30	500±30	4
34.27	350±40	4
34.24	250±40	2
35.24	370±30	2
36.26	300±20	3
38.25	310±30	4
39.29	310±20	4
40.25	290±20	4
41.22	260±10	2
45.23	220±20	4
53.23	280±20	3
58.21	260±20	4
64.18	<230	4
67.21	150±10	3
71.17	210±20	3
73.16	250±20	4

78.14	190±10	3
81.13	170±10	4
85.12	180±20	4
88.11	230±40	4
95.10	240±30	4
105.07	<190	4
110.06	<180	4
113.05	210±20	4
116.04	170±20	4
122.02	190±20	4
127.01	<180	4
142.96	280±20	4

Table C.1: List of observations made using AMI-LA at 15.5 GHz. Each with the time since burst (T_0), the flux density and uncertainties (including statistical and 5 % calibration error) and duration. On occasions where the source was not detected we provide a 3 σ upper limit with the prefix ‘<’.

T-T_0(days)	Flux (μJy/beam)	Duration (hrs)
3.28	840±130	1.33
6.11	1040±150	0.72
9.10	1380±200	0.72
13.10	1330±190	0.72
19.13	1520±220	0.27
24.34	740±110	0.47
31.12	870±130	0.27
39.18	690±100	0.57
48.26	560±80	0.38
61.29	400±70	0.42

Table C.2: List of observations made with MeerKAT at 1.3 GHz. Each with the time since burst (T_0), the flux density with uncertainties (including statistical and 10 % calibration error) and duration.

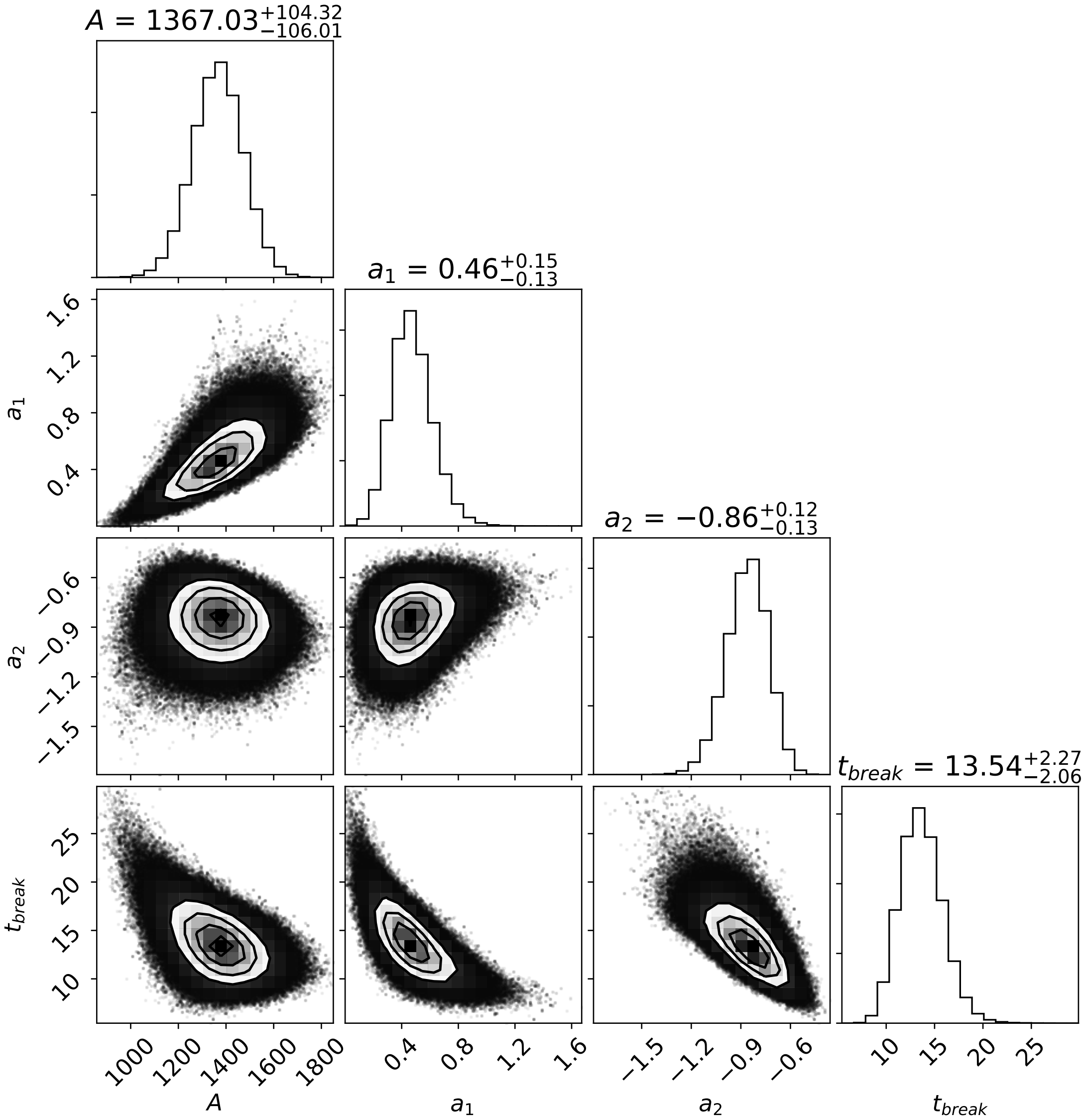

Figure C.1: Corner plots from MCMC fitting code for fitting a broken power law to the 1.3 GHz MeerKAT data. A is the flux density at the peak of the light curve: time t_{break}. α_1 and α_2 are the power law exponents.

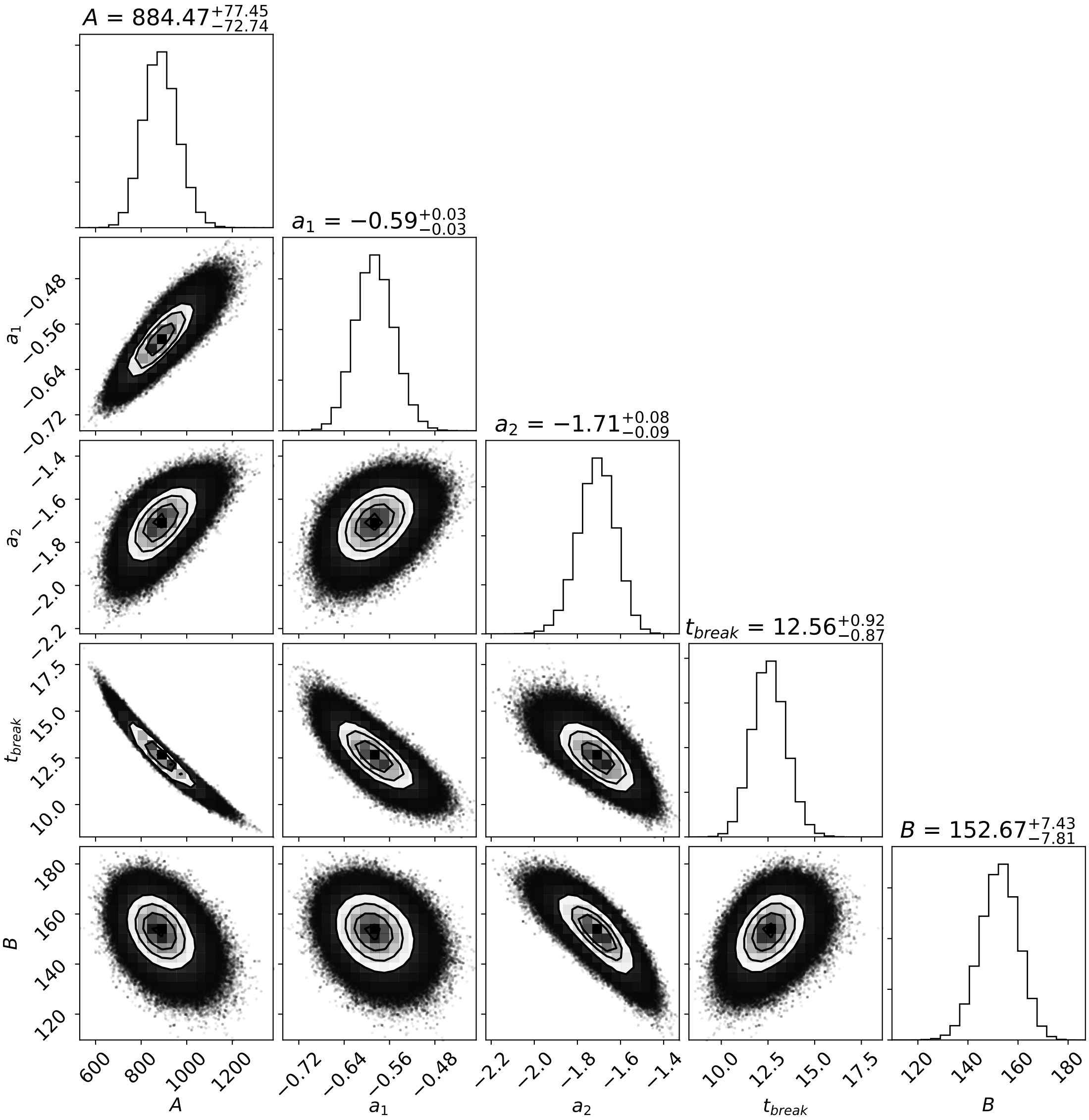

Figure C.2: Corner plots from MCMC fitting code to fit a broken power law with a constant component to 15.5GHz AMI-LA data. *A* is the flux density at the peak of the light curve: time t_{break}. α_1 and α_2 are the power law exponents. *B* is the flux density of the constant plateau component attributed to the host galaxy.

Appendix D

Swift J1858.6-0814 radio data

Start time (MJD)	Flux density (μJy/beam)	Duration (hrs)
58424.574	310±50	2
58425.712	390±40	2
58427.546	590±60	4
58430.605	390±40	2
58440.540	360±30	3
58454.537	300±40	3
58464.501	330±20	4
58468.440	360±30	4
58475.421	<200	4
58482.523	310±30	4
58489.385	180±40	4
58496.363	280±20	4
58503.344	300±30	4
58513.350	<170	4
58517.185	340±40	4
58524.270	<230	4

58531.266	370±30	6
58538.199	160±10	6
58544.306	<130	6
58559.144	200±20	6
58565.211	<110	6
58587.060	180±20	5
58606.013	<270	6
58614.026	<230	6
58620.983	<450	6
58634.955	<230	8
58640.913	<140	6
58648.928	<140	6
58655.872	<370	7
58662.853	<170	7
58669.871	<220	6
58676.818	<250	8
58686.949	160±10	6
58697.844	260±10	4
58700.836	200±20	4
58701.852	300±20	3.5
58711.846	<340	3
58725.773	220±20	4
58729.189	180±10	6
58732.748	240±20	3.8
58739.741	280±20	4
58746.710	200±10	4
58760.672	160±10	4

58775.631	<140	4
58781.614	<360	1
58795.576	240±30	4
58802.557	170±10	4
58809.538	<190	4
58816.519	120±10	4
58822.500	350±60	2
58851.423	<230	4
58858.404	<140	4
58867.380	160±20	4
58872.366	290±20	4
58879.350	370±50	4
58886.330	200±10	4
58911.260	<290	4
58914.251	<180	4
58924.224	<200	4

Table D.1: List of observations made with AMI-LA with 15.5 GHz. Each with date, start time, the flux density and duration. The uncertainties quoted are the statistical error and a 5% calibration uncertainty added in quadrature. For epochs where we did not detect J1858, we provide a 3σ upper limit with the prefix '<'.

Start Time (MJD)	Flux density (μJy/beam)	Duration (hrs)
58432.505	126±20	0.25
58439.491	84±12	0.25
58446.458	114±14	0.25
58454.434	132±15	0.25
58460.416	126±17	0.25
58467.626	101±13	0.25
58474.592	62±14	0.25
58481.571	<57	0.25
58488.107	119±18	0.25
58530.178	993±101	0.25
58543.126	102±17	0.25
58551.081	76±9	0.25
58560.121	<60	0.25
58567.121	<48	0.25
58574.107	85±15	0.25
58582.101	94±10	0.25
58588.101	<57	0.25
58593.123	57±9	0.25
58602.193	<57	0.25
58607.997	62±7	0.25
58614.942	<63	0.25
58621.931	<57	0.25
58626.053	<54	0.25
58700.766	83±9	1.0
58910.193	<63	0.25

Table D.2: List of observations made with MeerKAT at 1.4 GHz. Each with date, start time, the flux density and duration. The uncertainties are calculated by adding the statistical and 10% calibration uncertainty in quadrature. On occasions where the source was not detected we provide a 3σ upper limit with the prefix '<'.

Table D.3: List of the spectral index calculations of both the new data presented in this table as well as epochs used from Van den Eijnden et al. (2020). This data is shown in the second panel of Figure 4.6.

Date (MJD)	Spectral Index	Frequency Range (GHz)
58530.178	0.9 ± 0.5	1.0-1.6
58432.227	1.1 ± 0.1	1.3-4.5
58439.168	1.1 ± 0.1	1.3-4.5
58700.905	0.6 ± 0.1	1.3-4.5
58566.800	0.8 ± 0.1	1.3-4.5
58431.954	0.4 ± 0.2	4.5-7.5
58436.072	0.3 ± 0.2	4.5-7.5
58437.060	0.1 ± 0.1	4.5-7.5
58438.835	0.6 ± 0.2	4.5-7.5
58443.748	0.6 ± 0.3	4.5-7.5
58443.922	0.6 ± 0.3	4.5-7.5
58534.498	0.0 ± 0.2	4.5-7.5
58566.479	0.7 ± 0.3	4.5-7.5
58701.035	0.1 ± 0.1	4.5-7.5
58430.207	0.4 ± 0.1	5.5-9.0
58430.405	-0.1± 0.1	5.5-15.5
58439.491	0.6 ± 0.1	1.3-15.5
58454.434	0.3 ± 0.1	1.3-15.5
58467.630	0.5 ± 0.1	1.3-15.5
58474.592	0.7 ± 0.1	1.3-15.5
58488.508	0.2 ± 0.1	1.3-15.5
58543.126	0.0 ± 0.1	1.3-15.5
58607.997	0.8 ± 0.1	1.3-15.5
58560.121	0.5 ± 0.1	1.3-15.5
58614.956	0.7 ± 0.1	1.3-15.5
58700.776	0.5 ± 0.1	1.3-15.5

Bibliography

Abbott B. P., et al., 2017a, ApJL, 848, L12

Abbott B. P., et al., 2017b, ApJL, 848, L13

Abdalla H., et al., 2019, Nature, 575, 464

Ackermann M., et al., 2013, ApJS, 209, 11

Ackermann M., et al., 2014, Science, 343, 42

Aguilera-Dena D. R., Langer N., Moriya T. J., Schootemeijer A., 2018, ApJ, 858, 115

Ahumada T., et al., 2020a, GRB Coordinates Network, 28295, 1

Ahumada T., Singer L., Kumar H., Reusch S., Ztf Growth Collaborations 2020b, GRB Coordinates Network, 28727, 1

Ajello M., et al., 2019, ApJ, 878, 52

Aksulu M. D., Wijers R. A. M. J., Van Eerten H. J., Van der Horst A. J., 2022, MNRAS, 511, 2848

Alexander K. D., et al., 2019, ApJ, 870, 67

Alexander K. D., van Velzen S., Horesh A., Zauderer B. A., 2020a, Space Sci. Rev., 216, 81

Alexander K. D., Fong W., Paterson K., Rastinejad J., 2020b, GRB Coordinates Network, 28302, 1

Alexander K. D., et al., 2021, GRB Coordinates Network, 30218, 1

Alpar M. A., Cheng A. F., Ruderman M. A., Shaham J., 1982, Nature, 300, 728

Amati L., et al., 2002, A&A, 390, 81

Anderson G. E., et al., 2014, MNRAS, 440, 2059

Anderson G. E., et al., 2018, MNRAS, 473, 1512

Andersson A., et al., 2022, Monthly Notices of the Royal Astronomical Society, 513, 3482

Andreoni I., et al., 2022a, Transient Name Server AstroNote, 38, 1

Andreoni I., et al., 2022b, GRB Coordinates Network, 31590, 1

Archibald A. M., et al., 2009, Science, 324, 1411

Axelsson M., Bissaldi E., Cheung C. C., La Mura G., 2021, The Astronomer's Telegram, 14948, 1

Backer D. C., Kulkarni S. R., Heiles C., Davis M. M., Goss W. M., 1982, Nature, 300, 615

Bahramian A., et al., 2018, Radio/X-ray correlation database for X-ray binaries, doi:10.5281/zenodo.1252036, `https://doi.org/10.5281/zenodo.1252036`

Barniol Duran R., Nakar E., Piran T., 2013, ApJ, 772, 78

Barthelmy S. D., et al., 2005, Space Sci. Rev., 120, 143

Beardmore A. P., et al., 2020, GRB Coordinates Network, 29061, 1

Belkin S., Pozanenko A., Krugov M., Levkina P., Klunko E., Pankov N., GRB IKI FuN 2020, GRB Coordinates Network, 29210, 1

Bell A. R., 1978, MNRAS, 182, 147

Belloni T. M., Motta S. E., 2016, Transient Black Hole Binaries. "Springer", p. 61, doi:10.1007/978-3-662-52859-4_2

Berger E., 2007, ApJ, 670, 1254

Berger E., Kulkarni S. R., Frail D. A., 2004, ApJ, 612, 966

Berger E., et al., 2005, Nature, 438, 988

Bernardini M. G., et al., 2021, GRB Coordinates Network, 30523, 1

Berti A., et al., 2019, in 36th International Cosmic Ray Conference (ICRC2019). p. 633 (`arXiv:1909.02798`)

Bietenholz M. F., Bartel N., Argo M., Dua R., Ryder S., Soderberg A., 2021, ApJ, 908, 75

Blanch O., et al., 2020a, GRB Coordinates Network, 28659, 1

Blanch O., et al., 2020b, GRB Coordinates Network, 29075, 1

Blandford R. D., Königl A., 1979, ApJ, 232, 34

Blandford R. D., McKee C. F., 1976, Physics of Fluids, 19, 1130

Blandford R., Meier D., Readhead A., 2019, ARA&A, 57, 467

Bozzo E., Ferrigno C., Savchenko V., Ducci L., Kuulkers E., 2018, The Astronomer's Telegram, 12167

Bright J. S., et al., 2018a, MNRAS, 475, 4011

Bright J., Fender R., Motta S., Rhodes L., Titterington D., Perrott Y., 2018b, The Astronomer's Telegram, 12184, 1

Bright J. S., et al., 2019, MNRAS, 486, 2721

Bright J. S., et al., 2020, Nature Astronomy, 4, 697

Buisson D. J. K., et al., 2020a, MNRAS, 499, 793

Buisson D. J. K., Altamirano D., Remillard R., Arzoumanian Z., Gendreau K., Gandhi P., Vincentelli F., 2020b, The Astronomer's Telegram, 13536, 1

Buisson D. J. K., et al., 2020c, The Astronomer's Telegram, 13563

Buisson D. J. K., et al., 2021, MNRAS, 503, 5600

Burrows D. N., et al., 2005, Space Sci. Rev., 120, 165

CHIME/FRB Collaboration et al., 2021, ApJS, 257, 59

Campana S., Lazzati D., Perna R., Grazia Bernardini M., Nava L., 2021, A&A, 649, A135

Cano Z., et al., 2014, Astron. Astrophys, 568, A19

Cao D., Wang X.-Y., 2012, ApJ, 761, 111

Carotenuto F., et al., 2021, MNRAS, 504, 444

Castro Segura N., et al., 2022, Nature, 603, 52

Castro-Tirado A. J., et al., 2019, GRB Coordinates Network, 23708, 1

Chandra P., Frail D. A., 2012, ApJ, 746, 156

Chandra P., et al., 2008, ApJ, 683, 924

Chandra P., Nayana A. J., Bhattacharya D., Cenko S. B., Corsi A., 2018, GRB Coordinates Network, 23073, 1

Chandra P., Purkayastha S., Bhalerao V., Kumar H., Kasliwal M., 2020, GRB Coordinates Network, 28410, 1

Chen W. J., Urata Y., Huang K., Takahashi S., Petitpas G., Asada K., 2020, ApJ, 891, L15

Chevalier R. A., 1998, ApJ, 499, 810

Chevalier R. A., Li Z.-Y., 1999, ApJL, 520, L29

Chevalier R. A., Li Z.-Y., 2000, ApJ, 536, 195

Coppejans D. L., Knigge C., 2020, New Astron. Rev., 89, 101540

Coppejans D. L., et al., 2020, ApJ, 895, L23

Corbel S., Fender R. P., Tzioumis A. K., Nowak M., McIntyre V., Durouchoux P., Sood R., 2000, A&A, 359, 251

Corbel S., Fender R. P., Tzioumis A. K., Tomsick J. A., Orosz J. A., Miller J. M., Wijnands R., Kaaret P., 2002, Science, 298, 196

Corbel S., Nowak M. A., Fender R. P., Tzioumis A. K., Markoff S., 2003, A&A, 400, 1007

Corbel S., Fender R. P., Tomsick J. A., Tzioumis A. K., Tingay S., 2004, ApJ, 617, 1272

Cordes J. M., Lazio T. J. W., 2002, arXiv e-prints, pp astro–ph/0207156

Cucchiara A., et al., 2011, ApJ, 736, 7

D'Ai A., et al., 2020, GRB Coordinates Network, 28300, 1

De Colle F., Kumar P., Aguilera-Dena D. R., 2018, ApJ, 863, 32

De Naurois M., H. E. S. S. Collaboration 2019, GRB Coordinates Network, 25566, 1

De Ugarte Postigo A., Thoene C., Agui Fernandez J. F., Blazek M., Kann D. A., Fynbo J. P. U., Izzo L., Garcia Alvarez D., 2021, GRB Coordinates Network, 30194, 1

Degenaar N., et al., 2016, MNRAS, 461, 4049

Deller A. T., et al., 2015, ApJ, 809, 13

Dermer C. D., Giebels B., 2016, Comptes Rendus Physique, 17, 594

Dichiara S., et al., 2019, GRB Coordinates Network, 25552, 1

Done C., Gierliński M., Kubota A., 2007, A&ARv, 15, 1

Driessen L. N., et al., 2020, MNRAS, 491, 560

Driessen L. N., et al., 2022, MNRAS, 512, 5037

Duchêne G., Kraus A., 2013, ARA&A, 51, 269

Eichler D., Livio M., Piran T., Schramm D. N., 1989, Nature, 340, 126

Espinasse M., Fender R., 2018, MNRAS, 473, 4122

Espinasse M., et al., 2020, ApJ, 895, L31

Evans P. A., Swift-XRT Team 2021, GRB Coordinates Network, 29280, 1

Evans P. A., et al., 2007, A&A, 469, 379

Evans P. A., et al., 2009, MNRAS, 397, 1177

Evans P. A., et al., 2010, A&A, 519, A102

Evans P., Goad M., Osborne J., Beardmore A., 2019, GRB Coordinates Network, 25567, 1

Fan Y.-Z., Piran T., Narayan R., Wei D.-M., 2008, MNRAS, 384, 1483

Fender R. P., 2001, MNRAS, 322, 31

Fender R., Belloni T., 2004, ARA&A, 42, 317

Fender R., Bright J., 2019, MNRAS, 489, 4836

Fender R., Gallo E., 2014, Space Sci. Rev., 183, 323

Fender R. P., Pooley G. G., 2000, MNRAS, 318, L1

Fender R. P., Garrington S. T., McKay D. J., Muxlow T. W. B., Pooley G. G., Spencer R. E., Stirling A. M., Waltman E. B., 1999a, MNRAS, 304, 865

Fender R., et al., 1999b, ApJ, 519, L165

Fender R. P., Belloni T. M., Gallo E., 2004a, MNRAS, 355, 1105

Fender R., Wu K., Johnston H., Tzioumis T., Jonker P., Spencer R., Van der Klis M., 2004b, Nature, 427, 222

Fender R. P., Dahlem M., Homan J., Corbel S., Sault R., Belloni T. M., 2007, MNRAS, 380, L25

Fender R. P., Homan J., Belloni T. M., 2009, MNRAS, 396, 1370

Fender R., et al., 2016, in MeerKAT Science: On the Pathway to the SKA. p. 13 (`arXiv:1711.04132`)

Fender R., Bright J., Mooley K., Miller-Jones J., 2019, MNRAS, 490, L76

Fermi E., 1949, Phys. Rev., 75, 1169

Fermi GBM Team 2019, GRB Coordinates Network, 25551, 1

Fermi GBM Team 2020, GRB Coordinates Network, 28284, 1

Filgas R., et al., 2011, A&A, 526, A113

Fitzpatrick E. L., 1999, PASP, 111, 63

Fletcher C., Meegan C., 2021, GRB Coordinates Network, 30913, 1

Fomalont E. B., Geldzahler B. J., Bradshaw C. F., 2001, ApJ, 558, 283

Fong W., et al., 2014, ApJ, 780, 118

Fong W., Berger E., Margutti R., Zauderer B. A., 2015, ApJ, 815, 102

Fong W., et al., 2021, ApJ, 906, 127

Foreman-Mackey D., Hogg D. W., Lang D., Goodman J., 2013, PASP, 125, 306

Fraija N., et al., 2019, ApJ, 885, 29

Frail D. A., Kulkarni S. R., Nicastro L., Feroci M., Taylor G. B., 1997, Nature, 389, 261

Frail D. A., et al., 2000a, ApJ, 534, 559

Frail D. A., Waxman E., Kulkarni S. R., 2000b, ApJ, 537, 191

Frail D. A., et al., 2001, ApJ, 562, L55

Frail D. A., Soderberg A. M., Kulkarni S. R., Berger E., Yost S., Fox D. W., Harrison F. A., 2005, ApJ, 619, 994

Fruchter A. S., et al., 2006, Nature, 441, 463

Fuller J., Ro S., 2018, MNRAS, 476, 1853

Fynbo J. P. U., Izzo L., De Ugarte Postigo A., Malesani D. B., Pursimo T., 2021, GRB Coordinates Network, 30182, 1

Galama T. J., et al., 1998, Nature, 395, 670

Galeev A. A., Rosner R., Vaiana G. S., 1979, ApJ, 229, 318

Gallo E., Fender R. P., Pooley G. G., 2003, MNRAS, 344, 60

Gallo E., Degenaar N., Van den Eijnden J., 2018, MNRAS, 478, L132

Gao H., Lei W.-H., Zou Y.-C., Wu X.-F., Zhang B., 2013, New Astron. Rev., 57, 141

Garrington S., Beswick R., 2016, Astronomy and Geophysics, 57, 3.28

Gehrels N., et al., 2004, ApJ, 611, 1005

Gehrels N., Ramirez-Ruiz E., Fox D. B., 2009, Annu. Rev. Astron. Astrophys., 47, 567

Gezari S., Halpern J. P., Komossa S., Grupe D., Leighly K. M., 2003, ApJ, 592, 42

Ghirlanda G., Ghisellini G., Firmani C., 2005, MNRAS, 361, L10

Giacconi R., Gursky H., Waters J. R., 1964, Nature, 204, 981

Gokuldass P., Morris D., Orange N., Strausbaugh R., Cucchiara A., 2021, GRB Coordinates Network, 29674, 1

Gold T., 1968, Nature, 218, 731

Goldstein A., Connaughton V., Briggs M. S., Burns E., 2016, ApJ, 818, 18

Goodman J., 1997, New Astron., 2, 449

Granot J., Sari R., 2002, ApJ, 568, 820

Granot J., Van der Horst A. J., 2014, Publ. Astron. Soc. Australia, 31, e008

Granot J., Panaitescu A., Kumar P., Woosley S. E., 2002, ApJ, 570, L61

Güdel M., 2002, ARA&A, 40, 217

Gusinskaia N. V., et al., 2017, MNRAS, 470, 1871

Güver T., Özel F., 2009, MNRAS, 400, 2050

H. E. S. S. Collaboration et al., 2014, Astron. Astrophys, 565, A16

H. E. S. S. Collaboration et al., 2021, Science, 372, 1081

Hajela A., et al., 2021, arXiv e-prints, p. arXiv:2104.02070

Halpern J. P., Gezari S., Komossa S., 2004, ApJ, 604, 572

Hare J., et al., 2020, ApJ, 890, 57

Harrison F. A., et al., 2001, ApJ, 559, 123

Hasinger G., Van der Klis M., 1989, A&A, 225, 79

Heintz K. E., Fynbo J. P. U., Jakobsson P., Xu D., Perley D. A., Malesani D. B., Viuho J., 2019, GRB Coordinates Network, 25563, 1

Hewish A., Bell S. J., Pilkington J. D. H., Scott P. F., Collins R. A., 1968, Nature, 217, 709

Hewitt D. M., et al., 2020, MNRAS, 496, 2542

Heywood I., 2020, oxkat: Semi-automated imaging of MeerKAT observations (ascl:2009.003)

Hickish J., et al., 2018, MNRAS, 475, 5677

Hirata K., et al., 1987, Phys. Rev. Lett., 58, 1490

Hjellming R. M., Rupen M. P., 1995, Nature, 375, 464

Hjorth J., et al., 2003, Nature, 423, 847

Ho A. Y. Q., et al., 2020, ApJ, 895, 49

Hoischen C., et al., 2022, arXiv e-prints, p. arXiv:2203.05458

Homan J., et al., 2006, The Astronomer's Telegram, 725, 1

Homan J., et al., 2007, ApJ, 656, 420

Homan J., et al., 2010, ApJ, 719, 201

Horesh A., Cenko S. B., Arcavi I., 2021, Nature Astronomy, 5, 491

Hovatta T., Nieppola E., Tornikoski M., Valtaoja E., Aller M. F., Aller H. D., 2008, A&A, 485, 51

Izzo L., Malesani D. B., Zhu Z. P., Xu D., De Ugarte Postigo A., Pursimo T., 2020a, GRB Coordinates Network, 28661, 1

Izzo L., Malesani D. B., Kann D. A., 2020b, GRB Coordinates Network, 29066, 1

Jacovich T. E., Beniamini P., Van der Horst A. J., 2021, MNRAS, 504, 528

Jakobsson P., Hjorth J., Fynbo J. P. U., Watson D., Pedersen K., Björnsson G., Gorosabel J., 2004, ApJ, 617, L21

Janssen M., et al., 2021, Nature Astronomy, 5, 1017

Jelinek M., et al., 2020, GRB Coordinates Network, 29070, 1

Jin Z.-P., et al., 2018, ApJ, 857, 128

Jonas J., MeerKAT Team 2016, in MeerKAT Science: On the Pathway to the SKA. p. 1

Kamble A., Misra K., Bhattacharya D., Sagar R., 2009, MNRAS, 394, 214

Kann D. A., De Ugarte Postigo A., Thoene C., Blazek M., Agui Fernandez J. F., Martin-Fernandez P., 2021, GRB Coordinates Network, 30391, 1

Kellermann K. I., Pauliny-Toth I. I. K., 1969, ApJ, 155, L71

Kennea J. A., Krimm H. A., 2018, The Astronomer's Telegram, 12160

Kent B. R., et al., 2018, in American Astronomical Society Meeting Abstracts #231. p. 342.14

Keshet U., Katz B., Spitkovsky A., Waxman E., 2009, ApJ, 693, L127

Kim V., Pozanenko A., Krugov M., Belkin S., Pankov N., IKI FuN G., 2021, GRB Coordinates Network, 30384, 1

Klebesadel R. W., Strong I. B., Olson R. A., 1973a, The Astrophysical Journal, 182, L85

Klebesadel R. W., Strong I. B., Olson R. A., 1973b, ApJL, 182, L85

Kouveliotou C., Meegan C. A., Fishman G. J., Bhat N. P., Briggs M. S., Koshut T. M., Paciesas W. S., Pendleton G. N., 1993, ApJL, 413, L101

Krimm H. A., et al., 2013, ApJS, 209, 14

Krimm H. A., et al., 2018, The Astronomer's Telegram, 12151

Krühler T., et al., 2011, A&A, 534, A108

Kumar P., Barniol Duran R., Bošnjak Ž., Piran T., 2013, MNRAS, 434, 3078

Lamb G. P., et al., 2019, ApJ, 883, 48

Lan M.-X., Wu X.-F., Dai Z.-G., 2018, ApJ, 860, 44

Langer N., 1989, A&A, 210, 93

Langer N., Hamann W. R., Lennon M., Najarro F., Pauldrach A. W. A., Puls J., 1994, A&A, 290, 819

Laskar T., 2022, GRB Coordinates Network, 31385, 1

Laskar T., et al., 2013, ApJ, 776, 119

Laskar T., et al., 2014, ApJ, 781, 1

Laskar T., et al., 2019, ApJ, 878, L26

Lasota J.-P., 2001, New Astron. Rev., 45, 449

Leung J. K., et al., 2021, MNRAS, 503, 1847

Levan A., Crowther P., De Grijs R., Langer N., Xu D., Yoon S.-C., 2016, Space Sci. Rev., 202, 33

Levan A. J., Campana S., Kann D. A., D'Avanzo P., 2021, GRB Coordinates Network, 30381, 1

Lewin W. H. G., Vacca W. D., Basinska E. M., 1984, ApJ, 277, L57

Lightfoot J. F., Glencross W. M., 1986, MNRAS, 221, 47P

Lloyd-Ronning N., 2018, Galaxies, 6, 103

Lorimer D., Kramer M., 2005, Handbook of Pulsar Astronomy. Cambridge Observing Handbooks for Research Astronomers, Cambridge University Press, `https://books.google.co.uk/books?id=OZ8tdN6qJcsC`

Lorimer D. R., Bailes M., McLaughlin M. A., Narkevic D. J., Crawford F., 2007, Science, 318, 777

Lovell J. E. J., et al., 2008, ApJ, 689, 108

Ludlam R. M., et al., 2018, The Astronomer's Telegram, 12158, 1

Ludlam R. M., et al., 2019, ApJ, 873, 99

MAGIC Collaboration et al., 2019a, Nature, 575, 455

MAGIC Collaboration et al., 2019b, Nature, 575, 459

Macquart J. P., et al., 2020, Nature, 581, 391

Margutti R., et al., 2018, ApJ, 856, L18

Marscher A. P., Jorstad S. G., Gómez J.-L., Aller M. F., Teräsranta H., Lister M. L., Stirling A. M., 2002, Nature, 417, 625

Matsuoka M., et al., 2009, PASJ, 61, 999

Mauch T., et al., 2020, ApJ, 888, 61

Mazzali P. A., Pian E., Bufano F., Ashall C., 2021, MNRAS, 505, 4106

Mazzola S. M., et al., 2021, arXiv e-prints, p. arXiv:2108.00729

McClintock J. E., Remillard R. A., 2006, in , Vol. 39, Compact stellar X-ray sources. pp 157–213

McMullin J. P., Waters B., Schiebel D., Young W., Golap K., 2007a, CASA Architecture and Applications. Astronomical Society of the Pacific, p. 127

McMullin J. P., Waters B., Schiebel D., Young W., Golap K., 2007b, in Shaw R. A., Hill F., Bell D. J., eds, Astronomical Society of the Pacific Conference Series Vol. 376, Astronomical Data Analysis Software and Systems XVI. p. 127

Metzger B. D., Piro A. L., 2014, MNRAS, 439, 3916

Metzger B. D., Giannios D., Mimica P., 2012, MNRAS, 420, 3528

Migliari S., Fender R. P., 2006, MNRAS, 366, 79

Migliari S., Fender R. P., Rupen M., Jonker P. G., Klein-Wolt M., Hjellming R. M., Van der Klis M., 2003, MNRAS, 342, L67

Migliari S., Fender R. P., Rupen M., Wachter S., Jonker P. G., Homan J., Van der Klis M., 2004, MNRAS, 351, 186

Miller-Jones J. C. A., et al., 2010, ApJ, 716, L109

Miller-Jones J. C. A., et al., 2012, MNRAS, 421, 468

Mimica P., Giannios D., Metzger B. D., Aloy M. A., 2015, Monthly Notices of the Royal Astronomical Society, 450, 2824

Mirabel I. F., Rodríguez L. F., 1994, Nature, 371, 46

Misra K., et al., 2021, MNRAS, 504, 5685

Mitsuda K., et al., 1984, PASJ, 36, 741

Miyamoto S., Kitamoto S., 1991, ApJ, 374, 741

Moldon J., 2021, eMCP: e-MERLIN CASA pipeline (ascl:2109.006)

Monageng I. M., Motta S. E., Fender R., Yu W., Woudt P. A., Tremou E., Miller-Jones J. C. A., Van der Horst A. J., 2021, MNRAS, 501, 5776

Mooley K. P., Frail D. A., Ofek E. O., Miller N. A., Kulkarni S. R., Horesh A., 2013, ApJ, 768, 165

Mooley K. P., et al., 2016, ApJ, 818, 105

Mooley K. P., et al., 2018a, Nature, 561, 355

Mooley K. P., et al., 2018b, ApJL, 868, L11

Mooley K. P., et al., 2022, ApJ, 924, 16

Morsony B. J., Lazzati D., Begelman M. C., 2007, ApJ, 665, 569

Muñoz-Darias T., Fender R. P., Motta S. E., Belloni T. M., 2014, MNRAS, 443, 3270

Muñoz-Darias T., Jimenez-Ibarra F., Armas Padilla M., Casares J., Cuneo V., Panizo-Espinar G., Sanchez-Sierras J., Torres M. A. P., 2019, The Astronomer's Telegram, 12881, 1

Muñoz-Darias T., et al., 2020, ApJ, 893, L19

Myers S. T., Baum S. A., Chandler C. J., 2014, in American Astronomical Society Meeting Abstracts #223. p. 236.01

Nakar E., Piran T., 2017, ApJ, 834, 28

Nakar E., Ando S., Sari R., 2009, ApJ, 703, 675

Narayan R., Yi I., 1995, The Astrophysical Journal, 452, 710

Negoro H., et al., 2020, The Astronomer's Telegram, 13455, 1

Novikov I. D., Thorne K. S., 1973, in Black Holes (Les Astres Occlus). pp 343–450

Oates S. R., Beardmore A. P., Swift/UVOT Team 2020, GRB Coordinates Network, 29071, 1

Offringa A. R., et al., 2014, MNRAS, 444, 606

Osten R. A., 2008, arXiv e-prints, p. arXiv:0801.2573

Pacholczyk A. G., 1970, Radio astrophysics. Nonthermal processes in galactic and extragalactic sources. W. H. Freeman and Company

Page K. L., Gropp J. D., Kennea J. A., Marshall F. E., Palmer D. M., Siegel M. H., Neil Gehrels Swift Observatory Team 2021, GRB Coordinates Network, 30170, 1

Paice J. A., Gandhi P., Dhillon V. S., Marsh T. R., Green M., Breedt E., 2018, The Astronomer's Telegram, 12197, 1

Panaitescu A., Mészáros P., Rees M. J., 1998, ApJ, 503, 314

Panurach T., et al., 2021, ApJ, 923, 88

Parikh A. S., Wijnands R., Altamirano D., 2020, The Astronomer's Telegram, 13725, 1

Penacchioni A. V., Ruffini R., Bianco C. L., Izzo L., Muccino M., Pisani G. B., Rueda J. A., 2013, A&A, 551, A133

Peng F., Königl A., Granot J., 2005, ApJ, 626, 966

Penninx W., Lewin W. H. G., Zijlstra A. A., Mitsuda K., van Paradijs J., 1988, Nature, 336, 146

Perley R., et al., 2009a, IEEE Proceedings, 97, 1448

Perley D. A., et al., 2009b, AJ, 138, 1690

Perley D. A., et al., 2014, ApJ, 781, 37

Perrott Y. C., et al., 2013, MNRAS, 429, 3330

Pietka M., Fender R. P., Keane E. F., 2014, Monthly Notices of the Royal Astronomical Society, 446, 3687

Pietka M., Staley T. D., Pretorius M. L., Fender R. P., 2017, MNRAS, 471, 3788

Piran T., 2003, Nature, 422, 268

Platts E., Weltman A., Walters A., Tendulkar S. P., Gordin J. E. B., Kandhai S., 2019, Phys. Rep., 821, 1

Predehl P., Schmitt J. H. M. M., 1995, A&A, 500, 459

Racusin J. L., et al., 2008, Nature, 455, 183

Rajwade K. M., et al., 2019, The Astronomer's Telegram, 12499

Ramirez-Ruiz E., Celotti A., Rees M. J., 2002, MNRAS, 337, 1349

Rana V., et al., 2016, ApJ, 821, 103

Rani B., La Mura G., Cheung C. C., 2021, The Astronomer's Telegram, 14939, 1

Rastinejad J. C., et al., 2022, arXiv e-prints, p. arXiv:2204.10864

Rees M. J., 1988, Nature, 333, 523

Rees M. J., Meszaros P., 1992, MNRAS, 258, 41

Remillard R. A., McClintock J. E., 2006, ARA&A, 44, 49

Resmi L., Zhang B., 2016, ApJ, 825, 48

Resmi L., et al., 2005, A&A, 440, 477

Rhodes L., et al., 2020, MNRAS, 496, 3326

Rhodes L., Fender R., Williams D. R. A., Mooley K., 2021a, MNRAS, 503, 2966

Rhodes L., Van der Horst A., Chastain S., Fender R., Tremou E., ThunderKAT Collaboration. 2021b, GRB Coordinates Network, 30924, 1

Rhodes L., van der Horst A. J., Fender R., Aguilera-Dena D. R., Bright J. S., Vergani S., Williams D. R. A., 2022a, Monthly Notices of the Royal Astronomical Society, 513, 1895

Rhodes L., Fender R. P., Motta S., van den Eijnden J., Williams D. R. A., Bright J., Sivakoff G. R., 2022b, Monthly Notices of the Royal Astronomical Society, 513, 2708

Rickett B. J., 1977, ARA&A, 15, 479

Roming P. W. A., et al., 2005, Space Sci. Rev., 120, 95

Russell D. M., Miller-Jones J. C. A., Maccarone T. J., Yang Y. J., Fender R. P., Lewis F., 2011, ApJ, 739, L19

Russell T. D., et al., 2019, ApJ, 883, 198

Russell T. D., et al., 2021, MNRAS, 508, L6

Rybicki G. B., Lightman A. P., 1986, Radiative Processes in Astrophysics. Wiley

Saikia P., Russell D. M., Baglio M. C., Bramich D. M., Lewis F., 2020, The Astronomer's Telegram, 13719, 1

Sarbadhicary S. K., et al., 2021, ApJ, 923, 31

Sari R., 1997, ApJL, 489, L37

Sari R., Esin A. A., 2001, ApJ, 548, 787

Sari R., Piran T., Halpern J. P., 1999a, ApJ, 519, L17

Sari R., Piran T., Halpern J. P., 1999b, ApJ, 519, L17

Schlegel D. J., Finkbeiner D. P., Davis M., 1998, ApJ, 500, 525

Scholz P., et al., 2016, ApJ, 833, 177

Schroeder G., Alexander K. D., Fong W., Rouco Escorial A., Laskar T., Berger E., 2021, GRB Coordinates Network, 30658, 1

Schulze S., et al., 2011, A&A, 526, A23

Shahmoradi A., Nemiroff R. J., 2015, MNRAS, 451, 126

Shakura N. I., Sunyaev R. A., 1973, Symposium - International Astronomical Union, 55, 155–164

Shirey R. E., Bradt H. V., Levine A. M., 1999, ApJ, 517, 472

Shrestha M., Melandri A., Smith R., Steele I. A., Kobayashi S., Mundell C., Gomboc A., Guidorzi C., 2020, GRB Coordinates Network, 29085, 1

Siegel M. H., et al., 2018, GRB Coordinates Network, 22973, 1

Soderberg A. M., et al., 2006, ApJ, 650, 261

Solomon P. M., Rivolo A. R., Barrett J., Yahil A., 1987, ApJ, 319, 730

Staley T. D., Fender R., 2016, arXiv e-prints, p. arXiv:1606.03735

Staley T. D., et al., 2013, MNRAS, 428, 3114

Starling R. L. C., Wijers R. A. M. J., Hughes M. A., Tanvir N. R., Vreeswijk P. M., Rol E., Salamanca I., 2005, MNRAS, 360, 305

Starling R. L. C., van der Horst A. J., Rol E., Wijers R. A. M. J., Kouveliotou C., Wiersema K., Curran P. A., Weltevrede P., 2008, ApJ, 672, 433

Stewart A. J., Muñoz-Darias T., Fender R. P., Pietka M., 2018, MNRAS, 479, 2481

Svinkin D., Frederiks D., Ridnaia A., Tsvetkova A., Konus-Wind Team 2020, GRB Coordinates Network, 28301, 1

Swinbank J. D., et al., 2015, Astronomy and Computing, 11, 25

Tanvir N. R., et al., 2022, GRB Coordinates Network, 31602, 1

Tawara Y., et al., 1984, ApJ, 276, L41

Taylor G., 1950, Proceedings of the Royal Society of London Series A, 201, 159

Taylor G. B., Carilli C. L., Perley R. A., eds, 1999, Synthesis Imaging in Radio Astronomy II Astronomical Society of the Pacific Conference Series Vol. 180

Taylor G. B., Frail D. A., Berger E., Kulkarni S. R., 2004, ApJ, 609, L1

Tetarenko A. J., et al., 2017, MNRAS, 469, 3141

Thompson A. R., Clark B. G., Wade C. M., Napier P. J., 1980, ApJS, 44, 151

Thompson A. R., Moran J. M., Swenson George W. J., 2017, Interferometry and Synthesis in Radio Astronomy, 3rd Edition. Springer, doi:10.1007/978-3-319-44431-4

Toma K., Wu X.-F., Mészáros P., 2009, ApJ, 707, 1404

Tramper F., Sana H., De Koter A., 2016, ApJ, 833, 133

Tremou L., Heywood I., Vergani S. D., Woudt P. A., Fender R. P., Horesh A., Passmoor S., Goedhart S., 2019, GRB Coordinates Network, 23760, 1

Troja E., et al., 2019, MNRAS, 489, 1919

Ursi A., et al., 2021, GRB Coordinates Network, 30372, 1

Valeev A. F., et al., 2019, GRB Coordinates Network, 25565, 1

Valtaoja E., Terasranta H., Urpo S., Nesterov N. S., Lainela M., Valtonen M., 1992, A&A, 254, 80

Van Paradijs J., Kouveliotou C., Wijers R. A. M. J., 2000, Annu. Rev. Astron. Astrophys., 38, 379

Van den Eijnden J., et al., 2020, MNRAS, 496, 4127

Van der Horst A. J., et al., 2008, Astron. Astrophys, 480, 35

Van der Horst A. J., Kouveliotou C., Gehrels N., Rol E., Wijers R. A. M. J., Cannizzo J. K., Racusin J., Burrows D. N., 2009, ApJ, 699, 1087

Van der Horst A. J., et al., 2014, MNRAS, 444, 3151

Van der Klis M., 1989, in Hunt J., Battrick B., eds, ESA Special Publication Vol. 1, Two Topics in X-Ray Astronomy, Volume 1: X Ray Binaries. Volume 2: AGN and the X Ray Background. p. 203

Van der Klis M., 1994, ApJS, 92, 511

Vaughan S., Edelson R., Warwick R. S., Uttley P., 2003, MNRAS, 345, 1271

Vielfaure J. B., et al., 2020, GRB Coordinates Network, 29077, 1

Vink J. S., De Koter A., 2005, A&A, 442, 587

Vreeswijk P. M., et al., 2018, GRB Coordinates Network, 22996, 1

Walker M. A., 1998, MNRAS, 294, 307

Wang X.-Y., Mészáros P., 2006, ApJ, 643, L95

Watson A. M., et al., 2021, GRB Coordinates Network, 30534, 1

Woosley S. E., 1993, ApJ, 405, 273

Yoon S.-C., 2017, MNRAS, 470, 3970

Zaninoni E., Bernardini M. G., Margutti R., Amati L., 2016, MNRAS, 455, 1375

Zauderer B. A., et al., 2011, Nature, 476, 425

Zauderer B. A., et al., 2013, ApJ, 767, 161

Zhang W., Woosley S. E., Heger A., 2004, ApJ, 608, 365

Zhang L.-L., Ren J., Huang X.-L., Liang Y.-F., Lin D.-B., Liang E.-W., 2021, ApJ, 917, 95

Zwart J. T. L., et al., 2008, MNRAS, 391, 1545

de Ugarte Postigo A., et al., 2021, GRB Coordinates Network, 30392, 1

van den Eijnden J., et al., 2021, MNRAS, 507, 3899

van der Laan H., 1966, Nature, 211, 1131